

University of Nevada, Reno

**Time-Space Relationships between Sediment-Hosted Gold Mineralization and  
Intrusion-Related Polymetallic Mineralization at Kinsley Mountain, NV**

A thesis submitted in partial fulfillment of the requirements for the degree of Master of  
Science in Geology

by  
Tyler J. Hill

Dr. John L. Muntean/Thesis Advisor

May, 2016



THE GRADUATE SCHOOL

We recommend that the thesis  
prepared under our supervision by

**TYLER J. HILL**

Entitled

**Time-Space Relationships between Sediment-Hosted Gold Mineralization and  
Intrusion-Related Polymetallic Mineralization at Kinsley Mountain, Nevada**

be accepted in partial fulfillment of the  
requirements for the degree of

**MASTER OF SCIENCE**

**Dr. John L. Muntean**, Advisor

**Dr. Mike W. Ressel**, Committee Member

**Dr. Jennifer Hill**, Graduate School Representative

David W. Zeh, Ph.D., Dean, Graduate School

**May, 2016**

## ABSTRACT

Carlin-type gold deposits (CTGDs) in north-central Nevada contain a large endowment of gold, making Nevada one of the world's leading gold producers. Most CTGDs occur in four distinct clusters, known as the Carlin Trend, Cortez, Getchell, and Jerritt Canyon. These four camps of CTGDs are estimated to contain >200 million ounces of Au and share common features, including the occurrence of gold in solid solution or as submicron particles in disseminated arsenian pyrite in large carbonate replacement bodies where alteration is dominated by decarbonatization and silicification of silty carbonate host rocks. CTGDs can be confused with other disseminated gold deposits hosted by predominantly carbonate-bearing sedimentary rocks that share many features with CTGDs, but also have many distinctly different characteristics and generally have lower endowments of gold. These similar deposits, referred to as here sediment-hosted gold deposits (SHGD), include distal-disseminated deposits temporally and spatially associated with upper crustal felsic intrusions, epithermal deposits hosted by carbonate rocks, and epizonal orogenic deposits hosted by carbonate rocks. A very important question to resolve is whether CTGDs and SHGDs represent a spectrum of deposits with a shared origin, in which CTGDs are an endmember, or whether they have different origins that ultimately resulted in similar looking alteration and mineralization.

Kinsley Mountain lies approximately 150 km east of the majority of large CTGDs in Nevada. SHGDs, intrusion-related tungsten skarn, and polymetallic carbonate replacement vein deposits have been mined from Kinsley Mountain, proximal to an Eocene intrusive center. Stratigraphically and structurally controlled SHGDs occur as replacement bodies in Cambrian shelf carbonates and siliciclastics. The SHGDs at

Kinsley are broadly similar to the large CTGDs to the west, but key differences are highlighted in this paper.

Kinsley Mountain underwent multiple episodes of contraction and extensional deformation in the Mesozoic. During the Eocene, a granodiorite stock and associated dikes were emplaced at ~40 Ma, with slightly later Eocene extension and volcanism. High-angle basin and range faulting began in the Miocene continues through the present. Quartz veins containing polymetallic mineralization cut the stock and polymetallic veins replace carbonate country rock proximal to the stock. Molybdenite in skarn near the stock returned a Re-Os age of  $37.88 \pm 0.3$  Ma. Numerous cogenetic dikes extend up to 4 km north of the stock into the area of the SHGDs. SHG mineralization is primarily hosted by the Cambrian Dunderberg Shale and Secret Canyon Shale. These units contain interbedded shale and limestone with up to 50% ferroan dolomite in shale beds. In strongly mineralized intervals, ferroan dolomite has been replaced by quartz and pyrite. A  $39.7 \pm 0.6$  Ma mineralized dike places a maximum age constraint on mineralization, whereas ~36-37 Ma unmineralized dacite to rhyolite flows that flank both sides of Kinsley Mountain and onlap Cambrian stratigraphy, place a minimum age on mineralization.

SHG mineralization is characterized by diagenetic or hydrothermal pyrite cores surrounded by euhedral, oscillatory zoned Au-bearing arsenian-pyrite rims. Locally, pyrite cores are surrounded by stibnite or tennantite-tetrahedrite, which are enveloped by arsenian-pyrite rims. Gold strongly correlates (correlation coefficient >0.5) with Ag, As, Hg, Sb, Te, and Tl. The ore-stage pyrite at Kinsley contrasts with ore stage pyrite in CTGDs, where the arsenian-rims are typically “fuzzy” in appearance and do not display

zoning. Additionally, the presence of early base metals has not been documented in Carlin-type mineralization. Sulfur isotope data on pyrite revealed  $\delta^{34}\text{S}$  values of  $\sim 3\text{‰}$ - $8\text{‰}$  for pyrite proximal to the stock, while pyrite from the SHGDs were significantly heavier ( $16\text{‰}$ - $25\text{‰}$ ). The differences suggest a magmatic source of sulfur for pyrite proximal to the stock and a sedimentary source or mixed magmatic and sedimentary source of sulfur for pyrite in SHG mineralization.

The hydrothermal system at Kinsley had two sulfur sources – a magmatic source that formed the intrusion-related polymetallic mineralization and a sedimentary crustal source that formed the SHGDs. In the SHGDs, carbonate-bearing shales rocks were preferentially sulfidized by the ore-fluid, forming Au-bearing arsenian-pyrite as Fe was liberated from ferroan dolomite during decarbonatization. The presence of euhedral pyrite, carbonate in ore zones, and lack of marcasite, kaolinite, or dickite suggests ore fluids that were higher in temperature and less acidic than ore fluids that form the large CTGDS in Nevada. Aluminum in hornblende geobarometry, typical formation depths of tungsten skarn deposits, and the lack of faulting between the stock and the SHGDs suggest depths of  $\geq 3$  km for ore formation. However, such depths require significant uplift between 40 Ma and 36 Ma. Shallower depths for the SHGDs are possible if the range was tilted northward.

## ACKNOWLEDGEMENTS

This project would not have been possible without the strong support of Pilot Gold and the Ralph J. Roberts Center for Research in Economic Geology (CREG). The Society of Economic Geologists also provided a grant for this study. When I showed up in Wendover, NV during the summer of 2013, I had no idea what I was doing. Until that point I had never heard of decalcification, let alone argillization. Quickly, I was brought up to speed through the “Randy Hannink School of Logging”. I am grateful for the patience of Randy Hannink, Pete Shabestari, and Kent Samuelson as I asked many questions, probably some that had them wondering what I was doing there. Additionally, I would like to thank Moira Smith, Vance Spalding, Jamie Robinson, and Jason Babcock for their advice and help along the way.

To my advisor John Muntean, I can’t thank you enough for everything you’ve done. I have learned more than I ever thought possible in a short 2 ½ years, most of it from you. I can’t count the number of times I came to you with a question, big and small, only to have you take time out of your busy day to fully answer. Thank you for your patience, mentorship, guidance, and passion for geology. It inspires all of your students to achieve their full potential.

I would like to thank my committee members Mike Ressel and Jennifer Hill. Mike, thank you for your insight into my project. Like John, you always had an open door and your passion for teaching and geology inspires others.

Others that helped immensely along the way include Paul O’Sullivan and GeoSeps Inc. during the mineral separation process, Ray Donelick for the apatite fission track dating, Matt Coble at the Stanford SHRIMP lab, Dr. Simon Poulson for the

completion of sulfur isotope analyses, and Dr. John McCormack for assistance with the Scanning Electron Microscope. Each of you played an important role in the completion of this thesis, and for that I am grateful.

I would like to thank my fellow CREG students including Wilson Bonner, Steve Howell, and Sergey Konyshchev among others. Our discussions about geology and life are some I will take with me forever. Through the long days and nights, we did it together. I couldn't have asked for a better group of people to be surrounded by for the past 2 ½ years.

Finally, I would like to thank my parents Troy and Judy, and my grandmother Sharon for their love and support as I followed my dreams out west. It was your guidance and parenting that made me who I am today. Thank you for always instilling the value of education.

## Table of Contents

Abstract.....	i
Acknowledgements.....	iv
List of Tables .....	vii
List of Figures.....	viii
Introduction.....	1
Regional and District Geology.....	6
Methods.....	20
Igneous Rocks.....	25
Intrusion-Related Metamorphism, Alteration, and Mineralization.....	42
Sedimentary Rock Hosted Gold Mineralization .....	52
District Surface Geochemistry .....	88
Geochronology.....	94
Sulfur Isotopes .....	112
Discussion.....	119
Appendix A: Quartz and calcite solubility diagram .....	135
Appendix B: Microprobe Analyses of Hornblende .....	136
Appendix C: Whole-rock Geochemistry .....	141
Appendix D: Microprobe Data for Pyrite.....	145
Appendix E: SHRIMP Methods .....	156
Appendix F: SHRIMP Data.....	159
Appendix G: Apatite Fission Track Data.....	167
Appendix H: Scheelite Solubility Diagram .....	168
Appendix I: Additional SEM Images .....	169

## List of Tables

Table 1: Petrography of igneous rocks .....	27
Table 2: Al-in-hornblende results .....	30
Table 3: Selected microprobe analyses .....	79
Table 4: SHRIMP dates for intrusive and extrusive rocks .....	98
Table 5: SHRIMP dates for inherited zircon cores .....	101
Table 6. Re-Os date on molybdenite.....	107
Table 7. Apatite fission track analyses .....	110
Table 8. Sulfur isotope analyses .....	115
Table 9. Comparison between Kinsley and CTGDs.....	124

## List of Figures

Figure 1. A: Regional deposit map, B: District geologic map.....	4
Figure 2. Stratigraphic column .....	9
Figure 3. Geddes Limestone .....	13
Figure 4. Secret Canyon Shale.....	13
Figure 5. Clarks Spring Limestone .....	14
Figure 6. Hamburg Formation .....	14
Figure 7. Dunderberg Shale .....	15
Figure 8. Notch Peak Limestone .....	15
Figure 9. Ely Limestone.....	16
Figure 10. Pennsylvanian black shale.....	16
Figure 11. Geologic map of the southern portion of Kinsley .....	26
Figure 12. Map of aluminum-in-hornblende sample locations.....	30
Figure 13. Streckeisen diagram.....	35
Figure 14. TAS diagram .....	35
Figure 15. K <sub>2</sub> O vs SiO <sub>2</sub> diagram.....	36
Figure 16. Alumina saturation index .....	36
Figure 17. TiO <sub>2</sub> vs SiO <sub>2</sub> diagram .....	37
Figure 18. Zr vs SiO <sub>2</sub> diagram .....	38
Figure 19. REE diagram of intrusive rocks .....	39
Figure 20. REE diagram of all igneous rocks.....	39
Figure 21. REE diagram of extrusive rocks.....	40
Figure 22. Backscatter SEM image of garnet.....	43
Figure 23. Field photo of garnet at stock contact.....	43
Figure 24. A: Field photo of Hamburg Dolomite, B: Backscatter SEM image of mineralization .....	44
Figure 25. Field photo of gossan vein.....	46
Figure 26. A: Field photo of quartz vein, B: Field photo of jasperoid .....	47
Figure 27. Bar and whisker diagram for intrusion-related samples.....	48
Figure 28. Photomicrograph of secondary biotite.....	49
Figure 29. Backscatter SEM image of potassic alteration .....	49
Figure 30. Inset from figure 11 of jasperoid corridor .....	50
Figure 31. Paragenetic diagram for intrusion-related mineralization .....	51
Figure 32. District geologic map .....	53
Figure 33. Dunderberg Shale transect, A, C, E, G: hand sample, B, D, F, H: Backscatter SEM image.....	56
Figure 34. Secret Canyon Shale transect, A, C, E, G: hand sample, B, D, F, H: Backscatter SEM image.....	61
Figure 35. Backscatter SEM image of mineralized pyrite in calcite and quartz.....	63
Figure 36. Backscatter SEM image of secondary apatite .....	64

Figure 37. A. Reflected light photomicrograph of pyrite, B. Backscatter SEM image of pyrite .....	65
Figure 38. A: Backscatter SEM image of arsenian-pyrite, B: Backscatter SEM image of pyrite with galena.....	66
Figure 39. Historic mine area stacked assays and structural controls.....	67
Figure 40. Cross-section of historic mine area .....	68
Figure 41. Microprobe image and results from Dunderberg Shale pyrite .....	69
Figure 42. A: Backscatter SEM image of zoned arsenian-pyrite in the Secret Canyon Shale, B: Reflected light photomicrograph of pyrite in the Secret Canyon Shale.....	71
Figure 43. A: Backscatter SEM image of zoned arsenian-pyrite and stibnite in the Secret Canyon Shale, B: Backscatter SEM image of stibnite, tennantite-tetrahedrite, and an arsenian-pyrite rim in the Secret Canyon Shale.....	72
Figure 44. Microprobe image and results from Secret Canyon Shale pyrite.....	73
Figure 45. Plan view grade-thickness map of West Flank.....	74
Figure 46. Cross-section through West Flank.....	74
Figure 47. A: Bar and whisker diagram for Dunderberg Shale mineralized samples, B: Bar and whisker diagram for Secret Canyon Shale mineralized samples .....	75
Figure 48. A: Backscatter SEM image of pyrite from Secret Spot. B: Backscatter SEM image of pyrite with inclusions of sphalerite and sulfosalts from Secret Spot.....	77
Figure 49. Microprobe image and results from Secret Spot pyrite.....	78
Figure 50. Au vs As from microprobe data .....	80
Figure 51. Backscatter SEM image of scheelite enveloping arsenian-pyrite .....	82
Figure 52. Silicified and brecciated drill core interval containing base metals .....	82
Figure 53. Spearman correlation matrices, A: East side Dunderberg Shale oxide mineralization, B: East side Dunderberg Shale sulfide mineralization, C: West side Dunderberg Shale oxide mineralization, D: West side Dunderberg Shale sulfide mineralization, E: West Flank Secret Canyon Shale oxide mineralization, F: West Flank Secret Canyon Shale sulfide mineralization, G: Intrusion-related mineralization.....	84
Figure 54. A: As surface geochemistry, B: Au surface geochemistry .....	90
Figure 55. A: Hg surface geochemistry, B: Sb surface geochemistry, C: Tl surface geochemistry, D: Te surface geochemistry .....	91
Figure 56. A: Cu surface geochemistry, B: Mo surface geochemistry, C: Pb surface geochemistry, D: Zn surface geochemistry .....	92
Figure 57. A: Ag surface geochemistry, B: W surface geochemistry .....	93
Figure 58. Zircons in CL.....	94
Figure 59. SHRIMP dates and locations.....	95
Figure 60. SHRIMP dates through time by lithology.....	96
Figure 61. Tera-Wasserburg diagrams.....	97
Figure 62. Interpretation of Kinsley Mountain basement.....	100
Figure 63. A: Eu/Eu* diagram for Carlin zircons, B: Eu/Eu* diagram for Western Cascade zircons, C: Eu/Eu* diagram for Kinsley zircons .....	104

Figure 64. Molybdenite hand sample.....	106
Figure 65. Secondary apatite in transmitted light.....	109
Figure 66. Apatite fission track results.....	110
Figure 67. Sulfur isotope results.....	114
Figure 68. Seawater sulfate curve and sulfides from SHGDs.....	116
Figure 69. Schematic model of formation for Kinsley.....	122
Figure 70. Au vs S diagram.....	125

## I. Introduction

Carlin-type gold deposits (CTGDs) in north-central Nevada contain a large endowment of gold making Nevada one of the world's leading gold producers (Muntean et al., 2011). Most CTGDs occur in four distinct clusters, which are referred to as the Carlin Trend, Cortez, Getchell, and Jerritt Canyon. These four camps of CTGDs are estimated to contain >200 million ounces of Au and share common features. Shared features include the occurrence of gold in solid solution or as submicron particles in disseminated arsenian pyrite in large replacement bodies where alteration is characterized mainly by decarbonatization and silicification of carbonate-bearing lithologies (Hofstra and Cline, 2000; Cline et al., 2005; Muntean et al., 2011). The deposits are typically anomalous in Au, As, Hg, Sb, and Tl and contain low amounts of Ag and base metals (Hofstra and Cline, 2000). Although CTGDs have been intensely studied, there is currently no consensus on a model for their genesis. Various models for the origin of CTGDs incorporate (1) magmatic fluids (Sillitoe and Bonham, 1990; Henry and Ressel, 2000; Johnston and Ressel, 2004; Muntean et al., 2011), (2) meteoric water circulation (Illchik and Barton, 1997; Emsbo et al., 2003; Seedorff and Barton 2004), and (3) deep metamorphic fluids (Seedorff, 1990; Hofstra and Cline, 2000; Cline et al., 2005; Large et al., 2011).

As pointed out by Hofstra and Cline (2000), CTGDs can be confused with other disseminated gold deposits hosted predominantly by carbonate-bearing sedimentary rocks that share many features with CTGDs, but also have many distinctly different

characteristics and generally have lower endowments of gold. These similar deposits, referred to as here sediment-hosted gold deposits (SHGD), include distal-disseminated, epithermal deposits hosted by carbonate rocks, and epizonal orogenic deposits (Cline et al., 2005). Distal-disseminated deposits typically occur within 5 km of intrusions. Examples include Lone Tree, Cove, and Star Pointer (Nevada), Mercur and Barneys Canyon (Utah), Jeronimo (Chile), Bau (Malaysia), Mesel (Indonesia), and Zarshuran (Iran). A variant of distal disseminated systems are deposits associated with reduced intrusions and include Bald Mountain (Nevada), True North (Alaska), and Brewery Creek (Yukon). Examples of epithermal deposits hosted by carbonate rocks that have similarities to CTGDs include the Standard and Relief Canyon deposits, among others, in Nevada. Examples of epizonal orogenic deposits include Fosterville (Australia) and Reefton (New Zealand), and likely the deposits in the Golden Triangle (China) (Su et al., 2009).

Decarbonatization, silicification, and sulfidation are characteristic hydrothermal processes of CTGDs, but these processes were also operative in SHGDs. However, cooling hydrothermal fluids of differing origins, which are quartz-saturated and interacting with carbonate rocks at temperatures below 300° C and pressures below 500 bars, will tend to dissolve carbonate and precipitate quartz, because of the retrograde solubility of carbonate and the prograde solubility of quartz (Barton et al., 1997) (See Appendix A). This allows for a wide diversity of origins and fluid sources for SHGDs. Some of the key differences with CTGDs observed in distal disseminated deposits include the much higher abundance of base metal sulfides, a correlation between gold and base metals, higher silver concentrations, mineralized quartz veins, and the presence of

native gold (Alvarez, 1988; Flanigan et al., 2000; Goldfarb, 2004; Thompson, 2004; Reid, 2010). Epithermal SHGDs deposits commonly have higher silver grades than CTGDs and ore is commonly characterized by open space fillings, including quartz veins and matrices of breccias. Epizonal orogenic SHGDs have evidence of higher temperatures and pressures of formation, common carbonate-stable alteration, quartz veins, and no evidence of contemporaneous magmatism.

Future advances in understanding the large CTGDs in Nevada will come from a better understanding of SHGDs and their key differences and similarities in terms of hydrothermal processes. A very important question to resolve is whether CTGDs and SHGDs represent a spectrum of deposits with a shared origin, in which CTGDs are an endmember, or whether they have different origins that ultimately resulted in similar looking alteration and mineralization.

Kinsley Mountain lies approximately 150 km east of the majority of large CTGDs in Nevada (Fig. 1). SHGDs, intrusion-related tungsten skarn, and polymetallic vein deposits have been mined from Kinsley Mountain. In 2013 Pilot Gold Inc. began exploring for SHGDs, from which Alta Gold produced 138,000 oz of gold from 1995-1999 (Robinson, 2005). Kinsley Mountain contains stratigraphically and structurally controlled SHGDs that occur as replacement bodies in Cambrian shelf carbonates and siliciclastics. SHGDs at Kinsley Mountain are characterized by euhedral, well zoned, Au-bearing arsenian-pyrite rims surrounding diagenetic or pre-ore stage hydrothermal pyrite. These textures are broadly similar to the large CTGDs to the west, but, key differences are highlighted in this paper.

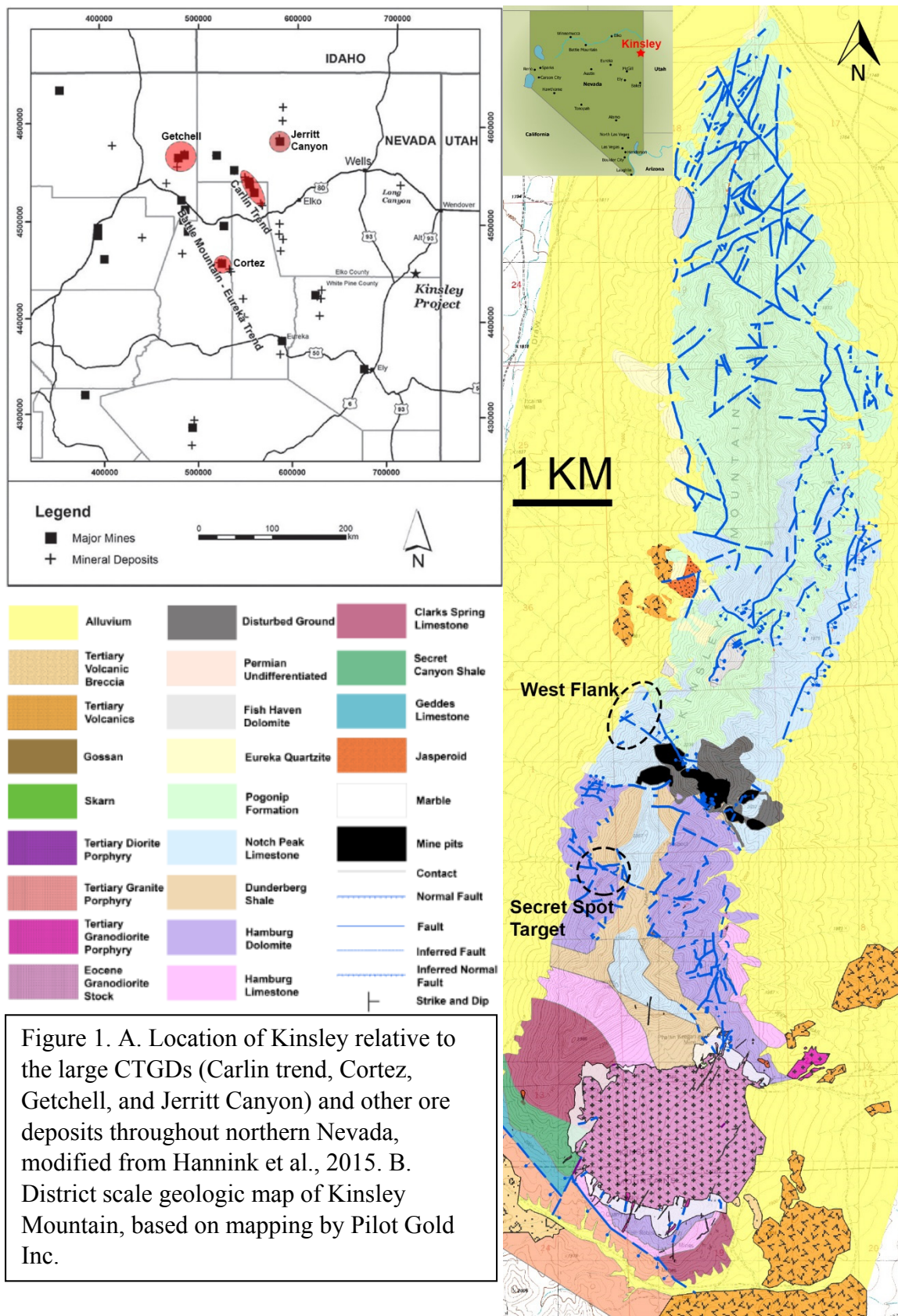


Figure 1. A. Location of Kinsley relative to the large CTGDs (Carlin trend, Cortez, Getchell, and Jerritt Canyon) and other ore deposits throughout northern Nevada, modified from Hannink et al., 2015. B. District scale geologic map of Kinsley Mountain, based on mapping by Pilot Gold Inc.

Three kilometers south of the SHGDs, a late Eocene intrusive center, characterized by a granodiorite stock and associated dikes, intrudes the Cambrian section forming a contact aureole with marble and lesser hornfels (Fig. 1). Mineralization spatially associated with the intrusive complex includes proximal metasomatic garnet-pyroxene skarn that was mined for tungsten and polymetallic mineralization associated with quartz veins and gossanous replacements that occur within 1.5 km of the stock. The skarn and polymetallic mineralization occur at approximately the same elevation as the SHGDs located 3 km to the north, and no major faults occur between the SHGDs and the intrusive complex. Dikes from the intrusive complex extend northward and are common in the area of the SHGDs. Andesitic to rhyolitic volcanic rocks, ~36 Ma in age, occur along the flanks of the range, and locally onlap Paleozoic strata. The volcanics are locally argillized, but are nowhere mineralized.

The focus of this study is to document, through detailed mapping, petrography, geochemistry, and geochronology, the time-space relationships between the Eocene intrusive rocks, and the various types of hydrothermal mineralization at Kinsley. Specific emphasis is placed on documenting the similarities and differences between the SHGDs and the intrusion-related skarn and polymetallic mineralization. Kinsley presents a unique opportunity to test the hypothesis of whether SHGDs, with many similarities to CTGDs are genetically related in time and space to granitic magmatism. Core logging and detailed geologic mapping focused on cross-cutting relationships between dikes and mineralization have been utilized to document time-space relationships.

## II. Regional and District Geology

### Regional Geology

Kinsley Mountain is located in northeastern Nevada in the eastern portion of the Great Basin physiographic province. The stratigraphic sequence in this part of Nevada is characterized by nearly continuous sedimentation along the western passive margin of North America from the upper Precambrian into the early Triassic (Cook, 2015). The age of Precambrian basement can be inferred from the age of older zircon cores contained in magmatic zircons from the stock and dikes dated in this study. U-Pb geochronology on detrital zircons found in the Neoproterozoic McCoy Creek Group, Prospect Mountain Quartzite, and Busby Group from the nearby Deep Creek and Pilot Ranges showed no detrital zircons older than 2.0 Ga. Analysis of sedimentary structures showed the sedimentary rocks, from which the zircons were analyzed, were locally derived, leading to the interpretation that the Yavapai Province (1.7 – 1.8 Ga) underlies northeastern Nevada (Perry, 2010).

From the Neoproterozoic through the Triassic, Kinsley Mountain and the surrounding region was located on the shelf of a passive continental margin. During the Neoproterozoic and Early Cambrian, sedimentation was clastic-dominant. The Middle Cambrian through the Triassic was dominated by carbonate deposition with intermittent episodes of siliciclastic input. Deposition was nearly continuous with minor episodic erosional regressions through the end of the Ordovician (Dickinson, 2006; Cook, 2015). The first orogenic event to affect Kinsley was likely the Middle Jurassic Elko Orogeny, though it is uncertain what structures formed at Kinsley during this event. The Elko

Orogeny is defined by eastward directed contractional deformation with the development of folding, thrusting, and east to south-east striking, high-angle tear faults (Thorman et al., 2004). Beginning in the Middle Triassic the Farallon plate began to subduct eastward beneath the North American plate. The Melrose pluton in the Dolly Varden Mountains (165 Ma), located 19 km northwest of Kinsley Mountain and the Whitehorse Mountain pluton (160 Ma), located 12 km north of Kinsley Mountain were emplaced in the Late Jurassic as part of back-arc magmatism (Miller and Hoisch, 1995 and Zamudio 1995). Copper, lead, silver, and zinc mineralization from a Jurassic intrusion-related skarn system is found in the Dolly Varden Mountains (Atkinson et al., 1982). Minor amounts of SHG mineralization have been found in the Whitehorse Mountains. The Sevier Orogeny began in the Early Cretaceous and continued into the Late Cretaceous (DeCelles, 2004). By the end of the Sevier Orogeny, the Great Basin was a broad, elevated plateau similar to the Altiplano of the modern Andes (Dickinson, 2006).

The subduction of the Farallon slab began to shallow around ~65 Ma, shutting off magmatism in Nevada. The shallow slab subduction continued until ~45 Ma. At ~45 Ma the Farallon slab began to delaminate or roll-back, resulting in a southwestward sweeping of magmatism across the Great Basin. It is during this time period that Carlin-type deposits were formed across Nevada (Hofstra et al., 1999; Arehart et al., 2003). Pre-basin and range extensional tectonism began to take place during slab rollback and is viewed as intra-arc or back-arc deformation characterized by detachment faulting (Dickinson, 2006). However, Eocene volcanism generally preceded major Basin and Range extensional deformation (Dickinson, 2002). As detailed below, Kinsley Mountain was uplifted prior to 36 Ma. Basin and Range extensional tectonism, characterized by high-

angle block faulting, began in the Early Miocene and continues through the present (Dickinson, 2006).

### Stratigraphy

Continuous stratigraphy, albeit complexly faulted, ranging from Middle Cambrian to Early Silurian is exposed at Kinsley (Fig. 2). The SHGDs are hosted by specific Cambrian units, mainly in the Dunderberg Shale, and carbonate-bearing shales in the Clarks Spring and Shale members of the Secret Canyon Shale. Lesser amounts of gold mineralization are hosted locally in the Notch Peak Limestone and the Hamburg Formation. The SHGDs that were previously mined were hosted by Dunderberg Shale and Notch Peak Limestone.

The Middle Cambrian Geddes Limestone (Nolan et al., 1956) is the oldest known stratigraphic unit at Kinsley Mountain and only crops out at the very southern extent of the range in the footwall of a large-displacement northwest-striking fault (Fig. 3). The unit's total thickness is unknown, but is at least 300 m thick where it has been intersected in drilling. It is a medium to dark blue gray limestone with common calcite veining, thin (1-2 cm) interbedded silty layers, and local zones of dolomitization and karsting.

The Secret Canyon Shale overlies the Geddes Limestone. The unit crops out in the southern portion of the range. This unit consists of a lower shale member and an upper interbedded limestone and shale member known as the Clarks Spring member of Middle Cambrian in age (Nolan, 1956). Based on drilling along the western flank, the unit is 100-150 m thick. Where low-angle faulting occurs, the lower shale section is

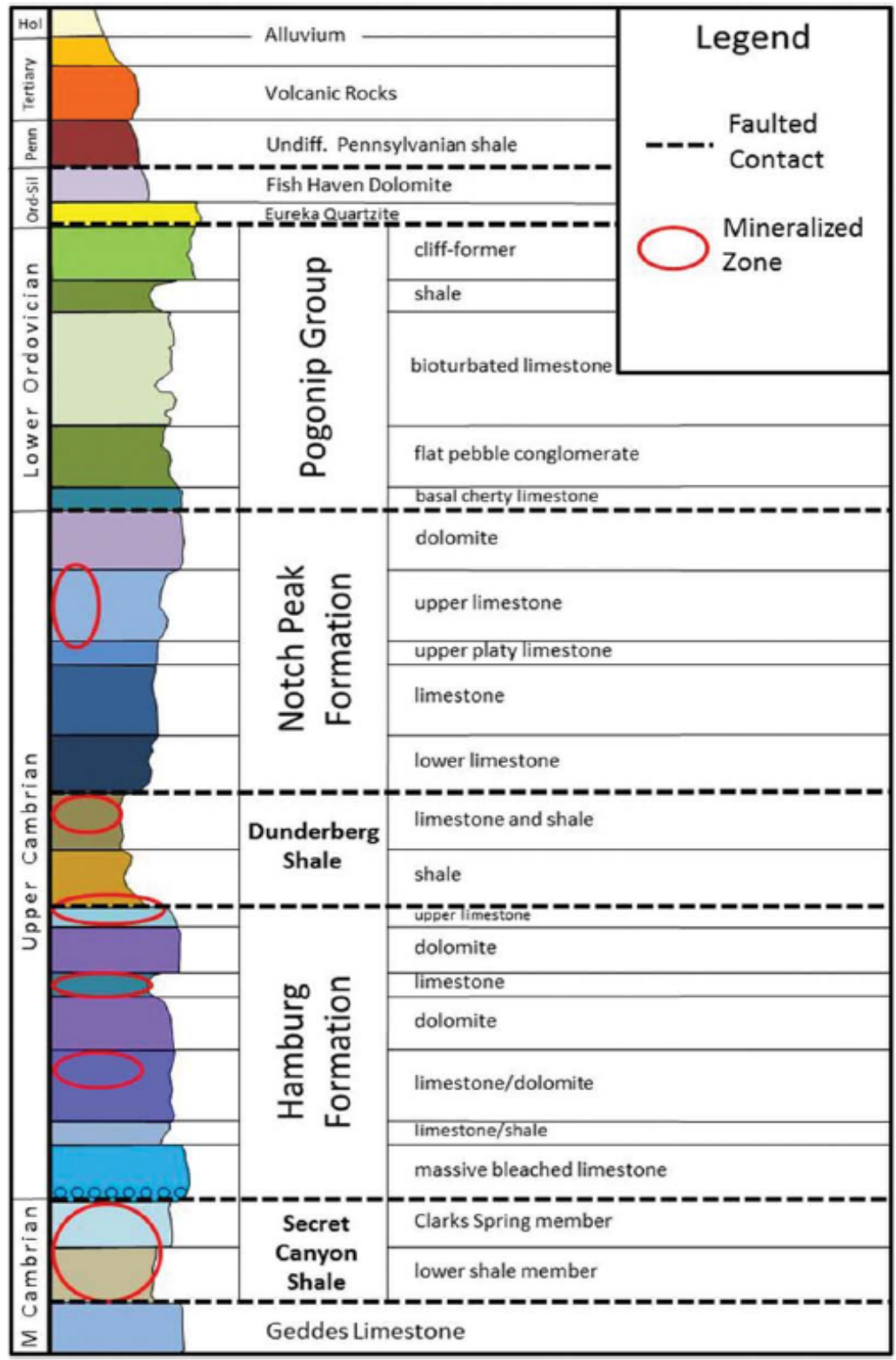


Figure 2. Stratigraphic column for Kinsley Mountain (Hannink et al., 2015). Shows stratigraphic units that host gold mineralization

thinned substantially, but there is only minor attenuation of the Clark Springs member. The lower shale interval is characterized by 1-10 m thick sections of dark gray shale composed of beds 1-10 cm thick with lesser amounts of interbedded 1-2m thick medium to dark gray limestone (Fig. 4). Trilobites and other fossil hash can be found in the Secret Canyon Shale. Where it is exposed in the southern portion of the range near the stock, it is commonly metamorphosed to biotite hornfels. The overlying Clarks Spring member contains 1-10 cm rhythmically interbedded calcareous shale and dark gray, locally nodular, limestone, with common dark gray limestone beds up to 5 m thick (Fig. 5). Gold mineralization is found in both the Clarks Spring member and the lower shale dominant portion of the Secret Canyon Shale.

The Late Cambrian Hamburg Formation (Nolan et al., 1956) is approximately 200 m thick and consists of dolostone, limestone, and shale units (Fig. 6). The base of the Hamburg is a massive medium to dark gray limestone. Overlying the massive limestone is a medium bedded limestone with thin (1-5 cm) shale interbeds that locally hosts gold mineralization. Units of medium to dark gray dolostone and limestone are characteristic of the middle portion of the Hamburg Formation. The dolostone is patchy, not stratabound, and contains local zebra textures, suggesting a hydrothermal origin, at least in part. The upper portion of the Hamburg is distinguished by a ~100 m thick section of medium grained, white to light gray dolostone. Drilling indicates this upper dolostone section is completely cut out along the western flank of Kinsley Mountain. Above this dolostone, the top of the Hamburg is characterized by a 5-15 m limestone bed that is typically altered to a gold-bearing jasperoid. However, this limestone bed is commonly cut out by low-angle faulting prior to mineralization.

The Late Cambrian Dunderberg Shale (Nolan et al., 1956) overlies the Hamburg Formation and based on drilling, consists of two subunits of interbedded limestone and shale (Fig. 7). In the lower subunit, thinly bedded shale 1-10 cm thick composes continuous sections of shale up to 5-10 m thick with minor amounts of interbedded medium to greenish gray limestone. The limestone beds locally occur in sections up to 5-10 m thick. The limestone beds are commonly nodular and discontinuous, a characteristic of soft sediment deformation (Harry Cook, 2014 pers. comm.). The upper subunit of the Dunderberg is characterized by a medium to greenish gray nodular limestone that commonly contains thinly bedded shale 1-10 cm thick with continuous shale sections ranging from 10 cm to 5 m thick. The Dunderberg Shale is an important host to SHGDs on both flanks of Kinsley Mountain.

The Late Cambrian Notch Peak Formation overlies the Dunderberg Shale. The contact with the Dunderberg Shale is commonly a low-angle fault. The Notch Peak consists of a ~100 m thick lower section of light to medium gray limestone with common 1-10 cm thick silty interbeds (Fig. 8). The upper section of the Notch Peak is a medium gray dolostone that is approximately 30 m thick. Karst features, bioturbation, and calcite veining are a common feature of the Notch Peak Formation. Gold ore was locally mined from the Notch Peak in the area of SHGDS.

The Pogonip Group of Ordovician age (Nolan et al., 1956) overlies the Notch Peak Formation. The Pogonip is characterized by cherty limestone, siltstone, flat pebble conglomerate, shale, and bioturbated limestone. The Pogonip Group is not known to be an important host to gold mineralization at Kinsley Mountain.

The Late Ordovician Eureka Quartzite and overlying Ordovician-Silurian Fish

Haven Dolomite overlies the Pogonip Group. The Eureka and Fish Haven are found along the ridge-crest of Kinsley Mountain, north of the area of known SHGDs. The Eureka Quartzite is also located along the west flank of the range where it is in low-angle fault contact with the Pogonip Formation.

Pennsylvanian and Permian stratigraphy has also been identified at Kinsley Mountain. South of the stock a northwest-striking normal fault places a complicated succession of sandstone, calcareous sandstone, calcareous siltstone, and minor dolomudstones of Permian and Pennsylvanian age against Middle Cambrian rocks (Fig. 9). The Permian rocks are likely part of the Arcturus Formation, while Pennsylvanian rocks are likely Ely Limestone, occurring as sequences in which well-bedded limestones are overlain by impure sandy limestone, calcareous siltstone, fine-grained variably calcareous sandstone, and minor lime mudstone and dolomudstone. Massive limestone units are mainly bioclastic packstones and wackestones. Fusulinids are common, in places occurring in rock-forming abundances. The Permian stratigraphy is ~425 m thick. An unnamed Pennsylvanian shale has been intersected in drill holes along the west flank of Kinsley Mountain. The Pennsylvanian unit is a limey black shale containing patchy ferroan dolomite, abundant zircon, monazite, and apatite (Fig. 10). Thin 1-2 cm sandstone interbeds are common throughout shale. This unit was dated with palynology and conodont samples and found to be time-correlative with the Ely Limestone (Atokan to Desmoinesian) (Zippi, 2014). The Pennsylvanian unit is in low-angle fault contact with underlying Notch Peak Limestone and Pogonip Group where intersected in drill holes.



Figure 3. Geddes Limestone. A. Drill core showing light gray limestone with thin siltstone beds. B. Photomicrograph showing ooids (cross polars).



Figure 4. Lower Shale Member of the Secret Canyon Shale. A. Exposure of interbedded limestone and shale and a small normal fault. B. Drill core of interbedded shale and limestone in the Secret Canyon Shale. C. Photomicrograph (crossed polars) showing contact between limestone (lighter area to left) that is composed of predominantly calcite with minor sericite and shale (darker area to right) composed predominantly of sericite with lesser pyrobitumen, quartz, and pyrite.

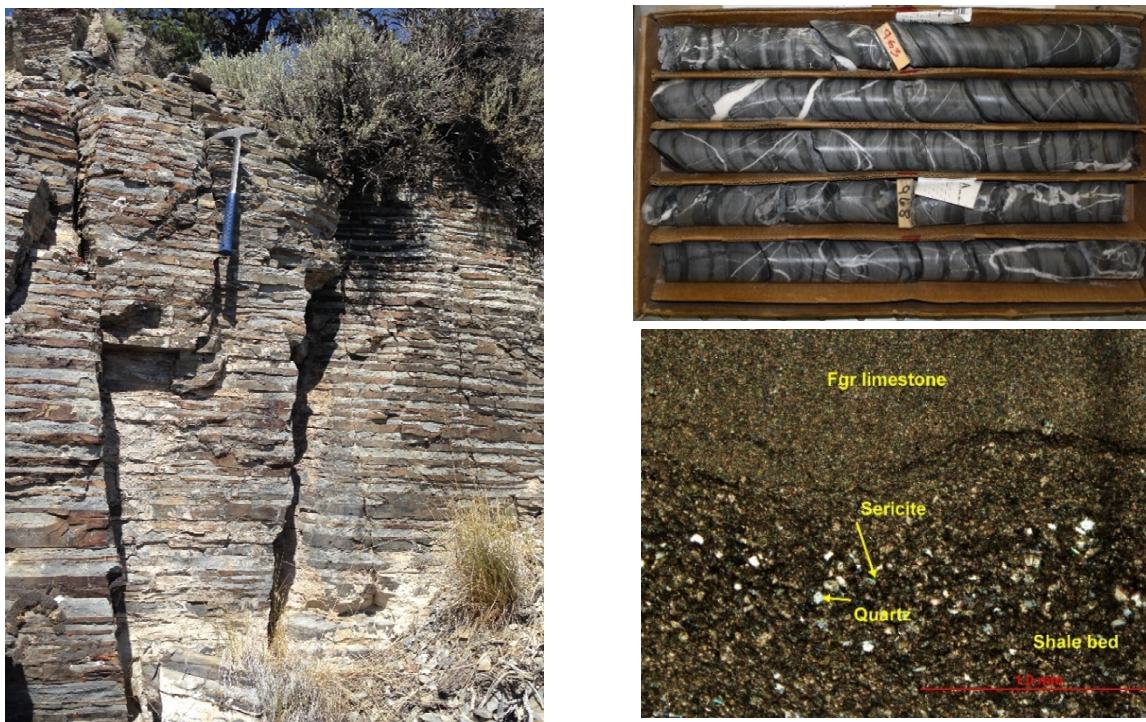


Figure 5. Clarks Spring Member of the Secret Canyon Shale. A. Outcrop showing rhythmic bedding between limestone and shale. The shale layers are brown due to contact metamorphism to biotite. B. Drill core showing interlayered limestone (gray) and unmetamorphosed shale (dark gray to black). C. Photomicrograph (crossed polars) showing contact between limestone (lighter area in top half that is fine grained calcite) and shale (darker area in bottom half that is composed predominantly of sericite with lesser quartz silt and pyrobitumen).



Figure 6. Hamburg Formation. A. Outcrop of Hamburg Formation showing medium gray limestone. B. Drill core of limestone. C. Drill core of dolomite.

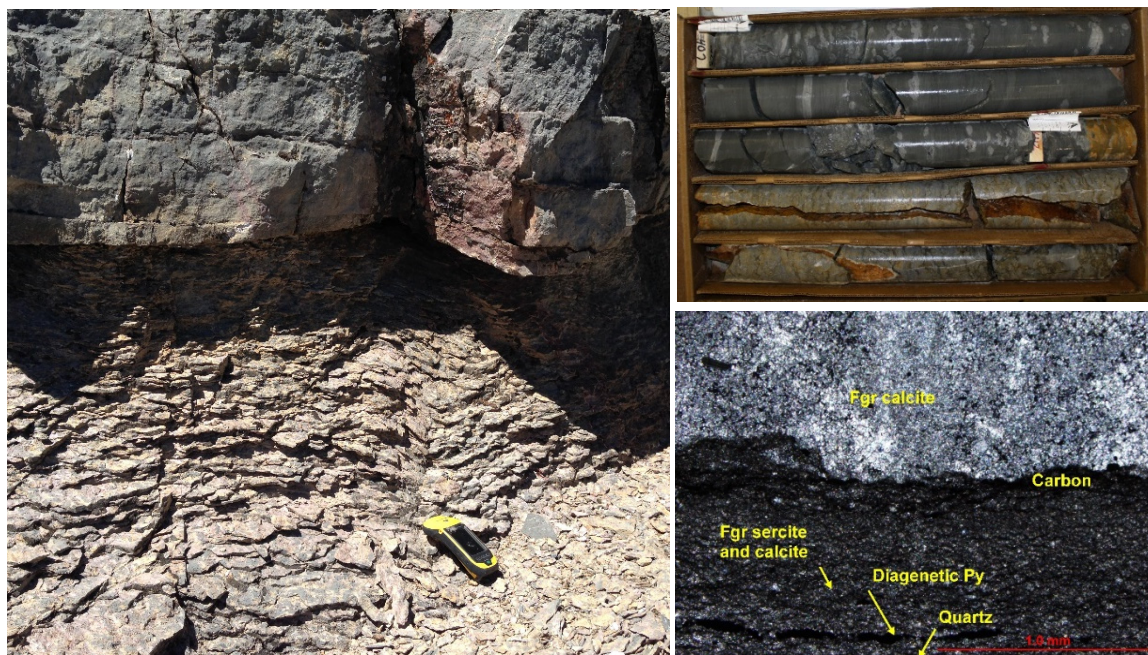


Figure 7. Dunderberg Shale. A. Surface exposure showing shale transitioning upward into limestone beds. B. Drill core showing limestone nodules in a matrix of shale. C. Photomicrograph (crossed polars), showing contact between limestone bed (top) composed of fine grained calcite and shale (bottom) composed of sericite, calcite, quartz, and diagenetic pyrite.



Figure 8. Notch Peak Formation A. Exposure of a siltstone bed between two beds of limestone. B. Drill core of light gray limestone. C. Photomicrograph (crossed polars) of silty layer in fine-grained limestone.

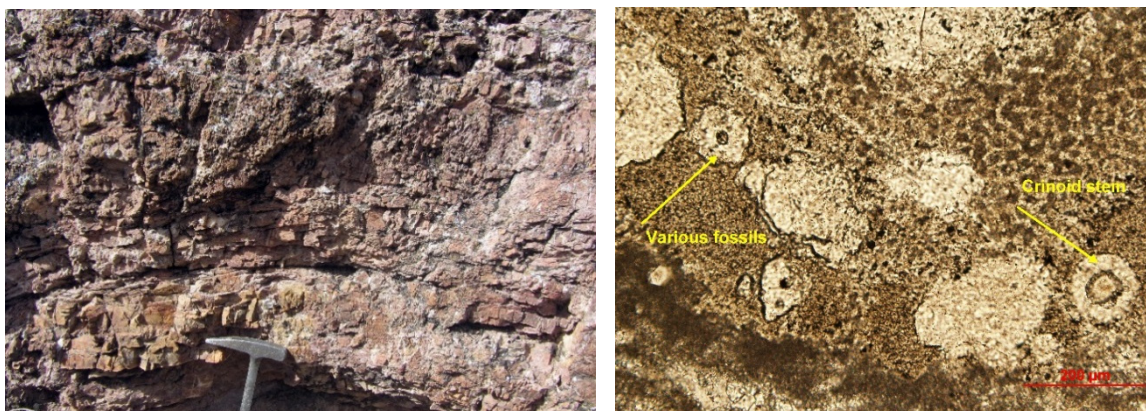


Figure 10. Pennsylvania Ely Limestone. A. Exposure of fossiliferous limestone south of Kinsley stock. B. Photomicrograph of fossiliferous limestone (uncrossed)



Figure 10. Pennsylvania black shale. A. Drill core. B. Photomicrograph showing interlayered carbonaceous shale and siltstone (quartz grains in illite matrix).

## Structural Geology

Kinsley Mountain is characterized by a gently north-northeast-plunging antiform that is cut by numerous high-angle north-northeast-striking faults, which are in turn cut by high-angle northwest-striking faults. The Kinsley Trend is a 750 m wide northwest-trending zone of deformation, which contains much of the SHG mineralization. The Kinsley Trend has been described as a left-lateral wrench fault system (Robinson, 2005). However, current modeling by Pilot Gold characterizes the trend as a fault zone with normal offset down to the north (Randy Hannink, pers. comm.).

As mentioned above, low-angle faults are common along bedding planes and cut out hundreds of meters of section. A black shale of Pennsylvanian age, intersected in drilling in the West Flank area (Fig. 10) is in low angle fault contact with Ordovician and Cambrian strata, chiefly the Notch Peak Limestone and Pogonip Group. North of the West Flank, Eureka Quartzite is in low-angle fault contact with the underlying Pogonip Group. Low-angle faulting likely formed during contraction deformation of the Elko and Sevier Orogeny, resulting in the formation of a district scale antiform. The low-angle faults were later reactivated as normal faults during extension. Kinsley may be analogous to the Eureka district where Long et al. (2014) documented the Late Cretaceous to Eocene collapse of a structural culmination that formed by out of sequence deformation in the hinterland of the Sevier Orogeny in the Early Cretaceous. Drill hole data combined with geochronology suggest significant low-angle faulting took place prior to the emplacement of the 40 Ma stock and cogenetic dikes and continued to ~37 Ma when volcanics began to erupt. It is unknown how much post-Eocene reactivation of the low angle faults has occurred since their formation.

South of the range, Permian strata are in the hanging wall of a high-angle fault with Cambrian Secret Canyon Shale and Hamburg Limestone in the footwall, indicating ~5 km of apparent normal offset. No dikes or intrusion-related mineralization are present in the hanging-wall Permian rocks, suggesting movement on the fault has occurred after emplacement of the stock. However, the fault does not appear to offset ~37-36 Ma volcanic rocks. It is unclear when the fault initially formed.

The temporal relationship between the emplacement of the stock and the formation of the northwest-striking Kinsley Trend is poorly understood. The Kinsley Trend possibly formed during the Elko, Sevier, or Laramide Orogeny as reactivation of a basement structure (Rhys, 2015). Deformation of biotite within a dacite dike dated at  $36.1 \pm 0.4$  Ma in the Kinsley Trend suggests faulting in the Kinsley Trend continued after volcanic flows and dikes were emplaced. High-angle normal faults characteristic of Miocene Basin and Range extension flank both sides of the range.

#### Intrusive complex and mineralization

A circular granitic stock, 1.5 km in diameter, is located at the south end of the range. It was previously dated  $33.4 \pm 0.7$  Ma using K-Ar on biotite (revised by McKee and Marvin, (1976) after Armstrong, (1963) and 41 Ma by Pb- $\alpha$  on zircon (Armstrong, 1963). New, more precise Eocene dates are presented below. Numerous diorite to granodiorite dikes extend outward from the central intrusion. Most of the dikes are 0.5-1 m in width and range up to over a kilometer in length. Polymetallic mineralization hosted by garnet-pyroxene skarn and marble, which was mined predominantly for tungsten, is found around the margin of the granitic intrusion. Polymetallic gossan replacement

bodies and jasperoids are found outward from the skarn. Periodic mining of this polymetallic mineralization from the 1860s to 1956, produced copper, lead, silver, and tungsten with lesser amounts of molybdenum and gold (LaPointe, 1991). Tertiary volcanic rocks are located on the western, south, and southeastern flanks of Kinsley Mountain. Field observations and drill hole data suggest volcanic rocks along the west flank of the range are in unconformable contact with the Pennsylvanian shale and Cambrian strata. The volcanic rocks are also cut by high-angle Basin and Range normal faults. To the south and southeast, the relationship of volcanic rocks with underlying rock is more ambiguous. They appear to lie unconformably over the stock on its eastern margin. However, a post-Eocene basin and range fault contact between the volcanic rocks and the stock cannot be ruled out (Muntean et al., 2015). The Eocene volcanic rocks unconformably overlie Permian rocks in the hanging wall of the large NW striking fault described above.

### III. Methods

Surface and drill core samples (>200) were collected during the summers of 2013 and 2014. Geologic mapping of a ~12 km<sup>2</sup> area centered on the stock was conducted during the summer of 2014 using a Trimble GeoExplorer with ArcPad, a high-precision GPS with submeter accuracy. The mapping was focused on the stock, dikes, mineralization, and volcanic rocks. The mapping was compiled in ArcGIS. Additional mapping of Paleozoic rocks and Eocene volcanic rocks in the area south of the intrusive center was conducted by John Muntean in 2015. Samples were cut into slabs and described with a binocular scope. Thin sections (125) were then examined using transmitted and reflected light microscopy. In the areas of SHG mineralization, sampling and petrography focused on transects in drill core from unmineralized (<5 ppb Au) to mineralized rock (>5 ppm Au), allowing documentation of the changes that were due to the hydrothermal system responsible for gold mineralization. In addition, 70 polished thin sections of gold, polymetallic, and skarn mineralization, as well as altered intrusions and unaltered sedimentary rock were examined with a JEOL 6010 scanning electron microscope (SEM), using back-scattered electron (BSE) imaging and energy dispersive spectroscopy (EDS) analysis. Images captured on the SEM typically used a voltage of 15 kV, spot size of 62, and a working distance of 10 mm.

Whole-rock geochemical analyses were conducted on 38 samples of the stock, dikes, and volcanic rocks by ALS Minerals (CCP-PKG03). This package combines the whole rock package ME-ICP06 plus carbon and sulfur by combustion furnace (ME-IR08) to quantify the major elements in a sample. Trace elements, including the full rare earth

element suites, are reported from three digestions with either ICP-AES or ICP-MS finish: a lithium borate fusion for the resistive elements (ME-MS81), a four acid digestion for the base metals (ME-4ACD81) and an aqua regia digestion for the volatile gold related trace elements (ME-MS42). The geochemical data were evaluated using ioGAS software. Over 50 variably mineralized rock-chip samples, collected during mapping, were assayed for gold and analyzed by ALS Minerals using ICP methods after an aqua regia digestion. The assay data from the rock-chip samples were combined with historic soil and rock-chip data to produce district-scale geochemical figures using the Geosoft Target software extension in ArcGIS. Spearman rank correlation matrices were created for the area containing SHG mineralization using geochemical data from Pilot Gold's downhole drill database in Microsoft Excel.

Zircon, apatite, muscovite, phlogopite, and biotite were separated from intrusive, sedimentary, and volcanic rocks for geochronology and thermochronology. Mineral separations of fourteen samples of shale and fifteen samples of igneous rocks were prepared at GeoSeps, Inc. The rock samples were crushed and sieved to a size <300 microns. Samples were then hand-washed to remove clays and other low-density particles and then set out to air dry. A heavy liquid, lithium metatungstate (specific gravity of 2.95) was used to separate muscovite, feldspars, and quartz from more dense minerals which include biotite, hornblende, apatite, zircon, and pyrite. Samples were then processed by magnetic separation using a Frantz at power levels of 0.5 mA and 1.0 mA to remove any minerals with a magnetic susceptibility including biotite, hornblende, and magnetite. The remaining non-magnetic fraction was then separated with methylene iodide (specific gravity of 3.33), which allows for the isolation of apatite in the less dense

fraction while pyrite and zircon remain in the dense fraction. Samples of intrusive rock with sericite alteration had abundant pyrite in the heavy fraction targeted for zircon. A large portion of the pyrite was able to be separated from zircon by processing the heavy fraction through the Frantz at the highest power.

All separated fractions were kept during the mineral separation process for further use. The low-density fraction from lithium metatungstate separation contained muscovite from shales. A binocular microscope was used to hand-pick the muscovite from the fraction for  $Ar^{40}/Ar^{39}$  dating. A separate of biotite from a fresh sample of dacite was prepared at the University of Nevada. The biotite was then hand-picked for use in  $Ar^{40}/Ar^{39}$  dating. A coarse, homogeneous sample of phlogopite was also separated by hand-picking. Pyrite from shales and intrusive rock was hand-picked from the zircon/pyrite fraction for analyses of sulfur isotopes.

Geochronology was used to date intrusions, volcanic rocks, mineralization and alteration. Methods employed include Re-Os, U-Pb,  $Ar^{40}/Ar^{39}$ , and apatite fission tracking dating. Molybdenite in a sample of a granodiorite dike near the stock was dated using by Re-Os at the University of Alberta. Fifteen U-Pb dates on zircons, including five with full trace element geochemical analyses were obtained with the Sensitive High Resolution Ion Microprobe (SHRIMP) at Stanford University. A full description of methods used on the SHRIMP is located in Appendix E. Two U-Pb zircon dates of intrusions were obtained from GeoSeps Inc. using the LA-ICP-MS at Washington State University. Mineral separates of phlogopite from retrograde skarn near the stock, biotite from andesite, and hydrothermal sericite from SHG mineralization were dated by  $^{40}Ar/^{39}Ar$  at geochronology lab of Auburn University. Results of the  $^{40}Ar/^{39}Ar$  dating

were not obtained in time to include in this thesis. Apatite fission track dating was conducted by A to Z Inc. on detrital apatites from shale in the area of the SHGDs using a LA-ICP-MS.

Sulfur isotope analysis was conducted on 22 samples of pyrite at the Nevada Stable Isotope Laboratory, University of Nevada. Sulfur isotope analyses are performed after the method of Giesemann et al. (1994) and Grassineau et al. (2001).  $V_2O_5$  is added to samples as a combustion aid.  $\delta^{34}S$  results are reported in units of ‰ vs. Vienna Canyon Diablo Troilite (VCDT). An uncertainty of  $\pm 0.2\%$  is recommended. The samples included six pyrite separates from intrusion-related quartz veins, gossans, and skarn near the stock. Other samples included seven pyrite separates from non-mineralized ( $< 5$  ppb Au) shale intervals, six from mineralized shale intervals ( $> 1$  ppm Au), and three from dikes with sericitic alteration. Two of the dikes from which pyrite was analyzed were located within 50 m of the stock. The third dike sample, located in the area of the SHGDs, was from a six foot interval that assayed 399 ppb Au.

Electron microprobe analyses of nine polished thin sections of mineralized drill core from the SHGDs at Kinsley was conducted at the University of Nevada – Las Vegas, using a JEOL-8900 Electron Probe Microanalyzer (EMPA) to locate and quantify gold and other trace elements in pyrite. Hornblende and plagioclase in three polished thin sections of the granodiorite stock were also analyzed for use in aluminum in hornblende geobarometry. Polished thin sections used for EMPA analysis were coated with carbon prior to use. All raw data collected are located in Appendix (D). Analyses containing analytical totals below 98% are likely the result of the following: 1) Slopes within the samples from poor polish or crystal boundaries, which scatter signal-rays and reduce

analytical totals, 2) elements present in the sample that were not included in analysis, and 3) analysis of a mineral with inclusions or a mixed phase, which can result in loss of counts and low totals (Newton, 2015).

#### IV. Igneous Rocks

The Eocene intrusive center is located 3 km south of the area of gold mineralization at the south end of the Kinsley Mountain. The intrusive center, ~40 Ma based on geochronological studies detailed below, is composed of a granodiorite stock and likely cogenetic dikes. The compilation of this mapping in the southern part of the Kinsley Mountains is shown in Figure 11. The petrography of the igneous rocks are summarized in Table 1.

##### Stock

The stock is ~1.8 km wide, circular in shape, and intrudes Cambrian strata. White to blueish colored marble is well developed along the margin of the stock where it is in contact with the Hamburg Dolomite. Interbedded marble and hornfels is present where the stock is in contact with the Secret Canyon Shale and Dunderberg Shale along the west and northern margins. Numerous porphyritic dikes cut the stock and extend outward along a north-northeast orientation up to 4 km from the stock. The dikes range in composition from diorite to granite. Volcanic rocks flank both sides of Kinsley Mountain and are also found south of the stock. The volcanic rocks are flows and flow breccias that range in composition from dacite to rhyolite.

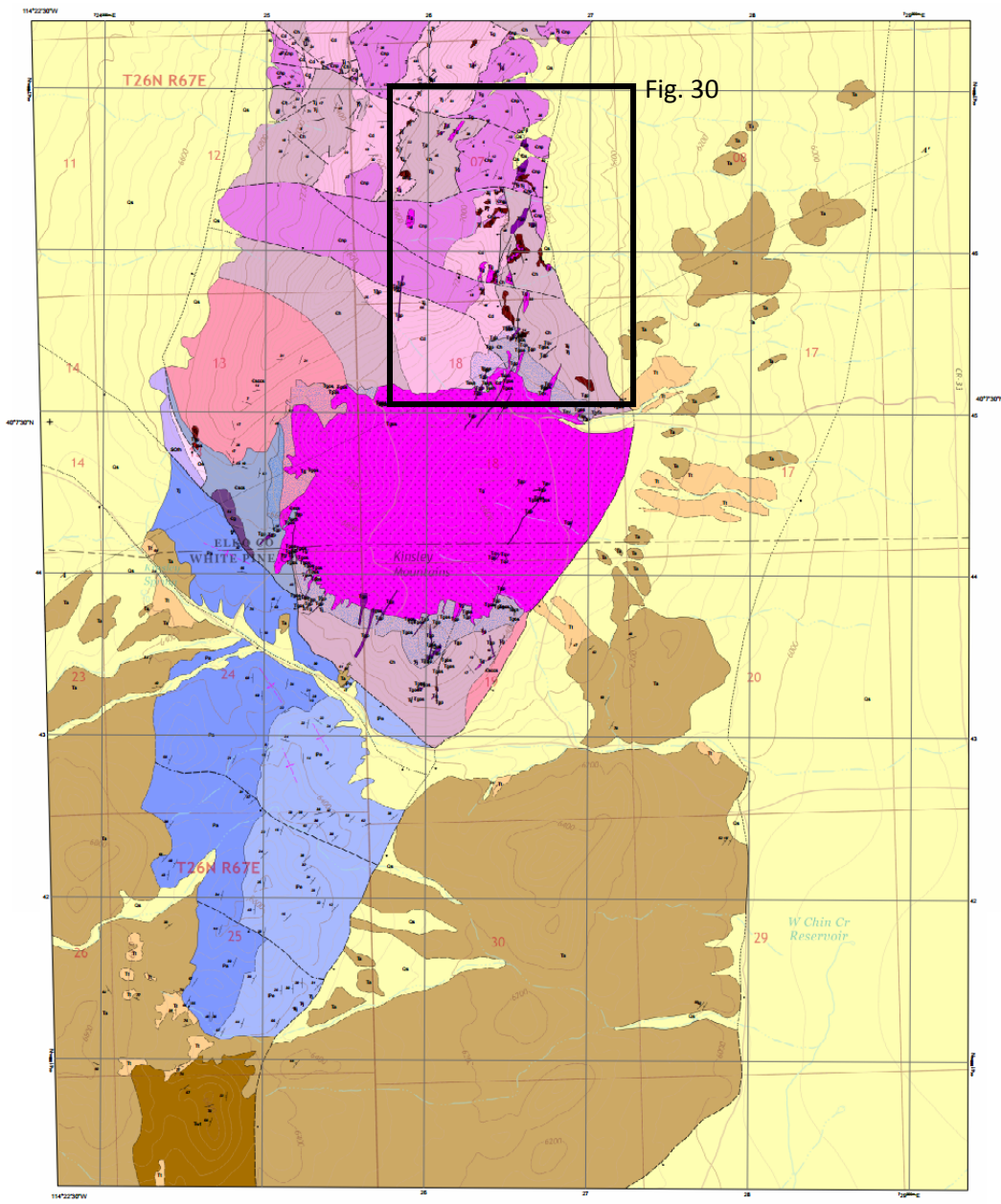


Fig. 30

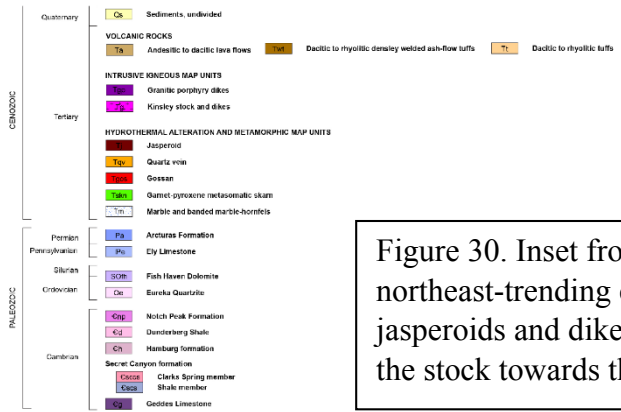


Figure 30. Inset from Figure 11 showing north-northeast-trending corridor of discontinuous jasperoids and dikes extending northward from the stock towards the area of SHGDs

Table 1. Rock descriptions for igneous rocks at Kinsley Mountain.

Sample	Mineralogy
Stock	45% euhedral 1-5 mm plagioclase, 25% euhedral 1-5 mm orthoclase, 20% anhedral, 0.5-3 mm quartz with most of the quartz being intergranular, 5% euhedral, 1-3 mm biotite, and 3% euhedral, fine grained (1-2 mm) hornblende. Accessory minerals (2%) include magnetite, sphene, zircon, and apatite
Granodiorite porphyry dike	10-20% 0.25-3 mm euhedral plagioclase, 5-10% 0.25-3 mm euhedral orthoclase, 5-10% 0.25-4 mm resorbed quartz, 1-3% 0.1-1 mm hornblende, 1-3% 0.1-2 mm biotite, groundmass is aphanitic and composed of quartz and orthoclase
Granite porphyry dike	2-6% resorbed quartz, 1-5% 0.5-3 mm euhedral orthoclase, 1-3% 0.5-3 mm euhedral plagioclase, 1-2% euhedral 0.1-1 mm biotite, groundmass is indistinguishable due to alteration
Diorite porphyry dike	15-20% 0.1-2 mm euhedral hornblende, 8-12 % 0.25-3 mm euhedral plagioclase, 5-8% 0.1-2 mm euhedral biotite, 1-3% 0.25-4 mm resorbed quartz, groundmass is aphanitic and composed of quartz and plagioclase
Andesite porphyry	5% euhedral 0.1-1 mm plagioclase, 3% euhedral 0.1-1 mm hornblende, 2% euhedral 0.1-0.5 mm biotite, 1% anhedral 0.1-0.5 mm quartz, groundmass is oxidized to hematite
Dacite porphyry	8% euhedral 0.1-1 mm plagioclase, 5% 0.1-2 mm euhedral foliated biotite, 2% 0.1-1 mm anhedral quartz, groundmass strongly altered to illite
Dacite flows and breccias	8-15% euhedral 0.1-1 mm plagioclase, 2-5% 0.1-1 mm euhedral biotite, 1-2% 0.1-0.5 mm euhedral hornblende, <1% 0.1-1 mm euhedral sanidine, groundmass is aphanitic quartz, plagioclase, and sanidine. Breccias flows have broken phenocrysts.
Rhyolite breccias	3% 0.1-2 mm anhedral quartz shards, 1% 0.1-1 mm anhedral sanidine, 1% 0.1-1 mm anhedral plagioclase, <1% euhedral 0.1-1 mm biotite, glassy groundmass of quartz and plagioclase

The granodiorite stock is relatively homogenous in composition, except for an area that is quartz monzonite in composition and contains K-feldspar megacrysts up to 5 cm in length near the stock's western margin. A northeast-striking fault zone appears to control a 50 m wide protrusion of the stock that extends up to 200 m northward. Other structurally controlled north to northeast oriented protrusions of the stock occur, but are not as prominent and are typically <10m wide. Three roof pendants in the stock were

identified. Roof pendants on the north and southwest portions of the stock are marbleized. The northern roof pendant has an exposure showing the transition from the stock, to garnet-pyroxene skarn, to marble. A small jasperoid body of the Hamburg Dolomite, exposed on the eastern margin of the stock, is thought to be a roof pendant as the jasperoid body is completely surrounded by the stock and there is no surface exposure of Cambrian strata within 500 m of the jasperoid body.

The granodiorite stock consists of euhedral medium-grained plagioclase, euhedral medium to coarse-grained orthoclase, anhedral fine to medium-grained quartz, euhedral fine to medium-grained biotite, and euhedral fine-grained hornblende. Accessory minerals include magnetite, sphene, zircon, and apatite. The stock has weak deuteric chloritic and sericitic alteration of mafic minerals and feldspars. No secondary biotite or potassium feldspar was recognized in the stock.

Hornblende from three sample of the granodiorite stock were analyzed using the JEOL-8900 EMPA at the University of Nevada Las Vegas in order to estimate emplacement depths using aluminum in hornblende geobarometry. Five hornblende phenocrysts from each sample were analyzed with four to eight spots per hornblende phenocryst for a total of 98 spots. Plagioclase phenocrysts adjacent to the hornblende phenocrysts were also analyzed for use in the hornblende-plagioclase thermometer to determine a temperature of formation needed in the calculation of pressure using the aluminum in hornblende geobarometer. Analyses from plagioclase phenocrysts were averaged to determine one temperature for each hornblende analyzed. Pressures were converted to depths assuming the rock overlying the stock at the time of emplacement had a density of  $2.8 \text{ g cm}^{-3}$ . Results were calculated in Microsoft Excel using values from

Holland and Blundy (1994) and Anderson and Smith (1995).

The aluminum in hornblende geobarometer was first proposed by Hammarstrom and Zen (1986) who were the first to demonstrate that the Al content of hornblende is dominantly controlled by pressure. The geobarometer is based on the total aluminum content ( $Al^T$ ) of amphibole and requires an equilibrium assemblage of quartz + K-feldspar + biotite + hornblende + plagioclase + sphene + magnetite or ilmenite. There are multiple calibrations for aluminum in hornblende geobarometry, including:

$$P (+3 \text{ kbar}) = -3.92 + 5.03 Al_{tot}, r^2 = 0.80 \text{ (Hammarstrom and Zen, 1986);}$$

$$P (+1 \text{ kbar}) = -4.76 + 5.64 Al_{tot}, r^2 = 0.97 \text{ (Hollister et al., 1987);}$$

$$P (+0.5 \text{ kbar}) = -3.46 + 4.23 Al_{tot}, r^2 = 0.99 \text{ (Johnson and Rutherford, 1989);}$$

$$P (+0.6 \text{ kbar}) = -3.01 + 4.76 Al_{tot}, r^2 = 0.99 \text{ (Schmidt, 1992).}$$

Anderson and Smith (1995) developed a temperature-corrected Al in hornblende geobarometer calibrated using the experiments by Schmidt (1992) at approximately 675 °C and those of Johnson and Rutherford (1989) at approximately 760 °C. The method used in this study is the new calibration of Anderson and Smith (1995), which is as follows:  $P (+0.6 \text{ kbar}) = 4.76 Al_{tot} - 3.01 \{ [T(^{\circ}C) - 675] / 85 \} \times \{ 0.530 Al_{tot} + 0.005294 [T(^{\circ}C) - 675] \}$ ,  $r^2 = 0.99$

Results and locations of the analyses are shown in Table 2 and Figure 12, respectively. The presence of roof pendants in the stock suggest the current erosion level has exposed the upper most portions of the stock. The results suggest the hornblende crystallized at depths between 5.5 and 7.5 km, which could represent the emplacement depth of the stock. However, the hornblende, which shows textural evidence of forming

prior to quartz and orthoclase, could have crystallized at depths of ~5.5-7.5 km and was then transported upward in the magma chamber, where later crystallization of quartz and feldspar took place. The Al-in-hornblende results indicate the emplacement depth of the stock cannot be greater than ~7.5 km.

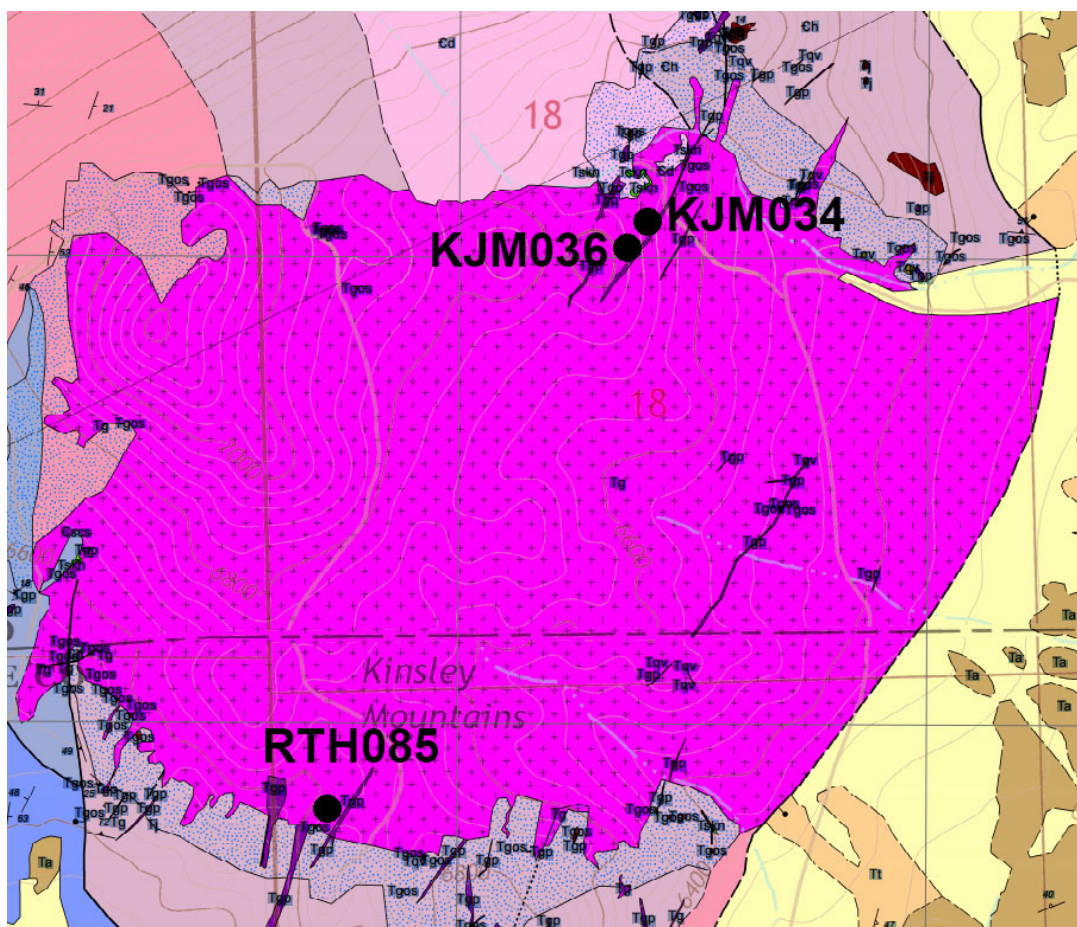


Figure 12. Locations of samples collected from the stock for aluminum in hornblende geobarometry.

Table 2. Results from the aluminum in hornblende analyses.

Sample	T °C	Pressure (kbar)	Depth (km)
KJM034	664	1.96	5.46
KJM036	633	2.1	5.88
RTH085	662	2.7	7.56

## Dikes

Three families of dikes are found proximal to the stock—granite dikes, diorite dikes and granodiorite dikes. Widths of all types of dikes range from 0.5 m to 15 m, with most dikes between 0.5 m and 3 m in width. Granite and diorite dikes cut the stock along its margins and extend outward into the Paleozoic rocks, commonly along north-northeast-striking faults and fractures. A few of these dikes were also mapped in the interior of the stock. These dikes appear to be similar to the stock, both geochemically and petrographically. Granodiorite dikes have been intersected in numerous drill holes on both sides of Kinsley Mountain and crop out as far as 4 km north of the stock. No cross-cutting relationships were observed between the different families of dikes.

The family of granite dikes was only mapped outside of the stock. The granite porphyry dikes were everywhere strongly altered to quartz+sericite+pyrite (mainly weathered to limonite), making them difficult to compare to other families of dikes. Staining by sodium cobaltinitrite and petrographic analysis of the dikes revealed potassic alteration in two granite porphyry dikes characterized by potassium feldspar flooding and development of secondary biotite as veinlets, local replacement of hornblende, and overgrowths on magmatic biotite. No core holes have intersected the granitic dikes in the area of the SHGDs. No polymetallic mineralization is spatially associated with the granitic dikes based on assays of rock-chip samples from the dikes and in the country rocks along their margins.

Granodiorite porphyry dikes near the stock are the most abundant family of dikes at Kinsley Mountain. Granodiorite dikes have an aphanitic groundmass composed of quartz and orthoclase. Phenocrysts in the dikes include fine to medium-grained

plagioclase, orthoclase, resorbed quartz, hornblende, and biotite in order of abundance. The granodiorite dikes commonly show weak to strong quartz+sericite+pyrite alteration and, near the stock, commonly host polymetallic mineralization along their margins. They extend outward south-southwestward and north-northeastward from the stock. Dikes of the granodiorite family occur up to 4 km north of the stock in drill core in the area of the SHGDs, where they constitute the vast majority of the dikes. Many of the granodiorite dikes can be traced to the margin of the stock, but only a few cut the stock, suggesting dike-forming magmas were focused along the margins of the stock the margin of the stock. Most of the dikes that are exposed in the area of SHG mineralization and have been intersected in drill core at Kinsley Mountain are part of the granodiorite porphyry dike family.

The family of diorite porphyry dikes cut the stock and extend outward into the Paleozoic rocks along the same north-northeast trends as the other dikes. Diorite porphyry dikes have an aphanitic groundmass composed of quartz and plagioclase. Phenocrysts are fine to medium grained and include hornblende, plagioclase, biotite, and resorbed quartz in order of abundance. The diorite dikes have weak deuteric chlorite and sericite alteration. They are commonly <3 m wide. However, a 10 m wide dike on the southwestern margin of the stock is a notable exception. No mineralization has been observed along their margins. No diorite dikes have been intersected in drill core in the area of the SHGDs.

## Volcanic Rocks

Volcanic rocks of dacitic to rhyolitic composition flank Kinsley Mountain. Dacite flows and flow breccias contain fine grained plagioclase, biotite, hornblende, and sanidine. Rhyolite breccia contains anhedral quartz shards, sanidine, plagioclase, and biotite. Dacite flows as thick as 600 m have been intersected in drill holes on the western pediment of Kinsley Mountain. The thick flows lie unconformably over Pennsylvanian, Ordovician, and Cambrian sedimentary rocks. Other volcanic flows have been intersected in drill holes along the west side of the mountain underlying Quaternary alluvium, Tertiary alluvium is locally interbedded with the volcanic flows. All volcanic flows display strong hematitic oxidation.

Dacite flows and flow breccias and a rhyolite breccia are exposed at the surface on the southeast side of Kinsley Mountain near the eastern and southeastern margin of the stock. The relationship of volcanic rocks with underlying rock is more ambiguous near the stock due to lack of drill data. A rhyolite breccia appears to lie unconformably over the stock on the east side of the stock. However, a post-Eocene basin and range fault contact between the volcanic rocks and the stock cannot be ruled out (Muntean et al., 2015). The Eocene volcanic rocks unconformably overlie Permian rocks in the hanging wall of the large NW striking fault described above.

An andesite porphyry dike and a dacite porphyry dike were intersected in drill core in the area of the SHGDs. The two dikes appear distinctly different due to alteration, but geochemical data and geochronology presented below suggest the dikes are cogenetic with the volcanic rocks. The dike from the west side of Kinsley Mountain is an andesite porphyry and is composed of fine-grained phenocrysts of biotite, hornblende, and

feldspar with minor magnetite in a strongly hematitic groundmass. It appears devoid of hydrothermal alteration and cuts a granodiorite dike that has kaolinite-smectite alteration. A dacite porphyry dike intersected in drilling on the east side of the mountain is green-colored due to strong alteration of the groundmass to illite. It contains fine-grained biotite and quartz phenocrysts. The biotite in the dike is sheared and locally kinked and crenulated, as described above. No surface exposures of andesite dikes have been mapped.

#### Whole-rock Geochemistry

Whole rock geochemical analyses were conducted on 38 samples of intrusive and volcanic rocks. Of the 38 samples, 15 are unaffected or very weakly affected by hydrothermal alteration, 12 are moderately to strongly hydrothermally altered, and 11 are considered fresh samples with minimal weathering. Alteration of the rocks results in inaccurate classification using schemes that use concentrations of major oxide (CaO, Na<sub>2</sub>O, MgO, SiO<sub>2</sub>) are used. Only fresh rocks can be accurately classified on such diagrams. The rocks were classified using a combination of diagrams that include both mobile and immobile elements.

Use of different classification diagrams resulted in variable classifications of the rocks at Kinsley Mountain. Unaltered samples of the stock and dikes are classified as monzogranites, granodiorites, quartz monzonites, and quartz monzodiorites when using the Streckeisen diagram (Fig. 13). The stock itself plots near the border of granodiorite, granite, quartz monzonite, and monzogranite. Using the TAS diagram, rocks plot as

rhyolites, trachytes, and dacites (Fig. 14). The volcanic rocks plotted on the TAS diagram are likely accurate. Based on petrographic analysis coupled with whole-rock geochemistry, the stock and majority of the dikes can be classified as metaluminous, high-potassium calc-alkaline granodiorites, whereas the remaining dikes should be classified as granites, diorites, and andesite and dacite porphyries (Figs. 14-16). All samples of granodiorite dikes in drill core have

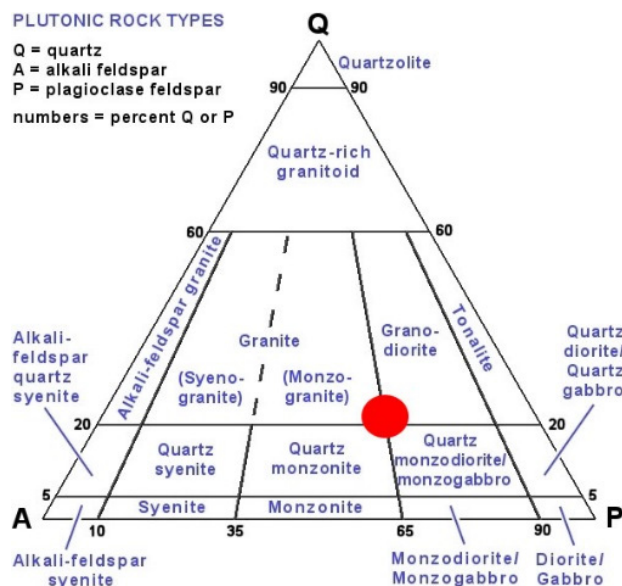


Figure 13. Streckeisen diagram. The red dot illustrates where samples of the stock and

dacite porphyries (Figs. 14-16). All samples of granodiorite dikes in drill core have

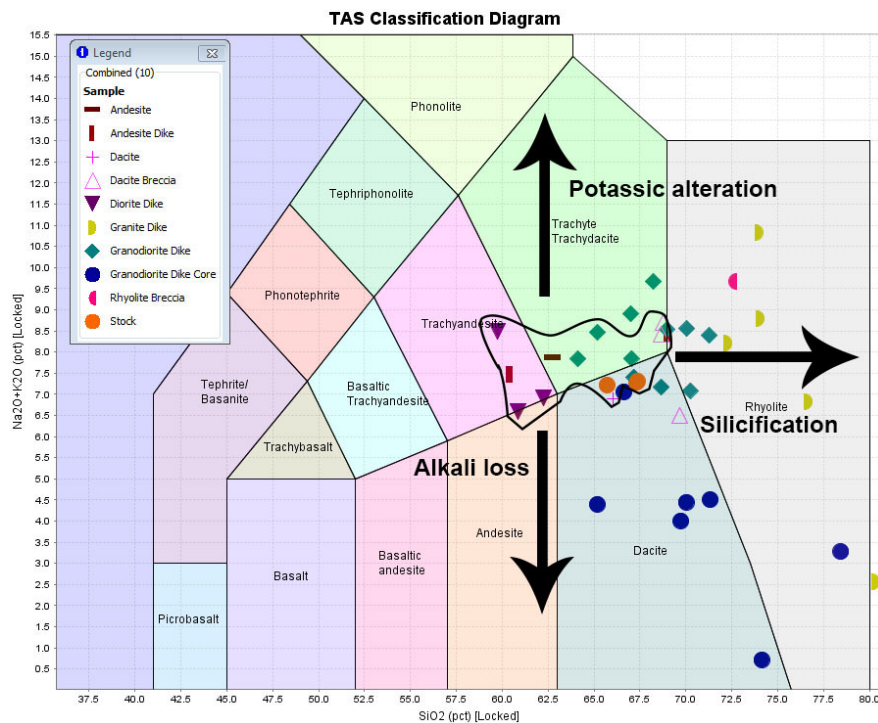


Figure 14. Total alkali-silica classification diagram for volcanic rocks showing Kinsley samples. Data within the black outline are samples considered unaffected by hydrothermal alteration (Middlemost, 1994).

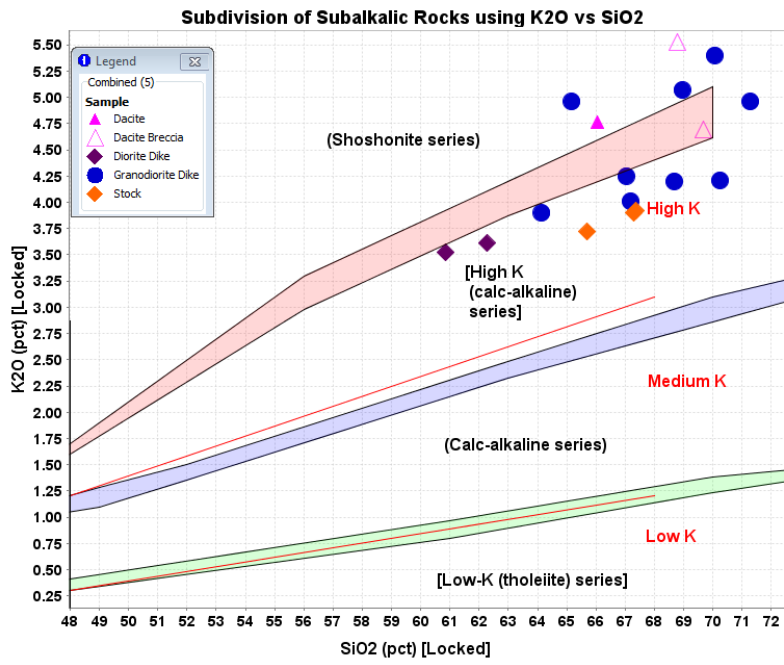


Figure 15. Subdivision of subalkalic rocks using K<sub>2</sub>O vs SiO<sub>2</sub> showing data from unaltered igneous rocks from Kinsely. All of the samples are high potassium calc-alkaline to shoshonitic (Rickwood, 1989).

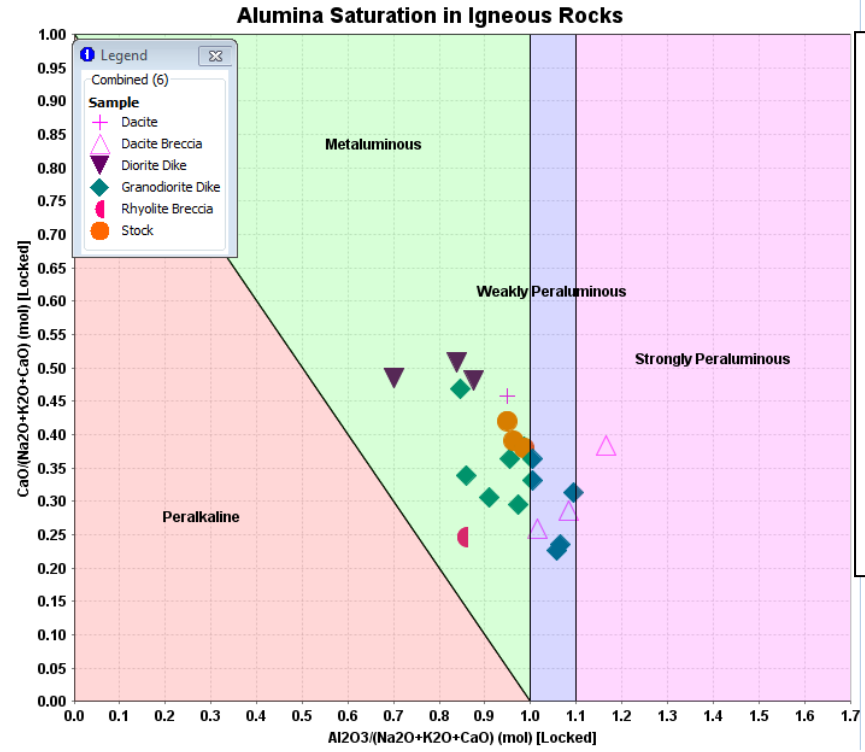


Figure 16. Alumina saturation index diagram (from Barton and Young, 2002) showing data from unaltered igneous rocks from Kinsley. Most intrusive rocks plot as metaluminous while volcanic rocks are more variable.

significant hydrothermal alteration, preventing accurate classification in diagrams where mobile elements are used. Petrographic analysis combined with rare earth element (REE) and immobile element (Ti, Al, and Zr) geochemistry results in classification of these rocks as granodiorites, equivalent to granodiorite dikes that are exposed near the stock.

Unaltered to weakly altered granodiorite dikes are metaluminous to weakly peraluminous (Fig. 16). Plots of oxides and oxides against trace elements display overlap of data between granodiorite dikes from both drill core and proximal to the stock and the stock itself (Figs. 17-18). Spider diagrams plotting REE values for the granodiorite dikes and the stock also show overlap (Fig. 19). The similarity of geochemical features suggests all the granodiorite dikes are cogenetic and that they are cogenetic with the stock.

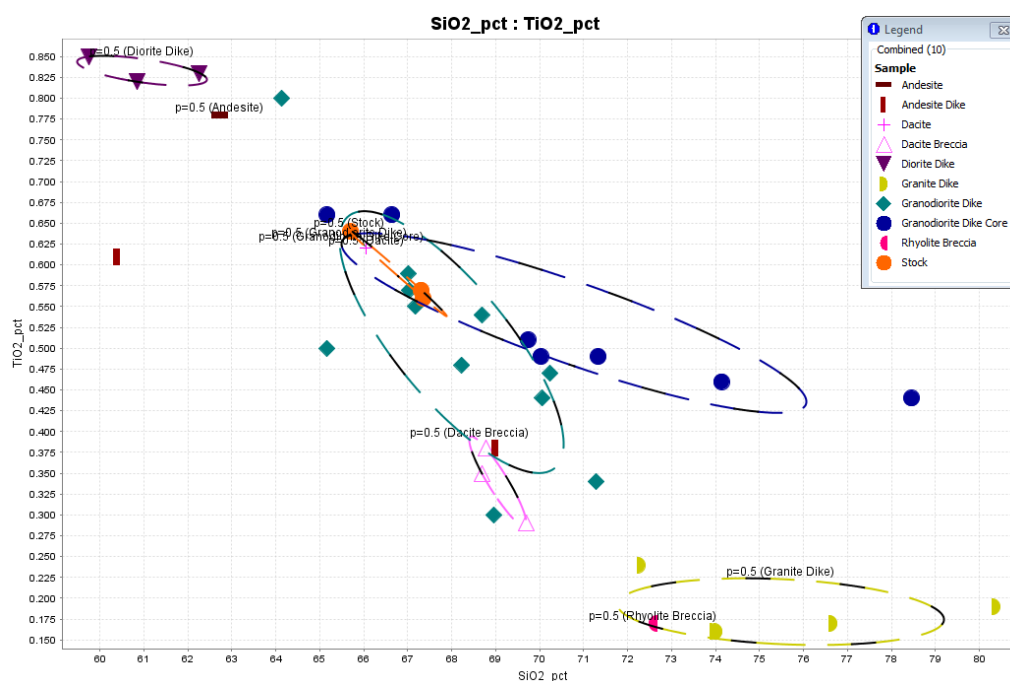


Figure 17. Plot of TiO<sub>2</sub> vs SiO<sub>2</sub>. Nicely shows fractionation trend from diorites to granodiorite to granite. The higher silica rocks have likely been affected by hydrothermal alteration.

Immobile element characteristics are used to differentiate granite porphyry dikes due to their strong alteration. Granite dikes have lower raw values of Ti, Al, and Zr compared to granodiorite dikes (Figs. 17, 18). Granite dikes have a stronger Eu anomaly than granodiorite dikes and are elevated in heavy rare earth elements (HREEs) (Fig. 19).

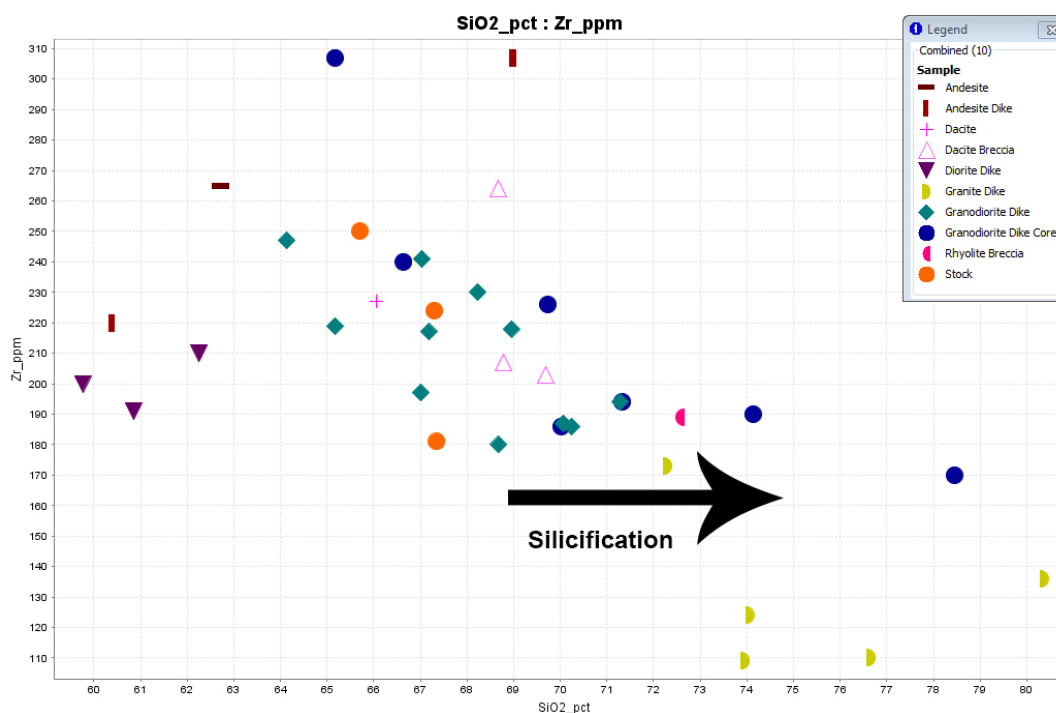


Figure 18. Plot of Zr vs SiO<sub>2</sub>. The diagram discriminates between different families of intrusive rocks.

Diorite dikes are relatively unaltered, which allow classification with TAS and Streckeisen diagrams. Using the TAS scheme, the diorites plot as monzonites, whereas they plot as diorites on the Streckeisen diagram. Diorite dikes contain elevated raw values of Ti when compared to granite and granodiorite dikes (Fig. 17). Raw values of Al and Zr are similar to granodiorite dikes (Fig. 18). Spider diagrams show the diorites have comparable REE values to granodiorite dikes (Fig. 20).

Andesite porphyry and dacite porphyry dikes plot as a trachyandesite and trachydacite, respectively, on a TAS diagram (Fig. 15). These dikes have raw values of Ti and Zr similar to granodiorite dikes, but are slightly elevated in Al (Figs. 17, 18). REE values of these dikes are similar to those of granodiorite dikes with the exception of the HREEs, which are elevated and more similar to granite dikes (Fig. 20).

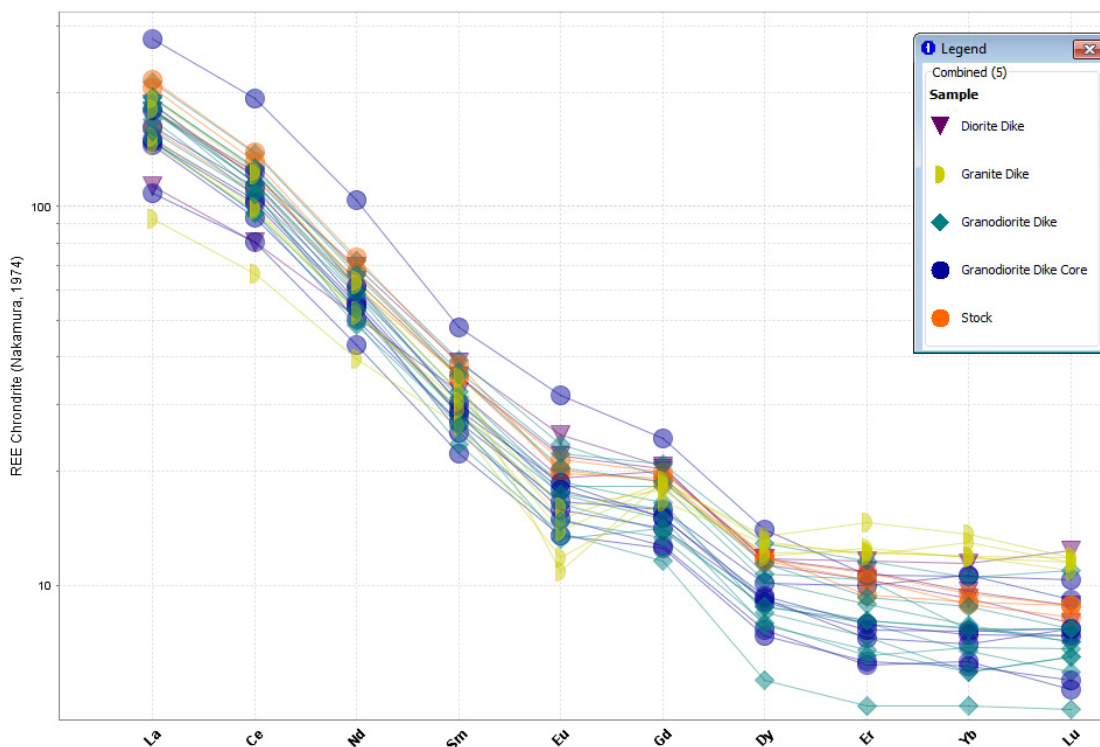


Figure 19. Chondrite normalized REE diagram for intrusive rocks at Kinsley (Nakamura, 1974).

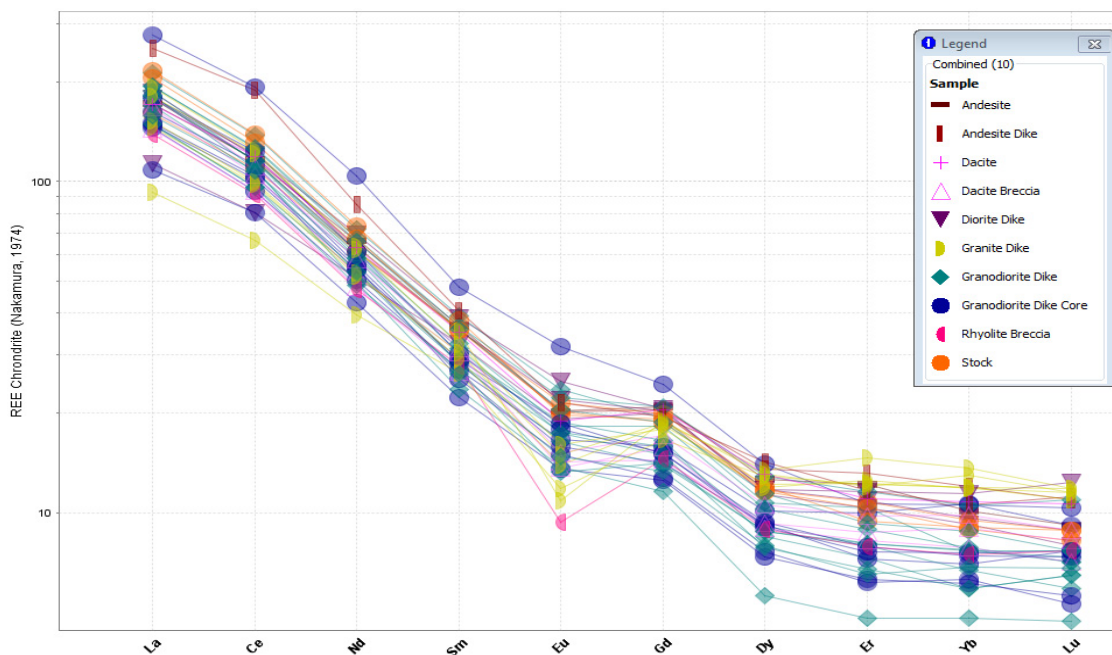


Fig 20. Chondrite normalized REE diagram. All whole-rock samples are plotted. (Nakamura, 1974).

Dacite flows plot as trachydacites or dacites, (Fig. 15). The dacite flows have similar raw values of Zr and Al as the granodiorite dikes, while raw Ti values are slightly lower (Figs. 17-18). REE values of the dacite flows are nearly identical to REE values of the granodiorite dikes and the stock (Fig. 21). The chemistry of the rhyolite breccia is significantly different than other extrusive and intrusive rocks at Kinsley. The rhyolite breccia has a much lower raw Al value than the other igneous rocks. However, its raw Ti value fits well with those of the granite dikes (Fig. 17 and 18). REE spider diagrams show the rhyolite breccia has a strong Eu anomaly, as do the granite porphyry dikes, but its LREEs and HREEs are comparable to the granodiorite dikes and the stock (Fig. 20).

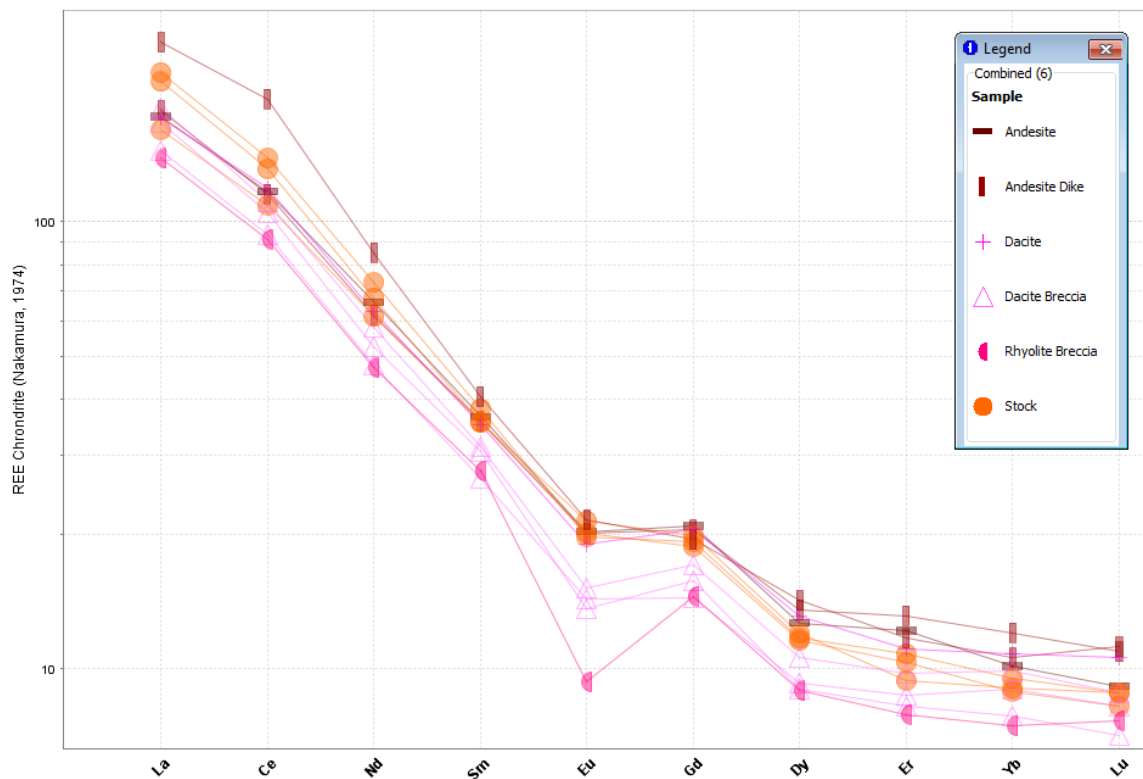


Figure 21. Chondrite normalized REE diagram for volcanic rocks. (Nakamura, 1974).

Whole-rock geochemistry suggests intrusive and extrusive rocks at Kinsley are cogenetic. Though diorite and granite porphyries have significantly different SiO<sub>2</sub> contents and petrographic appearances than the stock and granodiorite porphyries, REE values suggest they are cogenetic. Dacite flows and flow breccias share similar REE values to granodiorite dikes and the stock, while the rhyolite breccia has comparable REE and immobile element values to the granite dikes, suggesting a genetic link between the stock and granodiorite dikes and extrusive volcanic rocks. Though geochemical evidence is permissive that extrusive rocks are cogenetic with intrusive rocks, geochronology discussed below suggests the extrusive rocks at Kinsley Mountain post-date intrusive rocks by ~4 Ma. However, a preliminary <sup>40</sup>Ar/<sup>39</sup>Ar date of biotite from a dacite flow in the hanging wall of a basin and range fault indicates extrusive volcanism was active by 38.5 Ma. The temporal difference between cogenetic intrusive and extrusive rocks suggests a long-lived batholith at depth that gave rise to magmas of varying chemistries.

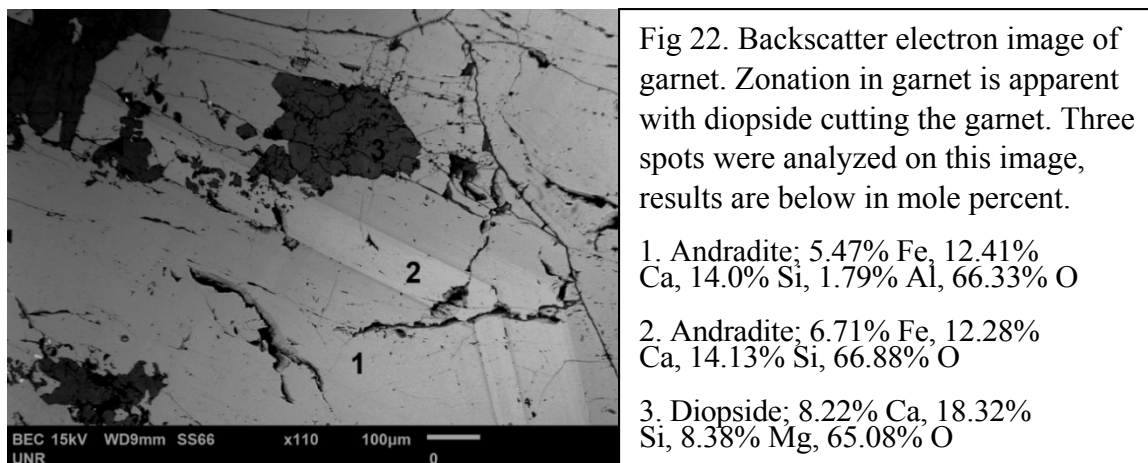
## V. Intrusion-Related Metamorphism, Alteration, and Mineralization

Marble, hornfels, metasomatic garnet-pyroxene skarn, gossanous replacement bodies, and quartz veins are found proximal to the stock. Numerous pits, shafts, and adits are found around the stock where previous small-scale mining occurred periodically from the 1860s to 1956. Intrusion-related polymetallic mineralization at Kinsley Mountain occurs primarily in Cambrian country rocks along the contact of the stock, the margins of dikes, and north-northeast-striking faults.

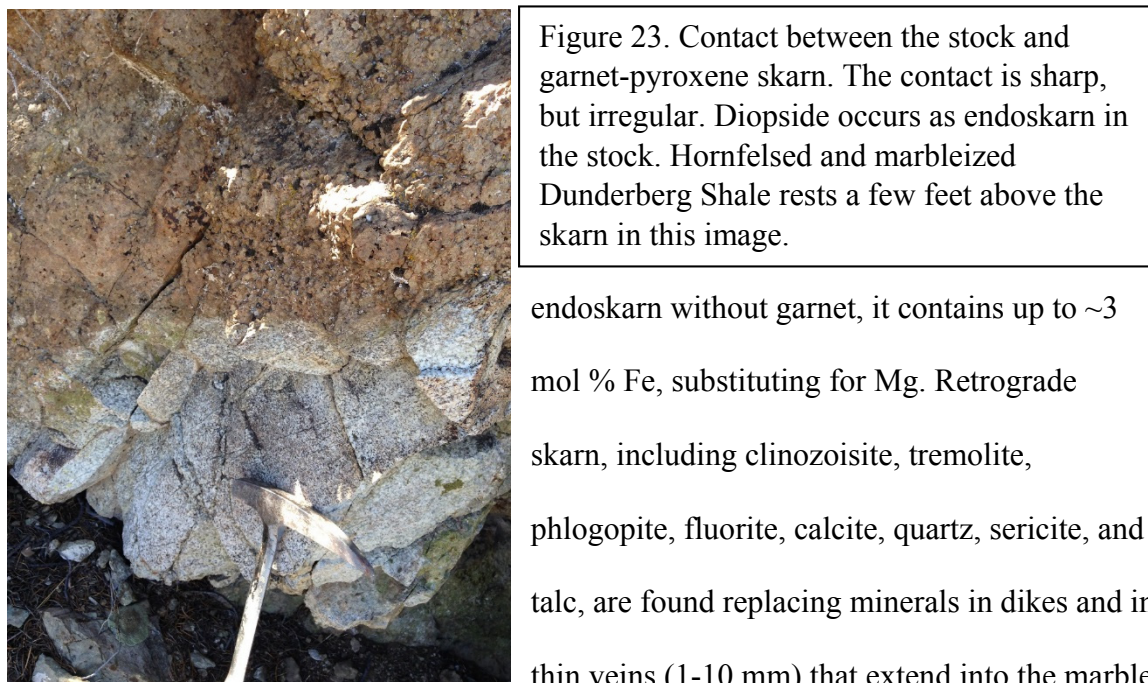
The contact metamorphic aureole, consisting predominantly of marble, is exposed on the north, west, and south sides of the stock and extends up to 150 m beyond the stock's margin. Where the stock is in contact with the Dunderberg Shale, Clarks Spring Limestone, and the Secret Canyon Shale biotite hornfels is developed as well as marble. Where the stock is in contact with the dolomite in the Hamburg Formation, dolomitic marble is developed. Porphyritic granodiorite and granite dikes commonly cut the marble. Thin (<1 cm) retrograde skarn veins and veinlets cut the marble near its contact with the stock. Small grains of euhedral tabular forsterite and euhedral equant to tabular phlogopite (<100  $\mu\text{m}$ ) have been identified in dolomitic marble. Fine grained disseminated pyrite (<50  $\mu\text{m}$ ) is commonly found in the marble.

Metasomatic garnet-pyroxene skarn locally occurs as endoskarn in the stock and dikes and as exoskarn along the contact of the stock, and locally outward along faults and dikes. Garnet-pyroxene skarn has been observed in Dunderberg Shale, Hamburg Formation, and the Clarks Spring member of the Secret Canyon Shale, where it typically occurs as bodies up to 5 m wide. The skarn is characterized by coarse green to brown

andradite (65-100 mol % andradite based on SEM EDS analyses) and grossular garnet (0-20 mol % andradite based on SEM EDS analyses) (5-20 mm) with diopside (0-3 mol % Fe) which is cut by late quartz and calcite (Fig. 22).

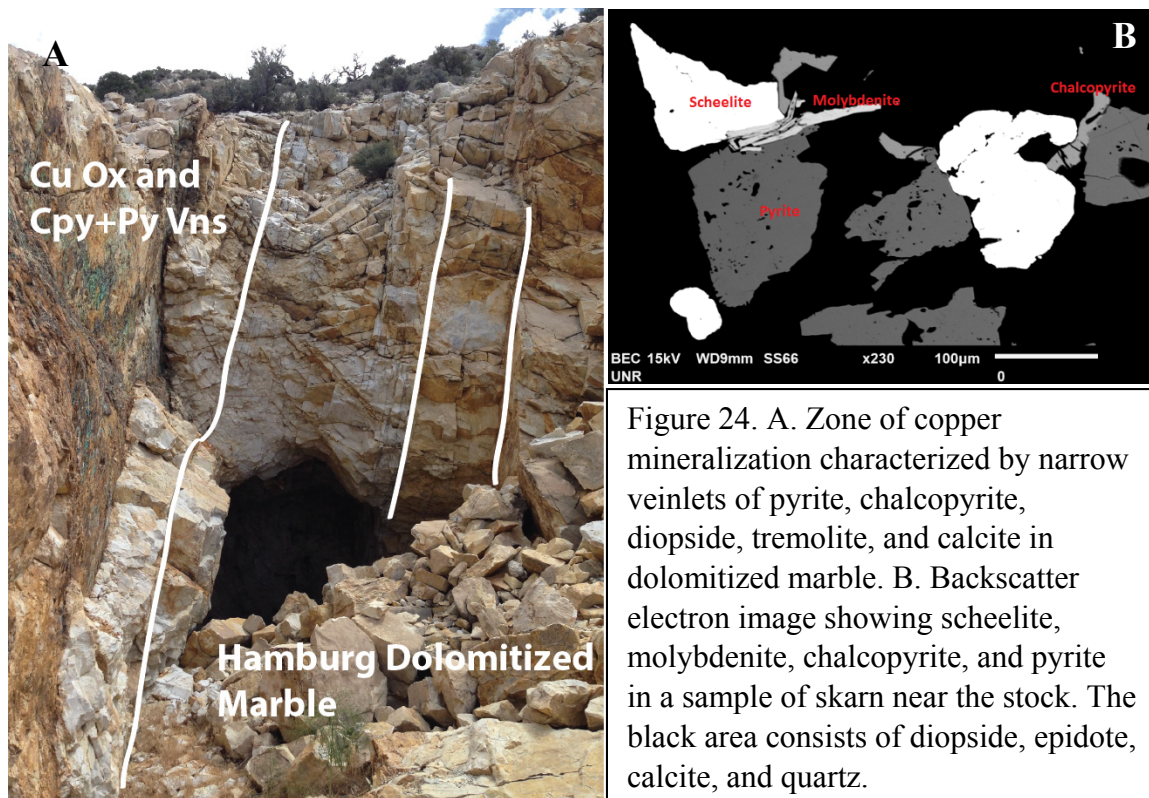


Endoskarn consisting of diopside and retrograde skarn minerals including tremolite, phlogopite, and clinozoisite locally occurs in the stock and dikes near occurrences of garnet-pyroxene skarn (Fig. 23). Where diopside is found as skarn and



endoskarn without garnet, it contains up to ~3 mol % Fe, substituting for Mg. Retrograde skarn, including clinozoisite, tremolite, phlogopite, fluorite, calcite, quartz, sericite, and talc, are found replacing minerals in dikes and thin veins (1-10 mm) that extend into the marble and Cambrian strata (Fig. 24A). Other than andradite and diopside, skarn minerals that

contain Fe, such as epidote and actinolite, are rare and are typically restricted to endoskarn in dikes with shale-dominant country rocks, suggesting iron was derived from the shales.



Scheelite veins and disseminations, where observed, cut the garnet-pyroxene skarn. Scheelite is also observed in marble near the contact with the stock. Malachite and azurite are common in surface exposures. Local relict disseminated pyrite, chalcopyrite, and molybdenite have been observed cutting garnet-pyroxene skarn in thin section. Disseminated mineralization, including molybdenite, scheelite, sphalerite, galena, chalcopyrite, and pyrite, typically occurs with diopside and retrograde minerals and can be found in both endoskarn and exoskarn (Fig. 24B). Scheelite appears to have formed during prograde skarn, as it does not cut retrograde skarn. However, other polymetallic sulfides cut retrograde skarn suggesting a separate hydrothermal event (Fig. 31).

Chalcopyrite, sphalerite, galena, and pyrite locally occur in <1 cm magnesian skarn veins that cut marble on the north side of the stock. The narrow veins have chalcopyrite, sphalerite, galena, pyrite, diopside, and tremolite interiors that grade outward to tremolite and a Mg-Ca-bearing clay and further outward to a calcite and Mg-Ca-bearing clay envelope. The veins cut dolomitic marble developed in the Hamburg Formation the north side of the stock.

Gossanous replacement bodies and replacement veins that formed by weathering of polymetallic massive sulfides occur up to 1.5 km from the stock, with most occurring within 200 m of the stock. Near vertical gossanous veins vary from 10 cm to 5 m wide and pinch and swell irregularly along strike (Fig. 25). The veins strike predominantly north-northeast and extend into the Cambrian strata along fault and fracture zones and dike margins. Northwest-striking faults and fractures may also control mineralization. A report by Hill (1916) indicates a polymetallic replacement vein containing Au, Ag, and Cu, striking north 86° east and dipping 50° north was mined southeast of the stock. Besides siliceous limonite, the gossanous veins commonly contain malachite and azurite with local relict disseminated chalcopyrite, sphalerite, galena and pyrite. Assay data from rock-chip samples indicates the gossans are rich in Ag, As, Bi, Cu, Pb, Se, Sb, Te, W, and Zn and can contain strongly anomalous concentrations of Au (<500 ppb), Hg, and Mo.

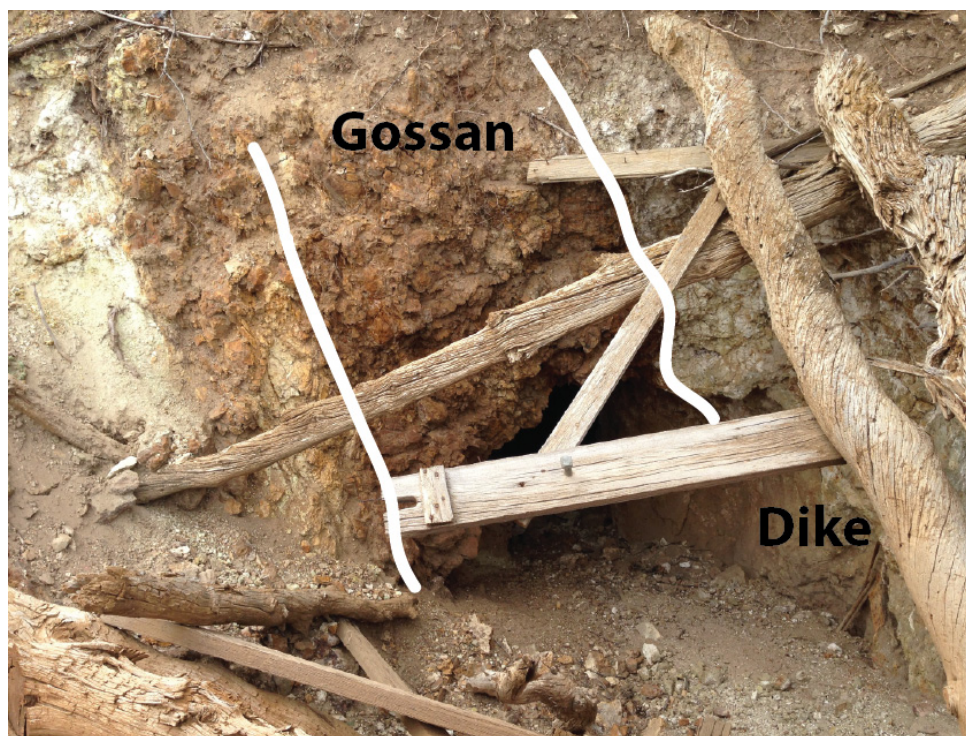


Figure 25. Old mine working developed on 2 meter-wide, gossanous polymetallic vein that formed along contact of dike (hanging wall, right) and dolomitic marble (footwall, left).

Polymetallic quartz veins occur within the granodiorite stock and extend along north-northeastward and south-southwestward trends into the Cambrian strata, commonly along dike margins. The quartz veins are composed of massive milky quartz and show no alteration envelopes. Most quartz veins that occur in the stock are located along its eastern side. The quartz veins vary from <1 mm wide to 1 m wide and typically cannot be traced for more than 50 m (Fig. 26A). Acanthite, chalcopyrite, galena, sphalerite, barite, stibnite, and pyrite occur in the quartz veins. Assay data from rock-chip samples show the quartz veins are commonly highly enriched in Ag, As, Bi, Cu, Pb, Sb, and Te, with lower enrichments of Hg, Se, W, and Zn.

Jasperoid occurs in the Cambrian strata surrounding the stock and appears to be related to the intrusion rather than the SHGDs based on geochemical signatures and

spatial relationship with dikes. The jasperoid bodies occur as large structurally controlled replacement masses in limestone, usually near or on the margins of intrusions, or along faults (Fig. 26B). The jasperoid bodies are typically found more distal to the stock (>0.5 km) than the gossan veins, and outside of the marble aureole. A ~0.5 km northeast trending zone north of the stock contains abundant structurally controlled, discontinuous jasperoid bodies (Fig. 30). The jasperoid bodies are up to 100 m long and 50 m wide with most <30 m in length and width. The original sulfide content of the jasperoids appears to have been low (<2 %) based on the lack of limonite and relict sulfides. A north-northeast trending jasperoid breccia body southwest of the stock assayed 7 ppm Au, 137 ppm Ag, and 18.7 % Pb. Larger jasperoid bodies north of the stock contain lower gold grades (<500 ppb). The typical elemental suite associated with these jasperoids includes Au Ag, As, Bi, Cu, Pb, Te, and Zn, locally with Sb, Se, and W.

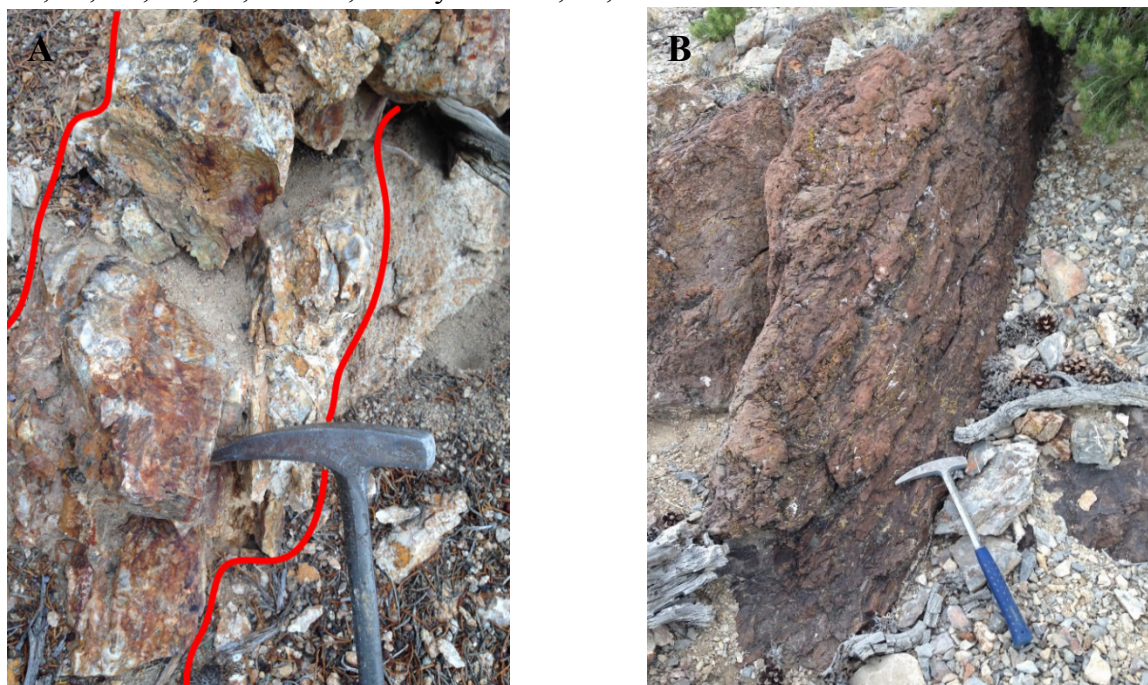


Figure 26. Polymetallic quartz veins and jasperoid. A. 0.5 m wide sulfide-bearing quartz vein cutting the stock. B. Jasperoid replacement body in the Hamburg Formation.

Bar and whisker diagrams were constructed using the 125 rock-chip samples collected proximal to the stock (<500 m) (Fig. 27). Samples were collected from gossans, skarn, quartz veins, and jasperoids. Samples were analyzed by ALS Minerals for 51 elements using ICP-MS/AES after aqua regia digestion. Values of samples collected near the stock are greatest in As, Cu, Pb, and Zn. >75 % of samples contained <100 ppb Au. Other elements that are associated with CTGD, such as Tl and Hg, have the lowest average values for any plotted elements.

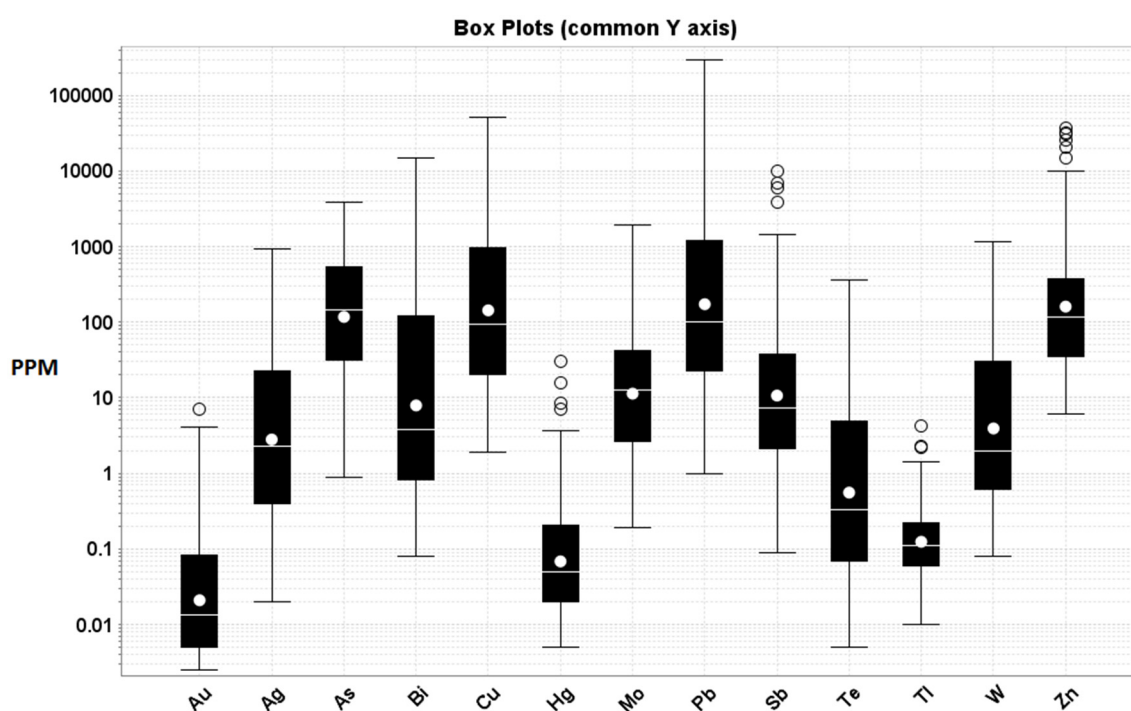


Figure 27. Bar and whisker diagram for 125 rock-chip samples collected within 500 m of the stock. In the box plot diagrams the central box is the middle 50% of the data between Q1 and Q3. A circle is an outlier further than  $1.5 \times (Q3 - Q1)$  from the box. Whiskers are extreme values that are not outliers. The white circle is the mean of values and the white line is the median.

No potassic alteration or quartz+sericite+pyrite alteration has been observed in the granodiorite stock. Granodiorite dikes near the stock commonly have moderate to strong quartz+sericite+pyrite alteration. However, a minority of the granodiorite dikes have very minimal alteration, while being spatially adjacent to moderate to strongly altered granodiorite dikes. Potassic alteration characterized by the development of secondary biotite on hornblende and biotite, and potassium feldspar flooding of the groundmass was observed in two granite dikes near the stock, as described below (Figs. 28 and 29). Strong quartz+sericite+pyrite alteration is also common in the granite dikes. The granite dikes also contain minor amounts of pyrrhotite (<0.1 %) of unknown origin that has been partially to fully replaced by pyrite.

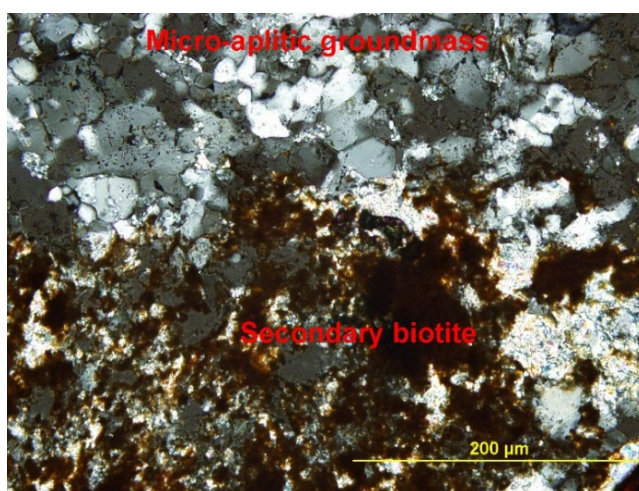


Figure 28. Photomicrograph (crossed polars) showing secondary biotite development in a granite porphyry dike with a micro-aplitic groundmass that has potassium feldspar flooding.

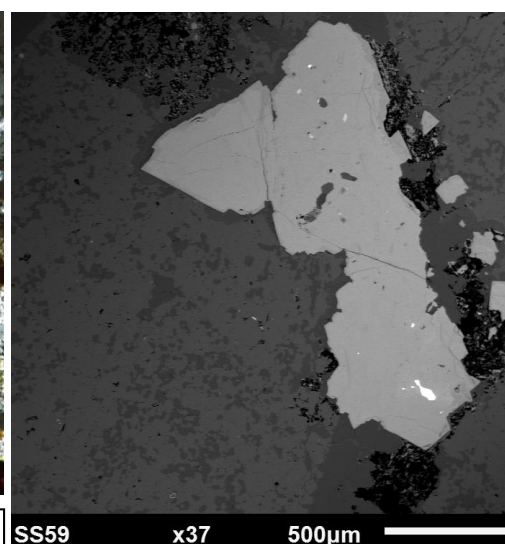


Figure 29. Backscatter electron image showing potassic alteration characterized by potassium feldspar flooding of the groundmass. Potassium feldspar is medium gray, quartz is dark gray, and goethite is light gray. Bright inclusions in the goethite are barite and relict pyrrhotite.

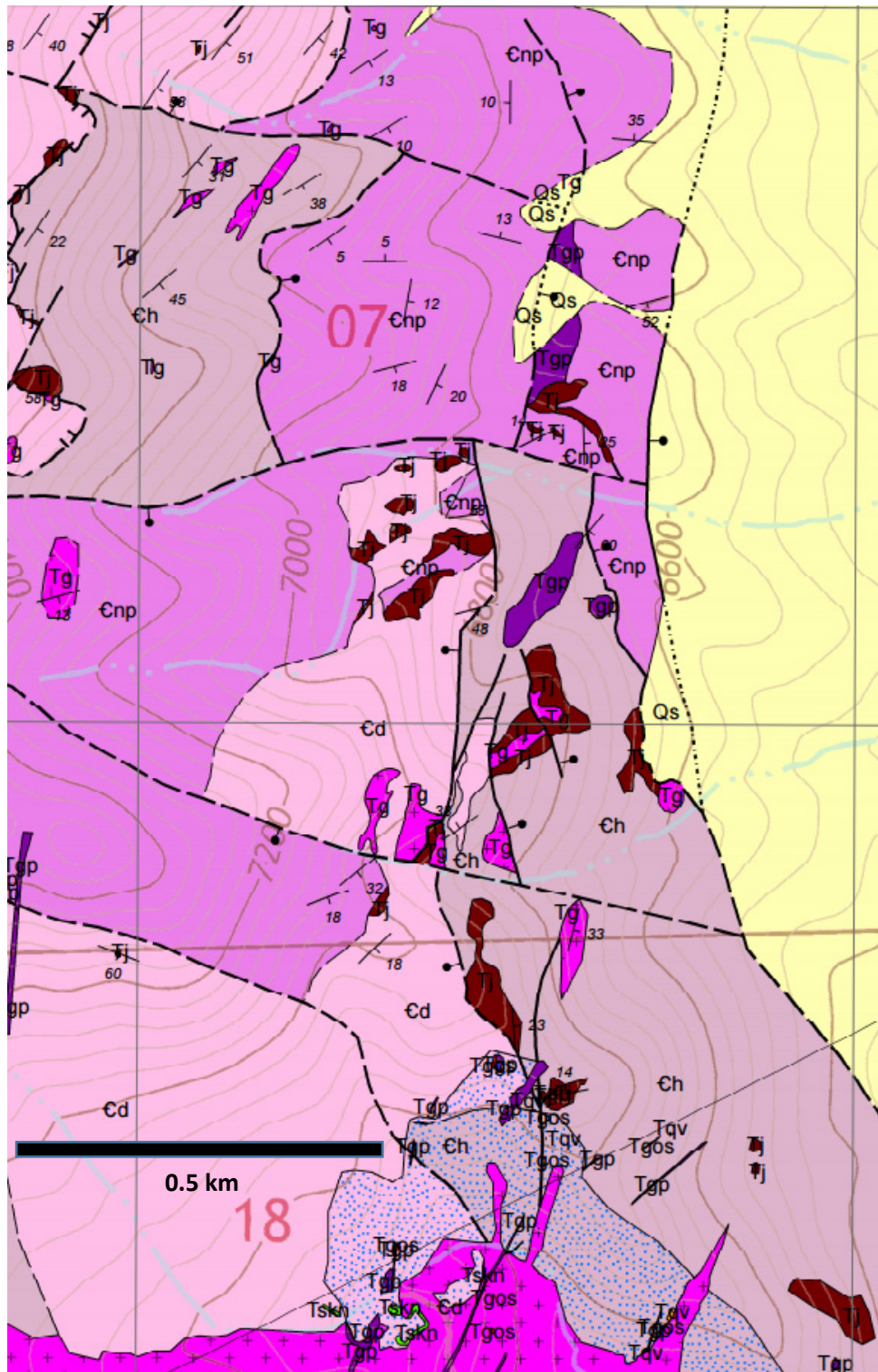


Figure 30. Inset from Figure 11 showing north-northeast-trending corridor of discontinuous jasperoids and dikes extending northward from the stock towards the area of SHGDs. Refer to legend in Figure 11.

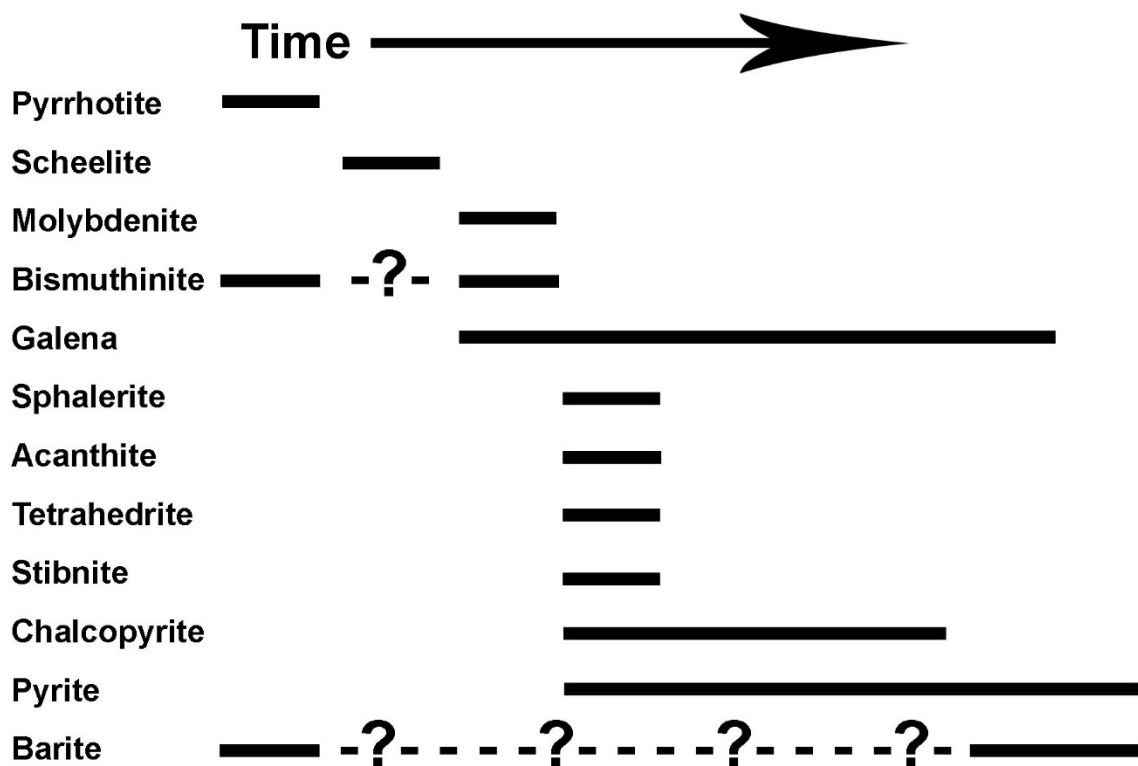


Figure 31. A paragenetic diagram for intrusion-related mineralization in polymetallic replacement veins, quartz veins, and skarn proximal to the stock.

## **VI. Sedimentary Rock Hosted Gold Mineralization**

Gold mineralization at Kinsley Mountain is characterized by fine grained (<100  $\mu\text{m}$ ), disseminated pyrite associated with decarbonatization and silicification of sedimentary host rocks. Paragenetically late realgar, orpiment, stibnite, and calcite are found within, and peripheral, to zones with gold mineralization. Gold mineralization in the Dunderberg Shale and Notch Peak Limestone was produced from eight pits and has also been discovered in the West Flank and Right Spot targets, approximately 0.5 km northwest and 0.5 km southwest of the old pits, respectively (Fig. 32). High-angle faults provide a primary control for mineralization with most mineralization located within a 1 km long, 0.5 km wide, northwest-trending fault system (Hannink et al., 2015). Stratigraphy provides a secondary control for mineralization as Au-bearing ore fluids sulfidized the iron-bearing Dunderberg Shale and Secret Canyon Shale, as argued below. Gold mineralization at Kinsley can be separated into three zones based on characteristics of the mineralization: 1) gold mineralization in the Dunderberg Shale, 2) gold mineralization in the Secret Canyon Shale in the West Flank, and 3) gold mineralization in the Secret Canyon Shale at Secret Spot. The Notch Peak Limestone and Hamburg Limestone host only minor amounts of gold mineralization and are not described here.

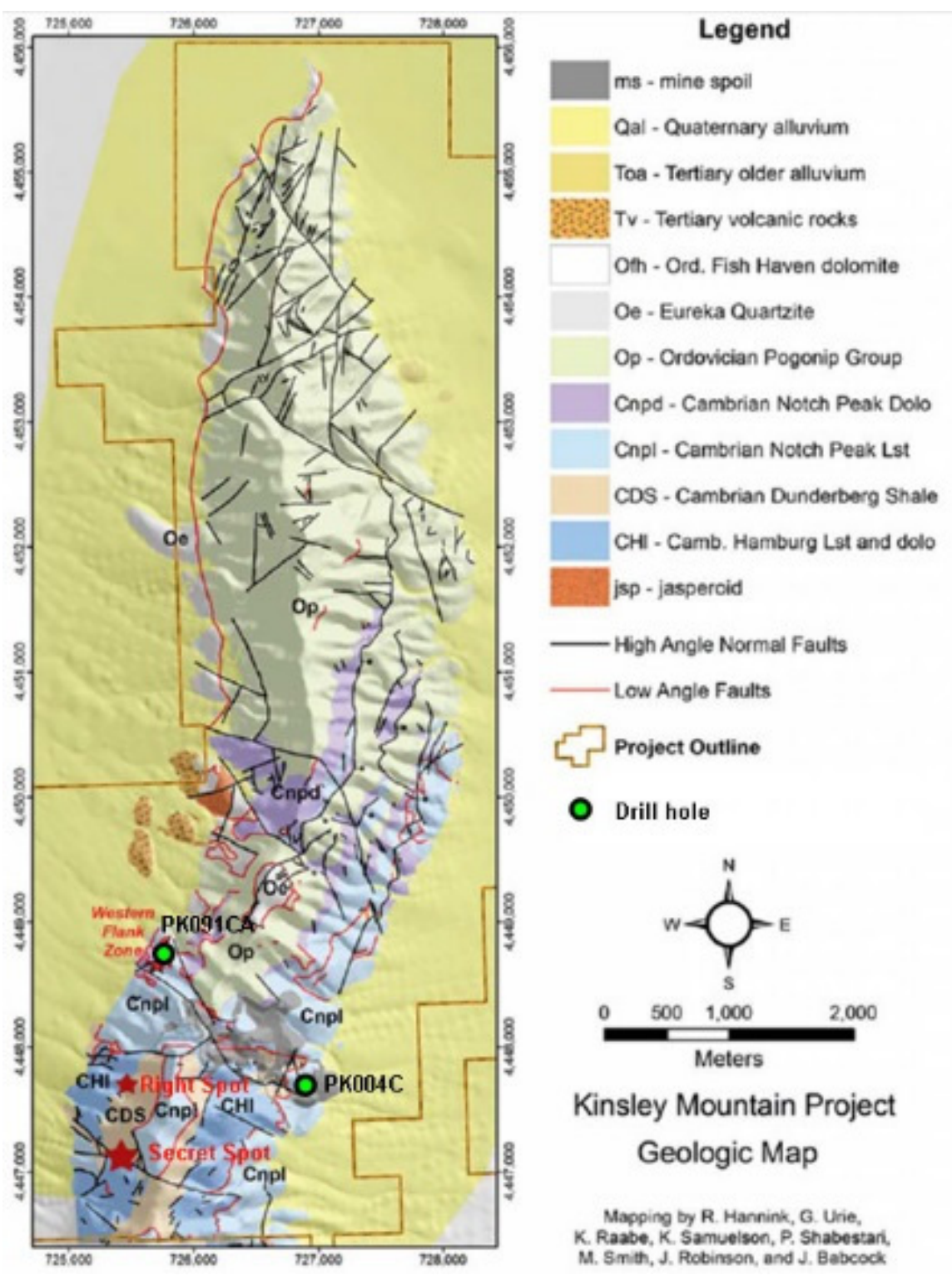


Figure 32. Geologic map of Kinsley Mountain. The West Flank, Right Spot, and Secret Spot targets are shown with red stars (Hannink et al., 2015). Locations of drill holes used for transects are plotted as green circles.

## Dunderberg Shale Transect

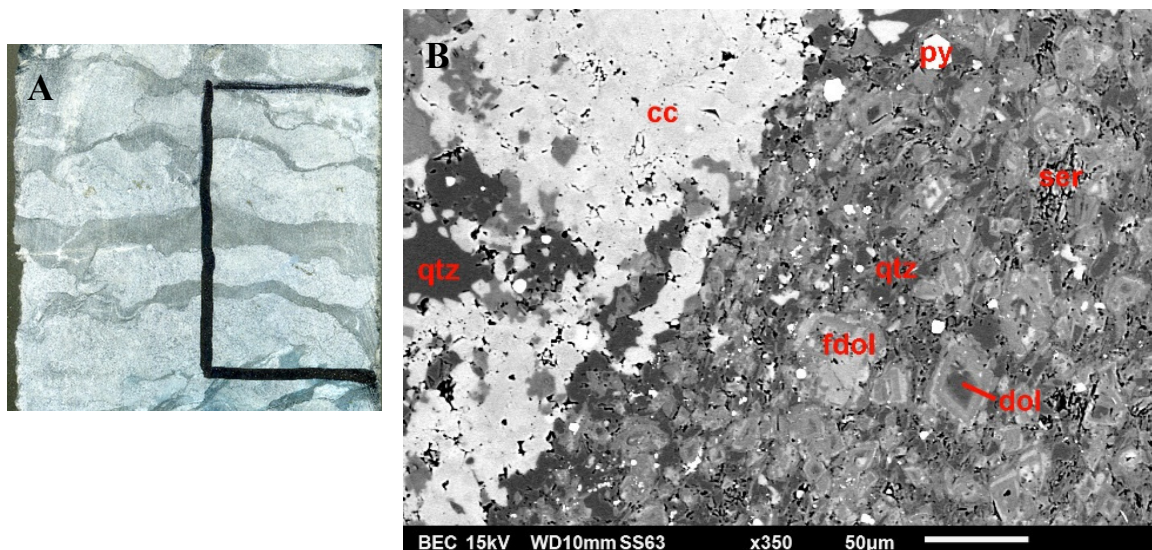
A transect of four samples over 84 feet of the Dunderberg Shale, which assayed from <5 ppb Au to 20.3 ppm Au, were collected from a drill hole on the east side of the range. The transect shows a change from interbedded fine-grained limestone and shale to hydrothermally altered rock that contains Au-bearing pyrite, quartz, muscovite, paragonite, apatite, with little to no relict carbonate (Fig. 33). The Dunderberg Shale is comprised of 1–10 cm thick limestone and shale beds with continuous intervals of limestone or shale up to 10 m thick (Fig. 33A). In samples that have not been hydrothermally altered (<5 ppb Au), the limestone beds are composed of <10  $\mu\text{m}$  euhedral calcite grains with <5 % clastic components that include quartz, sericite, apatite, and fossil fragments. The limestone beds locally show patchy replacement by dolomite.

In sample PK004C-217, which came from a three foot interval that assayed <5 ppb Au, the shale beds are composed of rhombic euhedral, 5–50  $\mu\text{m}$ , zoned, ferroan dolomite grains (50–60 %) with 30–40 % clastic material primarily consisting of sericite (<20  $\mu\text{m}$ ), with minor quartz, apatite, fossil fragments, and pyrobitumen (Fig. 33B). The ferroan dolomite grains commonly have iron-poor cores (0–4 wt % Fe) with iron-rich rims containing up to 10 wt % Fe. Calcite locally occurs interstitially to the ferroan dolomite grains and clastic components. Diagenetic pyrite is common in the shale intervals, but is far less abundant in limestone. The diagenetic pyrite ranges in size from <1–150  $\mu\text{m}$ , with >90 % of the pyrite being <5  $\mu\text{m}$ . The diagenetic pyrite is commonly framboidal, but is also present as subhedral to euhedral grains and typically comprises <0.1 % of the rock. Small clusters (<50  $\mu\text{m}$ ) of < 5  $\mu\text{m}$  framboids or subhedral to euhedral grains are common.

In sample PK004C-133, which came from a four foot interval that assayed 92 ppb Au, intergrown muscovite and paragonite up to 200  $\mu\text{m}$  in length is present (Fig. 33C-D). Based on preliminary  $^{40}\text{Ar}/^{39}\text{Ar}$  dating, the muscovite and paragonite are detrital and not part of the hydrothermal system. Finer grained ( $<10\ \mu\text{m}$ ), interstitial detrital sericite does not have any associated paragonite. Ferroan dolomite grains are still common ( $\sim 30\%$ ), but dissolution has caused the grains to become rounded. Non-interlocking, anhedral quartz is more abundant than the unaltered sample, but is still minor ( $\sim 5\%$ ). A slight increase in porosity has developed ( $3\text{--}5\%$ ) and pyrite is coarser ( $10\text{--}50\ \mu\text{m}$ ) and more abundant ( $1\text{--}2\%$ ). Limestone beds from this interval show minor, patchy replacement by quartz.

In sample PK004C-149.5, which came from a five foot wide shale interval that assayed 3.44 ppm Au, coarse grained ( $\sim 300\ \mu\text{m}$ ), detrital intergrown muscovite and paragonite are abundant (Fig. 33E-F). This muscovite and paragonite and sericite compose  $\sim 50\%$  of the shale, the apparent increase of which was likely due to dissolution of carbonate. Non interlocking, hydrothermal, anhedral quartz is a significant component of the sample ( $10\text{--}15\%$ ). The amount ferroan dolomite is significantly lower ( $\sim 15\%$ ) and it appears patchy and rounded, likely due to dissolution. Hydrothermal euhedral to subhedral pyrite constitutes  $\sim 5\%$  of the rock. Grain size varies from  $1\text{--}100\ \mu\text{m}$  and occurs as individual grains and clusters of multiple grains that have coalesced. Pore space is higher, varying between  $5\text{--}10\%$ . Limestone beds in this sample show  $40\text{--}60\%$  replacement by patchy, non-interlocking, anhedral quartz. Both limestone and shale beds show minor to moderate amounts of volume loss in the form of increased porosity and reduction of bed thickness from dissolution of carbonate.

In sample PK004C-154, which came from a five foot wide shale interval that assayed 13.45 ppm Au, detrital intergrown muscovite and paragonite, are abundant and up to 300  $\mu\text{m}$  in length, and along with detrital sericite comprise  $\sim 60\%$  of the shale (Fig. 33G-H). Non interlocking, hydrothermal, granular, anhedral quartz is abundant (25 %) and is coarser than the lower grade samples (50–200  $\mu\text{m}$ ). Ferroan dolomite is absent, but minor amounts of non-ferroan dolomite are present ( $\sim 5\%$ ). Euhedral to subhedral pyrite development is very strong and, locally comprises 10–20 % of the rock. Pore space is locally abundant to nearly absent, depending on whether open space was filled by late quartz, calcite, stibnite, orpiment, or realgar. Limestone beds in this sample are completely silicified and thinned significantly, as a result of dissolution. Shale beds have also experienced significant volume loss due to dissolution of ferroan dolomite.



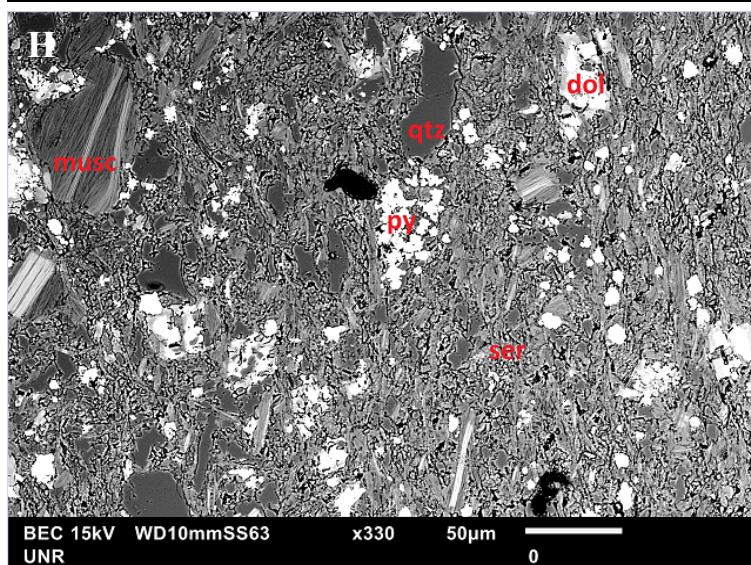
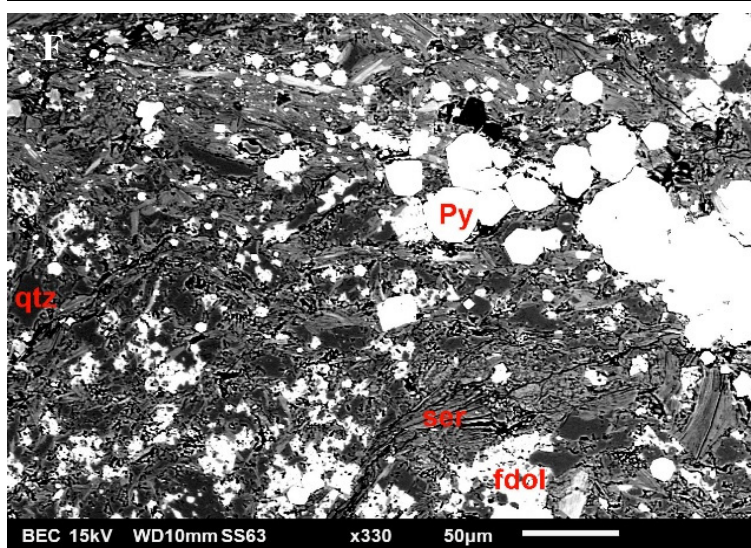
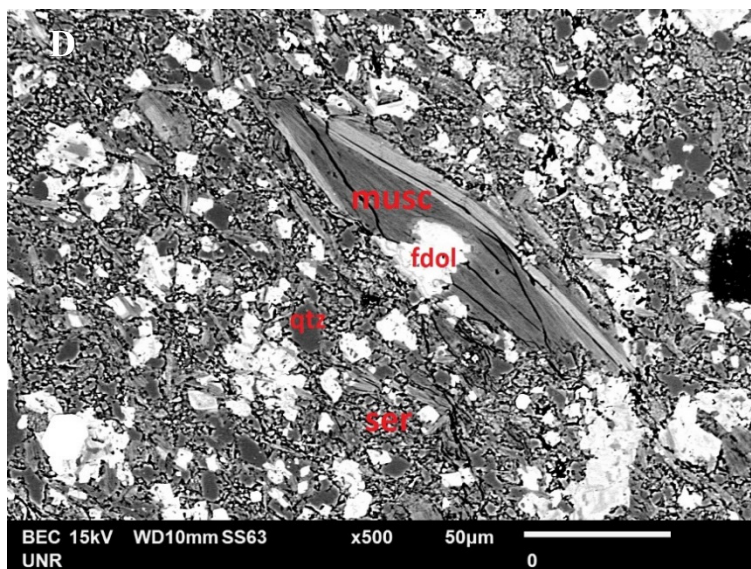


Figure 33. Samples and backscatter electron (BSE) images from Dunderberg Shale transect from unaltered rock to ore-grade material (PK004C over 84 feet). A. Unaltered interbedded limestone and shale. PK004C-217', three foot interval, <5 ppb Au. B. BSE image showing a limestone bed (left side) is in contact with a shale beds (right side). The limestone beds is composed of calcite (cc) with minor quartz (qtz). The shale bed contains mostly ferroan dolomite (fdol) and sericite (ser) with minor quartz (qtz). There is little to no pore space which is characterized by black space within the image. Note the zoning in the rhombohedral dolomite grains from iron-poor dolomite cores (dol) to brighter ferroan dolomite rims (fdol). C. Weakly altered and mineralized shale with limestone nodules. PK004C-133', four foot interval, 0.092 ppm Au. D. BSE image shows shale beds with rounded ferroan dol (fdol, bright), sericite (ser), and minor anhedral quartz. Rounding of ferroan dolomite and increased pore space is due to dissolution of carbonate. E. Moderately altered interlayered shale and limestone. PK004C-149.5', five foot interval, 3.44 ppm Au. F. BSE image shows hydrothermally altered and mineralized shale bed. Ferroan dolomite (fdol) is rounded and patchy due to dissolution. Quartz grains (qtz, dark) are anhedral, but do not interlock due to the abundance of sericite between grains. Fine-grained detrital sericite and coarse-grained detrital intergrown muscovite and paragonite are present. Euhedral, coarse pyrite (py, bright) is present. G. Strongly altered interlayered shale and limestone. PK004C-154', five foot interval, 13.45 ppm Au. H. BSE image shows shale bed where ferroan dolomite is absent. Dolomite is present in minor amounts (dol). Hydrothermal anhedral quartz (qtz, dark) is abundant an up to 50  $\mu\text{m}$  in size. Detrital, intergrown muscovite (musc, bright) and paragonite (musc, dark) are common and up to 300  $\mu\text{m}$  long. Hydrothermal pyrite (py, bright) forms individual grains and clusters of grains. Detrital sericite (ser) is more abundant due to volume loss from the dissolution of carbonate. Pore space (black) is locally abundant (up to 10%).

### Secret Canyon Shale Transect

A transect of four samples over 107 feet of the Secret Canyon Shale, which assayed from <5 ppb Au to 69.7 ppm Au, were collected from a drill hole in the West Flank. The transect shows a change from fine grained limestone and shale to rock that contains Au-bearing pyrite, hydrothermal apatite, and a loss of carbonate with the addition of silica (Fig. 34). The mineralogy and textures of unaltered samples of the

Secret Canyon Shale are nearly identical to the Dunderberg Shale as described above.

The Secret Canyon Shale has less detrital quartz and apatite.

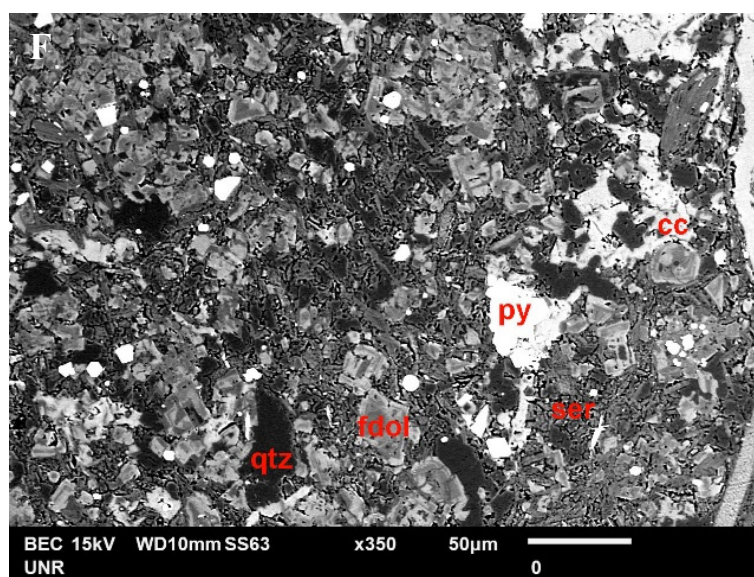
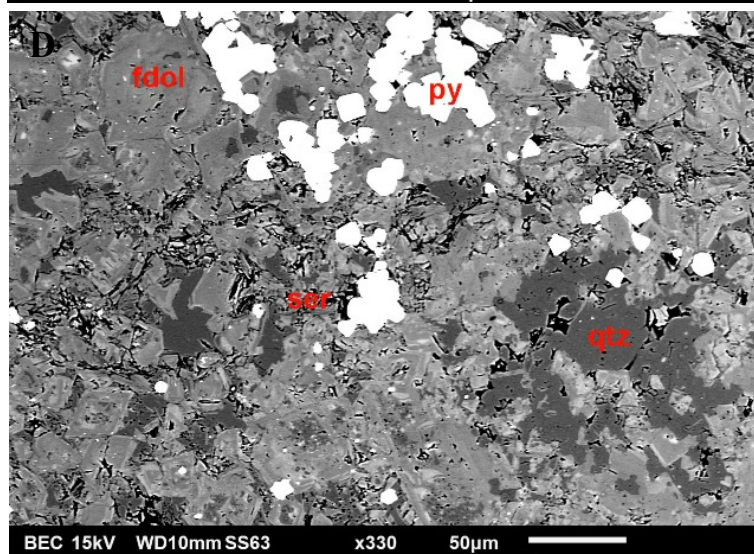
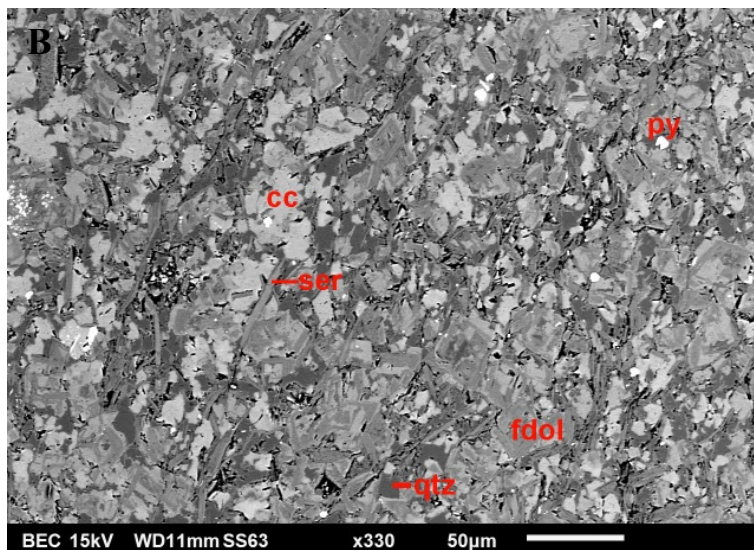
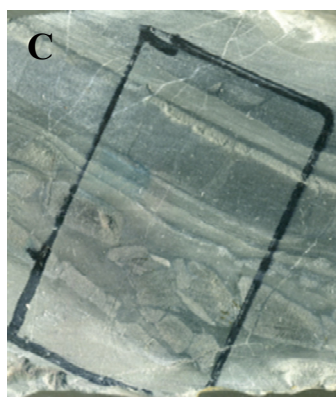
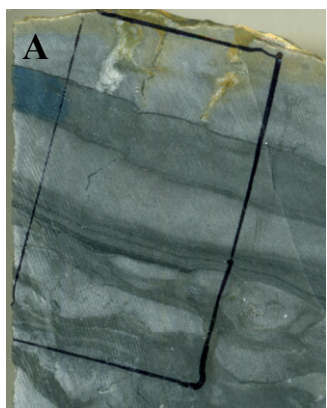
In sample PK091CA-808', which came from a five foot wide shale interval that assayed <5 ppb Au, sericite/muscovite grains are composed ~30 % of the shale and range from <5  $\mu\text{m}$  to 50  $\mu\text{m}$  in length, but none are more than 10  $\mu\text{m}$  in width (Fig. 34A-B). Ferroan dolomite and calcite are abundant. Ferroan dolomite grains are subhedral to euhedral, 5–50  $\mu\text{m}$  in size, zoned, and account for ~50 % of the shale. The compositional zoning of the ferroan dolomite is the same as observed in the Dunderberg Shale. Calcite is anhedral, patchy in appearance, and comprises ~15 % of the shale. Quartz and apatite are minor components, accounting for ~5 % of the shale. Pore space and diagenetic pyrite are minimal (<2 %).

In sample PK091CA-859, which came from a three foot wide shale interval that assayed 730 ppb Au, calcite is absent (Fig. 33C-D). Abundant ferroan dolomite occurs as rounded grains adjacent to quartz. The quartz comprises ~10% of the shale and is predominantly hydrothermal, occurring mainly as non-interlocking patches of anhedral grains that replace calcite and ferroan dolomite. Sericite grains remain unchanged in appearance and abundance. Pyrite is abundant and accounts for 3–5 % of the shale. It occurs as isolated subhedral to euhedral grains and clusters of coalesced grains up to 100  $\mu\text{m}$  across. Porosity is ~5 %, and limestone beds or nodules in this sample show patchy replacement by quartz.

In sample PK091CA-883, which came from a five and a half foot wide shale interval that assayed 3.3 ppm Au, dramatic dissolution of ferroan dolomite is evident (Fig. 34E-F). Ferroan dolomite is rounded, but accounts for only ~30 % of the shale.

Hydrothermal quartz occurs as patches of non-interlocking anhedral grains (<5–50  $\mu\text{m}$ ) and comprise ~20 % of the shale. Sericite, interpreted as pre-hydrothermal, accounts for ~35 % of the shale, the increase likely due to residual enrichment resulting from carbonate dissolution and volume loss. Calcite is present in minor amounts and is anhedral and patchy. Pyrite is abundant, occurs as subhedral to euhedral isolated grains and clusters of grains up to 100  $\mu\text{m}$ . Pyrite comprises 3–5 % of the shale, but is locally more abundant. Pore space remains unchanged or reduced from the previous sample, likely the result of quartz filling open space. Limestone beds in this interval display strong anhedral, patchy replacement by hydrothermal quartz, with some areas that are completely replaced by quartz.

In sample PK091CA-915, which came from a three foot wide shale interval that assayed 69.7 ppm Au, ferroan dolomite and calcite are absent (Fig. 34G-H). Hydrothermal quartz is abundant (~40 %), occurring as anhedral, <5–50  $\mu\text{m}$ , non-interlocking grains. Sericite is significantly more abundant due to volume loss of carbonates and comprises ~40 % of the shale. Pore space has increased significantly and accounts for 5–10 % of the rock. Pyrite is abundant (5–25 %) and, in hand sample, appears locally to have completely replaced shale beds, with areas up to ~40% pyrite. This strongly mineralized interval has undergone dramatic volume loss, commonly >75 % in the limestone beds, and >50 % in the shale beds, with the beds being as thin as 2–3 cm.



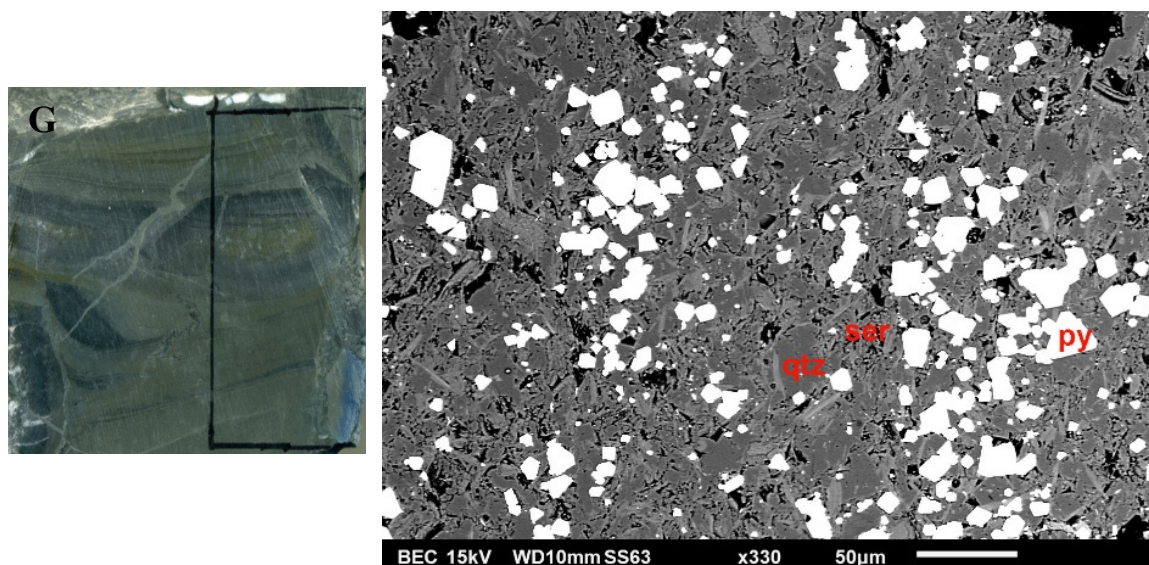


Figure 34. Samples and backscatter electron (BSE) images from Secret Canyon Shale transect from unaltered rock to ore-grade material (PK091CA over 107 feet). A. Unaltered interbedded limestone and shale. 808', five foot interval, <5 ppb Au. B. BSE image shows calcite (cc), quartz, (qtz), sericite (ser), ferroan dolomite (fdol), and pyrite (py). The ferroan dolomite is euhedral and zoned with higher iron contents on the outer portions of grains. Sericite grains are up to 50  $\mu\text{m}$  long, but <10  $\mu\text{m}$  wide. Very minor pore space (black). C. Weakly altered and mineralized shale with limestone nodules. 859', three foot interval, 730 ppb Au. D. BSE image shows weakly altered shale bed, Ferroan dolomite (fdol) grains are abundant, but have become rounded due to partial dissolution. Hydrothermal quartz (qtz, dark gray) is more abundant and some grains interlock to form 50–100  $\mu\text{m}$  patches. Hydrothermal, euhedral, coarse pyrite (py) occurs adjacent to ferroan dolomite. Pore space (black) has increased significantly. E. Moderately altered and mineralized interbedded shale and limestone. 883', five and a half foot interval, 3.3 ppm Au. F. BSE image shows shale containing ferroan dolomite (fdol), calcite (cc), hydrothermal pyrite (py, bright), detrital sericite, and detrital quartz. Ferroan dolomite grains are abundant, but have become rounded from dissolution. Calcite is nearly absent, but where present is anhedral and patchy. Hydrothermal quartz forms grains up to 50  $\mu\text{m}$ . Pore space is minor, but is greater than the unaltered sample. Hydrothermal pyrite forms individual euhedral grains and clusters of grains up to 50  $\mu\text{m}$  across. G. Strongly altered and mineralized interbedded shale and limestone. 915', three foot interval, 69.7 ppm Au. H. BSE image shows shale bed. Ferroan dolomite grains are absent. Hydrothermal quartz is abundant, but grains are not able to interlock due to abundant sericite. Hydrothermal, euhedral, coarse-grained pyrite is abundant. Pore space has increased significantly due to dissolution of ferroan dolomite and calcite.

Collapse breccias are present where there is significant volume loss, typically where limestone beds are more abundant than shale beds. Where limestone beds are recognizable, they have been completely replaced by quartz in the form of jasperoid. The jasperoid is composed of 5–300  $\mu\text{m}$  anhedral quartz crystals displaying a xenomorphic fabric. There are, however, local areas of calcite in strongly altered and mineralized rock. In these areas the calcite is coarse-grained and contains inclusions of coarse (up to 500  $\mu\text{m}$ ), euhedral, quartz crystals, as well as ore-stage arsenian–pyrite (Fig. 35). These areas of calcite, quartz, and pyrite are likely a result of variations in ore fluid chemistry near carbonate saturation during hydrothermal alteration, resulting in dissolution and local re-precipitation of carbonate.

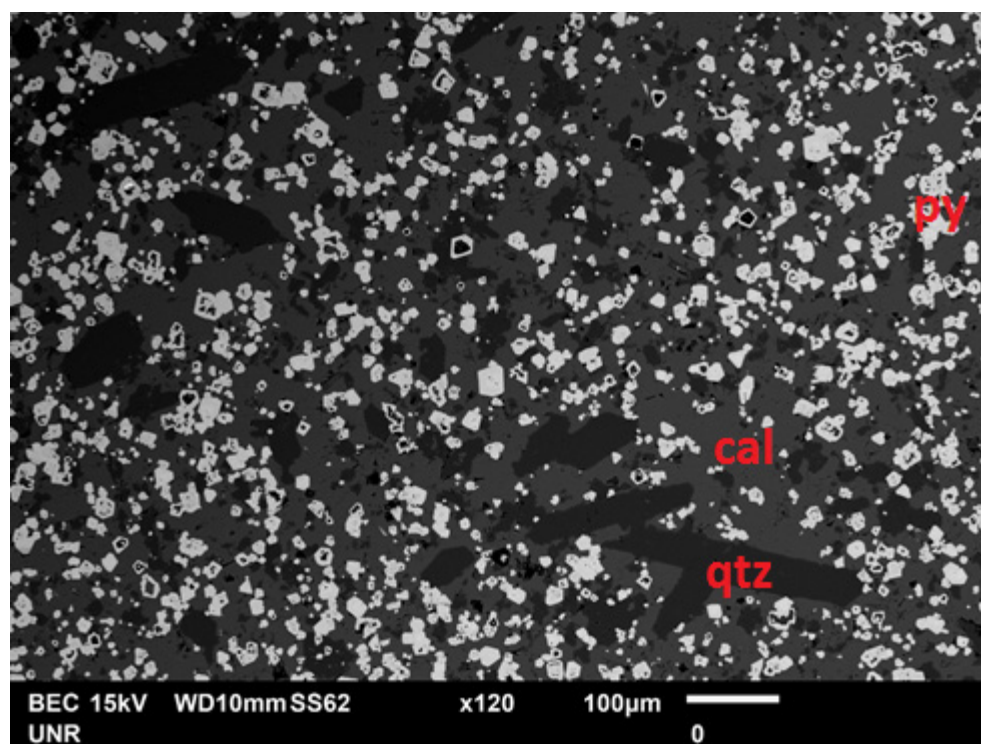


Figure 35. Backscatter electron image of high-grade sample from three foot interval that assayed 69.7 ppm in the Secret Canyon Shale. Mineralized pyrite in optically continuous coarse calcite with euhedral reticulate coarse-grained quartz from the Secret Canyon Shale (69.7 ppm Au over 5 ft).

Secondary apatite occurs in all mineralized samples of Dunderberg Shale and Secret Canyon Shale as uranium–poor, fluoride–rich apatite rims enveloping detrital apatite (Fig. 36). The presence of euhedral pyrite grains with arsenian–pyrite rims this this apatite suggests a hydrothermal origin. This interpreted hydrothermal apatite also occurs as narrow (<25  $\mu\text{m}$ ) veinlets.

Changes in rock characteristics from unmineralized samples to mineralized samples show similar features in both the Dunderberg Shale and Secret Canyon Shale. In both stratigraphic intervals, quartz replaces carbonate and Au– bearing arsenian–pyrite forms as ore fluids sulfidize the shales, as detailed below. Pore space increases as a result of dissolution of carbonate and collapse breccias may form.

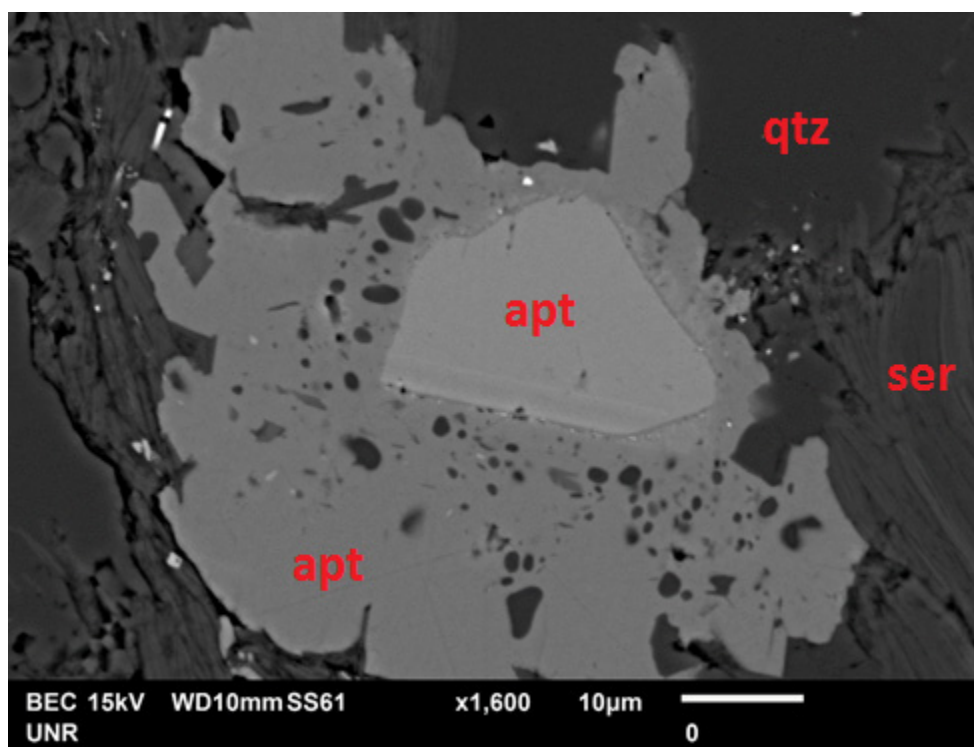


Figure 36. Backscatter image of hydrothermal apatite (4.43 wt % F) enveloping a detrital apatite (3.76 wt % F) with small inclusions of pyrite (bright grains). (PK004C-154', five foot interval that assayed 13.45 ppm Au)

## Dunderberg Shale mineralization

Unoxidized portions of the gold mineralization in the Dunderberg Shale is characterized by gold-bearing arsenian-pyrite rims on preexisting pyrite. Ore-stage pyrite is defined as arsenian-pyrite (>2 wt % As) containing detectable gold with an electron microprobe. The preexisting pyrite is interpreted to be pre-ore and diagenetic in origin. The pyrite ranges in size from <1–150  $\mu\text{m}$ , though pyrite grains <20  $\mu\text{m}$  are most abundant (Fig. 37A), with an average size to 10  $\mu\text{m}$ . Patches of pyrite (>100  $\mu\text{m}$ ) are

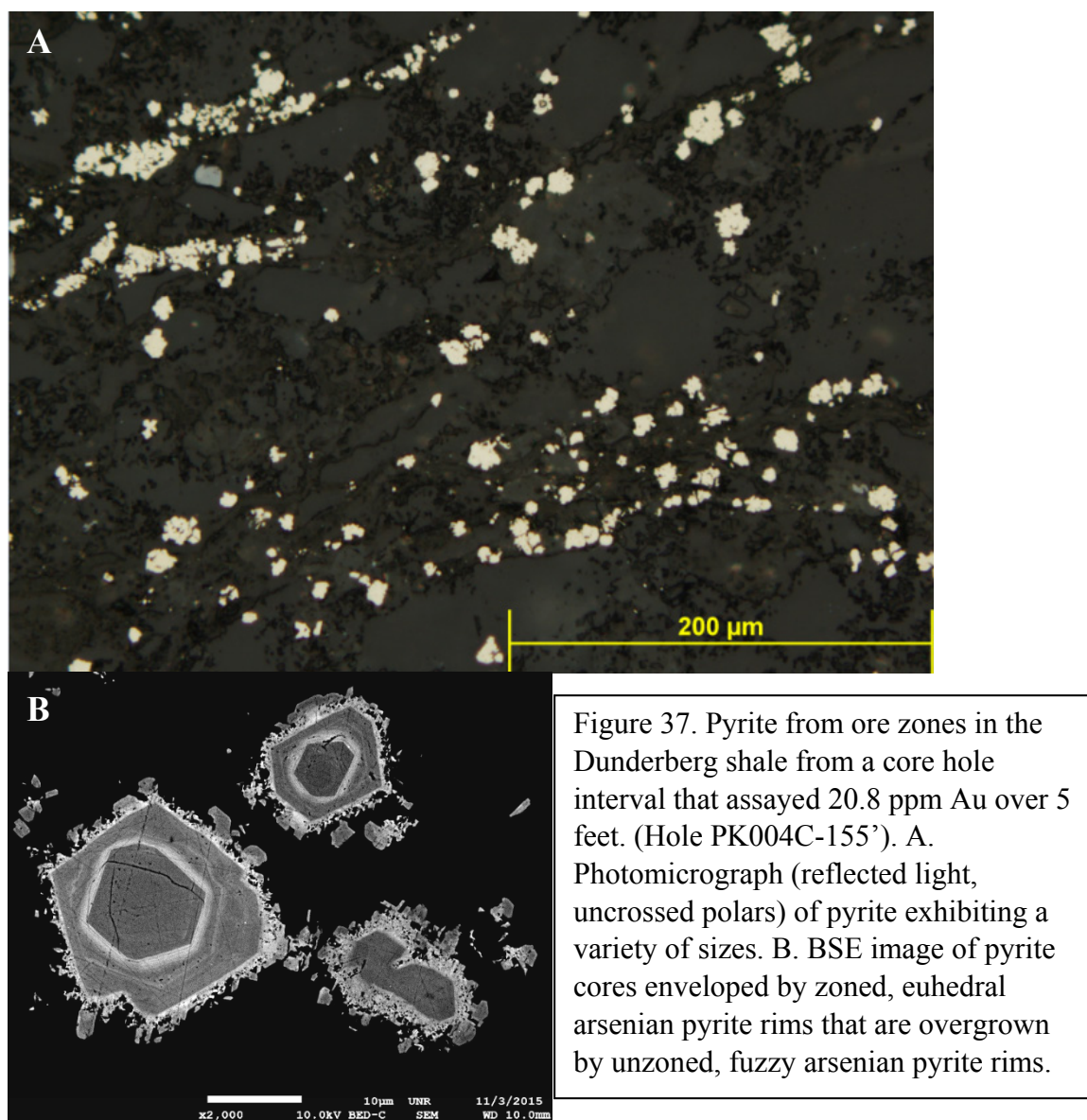


Figure 37. Pyrite from ore zones in the Dunderberg shale from a core hole interval that assayed 20.8 ppm Au over 5 feet. (Hole PK004C-155'). A. Photomicrograph (reflected light, uncrossed polars) of pyrite exhibiting a variety of sizes. B. BSE image of pyrite cores enveloped by zoned, euhedral arsenian pyrite rims that are overgrown by unzoned, fuzzy arsenian pyrite rims.

typically the result of coalescence of smaller individual grains. Some of the pyrite display compositionally zoned (As), euhedral, arsenian–pyrite rims, while other pyrites exhibit fuzzy rims with little to no zonation (Fig. 37B). Minor amounts of sphalerite are present with gold ore (unoxidized intervals range up to 348 ppm Zn). Sphalerite has been observed enveloping arsenian–pyrite rims, as inclusions in pyrite, and as anhedral grains, indicating sphalerite pre-dated and post-dated arsenian–pyrite (Fig. 38A). Galena locally occurs as  $<5\ \mu\text{m}$  inclusions in pyrite (Fig. 38B), suggesting not all of the preexisting pyrite was of diagenetic origin. Some of the “preexisting” pyrite was of likely of hydrothermal origin, possibly related to intrusion–related mineralization. Though the galena has been observed in many mineralized intervals, it is only present in small amounts ( $\leq 66\ \text{ppm Pb}$  in assayed drill intervals). Arsenopyrite occurs as  $<5\ \mu\text{m}$  inclusions in arsenian–pyrite rims and less commonly as subhedral to euhedral grains that

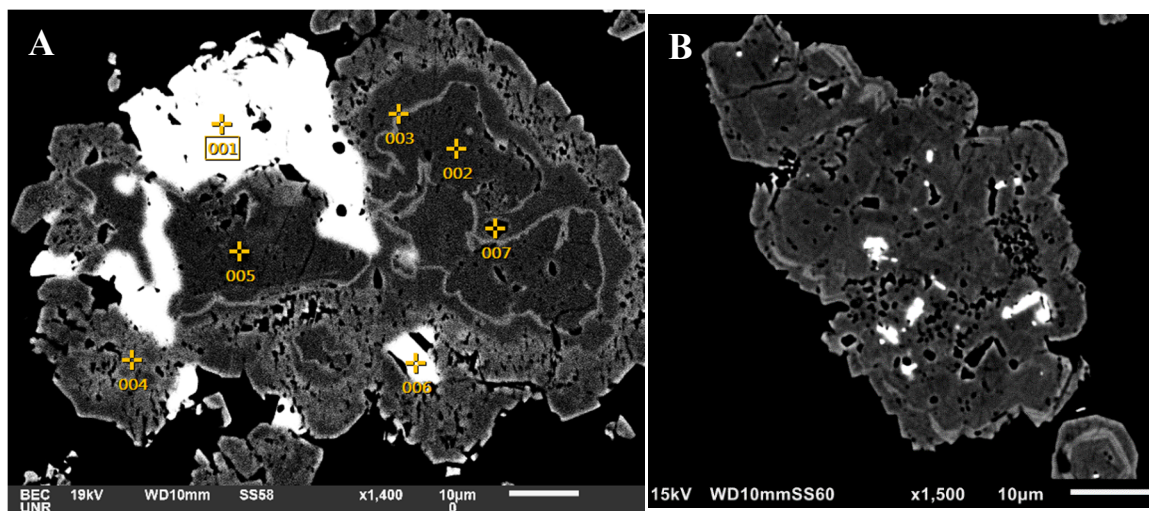


Figure 38. Backscattered electron images of ore-stage pyrite hosted by Dunderberg Shale (PK004C-154, five foot interval that assayed 13.45 ppm Au). A. A large irregular pyrite core (002 and 005) with a thin arsenian pyrite zone (003) followed by more pyrite with a surrounding envelope of arsenian pyrite (004). Sphalerite (001) appears to have formed after the arsenian–pyrite rim. B. Small galena inclusions in pyrite, overgrown by an arsenian–pyrite rim.

formed after the arsenian–pyrite rims. Late realgar, orpiment, and stibnite are present, and formed in open spaces in the Dunderberg Shale, both within and outside ore zones.

Stibnite crystals up to 5 cm in length formed where open space was abundant, but stibnite is also commonly present as isolated grains, or clusters of grains.

The silver to gold ratio in unoxidized portions of mineralization hosted by the Dunderberg Shale ranges from 1:1 to 1:5, with an average of 1:2. Arsenic weight percentages, determined with EDS using the SEM, in arsenian–pyrite rims range from 1–11 % with an average of 4 %. Native gold was reported by Cominco as particles from <1  $\mu\text{m}$  to 80  $\mu\text{m}$  in size in close association with limonite in oxidized ore, but has not been observed during this study or other recent studies of unoxidized mineralization (Gustin et al., 2012). A northwest control on mineralization is apparent (Fig. 39). North to northeast high-angle faults likely served as fluid pathways for ore fluids (Fig. 40).

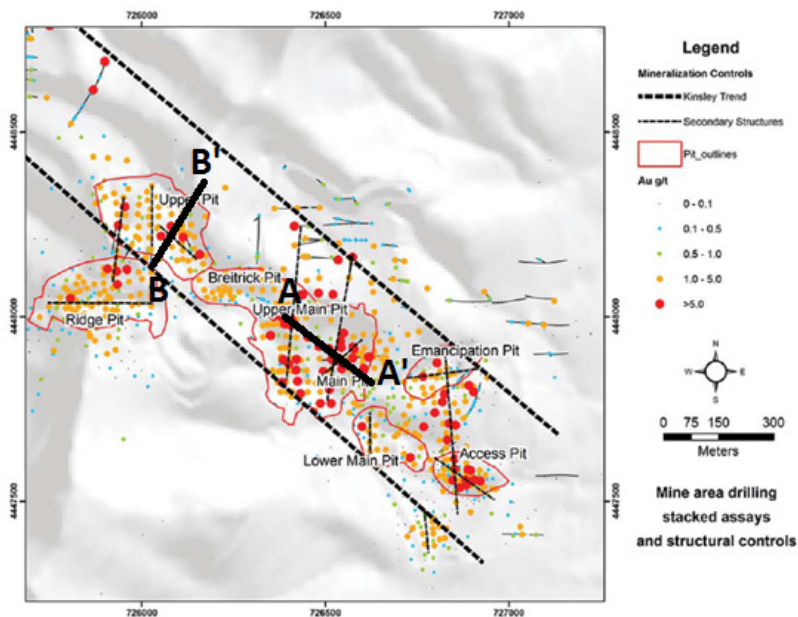


Figure 39. Map of the Kinsley Mine area showing the northwest-trending fault zone and possible secondary structural controls based on development drilling. Each point is a drill or blast hole. The highest Au grade from each hole is projected to the surface as a point (modified from Hannink et al., 2015).

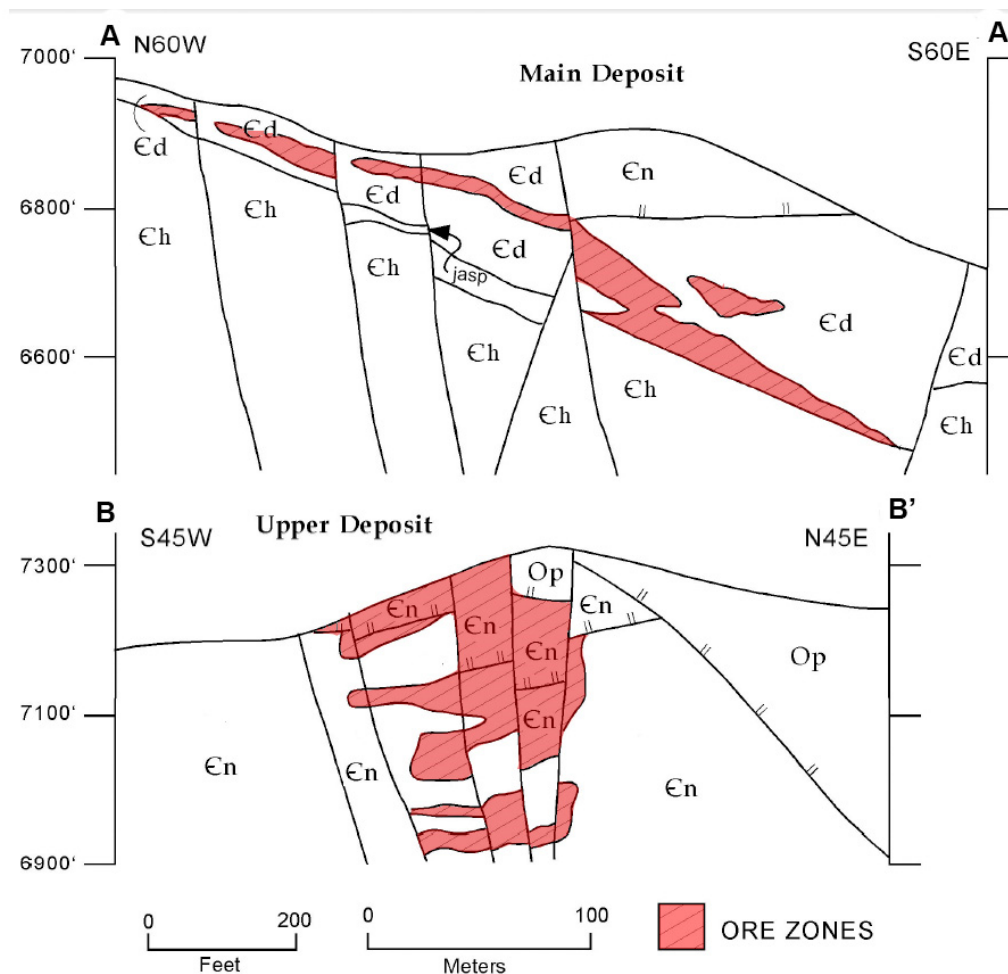


Figure 40. Cross-section through the Main Pit and Upper Main Pit (modified from Robinson, 2005).

Electron microprobe analysis was conducted at the University of Nevada Las Vegas to determine the chemical composition of the arsenian–pyrite rims. Results demonstrate gold concentrations as high as 620 ppm in arsenian–pyrite rims in the Dunderberg Shale (Fig. 41). However, gold does not correlate with arsenic. Diagenetic pyrite does not contain detectable gold or mercury, but typically contains <1 wt % As, <400 ppm Tl, <500 ppm Cu, >1000 ppm Co, >300 ppm Ni, and <100 ppm Sn. In contrast, arsenian-pyrite rims on average contain >1 wt % As, >400 ppm Tl, >500 ppm

Cu, <300 ppm Ni, and <750 ppm Co. However, pyrite cores can also contain similar quantities of arsenic, copper, thallium, and antimony as those found in arsenian–pyrite rims, suggesting those cores are hydrothermal rather than diagenetic in origin, discussed above. Tellurium concentrations was below detection limit in all analyses (50 ppm), both in hydrothermal and diagenetic pyrites. A full list of microprobe data is located in Appendix D.

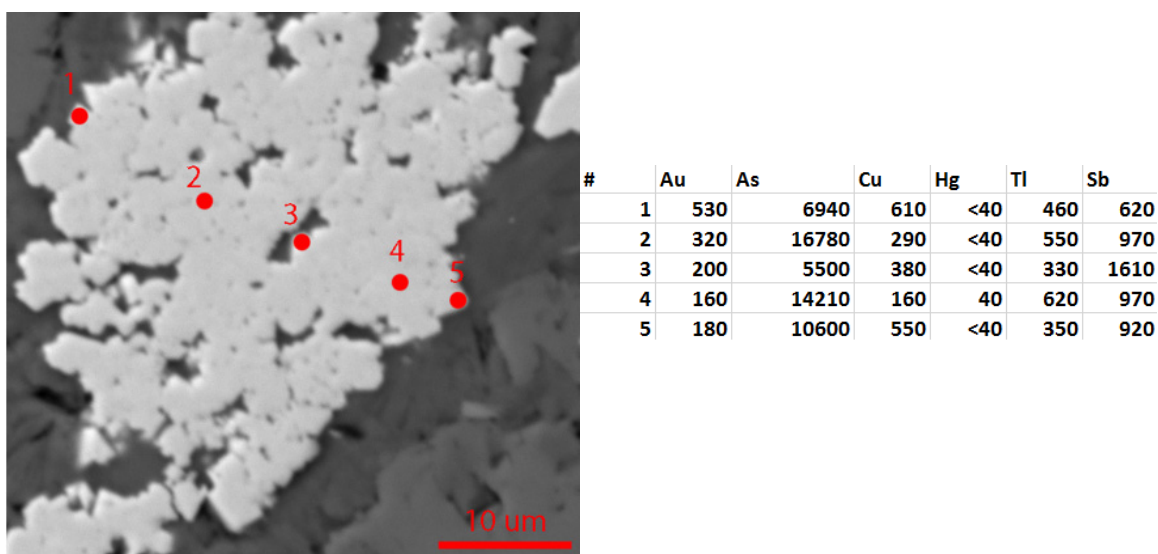


Figure 41. Backscattered electron images of ore-stage pyrite hosted in the Dunderberg Shale showing electron microprobe transect across a cluster of pyrite grains (PK004C-154', five foot interval that assayed 13.45 ppm Au). The concentrations for gold, copper, mercury, thallium, and Sb (all in ppm) are shown in the table. No pyrite cores were analyzed in this transect.

#### Secret Canyon Shale mineralization

Significant gold mineralization in the Secret Canyon Shale has only been discovered on the west side of Kinsley Mountain in the mineralized area known as the West Flank (Fig. 1). Mineralization is characterized by <1–100 µm euhedral zoned arsenian–pyrites with an average size of 20 µm (Fig. 42). In places, many small pyrite

grains coalesce into clusters that can be up to 1 mm in diameter. The arsenian–pyrite rims often contain a small diagenetic or pre–ore stage hydrothermal pyrite core ranging in size from <1–10  $\mu\text{m}$ , though many of the arsenian–pyrite grains appear to have no pre–ore pyrite cores. Grains that do have pyrite cores will often show a small zone of sericite surrounding the core, followed by arsenian–pyrite (Fig 42B). Rarely, <5  $\mu\text{m}$  galena will be surrounded by pre–ore stage pyrite with an overgrowth of zoned arsenian–pyrite. Sphalerite has been recognized as 5–30  $\mu\text{m}$  anhedral grains with no obvious paragenetic relationship with the arsenian–pyrite, as is found in the Dunderberg Shale. Arsenopyrite occurs in minor amounts as <5  $\mu\text{m}$  inclusions in arsenian–pyrite rims and as subhedral to anhedral <10  $\mu\text{m}$  grains that formed on arsenian–pyrite rims. Gold mineralization in the Secret Canyon Shale is commonly characterized euhedral, oscillatory zoned arsenian–pyrite. The arsenian–pyrite rims are relatively large (5–15  $\mu\text{m}$ ) and typically compose >80% of the volume of pyrite grains. Some of the arsenian pyrite crystals (<1%) contain a diagenetic pyrite core with a surrounding layer of stibnite or tennantite–tetrahedrite with an outer overgrowth of arsenian–pyrite (Fig. 43A-B). Tennantite–tetrahedrite has also been observed surrounding arsenian–pyrite rims indicating it also locally formed later. EDS analyses using the SEM shows the tennantite–tetrahedrite contains silver and zinc in solid–solution. Native gold grains have been observed in zones of high grade sulfide mineralization (>30 ppm Au). The gold grains are <5  $\mu\text{m}$  in size, contain ~10 wt % Ag, and are not found in pyrite, but are located adjacent to pyrite and surrounded by quartz. Arsenian–pyrite rims range from 2–12 % As with an average of 5%. Silver to gold ratios from down hole assays in ore zones at West Flank range from 1:1 to 1:25, with an average of 1:7. As in the Dunderberg Shale, stibnite, realgar, and orpiment are

locally present and fill open space within ore zones and where little to no mineralization occurs.

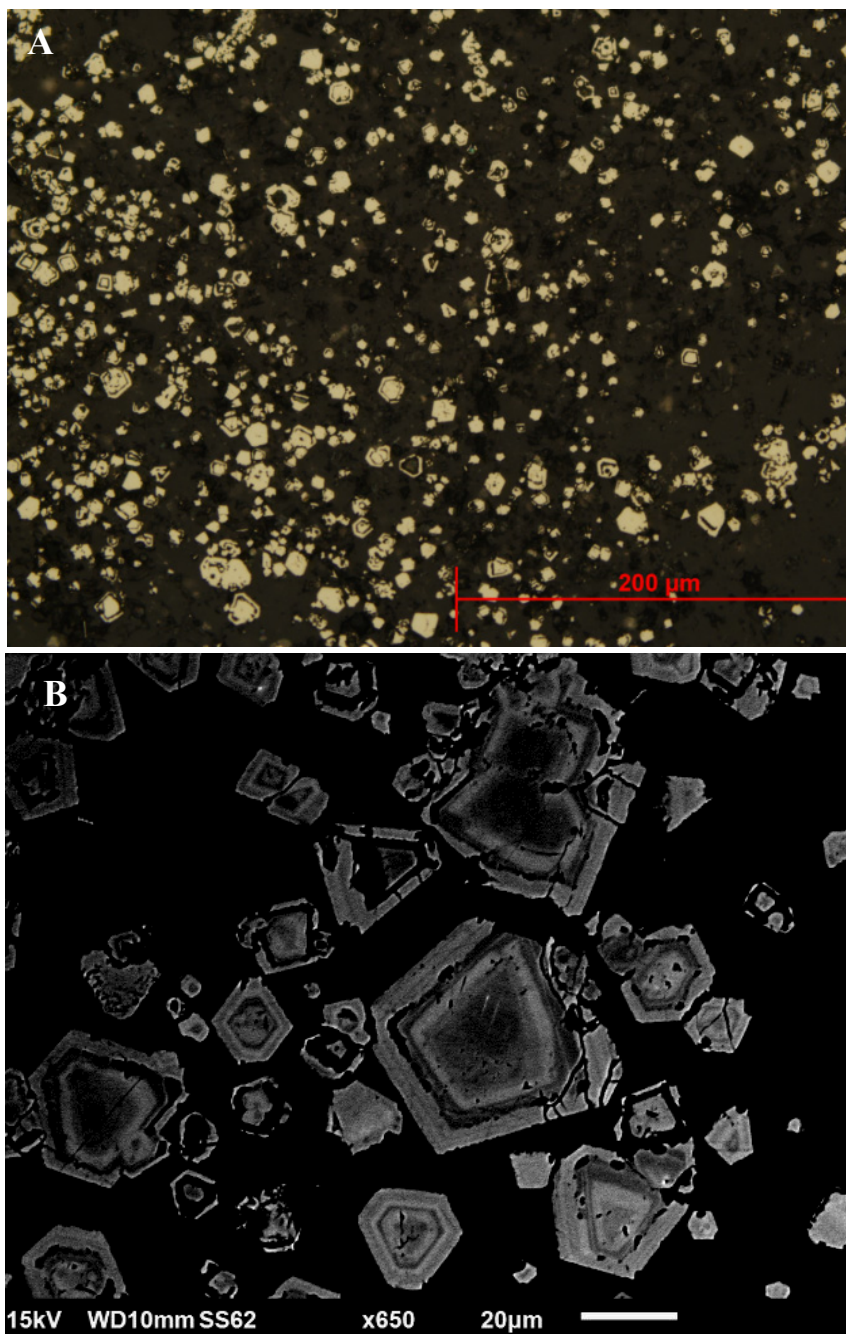


Figure 42. Ore-stage pyrite from the SHGD at West Flank. A. Reflected light photomicrograph (uncrossed polars) illustrating variety of pyrite textures and grain sizes. B. Backscatter electron image showing well-developed oscillatory As zoning in the pyrite. Note the euhedral nature of the growth zones and grains. Areas of black surrounding pyrite cores are composed of sericite.

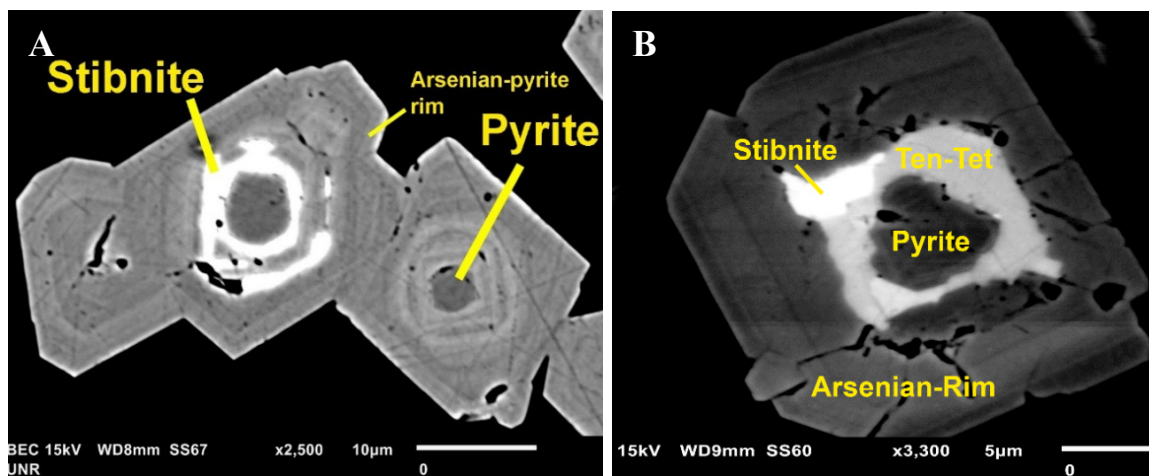
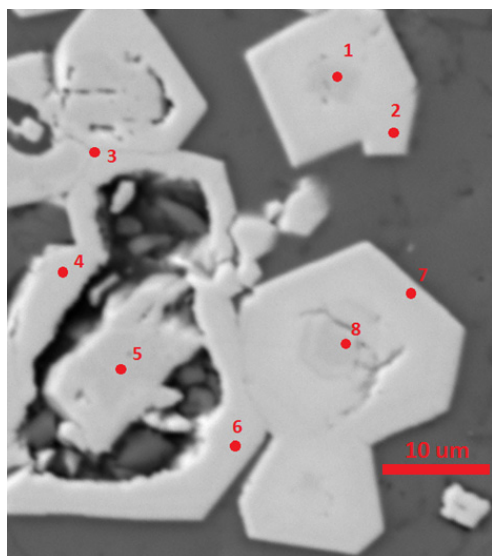


Figure 43. Ore-stage pyrite hosted in Secret Canyon Shale from the SHGD at West Flank showing relationships with stibnite and tetrahedrite-tennantite (PK137CA-918, and footage, five foot interval that assayed 38.8 ppm Au). A. Stibnite over-growing non-arsenian pyrite core. Note intergrowths of stibnite and arsenian pyrite. B. Tetrahedrite-tennantite and stibnite overgrowing non-arsenian pyrite core. Arsenian pyrite appears to have overgrown the tetrahedrite-tennantite and stibnite.

Microprobe analyses confirm that arsenian-pyrite rims are gold-bearing (up to 2090 ppm), whereas most cores do not contain detectable gold (Fig. 44). Locally cores contain significant amounts of gold (up to 1260 ppm Au) and other Carlin-Type pathfinder elements (Fig. 44, spot 1), suggesting some cores are part of the hydrothermal SHG system. Pyrite cores that do not contain detectable Au are likely diagenetic in origin. Diagenetic pyrite have no detectable Au or Hg, contain on average <1.0 wt % As, <400 ppm Tl, <500 ppm Cu, >1000 ppm Co, >300 ppm Ni, and <100 ppm Sn. In contrast, gold-bearing arsenian-pyrite rims in the Secret Canyon Shale contain on average >2.0 wt % As, >400 ppm Tl, >500 ppm Cu, <750 ppm Co, <300 ppm Ni, and >100 ppm Sn. Cores that do not contain detectable Au, but >2.0 wt % As may have formed during the hydrothermal SHG system, but prior to the deposition of significant Au (Fig. 44, spots 5, and 8). Mercury concentrations in arsenian-pyrite range from below detection

limit (40 ppm) to 120 ppm. No tellurium was detected (<50 ppm) in any arsenian-pyrite.



#	Au (ppm)	As	Cu	Hg	Tl	Sb
1	1030	58780	1910	<40	380	70
2	1260	64380	1400	<40	<160	120
3	390	25950	1240	<40	<160	600
4	<100	7970	270	<40	170	590
5	<100	5790	170	<40	390	300
6	1560	43530	1820	<40	750	310
7	1820	67500	2810	80	<160	120
8	<100	35760	210	<40	<160	90

Figure 44. Backscatter electron image showing microprobe spot analyses of ore-stage pyrite hosted in the Secret Canyon Shale at the West Flank SHGD. (PK137CA-857' three foot interval that assayed 95.2 ppm Au) The concentrations for gold, copper, mercury, thallium, and Sb (all in ppm) are shown in the table.

Structurally, the West Flank is located at the intersection of the northwest Kinsley Trend and a northeast fault zone (Fig. 45). Mineralization is hosted in both the Clarks Spring Limestone member of the Secret Canyon Shale and its lower Shale member. North to northeast high-angle faults appear to have been pathways for ore fluids (Fig. 46).

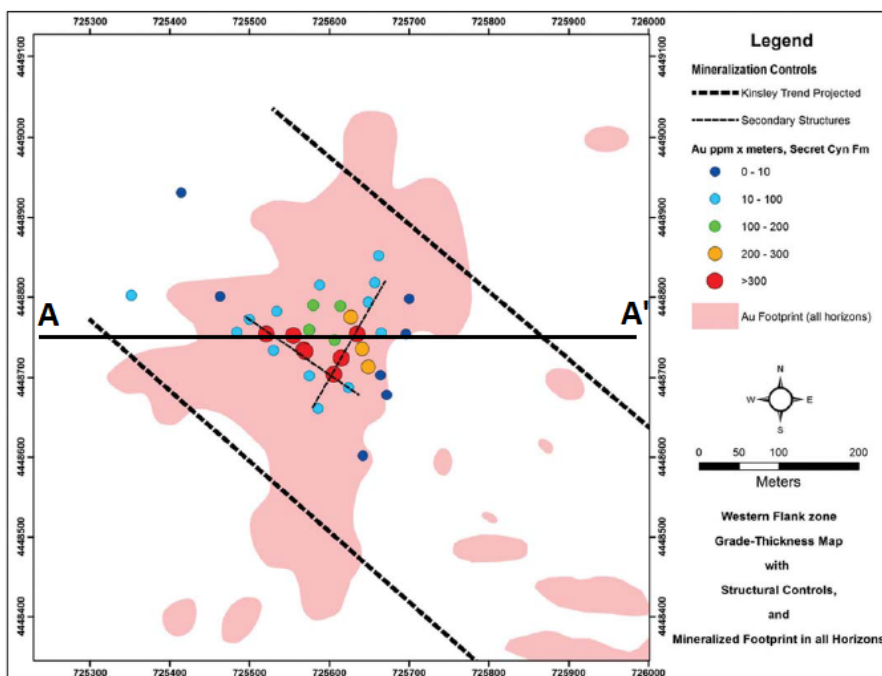


Figure 45. Plan view map of the West Flank SHGD. Points represent drill holes from which the highest Au grade from each hole is projected to the surface (modified from Hannink et al., 2015).

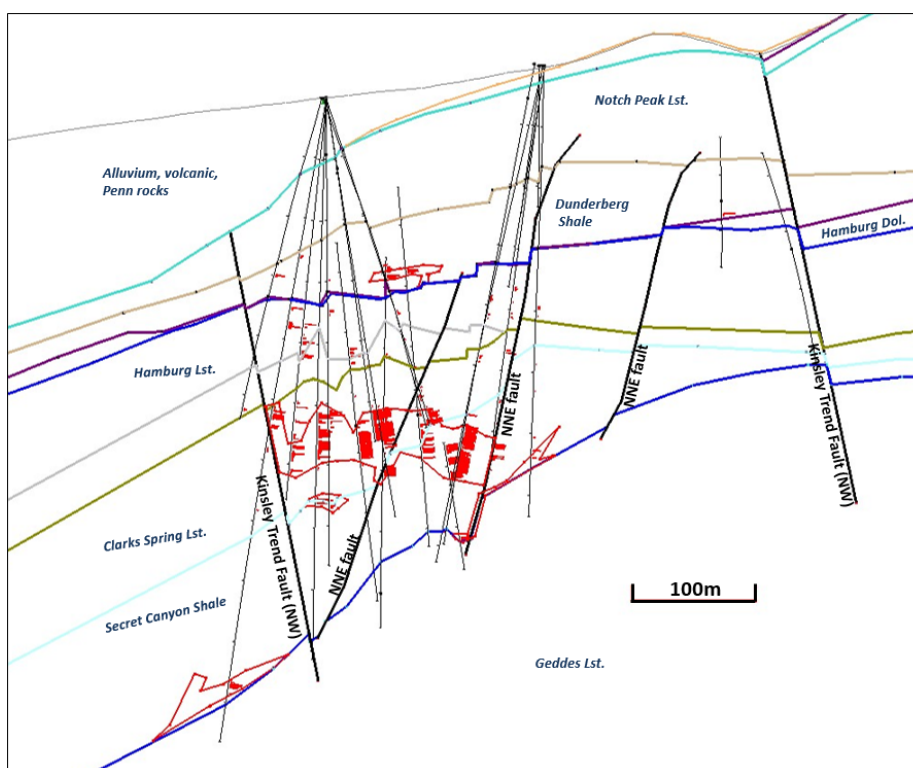
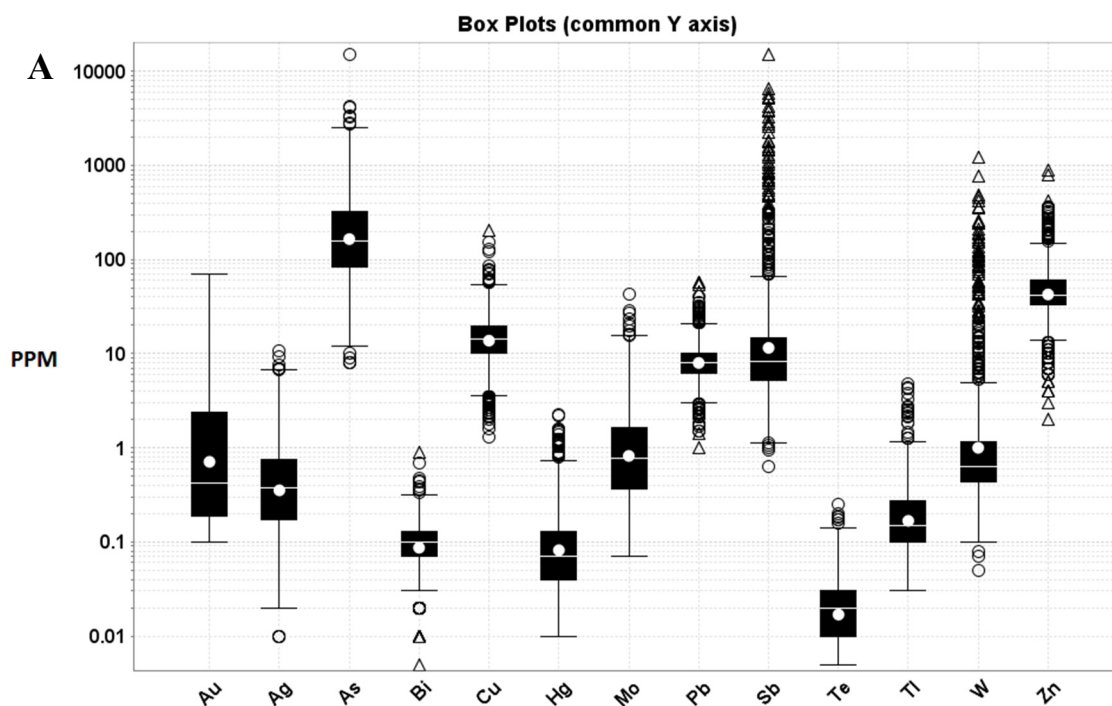


Figure 46. East-west cross-section through the West Flank.

Bar and whisker diagrams were constructed from down-hole drill data. Two domains were used, sulfide intervals containing >100 ppb Au from the Dunderberg Shale and sulfide intervals containing >100 ppb Au from the Secret Canyon Shale. Bar and whisker diagrams for the Dunderberg Shale and Secret Canyon Shale are very similar. The Secret Canyon Shale has a higher average As, Hg, Te, and Tl content than the Dunderberg Shale. Conversely, the Dunderberg Shale has significantly more outliers of Sb and W than the Secret Canyon Shale, though averages are approximately the same (Fig. 47A-B).



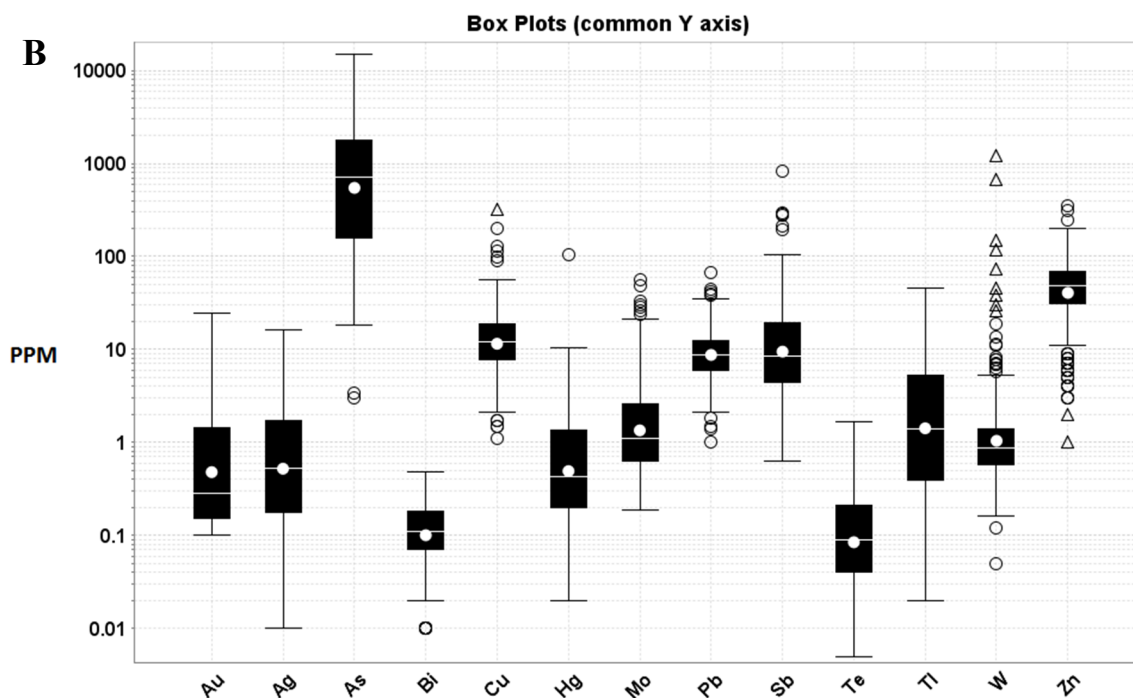


Figure 47. Bar and whisker diagrams. A. Dunderberg Shale samples containing >100 ppb Au. B. Secret Canyon Shale samples containing >100 ppb Au. The central box is the middle 50% of the data between Q1 and Q3. A circle is an outlier further than  $1.5 \times (Q3 - Q1)$  from the box. Whiskers are extreme values that are not outliers. The white circle is the mean of values and the white line is the median.

### Secret Spot mineralization

The Secret Spot target is located 1 km south of the West Flank and approximately 2 km northwest of the stock (Fig. 31) and contains mineralization in the Secret Canyon Shale. A sample from a 5 foot drill interval that assayed 7 ppm Au, 33 ppm Ag, and 826 ppm Sb contains several sulfosalts, pyrite with arsenian rims, and native gold. Other minerals include sphalerite, stibnite, arsenopyrite, acanthite, stromeyerite ( $\text{AgCuS}$ ), and other unidentified sulfosalts containing varying amounts of Ag, Cu, Fe, Pb, Sb, and S. Pyrite in this sample ranges from 20–500  $\mu\text{m}$  in size and commonly shows two generations of hydrothermal pyrite, identifiable by their different Fe contents (Fig. 48A).

The pyrite is typically much coarser and cubic than pyrite found at West Flank. Euhedral arsenian–pyrite rims are developed around many of the pyrite grains, though the rims lack oscillatory zoning that is characteristic of arsenian–pyrite rims found in the West Flank (Fig. 48B). Arsenopyrite has been observed as small 1–2  $\mu\text{m}$  grains within the arsenian–pyrite rims. Acanthite, stibnite, sphalerite, galena, chalcopyrite, and various sulfosalts are found as inclusions in the hydrothermal pyrite, in the arsenian–pyrite rims, and as grains along the edges of pyrite. Two grains of electrum (20–40 wt % Ag) occurred as  $<5 \mu\text{m}$  grains in quartz associated with pyrite. The pyrite from Secret Spot appear to be of hydrothermal in origin due to their size and texture and likely formed during the intrusion–related mineralization event. Mineralization at Secret Spot displays evidence of dissolution of ferroan dolomite and silicification similar to mineralization in the Dunderberg Shale and Secret Canyon Shale further north.

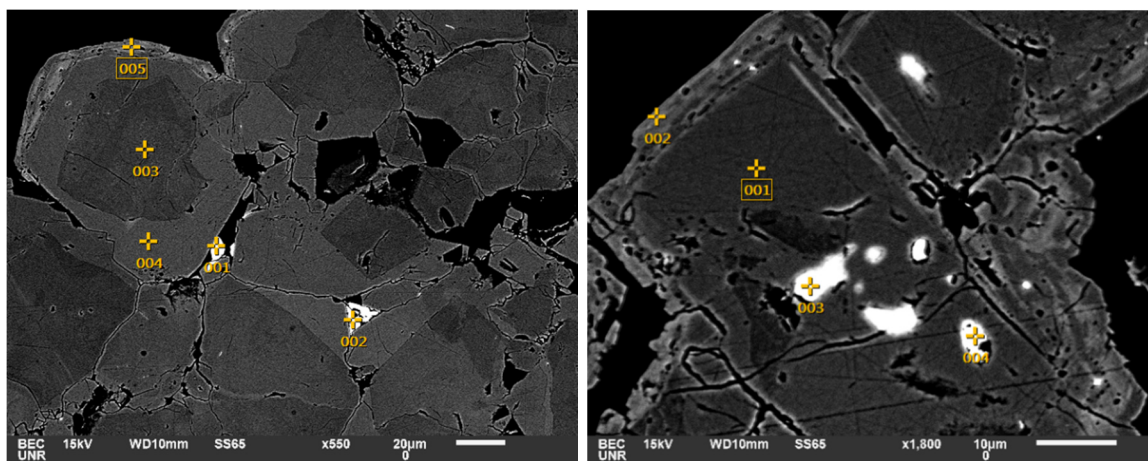
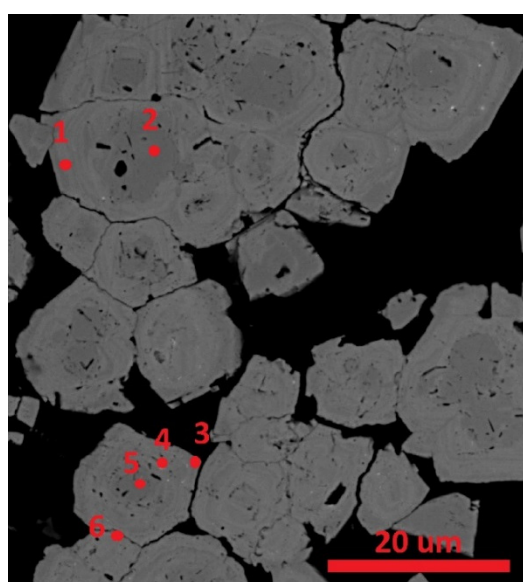


Figure 48. Backscatter electron images of ore-stage pyrite at the Secret Spot SHGD target (PK153-1575', five foot interval that assayed 6.74 ppm Au). A. Two stages of hydrothermal pyrite. The bright spots (001 and 002) are sphalerite. B. Cubic pyrite with inclusions of sphalerite (003) and a Pb-Sb-Ag-sulfosalt (004), and arsenian–pyrite rims (002).

Microprobe analyses demonstrate the chemistry of the arsenian–pyrite rims at Secret Spot are significantly different than arsenian–pyrite rims in the West Flank (Fig. 49). Little to no gold was detected in the arsenian–pyrite rims despite their high arsenic contents (up to 6%), in sharp contrast to West Flank pyrite where arsenic correlates with gold (Fig. 50). Pyrite from Secret Spot contains similar arsenic concentrations to those at West Flank. However, concentrations of copper and antimony are consistently greater than values measured from arsenian–pyrite at West Flank. The arsenian-pyrite at Secret Spot also contain measureable amounts of silver (up to 430 ppm) and contain inclusions of Ag-rich minerals (up to 9% Ag). However, like West Flank, mercury and tellurium concentrations of pyrite at Secret Spots are near or below detection limit. It is possible that gold is present in the pyrite at Secret Spot, but in concentrations below the detection limit of the microprobe (~100 ppm Au). Table 3 contains selected microprobe analyses and shows elemental differences between pyrite types.



#	Au (ppm)	Ag	As	Hg	Tl	Cu	Sb
1	<100	<30	44280	80	530	1910	660
2	<100	<30	1280	<40	210	80	80
3	<100	430	44660	<40	460	2400	2150
4	<100	80	42730	<40	430	940	1390
5	<100	<30	22530	<40	340	590	1130
6	<100	40	44850	<40	560	2380	840

Figure 49. Backscatter electron image showing microprobe spot analyses of ore-stage pyrite hosted in the Secret Canyon Shale at the Secret Spot SHGD target (PK153-1575', five foot interval that assayed 6.74 ppm Au). The concentrations for gold, copper, mercury, thallium, and Sb (all in ppm) are shown in the table.

Table 3. Selected microprobe analyses for various types of pyrite.

	Na	Ag	Au	Si	As	Hg	Tl	Zn	Se	Pb	Bi	Al	W	Cu	Te	Co	Sb	Ni	Sn	Fe	Mo	Ti	S	Ca	Total	
Detection Limit (ppm)	ppm	ppm	ppm	% wt	% wt	ppm	ppm	ppm	ppm	ppm	ppm	ppm	ppm	ppm	ppm	ppm	ppm	ppm	ppm	% wt	ppm	ppm	% wt	ppm	% wt	
	50	30	100	26	40	40	160	45	45	100	100	10	100	60	50	50	30	50	30	60	50	25	20	20		
<b>Diagenetic pyrite</b>																										
pk137CA857-3 4	560	BDL	BDL	0.32	0.44	BDL	210	490	BDL	BDL	BDL	1180	BDL	270	BDL	1750	440	520	80	45.89	7070	BDL	42.84	BDL	90.75	
pk137CA857-3 7	120	BDL	BDL	0.06	0.15	BDL	250	190	BDL	BDL	BDL	160	BDL	280	BDL	1180	300	100	80	46.18	7970	BDL	49.52	BDL	96.99	
pk004C-330-3 7	370	BDL	BDL	6.43	0.33	BDL	370	BDL	BDL	BDL	BDL	44070	BDL	100	BDL	500	800	BDL	BDL	36.06	6460	BDL	40.12	BDL	88.20	
pk004C-154-3 1	560	BDL	BDL	1.95	0.71	BDL	370	60	BDL	BDL	BDL	16720	BDL	200	BDL	1080	560	480	BDL	40.39	7560	BDL	46.06	BDL	91.87	
pk004C-154-3 2	390	BDL	BDL	0.60	0.32	BDL	270	BDL	BDL	BDL	BDL	5160	BDL	140	BDL	1170	420	490	60	44.89	8440	BDL	50.96	BDL	98.43	
pk141C-453-1 4	BDL	BDL	BDL	0.03	0.14	BDL	200	70	BDL	BDL	BDL	30	BDL	110	BDL	2140	510	540	BDL	44.40	8230	BDL	50.71	6220	97.10	
pk141C-453-2 3	BDL	BDL	BDL	3.50	1.15	BDL	BDL	70	BDL	BDL	BDL	2280	BDL	340	BDL	1030	460	400	60	40.77	7590	BDL	45.78	3370	92.79	
pk141C-453-2 4	70	BDL	BDL	0.95	1.68	BDL	260	BDL	BDL	BDL	BDL	9140	BDL	490	BDL	1240	610	740	BDL	42.92	8060	BDL	48.42	2390	96.28	
pk141C-453-4 4	490	BDL	BDL	8.12	1.37	BDL	290	190	BDL	BDL	BDL	8100	BDL	270	BDL	990	490	330	BDL	33.30	6580	BDL	39.72	2250	84.51	
<b>Dunderberg Shale Mineralized</b>																										
pk004C-154-1 1	510	30	530	6.88	0.69	BDL	460	BDL	BDL	BDL	BDL	87380	BDL	610	BDL	270	620	BDL	BDL	26.24	4800	BDL	30.19	4040	73.93	
pk004C-154-1 2	150	BDL	320	0.28	1.68	BDL	550	BDL	BDL	BDL	BDL	2350	BDL	290	BDL	580	970	BDL	30	44.67	8000	BDL	50.98	160	98.95	
pk004C-154-1 4	70	BDL	160	0.08	1.42	40	620	BDL	BDL	BDL	BDL	480	BDL	160	BDL	600	970	BDL	BDL	45.08	8240	BDL	51.28	1040	99.10	
pk004C-154-1 5	110	BDL	180	0.37	1.06	BDL	350	210	BDL	BDL	BDL	3120	BDL	550	BDL	600	920	BDL	BDL	44.70	8270	BDL	51.28	1780	99.02	
pk004C-154-1 2	480	90	150	0.08	1.82	70	700	BDL	BDL	BDL	BDL	460	BDL	740	BDL	560	1220	500	100	44.93	8010	BDL	50.60	2070	98.93	
pk004C-154-2 3	640	BDL	210	8.22	0.69	BDL	660	100	BDL	BDL	BDL	10660	BDL	690	BDL	440	790	400	70	32.71	6240	BDL	39.06	3570	83.08	
pk004C-154-6 5	BDL	90	110	0.57	2.87	BDL	1020	80	BDL	BDL	BDL	4960	BDL	1210	BDL	940	1140	340	70	43.02	7730	390	47.58	560	95.90	
<b>Secret Canyon Mineralized</b>																										
pk137CA-918WF_1 2	BDL	BDL	610	0.07	4.68	70	230	BDL	BDL	BDL	BDL	90	BDL	1880	BDL	530	240	170	210	43.89	7890	BDL	44.27	10	94.10	
pk137CA-918WF_1 4	BDL	BDL	1260	0.01	5.49	BDL	210	BDL	BDL	BDL	BDL	BDL	130	2390	BDL	510	940	BDL	130	43.13	7630	BDL	42.84	240	92.81	
pk137CA-918WF_2 2	BDL	BDL	1540	0.06	6.54	120	370	BDL	BDL	BDL	BDL	BDL	BDL	2520	BDL	630	170	BDL	110	43.33	7830	BDL	42.90	30	94.15	
pk137CA-918WF_2 4	130	BDL	580	0.94	4.35	BDL	540	50	BDL	BDL	BDL	BDL	BDL	1470	BDL	640	200	BDL	190	42.60	7600	BDL	42.63	10	91.66	
pk137CA-918WF_3 1	BDL	BDL	1030	0.00	5.88	BDL	380	BDL	BDL	BDL	BDL	40	BDL	1910	BDL	590	70	200	170	43.81	7820	BDL	43.79	BDL	94.70	
pk137CA-918WF_3 2	BDL	BDL	1260	0.00	6.44	BDL	BDL	BDL	BDL	BDL	BDL	BDL	BDL	1400	BDL	510	120	120	130	43.85	7660	310	43.12	10	94.57	
pk137CA-918WF_3 3	90	BDL	390	0.13	2.60	BDL	BDL	120	BDL	BDL	BDL	1660	BDL	1240	BDL	580	600	90	140	44.93	8210	BDL	45.25	140	94.24	
pk137CA-918WF_3 6	490	BDL	1560	4.34	4.35	BDL	750	BDL	BDL	BDL	BDL	1600	BDL	1820	BDL	450	310	BDL	120	36.34	6120	BDL	33.89	30	80.24	
pk137CA-918WF_3 7	70	BDL	1820	BDL	6.75	80	BDL	BDL	BDL	BDL	BDL	BDL	BDL	2810	BDL	560	120	BDL	230	43.54	7530	BDL	43.16	BDL	94.79	
pk137CA-918WF_4 2	BDL	BDL	1120	0.35	8.12	BDL	530	BDL	BDL	BDL	BDL	120	BDL	540	BDL	570	240	BDL	250	43.19	7380	BDL	42.25	BDL	94.97	
pk137CA-918WF_4 4	BDL	BDL	1340	7.59	6.83	40	540	BDL	BDL	BDL	BDL	1240	BDL	1320	BDL	560	380	440	120	40.40	6980	BDL	39.38	70	95.51	
<b>Secret Spot Unmineralized</b>																										
pk153-1575-1 1	110	BDL	BDL	BDL	BDL	BDL	240	BDL	BDL	BDL	BDL	50	210	BDL	BDL	500	40	BDL	140	47.10	8500	BDL	52.55	220	100.66	
pk153-1575-1 2	BDL	BDL	BDL	0.02	3.38	BDL	270	BDL	BDL	BDL	BDL	50	160	710	BDL	680	60	BDL	90	46.01	8080	BDL	49.98	330	100.44	
pk153-1575-1 3	420	150	BDL	0.06	3.75	BDL	590	230	BDL	BDL	BDL	19530	BDL	1050	BDL	490	500	20	90	42.84	6890	120	42.94	2040	92.80	
pk153-1575-1 4	120	30	BDL	0.05	1.89	BDL	BDL	50	BDL	BDL	BDL	3810	BDL	540	BDL	1220	430	330	50	45.58	8090	BDL	50.15	BDL	99.15	
pk153-1575-1 5	80	BDL	BDL	BDL	0.02	BDL	BDL	140	BDL	BDL	BDL	20	160	130	BDL	610	130	BDL	90	46.17	8480	BDL	52.03	BDL	99.22	
pk153-1575-2 1	BDL	40	BDL	0.03	0.20	BDL	BDL	90	BDL	BDL	BDL	6040	BDL	590	80	330	590	60	BDL	26.40	3320	BDL	20.30	209850	69.03	
pk153-1575-2 2	BDL	70	BDL	0.04	0.96	BDL	290	BDL	BDL	BDL	BDL	250	BDL	1490	BDL	500	960	80	BDL	46.12	8470	BDL	51.45	970	99.87	
pk153-1575-2 3	920	90990	BDL	0.41	5.99	3100	BDL	15120	BDL	BDL	BDL	8510	BDL	####	BDL	210	1E+05	370	BDL	14.90	5290	BDL	30.90	3400	100.32	
pk153-1575-2 4	BDL	50	BDL	BDL	36.99	BDL	1280	BDL	BDL	BDL	BDL	1200	BDL	450	BDL	600	330	1380	80	37.04	3840	BDL	23.68	BDL	98.62	
pk153-1575-2 5	BDL	1320	BDL	BDL	3.72	BDL	580	BDL	BDL	BDL	BDL	920	BDL	1100	BDL	530	1E+05	190	BDL	39.25	7630	BDL	46.12	36740	106.46	
pk153-1575-2 6	300	10470	BDL	0.53	1.36	BDL	BDL	310	BDL	BDL	BDL	9240	BDL	960	BDL	700	6190	380	BDL	43.18	8060	BDL	50.07	1960	98.99	
pk153-1575-3 1	BDL	330	BDL	2.49	0.15	BDL	240	60	BDL	BDL	BDL	17960	BDL	1040	BDL	500	2630	90	BDL	41.40	7010	BDL	46.44	890	93.55	
pk153-1575-3 2	BDL	600	BDL	BDL	3.39	BDL	BDL	150	BDL	BDL	BDL	30	200	7360	BDL	510	1460	BDL	100	44.71	8230	BDL	49.95	450	99.99	
pk153-1575-3 3	BDL	320	BDL	0.02	4.60	BDL	280	BDL	BDL	BDL	BDL	30	BDL	1680	BDL	670	1010	770	70	44.96	8050	BDL	49.18	240	100.07	
pk153-1575-3 4	BDL	110	BDL	0.30	3.04	BDL	400	BDL	BDL	BDL	BDL	1450	BDL	640	BDL	540	1080	220	50	44.92	8030	BDL	49.54	310	99.09	
pk153-1575-4 1	BDL	BDL	BDL	BDL	0.92	BDL	230	BDL	BDL	BDL	BDL	BDL	390	1110	BDL	560	1170	BDL	50	46.18	8590	BDL	51.76	370	100.11	
pk153-1575-4 2	BDL	BDL	BDL	BDL	1.58	BDL	BDL	770	BDL	BDL	BDL	BDL	100	990	BDL	660	1190	BDL	30	45.86	8370	BDL	51.46	350	100.15	
pk153-1575-4 3	BDL	3980	BDL	BDL	2.94	BDL	340	BDL	BDL	BDL	BDL	50	130	1170	BDL	540	2580	BDL	90	45.16	8110	BDL	45.56	930	95.45	
pk153-1575-4 4	BDL	BDL	BDL	0.18	2.04	BDL	200	310	BDL	BDL	BDL	1500	BDL	980	BDL	650	540	270	130	44.92	8260	2090	46.39	150	95.04	
pk153-1575-4																										

### Temporal relationship between dikes and SHG mineralization

Most of the dikes are located on the eastern flank of the range and are of granodiorite composition. No dikes have been encountered at West Flank. Nearly all of the dikes, the margins of the dikes, or the country rocks along dike contacts assay <5 ppb. However, gold mineralization was documented in three dikes in drill core on the east side of Kinsley Mountain. The highest concentration of Au in a dike is 399 ppb over a six foot interval. A sample was collected from this interval and analyzed using the SEM, microprobe, and dated with the SHRIMP. Images collected on a SEM using BSE revealed pyrite in the dike was coarse-grained, subhedral to euhedral, and contained thin arsenian-pyrite rims (1–3  $\mu\text{m}$ ). Microprobe analysis demonstrated that the arsenian-pyrite rims contained Au and the pyrite cores did not contain detectable Au.

### Temporal relationship between SHG mineralization and intrusion-related mineralization

Only a handful of temporal relationships exist between SHG mineralization and what is likely intrusion-related mineralization. The most common relationship is the appearance of small <5  $\mu\text{m}$  grains of galena in pyrite. The inclusions of galena are found in all areas of SHG mineralization. Scheelite has been observed enveloping arsenian-pyrite in a sample from the West Flank, approximately 3 km from the stock (Fig. 51). However, the scheelite was likely remobilized from its initial deposition near the stock as there is no indication that the rock was ever at the high temperature (>500 °C) that is needed to form scheelite in the skarn environment (see Appendix H). Tungsten from scheelite may be remobilized in low-temperature environments as a heteropoly-tungstate (Newberry and Einaudi, 1981). In addition, the presence of early stibnite and Ag/Zn-

bearing tennantite–tetrahedrite inclusions in pyrite from the West Flank suggests distal intrusion–related mineralization formed prior to arsenian–pyrite rims from the SHG system. However, tennantite–tetrahedrite has also been observed enveloping pyrite with arsenian–pyrite rims in the West Flank. Further evidence is pyrite and arsenian–pyrite rims from Secret Spot that contain numerous inclusions of sphalerite, galena, chalcopyrite, and sulfosalts. Sphalerite, chalcopyrite, and sulfosalts are also present forming after arsenian–pyrite rims at Secret Spot. Furthermore, polymetallic carbonate replacement veins occur up to 3 km from the stock in the area of SHG mineralization (Fig. 52). However, no cross–cutting relationships between polymetallic replacement veins and SHG mineralization were recognized. The polymetallic carbonate replacement veins are up to 1 m wide, silicified, brecciated, commonly oxidized and contain high concentrations of Ag, Cu, Ni, Pb, Sb, W, and Zn, but contain little to no gold (<50 ppb) and arsenic (<100 ppm).

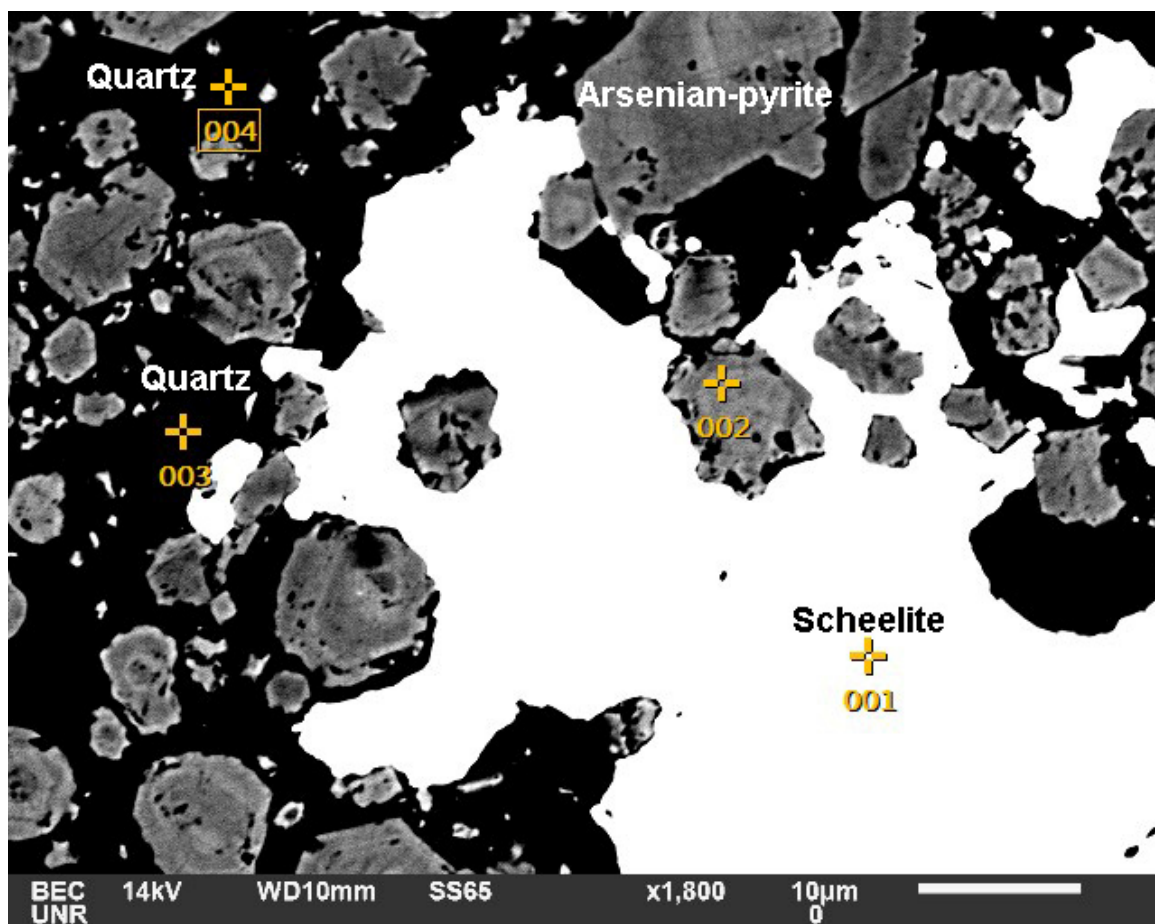


Figure 51. Backscatter electron image showing late scheelite enveloping arsenian-pyrite from mineralization at West Flank (PK173-871', five foot interval that assayed 3.76 ppm Au)



Figure 52. Drill core from Hamburg Limestone showing brecciated jasperoid veined by milky white quartz. The interval shown contains 0.06 ppm Au, 71 ppm As, 2790 ppm Ag, 4670 ppm Cu, 385 ppm Ni, and 1800 ppm W (PK005C-547'-550').

## Correlation matrices of multi-element data in SHG and intrusion-related mineralization

Spearman rank correlation matrices of multi-element analyses were constructed for different areas and mineralization types. Using assays from down-hole drill data, correlation matrices of both oxidized and unweathered sulfide mineralization (>100 ppb Au) in the Dunderberg Shale and Secret Canyon Shale were generated. The Dunderberg Shale data were split into two domains, drill hole data from the west and east sides of the range. In unoxidized mineralized intervals in Dunderberg Shale, gold strongly correlates with Ag, As, Hg, S, Sb, Te, Tl, ( $R > 0.5$ ) and shows a moderate correlation with Zn, Bi, Cu, Fe, Pb, and W ( $0.3 < R < 0.5$ ) (Fig. 53A-D). Unoxidized mineralized intervals in Secret Canyon Shale from the West Flank show a strong correlation between Au and Ag, As, Hg, S, Te, Tl and Zn, with moderate correlations with Cu and Sb (Fig. 53E-F).

A correlation matrix was also created using 125 rock-chip samples from mostly oxidized gossan, skarn, quartz veins, and mineralized dikes in the area of the stock (Fig. 53G). The elemental associations with gold from the samples near the stock differ from the elemental associations in the SHGDs in the SHG system. In the 125 samples, gold correlates strongly with As, and moderately with Ag, Bi, Cu Hg, Mo, Pb, Sb, Te, and Zn. There is no correlation between Au and Tl. The data further suggests that SHG mineralization in the Dunderberg Shale and Secret Canyon Shale is part of one system, with mineralization in the Dunderberg Shale having a greater component of base metals.

A	Au_ppm	Ag_ppm	Al_pct	As_ppm	Bi_ppm	Ca_pct	Cu_ppm	Fe_pct	Hg_ppm	K_pct	Mg_pct	Ni_ppm	P_ppm	Pb_ppm	S_ppm	Sb_ppm	Sr_ppm	Te_ppm	Tl_ppm	W_ppm	Zn_ppm
Au_ppm	1.00	0.43	1.00	0.18	0.47	0.23	0.38	0.27	0.48	0.22	0.00	0.28	0.26	0.43	0.03	0.50	-0.09	0.56	0.34	0.19	0.29
Ag_ppm	0.43	1.00	-0.22	-0.18	-0.10	-0.47	0.06	-0.22	0.44	-0.10	-0.44	-0.26	0.05	-0.02	0.34	0.47	-0.21	0.46	-0.11	-0.18	-0.14
Al_pct	0.18	-0.22	1.00	0.66	0.59	0.24	0.41	0.74	0.03	0.93	0.36	0.75	0.42	0.55	-0.29	0.15	0.38	0.23	0.56	0.00	0.36
As_ppm	0.47	-0.18	0.66	1.00	0.66	0.20	0.54	0.84	0.32	0.64	0.33	0.79	0.23	0.64	-0.08	0.43	0.20	0.36	0.71	0.15	0.46
Bi_ppm	0.23	-0.10	0.59	0.66	1.00	0.15	0.60	0.72	0.27	0.59	0.23	0.72	0.23	0.69	-0.09	0.39	0.10	0.27	0.56	0.00	0.45
Ca_pct	-0.16	-0.47	0.24	0.20	0.15	1.00	0.08	0.10	-0.22	0.15	0.74	0.13	0.05	0.10	-0.36	-0.19	0.61	-0.25	0.15	0.00	0.10
Cu_ppm	0.38	0.06	0.41	0.54	0.60	0.08	1.00	0.54	0.29	0.43	0.20	0.57	0.14	0.50	0.01	0.31	-0.02	0.30	0.55	0.12	0.45
Fe_pct	0.27	-0.22	0.74	0.84	0.72	0.10	0.54	1.00	0.26	0.71	0.29	0.89	0.27	0.72	-0.09	0.37	0.09	0.36	0.71	0.11	0.46
Hg_ppm	0.48	0.44	0.03	0.32	0.27	-0.22	0.29	0.26	1.00	0.11	-0.07	0.22	0.07	0.36	0.24	0.66	-0.25	0.47	0.46	0.10	0.37
K_pct	0.22	-0.10	0.93	0.64	0.59	0.15	0.43	0.71	0.11	1.00	0.26	0.72	0.41	0.55	-0.25	0.22	0.33	0.27	0.56	-0.01	0.36
Mg_pct	0.00	-0.44	0.36	0.33	0.23	0.74	0.20	0.29	-0.07	0.26	1.00	0.35	0.13	0.22	-0.33	0.01	0.40	-0.10	0.38	0.05	0.20
Ni_ppm	0.28	-0.26	0.75	0.79	0.72	0.13	0.57	0.89	0.22	0.72	0.35	1.00	0.28	0.68	-0.16	0.31	0.10	0.28	0.73	0.16	0.51
P_ppm	0.26	0.06	0.42	0.23	0.23	0.05	0.14	0.27	0.07	0.41	0.13	0.28	1.00	0.41	-0.16	0.26	0.35	0.40	0.25	0.03	0.25
Pb_ppm	0.43	-0.02	0.55	0.64	0.69	0.10	0.50	0.72	0.36	0.55	0.22	0.68	0.41	1.00	-0.08	0.51	0.11	0.48	0.57	0.11	0.43
S_ppm	0.03	0.34	-0.29	-0.08	-0.09	-0.36	0.01	-0.09	0.24	-0.25	-0.33	-0.16	-0.16	-0.08	1.00	1.00	-0.24	0.10	0.03	0.02	-0.17
Sb_ppm	0.50	0.47	0.15	0.43	0.39	-0.19	0.31	0.37	0.66	0.22	0.01	0.31	0.26	0.51	0.14	1.00	-0.13	0.57	0.42	-0.01	0.19
Sr_ppm	-0.09	-0.21	0.38	0.20	0.10	0.61	-0.02	0.09	-0.25	0.33	0.40	0.10	0.35	0.11	-0.24	-0.13	1.00	0.00	0.10	-0.13	-0.02
Te_ppm	0.56	0.46	0.23	0.36	0.27	-0.25	0.30	0.36	0.47	0.27	-0.10	0.28	0.40	0.48	0.10	0.57	0.00	1.00	0.31	0.07	0.10
Tl_ppm	0.34	-0.11	0.56	0.71	0.56	0.15	0.55	0.71	0.46	0.56	0.38	0.73	0.25	0.57	0.03	0.42	0.10	0.31	1.00	0.10	0.42
W_ppm	0.19	-0.18	0.00	0.15	0.00	0.00	0.12	0.11	0.10	-0.01	0.05	0.16	0.03	0.11	0.02	-0.01	-0.13	0.07	0.10	1.00	0.21
Zn_ppm	0.29	-0.14	0.36	0.46	0.45	0.10	0.45	0.46	0.37	0.36	0.20	0.51	0.25	0.43	-0.17	0.19	-0.02	0.10	0.42	0.21	1.00

B	Au_ppm	Ag_ppm	Al_pct	As_ppm	Bi_ppm	Ca_pct	Cu_ppm	Fe_pct	Hg_ppm	K_pct	Mg_pct	Ni_ppm	P_ppm	Pb_ppm	S_ppm	Sb_ppm	Sr_ppm	Te_ppm	Tl_ppm	W_ppm	Zn_ppm	
Au_ppm	1.00	0.54	1.00	0.16	0.48	0.35	-0.11	0.34	0.33	0.21	0.04	0.31	0.08	0.40	0.53	0.43	-0.01	0.53	0.59	0.20	0.37	
Ag_ppm	0.54	1.00	0.02	0.02	0.30	0.18	-0.37	0.28	0.12	0.65	0.12	-0.12	0.11	0.07	0.28	0.35	0.73	-0.31	0.63	0.50	0.36	0.27
Al_pct	0.16	0.02	1.00	0.61	0.65	-0.34	0.45	0.68	0.22	0.93	0.16	0.65	-0.14	0.45	0.38	0.16	-0.32	0.15	0.46	-0.07	0.62	
As_ppm	0.48	0.30	0.61	1.00	0.69	-0.35	0.59	0.77	0.60	0.66	0.09	0.79	-0.32	0.50	0.70	0.42	-0.25	0.48	0.84	0.14	0.72	
Bi_ppm	0.35	0.18	0.65	0.69	1.00	-0.58	0.76	0.86	0.43	0.68	0.02	0.88	-0.31	0.55	0.69	0.26	-0.51	0.31	0.64	0.24	0.88	
Ca_pct	-0.11	-0.37	-0.34	-0.35	-0.58	1.00	-0.53	-0.56	-0.28	-0.42	0.29	-0.56	0.33	-0.35	-0.36	-0.32	0.92	-0.21	-0.27	-0.27	-0.60	
Cu_ppm	0.34	0.28	0.45	0.59	0.76	-0.53	1.00	0.72	0.45	0.52	-0.04	0.74	-0.35	0.40	0.58	0.32	-0.43	0.36	0.58	0.28	0.79	
Fe_pct	0.33	0.12	0.68	0.77	0.86	-0.56	0.72	1.00	0.41	0.76	0.24	0.94	-0.41	0.42	0.71	0.22	-0.46	0.27	0.66	0.15	0.84	
Hg_ppm	0.54	0.65	0.22	0.60	0.43	-0.28	0.45	0.41	1.00	0.26	-0.07	0.43	-0.26	0.26	0.54	0.61	-0.26	0.76	0.81	0.37	0.41	
K_pct	0.21	0.12	0.93	0.66	0.68	-0.42	0.52	0.76	0.26	1.00	0.23	0.70	-0.15	0.46	0.47	0.24	-0.32	0.22	0.52	-0.09	0.67	
Mg_pct	0.04	-0.12	0.16	0.65	0.09	0.02	0.29	-0.04	-0.07	0.23	1.00	0.12	-0.07	-0.04	0.15	-0.19	0.36	-0.16	0.09	-0.19	0.03	
Ni_ppm	0.31	0.11	0.65	0.79	0.88	-0.56	0.74	0.94	0.43	0.70	0.12	1.00	-0.47	0.43	0.70	0.21	-0.48	0.29	0.66	0.18	0.85	
P_ppm	0.08	0.07	-0.14	-0.32	-0.31	-0.32	-0.35	-0.41	-0.26	-0.15	-0.07	-0.47	1.00	0.19	0.19	0.35	0.08	0.31	-0.07	-0.28	-0.33	
Pb_ppm	0.40	0.28	0.45	0.50	0.55	-0.35	0.40	0.42	0.26	0.46	-0.04	0.43	0.19	1.00	0.35	0.37	-0.25	0.20	0.46	0.16	0.56	
S_ppm	0.53	0.35	0.38	0.70	0.69	-0.36	0.58	0.71	0.54	0.47	0.15	0.70	-0.35	0.35	1.00	0.37	-0.23	0.37	0.69	0.26	0.68	
Sb_ppm	0.43	0.73	0.16	0.16	0.42	0.26	-0.32	0.32	0.22	0.61	0.24	0.21	0.08	0.37	0.37	1.00	-0.34	0.60	0.59	0.38	0.55	
Sr_ppm	-0.01	-0.31	-0.32	-0.25	-0.51	0.92	-0.43	-0.46	-0.26	-0.32	0.36	-0.48	0.31	-0.25	-0.23	-0.34	1.00	-0.19	-0.21	-0.30	-0.52	
Te_ppm	0.53	0.63	0.15	0.48	0.31	-0.21	0.36	0.27	0.76	0.22	-0.16	0.29	-0.07	0.20	0.37	0.60	-0.19	1.00	0.62	0.22	0.34	
Tl_ppm	0.59	0.50	0.46	0.84	0.64	-0.27	0.58	0.66	0.81	0.52	0.09	0.66	-0.28	0.46	0.69	0.59	-0.21	0.62	1.00	0.28	0.64	
W_ppm	0.20	0.36	-0.07	0.14	0.24	-0.27	0.28	0.15	0.37	-0.09	-0.19	0.18	-0.13	0.16	0.26	0.38	-0.30	0.22	0.28	1.00	0.24	
Zn_ppm	0.37	0.27	0.62	0.72	0.88	-0.60	0.79	0.84	0.41	0.67	0.03	0.85	-0.33	0.56	0.68	0.35	-0.52	0.34	0.64	0.24	1.00	

	Au_ppm	Ag_ppm	Al_pct	As_ppm	Bi_ppm	Ca_pct	Cu_ppm	Fe_pct	Hg_ppm	K_pct	Mg_pct	Ni_ppm	P_ppm	Pb_ppm	S_ppm	Sb_ppm	Sr_ppm	Te_ppm	Tl_ppm	W_ppm	Zn_ppm
Au_ppm	1.00	0.61	0.34	0.57	0.29	-0.34	0.38	0.45	0.40	0.44	0.02	0.43	0.39	0.40	0.00	0.51	-0.20	0.61	0.54	0.40	0.35
Ag_ppm	0.61	1.00	0.01	0.25	0.13	-0.19	0.04	0.10	0.33	0.13	0.12	0.00	0.13	0.25	0.10	0.56	-0.18	0.50	0.28	0.17	-0.03
Al_pct	0.34	0.01	1.00	0.66	0.70	-0.43	0.59	0.73	0.05	0.94	0.11	0.78	0.53	0.59	-0.18	0.13	-0.22	0.19	0.47	0.02	0.66
As_ppm	0.57	0.25	0.66	1.00	0.68	-0.35	0.59	0.78	0.34	0.66	0.09	0.72	0.40	0.64	-0.08	0.38	-0.20	0.44	0.63	0.20	0.68
Bi_ppm	0.29	0.13	0.70	0.68	1.00	-0.40	0.63	0.81	-0.01	0.69	0.18	0.72	0.20	0.72	-0.05	0.18	-0.30	0.20	0.44	-0.04	0.61
Ca_pct	-0.34	-0.19	-0.43	-0.35	-0.40	1.00	-0.49	-0.43	-0.17	-0.40	0.07	-0.40	-0.10	-0.37	0.07	-0.38	0.86	-0.16	-0.26	-0.18	-0.44
Cu_ppm	0.38	0.04	0.59	0.59	0.63	-0.49	1.00	0.68	0.38	0.53	-0.07	0.75	0.36	0.64	-0.22	0.38	-0.22	0.31	0.44	0.22	0.76
Fe_pct	0.45	0.10	0.73	0.78	0.81	-0.43	0.68	1.00	0.15	0.73	0.32	0.86	0.26	0.69	-0.14	0.28	-0.29	0.29	0.56	0.08	0.71
Hg_ppm	0.40	0.33	0.05	0.34	-0.01	-0.17	0.38	0.15	1.00	0.02	0.22	0.15	0.25	0.26	0.03	0.51	-0.10	0.50	0.52	0.42	0.28
K_pct	0.44	0.13	0.94	0.66	0.69	-0.40	0.53	0.73	0.02	1.00	0.16	0.75	0.55	0.57	-0.20	0.17	-0.19	0.24	0.49	0.06	0.60
Mg_pct	0.02	0.12	0.11	0.09	0.18	0.07	-0.07	0.22	-0.32	0.16	1.00	0.09	-0.06	0.06	-0.07	0.00	-0.06	-0.16	-0.18	-0.30	0.03
Ni_ppm	0.43	0.00	0.78	0.72	0.72	-0.40	0.75	0.86	0.15	0.75	0.09	1.00	0.39	0.67	-0.22	0.25	-0.16	0.29	0.55	0.14	0.80
P_ppm	0.39	0.13	0.53	0.40	0.20	-0.10	0.36	0.26	0.25	0.55	-0.06	0.39	1.00	0.32	-0.21	0.21	0.12	0.30	0.39	0.21	0.34
Pb_ppm	0.40	0.25	0.59	0.64	0.72	-0.37	0.64	0.69	0.26	0.57	0.06	0.67	0.32	1.00	-0.16	0.43	-0.23	0.36	0.50	0.11	0.66
S_ppm	0.00	0.10	-0.18	-0.08	-0.05	0.07	-0.22	-0.14	0.03	-0.20	-0.07	0.25	0.21	-0.16	1.00	-0.13	-0.03	-0.03	-0.08	-0.13	-0.20
Sb_ppm	0.51	0.56	0.13	0.38	0.18	-0.38	0.38	0.28	0.51	0.17	0.00	0.25	0.21	0.43	0.35	1.00	-0.31	0.35	0.42	0.54	0.30
Sr_ppm	-0.20	-0.18	-0.22	-0.20	-0.30	0.86	-0.22	-0.29	-0.10	-0.19	-0.06	-0.16	0.12	-0.23	-0.03	-0.31	1.00	-0.04	-0.14	-0.10	-0.24
Te_ppm	0.61	0.50	0.19	0.44	0.20	-0.16	0.31	0.29	0.50	0.24	-0.16	0.29	0.30	0.36	-0.03	0.35	-0.04	1.00	0.51	0.16	0.22
Tl_ppm	0.54	0.28	0.47	0.63	0.44	-0.26	0.44	0.56	0.52	0.49	-0.18	0.55	0.39	0.50	-0.08	0.42	-0.14	0.51	1.00	0.38	0.50
W_ppm	0.40	0.17	0.02	0.20	-0.04	-0.18	0.22	0.08	0.42	0.06	-0.30	0.14	0.21	0.11	-0.13	-0.13	0.54	-0.10	0.16	0.38	0.24
Zn_ppm	0.35	-0.03	0.66	0.68	0.61	-0.44	0.76	0.71	0.28	0.60	0.03	0.80	0.34	0.66	-0.20	0.30	-0.24	0.22	0.50	0.24	1.00

	Au_ppm	Ag_ppm	Al_pct	As_ppm	Bi_ppm	Ca_pct	Cu_ppm	Fe_pct	Hg_ppm	K_pct	Mg_pct	Ni_ppm	P_ppm	Pb_ppm	S_ppm	Sb_ppm	Sr_ppm	Te_ppm	Tl_ppm	W_ppm	Zn_ppm
Au_ppm	1.00	0.79	0.29	0.56	0.34	-0.50	0.35	0.41	0.57	0.34	-0.02	0.33	0.16	0.43	0.65	0.66	-0.35	0.56	0.61	0.36	0.55
Ag_ppm	0.79	1.00	0.23	0.57	0.17	-0.46	0.14	0.25	0.61	0.28	0.02	0.20	0.35	0.41	0.52	0.75	-0.35	0.68	0.62	0.36	0.41
Al_pct	0.29	0.23	1.00	0.55	0.69	-0.64	0.61	0.69	0.33	0.92	0.03	0.67	0.13	0.43	0.55	0.17	-0.48	0.25	0.49	0.27	0.60
As_ppm	0.56	0.57	0.55	1.00	0.56	-0.73	0.44	0.67	0.71	0.58	0.04	0.60	0.24	0.47	0.74	0.51	-0.55	0.60	0.84	0.31	0.69
Bi_ppm	0.34	0.17	0.69	0.56	1.00	-0.70	0.82	0.89	0.30	0.73	-0.04	0.87	-0.21	0.58	0.70	0.23	-0.56	0.22	0.45	0.20	0.73
Ca_pct	-0.50	-0.46	-0.64	-0.73	-0.70	1.00	-0.64	-0.81	-0.57	-0.68	-0.06	-0.74	-0.06	-0.47	-0.74	-0.43	0.87	-0.48	-0.68	-0.36	-0.79
Cu_ppm	0.35	0.14	0.61	0.44	0.82	-0.64	1.00	0.82	0.28	0.63	-0.05	0.83	-0.16	0.52	0.63	0.30	-0.44	0.17	0.33	0.27	0.74
Fe_pct	0.41	0.25	0.69	0.67	0.89	-0.81	0.82	1.00	0.39	0.74	0.09	0.93	-0.16	0.53	0.79	0.29	-0.61	0.30	0.54	0.22	0.80
Hg_ppm	0.57	0.61	0.33	0.71	0.30	-0.57	0.70	0.63	1.00	0.28	-0.22	0.34	0.36	0.33	0.58	0.55	-0.50	0.81	0.88	0.39	0.59
K_pct	0.34	0.28	0.92	0.58	0.73	-0.68	0.63	0.74	0.28	1.00	0.10	0.73	0.03	0.46	0.60	0.23	-0.51	0.22	0.47	0.22	0.62
Mg_pct	-0.02	0.02	0.03	0.04	-0.04	-0.06	-0.05	0.09	-0.22	0.10	1.00	0.07	-0.10	-0.04	-0.01	0.01	-0.07	-0.18	-0.13	-0.08	-0.01
Ni_ppm	0.33	0.20	0.67	0.60	0.87	-0.74	0.83	0.93	0.34	0.73	0.07	1.00	-0.18	0.51	0.70	0.28	-0.55	0.24	0.47	0.21	0.80
P_ppm	0.16	0.35	0.13	0.24	-0.21	-0.06	-0.16	-0.16	0.36	0.03	-0.10	-0.18	1.00	1.00	-0.01	0.20	0.00	0.41	0.37	0.21	0.04
Pb_ppm	0.43	0.41	0.43	0.47	0.58	-0.47	0.52	0.53	0.33	0.46	-0.04	0.51	0.13	1.00	0.53	0.45	-0.32	0.31	0.43	0.26	0.53
S_ppm	0.65	0.52	0.55	0.74	0.70	-0.74	0.63	0.79	0.58	0.60	-0.01	0.70	-0.01	0.53	1.00	0.45	-0.56	0.50	0.69	0.29	0.75
Sb_ppm	0.66	0.75	0.17	0.51	0.23	-0.43	0.30	0.29	0.55	0.23	0.01	0.58	0.20	0.45	1.00	0.28	-0.28	0.56	0.51	0.36	0.48
Sr_ppm	-0.36	-0.35	-0.48	-0.55	-0.56	0.87	-0.44	-0.61	-0.50	-0.51	-0.07	-0.25	0.00	-0.32	-0.56	-0.28	1.00	-0.43	-0.58	-0.31	-0.61
Te_ppm	0.56	0.68	0.25	0.60	0.22	-0.48	0.17	0.30	0.81	0.22	-0.18	0.24	0.41	0.31	0.50	0.56	-0.43	1.00	0.77	0.35	0.44
Tl_ppm	0.61	0.62	0.49	0.84	0.45	-0.68	0.33	0.54	0.88	0.47	-0.13	0.47	0.37	0.43	0.69	0.51	-0.58	0.77	1.00	0.36	0.62
W_ppm	0.36	0.36	0.27	0.31	0.20	-0.36	0.27	0.22	0.39	0.22	-0.08	0.21	0.21	0.26	0.29	0.36	-0.31	0.35	0.36	1.00	0.33
Zn_ppm	0.55	0.41	0.60	0.69	0.73	-0.79	0.74	0.80	0.59	0.62	-0.01	0.80	0.04	0.53	0.75	0.48	-0.61	0.44	0.62	0.33	1.00

	Au_ppm	Ag_ppm	Al_pct	As_ppm	Bi_ppm	Ca_pct	Cu_ppm	Fe_pct	Hg_ppm	K_pct	Mg_pct	Ni_ppm	P_ppm	Pb_ppm	S_ppm	Sb_ppm	Sr_ppm	Te_ppm	Tl_ppm	W_ppm	Zn_ppm
Au_ppm	1.00	0.79	0.23	0.85	0.18	-0.60	0.73	0.61	0.43	0.35	-0.43	0.51	-0.08	0.45	0.30	0.51	-0.42	0.68	0.22	0.29	0.67
Ag_ppm	0.79	1.00	0.24	0.72	0.20	-0.59	0.61	0.59	0.59	0.33	-0.38	0.46	0.19	0.47	0.29	0.54	-0.47	0.67	0.31	0.47	0.64
Al_pct	0.23	0.24	1.00	0.39	0.42	-0.50	0.40	0.54	0.10	0.95	-0.22	0.56	0.20	0.33	-0.02	-0.06	-0.27	0.19	0.58	0.15	0.26
As_ppm	0.85	0.72	0.39	1.00	0.26	-0.77	0.76	0.83	0.45	0.49	-0.48	0.67	0.00	0.49	0.30	0.44	-0.55	0.68	0.33	0.32	0.65
Bi_ppm	0.18	0.20	0.42	0.26	1.00	-0.36	0.39	0.48	0.03	0.43	-0.25	0.45	0.05	0.54	0.15	0.32	-0.18	0.03	0.18	0.10	0.31
Ca_pct	-0.60	-0.59	-0.50	-0.77	-0.36	1.00	-0.71	-0.80	-0.40	-0.52	0.56	-0.65	-0.23	-0.59	-0.15	-0.37	0.83	-0.56	-0.36	-0.45	-0.70
Cu_ppm	0.73	0.61	0.40	0.76	0.39	-0.71	1.00	0.75	0.38	0.44	-0.53	0.65	0.01	0.46	0.29	0.48	-0.49	0.62	0.23	0.37	0.61
Fe_pct	0.61	0.59	0.54	0.83	0.48	-0.80	0.75	1.00	0.32	0.62	-0.45	0.80	0.07	0.62	0.22	0.37	-0.58	0.54	0.36	0.33	0.61
Hg_ppm	0.43	0.59	0.10	0.45	0.03	-0.40	0.38	0.32	1.00	0.12	-0.25	0.24	0.37	0.27	0.14	0.32	-0.40	0.54	0.16	0.42	0.51
K_pct	0.35	0.33	0.95	0.49	0.43	-0.52	0.44	0.62	0.12	1.00	0.08	0.58	0.10	0.38	0.04	0.04	-0.27	0.23	0.55	0.10	0.34
Mg_pct	-0.43	-0.38	-0.22	-0.48	-0.25	0.56	-0.53	-0.45	-0.25	-0.25	1.00	-0.24	-0.11	-0.34	-0.04	-0.34	0.39	-0.39	-0.15	-0.39	-0.38
Ni_ppm	0.51	0.46	0.56	0.67	0.45	-0.65	0.65	0.80	0.24	0.58	-0.24	1.00	0.13	0.38	0.15	0.30	-0.46	0.41	0.38	0.32	0.48
P_ppm	-0.08	0.19	0.20	0.00	0.05	-0.23	0.01	0.07	0.37	0.10	-0.11	0.13	1.00	0.15	-0.08	-0.02	-0.34	0.24	0.13	0.47	0.06
Pb_ppm	0.45	0.47	0.33	0.49	0.54	-0.59	0.46	0.62	0.27	0.38	-0.34	0.38	0.15	1.00	0.05	0.44	-0.45	0.36	0.31	0.26	0.51
S_ppm	0.30	0.29	-0.02	0.30	0.15	-0.15	0.29	0.22	0.14	0.04	0.15	-0.08	0.15	-0.08	1.00	0.30	0.14	0.09	0.07	-0.02	0.25
Sb_ppm	0.51	0.54	-0.06	0.44	0.32	-0.37	0.48	0.37	0.32	0.04	-0.34	0.30	-0.02	0.44	0.30	1.00	-0.30	0.39	0.15	0.39	0.58
Sr_ppm	-0.42	-0.47	-0.27	-0.55	-0.18	0.83	-0.49	-0.58	-0.40	-0.27	0.39	-0.46	-0.34	-0.45	0.14	-0.30	1.00	-0.52	-0.12	-0.48	-0.63
Te_ppm	0.68	0.67	0.19	0.68	0.03	-0.56	0.62	0.54	0.54	0.23	-0.39	0.41	0.24	0.36	0.09	0.39	-0.52	1.00	0.18	0.42	0.44
Tl_ppm	0.22	0.31	0.58	0.33	0.18	-0.36	0.23	0.36	0.16	0.55	-0.15	0.38	0.13	0.31	0.07	0.15	-0.12	0.18	1.00	0.23	0.15
W_ppm	0.29	0.47	0.15	0.32	0.10	-0.45	0.37	0.33	0.42	0.10	-0.39	0.32	0.47	0.26	-0.02	0.39	-0.48	0.42	0.23	1.00	0.40
Zn_ppm	0.67	0.64	0.26	0.65	0.31	-0.70	0.61	0.61	0.51	0.34	-0.38	0.48	0.06	0.51	0.25	0.58	-0.63	0.44	0.15	0.40	1.00

	Au_ppm	Ag_ppm	Al_pct	As_ppm	Bi_ppm	Ca_pct	Cu_ppm	Fe_pct	Hg_ppm	K_pct	Mg_pct	Ni_ppm	P_ppm	Pb_ppm	S_ppm	Sb_ppm	Sr_ppm	Te_ppm	Tl_ppm	W_ppm	Zn_ppm
Au_ppm	1.00	0.79	0.12	0.75	0.09	-0.38	0.40	0.22	0.39	0.18	-0.19	0.20	-0.01	0.17	0.72	0.47	-0.16	0.60	0.52	0.26	0.52
Ag_ppm	0.79	1.00	0.06	0.60	0.07	-0.35	0.33	0.16	0.63	0.14	-0.24	0.14	0.07	0.18	0.67	0.48	-0.16	0.62	0.57	0.37	0.42
Al_pct	0.12	0.06	1.00	0.46	0.64	-0.67	0.61	0.74	0.01	0.94	0.11	0.76	0.10	0.38	0.40	0.18	-0.58	0.05	0.34	-0.11	0.47
As_ppm	0.75	0.60	0.46	1.00	0.46	-0.74	0.71	0.64	0.51	0.49	-0.12	0.61	-0.01	0.36	0.81	0.52	-0.51	0.53	0.58	0.15	0.72
Bi_ppm	0.09	0.07	0.64	0.46	1.00	-0.70	0.67	0.78	0.01	0.62	0.13	0.78	0.14	0.57	0.42	0.37	-0.60	0.08	0.27	-0.09	0.53
Ca_pct	-0.38	-0.35	-0.67	-0.74	-0.70	1.00	-0.83	-0.85	-0.31	-0.67	0.02	-0.83	-0.22	-0.43	-0.69	-0.46	0.82	-0.34	-0.49	-0.02	-0.75
Cu_ppm	0.40	0.33	0.61	0.71	0.67	-0.83	1.00	0.80	0.32	0.59	-0.08	0.78	0.19	0.45	0.67	0.50	-0.69	0.35	0.48	-0.01	0.72
Fe_pct	0.22	0.16	0.74	0.64	0.78	-0.85	0.80	1.00	0.08	0.73	0.11	0.94	0.07	0.45	0.58	0.36	-0.74	0.16	0.35	-0.12	0.65
Hg_ppm	0.59	0.63	0.01	0.51	0.01	-0.31	0.32	0.08	1.00	0.03	-0.28	0.06	0.14	0.16	0.50	0.51	-0.22	0.64	0.53	0.32	0.50
K_pct	0.18	0.14	0.94	0.49	0.62	-0.67	0.59	0.73	0.03	1.00	0.08	0.74	0.10	0.35	0.47	0.19	-0.55	0.08	0.36	-0.09	0.46
Mg_pct	-0.19	-0.24	0.11	-0.12	0.13	0.02	-0.08	0.11	-0.28	0.08	1.00	0.11	-0.24	0.02	-0.10	-0.15	-0.02	-0.24	-0.10	-0.28	-0.07
Ni_ppm	0.20	0.14	0.76	0.61	0.78	-0.83	0.78	0.94	0.06	0.74	0.11	1.00	0.07	0.43	0.56	0.34	-0.30	0.14	0.33	-0.12	0.63
P_ppm	-0.01	0.07	0.10	-0.01	0.14	-0.22	0.19	0.07	0.14	0.10	-0.24	0.07	1.00	0.10	0.15	0.12	-0.30	0.12	0.23	0.14	0.10
Pb_ppm	0.17	0.18	0.38	0.36	0.57	-0.43	0.45	0.45	0.16	0.35	0.02	0.43	0.10	1.00	0.34	0.42	-0.32	0.21	0.32	-0.07	0.38
S_ppm	0.72	0.67	0.40	0.81	0.42	-0.69	0.67	0.58	0.50	0.47	-0.10	0.56	0.15	0.34	1.00	0.53	-0.47	0.55	0.59	0.11	0.67
Sb_ppm	0.47	0.48	0.18	0.52	0.37	-0.46	0.50	0.36	0.51	0.19	-0.15	0.34	0.12	0.42	0.53	1.00	-0.29	0.43	0.41	0.28	0.49
Sr_ppm	-0.16	-0.16	-0.58	-0.51	-0.60	0.82	-0.69	-0.74	-0.22	-0.55	-0.02	-0.73	-0.30	-0.32	-0.47	-0.29	1.00	-0.20	-0.45	-0.13	-0.56
Te_ppm	0.60	0.62	0.05	0.53	0.08	-0.34	0.35	0.16	0.64	0.08	-0.24	0.14	0.12	0.21	0.55	0.43	-0.20	1.00	0.46	0.25	0.41
Tl_ppm	0.52	0.57	0.34	0.58	0.27	-0.49	0.48	0.35	0.53	0.36	-0.10	0.33	0.23	0.32	0.59	0.41	-0.45	0.46	1.00	0.11	0.45
W_ppm	0.26	0.37	-0.11	0.15	-0.09	-0.02	-0.01	-0.12	0.32	-0.09	-0.28	-0.12	0.14	-0.07	0.11	0.28	0.13	0.25	0.11	1.00	0.04
Zn_ppm	0.52	0.42	0.47	0.72	0.53	-0.75	0.72	0.65	0.50	0.46	-0.07	0.63	0.10	0.38	0.67	0.49	-0.56	0.41	0.45	0.04	1.00

G	Au_ppm	Ag_ppm	As_ppm	Bi_ppm	Ca_ppm	Cu_ppm	Fe_pct	Hg_ppm	K_ppm	Mg_ppm	Mo_ppm	Ni_ppm	P_ppm	Pb_ppm	S_ppm	Sb_ppm	Sr_ppm	Te_ppm	Tl_ppm	U_ppm	W_ppm	Zn_ppm	
Au_ppm	1.00	0.49	0.56	0.30	-0.13	0.32	0.42	-0.11	0.43	-0.11	-0.07	0.33	0.12	-0.05	0.34	0.28	0.43	-0.01	0.47	0.15	0.21	0.03	0.39
Ag_ppm	0.49	1.00	0.64	0.74	-0.46	0.78	0.61	0.52	-0.24	-0.24	-0.31	0.72	-0.18	-0.29	0.82	0.58	0.79	-0.24	0.77	0.09	0.61	0.51	0.69
As_ppm	0.56	0.64	1.00	0.53	-0.34	0.57	0.64	-0.07	0.64	-0.07	-0.28	0.59	0.15	-0.02	0.51	0.59	0.81	-0.02	0.60	0.35	0.56	0.26	0.56
Bi_ppm	0.30	0.74	0.53	1.00	-0.36	0.84	0.63	0.25	-0.11	-0.20	0.64	-0.11	-0.23	0.53	0.42	0.59	-0.30	0.54	0.09	0.54	0.39	0.74	0.47
Ca_ppm	-0.13	-0.46	-0.34	-0.36	1.00	-0.32	-0.26	-0.21	-0.18	0.75	-0.48	0.05	0.08	-0.36	-0.57	-0.48	0.57	-0.31	-0.15	-0.39	-0.19	-0.19	-0.17
Cu_ppm	0.32	0.78	0.57	0.84	-0.32	1.00	0.63	0.33	-0.17	-0.13	0.65	-0.08	-0.25	0.60	0.45	0.63	-0.24	0.73	0.12	0.57	0.60	0.60	0.63
Fe_pct	0.42	0.61	0.64	0.63	-0.26	0.63	1.00	0.32	0.01	-0.02	0.56	0.24	0.00	0.50	0.45	0.57	0.03	0.68	0.36	0.69	0.46	0.61	0.61
Hg_ppm	0.43	0.52	0.64	0.25	-0.21	0.33	0.32	1.00	-0.27	-0.23	0.41	0.19	-0.15	0.00	0.54	0.35	0.72	0.04	0.47	0.22	0.42	0.10	0.47
K_ppm	-0.11	-0.24	-0.07	-0.11	-0.18	-0.17	0.01	-0.27	1.00	-0.04	-0.15	0.30	0.56	-0.20	0.06	-0.14	0.13	-0.18	0.40	-0.12	-0.12	-0.23	-0.23
Mg_ppm	-0.07	-0.31	-0.28	-0.20	0.75	-0.13	-0.02	-0.23	-0.04	1.00	-0.34	0.05	-0.02	-0.28	-0.46	-0.37	0.48	-0.22	-0.06	-0.21	-0.04	0.00	0.00
Mo_ppm	0.33	0.72	0.59	0.64	-0.48	0.65	0.56	0.41	0.00	-0.34	1.00	0.04	0.04	-0.29	0.51	0.55	0.69	-0.37	0.58	0.28	0.59	0.59	0.52
Ni_ppm	0.12	-0.18	0.15	-0.11	0.05	-0.08	0.24	0.19	0.30	0.05	0.04	1.00	0.42	0.00	-0.17	0.00	0.04	0.22	-0.01	0.34	0.06	-0.04	-0.05
P_ppm	-0.05	-0.29	-0.02	-0.23	0.08	-0.25	0.00	-0.15	0.56	-0.02	-0.29	0.42	1.00	-0.19	0.02	-0.14	0.33	-0.16	0.24	-0.17	-0.26	-0.28	-0.28
Pb_ppm	0.34	0.82	0.51	0.53	-0.36	0.60	0.50	0.54	-0.20	-0.28	0.51	-0.17	-0.19	1.00	0.49	0.72	-0.20	0.66	-0.04	0.52	0.34	0.75	0.75
S_ppm	0.28	0.58	0.59	0.42	-0.57	0.45	0.45	0.35	0.06	-0.46	0.55	0.00	0.02	0.02	0.49	1.00	0.62	-0.19	0.36	0.26	0.35	0.14	0.40
Sb_ppm	0.43	0.79	0.81	0.59	-0.48	0.63	0.57	0.72	-0.14	-0.37	0.69	0.04	-0.14	0.72	0.62	1.00	-0.13	0.66	0.24	0.59	0.35	0.60	0.60
Sr_ppm	-0.01	-0.24	-0.02	-0.30	0.57	-0.24	0.03	0.13	0.48	-0.37	-0.37	0.22	0.33	-0.20	-0.19	-0.13	1.00	-0.18	0.22	-0.02	-0.22	-0.11	-0.11
Te_ppm	0.47	0.77	0.60	0.81	-0.31	0.73	0.68	0.47	-0.18	-0.22	0.58	-0.01	-0.16	0.66	0.36	0.66	-0.18	1.00	0.14	0.58	0.56	0.58	0.58
Tl_ppm	0.15	0.09	0.35	0.09	-0.15	0.12	0.36	0.22	0.40	-0.06	0.28	0.34	0.24	-0.04	0.26	0.24	0.24	0.22	1.00	0.27	1.00	0.14	0.14
U_ppm	0.21	0.61	0.56	0.54	-0.39	0.57	0.69	0.42	-0.12	-0.21	0.59	0.06	-0.17	0.52	0.35	0.59	-0.02	0.58	0.27	1.00	0.53	0.53	0.53
W_ppm	0.03	0.51	0.26	0.74	-0.19	0.60	0.46	0.10	-0.12	-0.04	0.59	-0.04	-0.26	0.34	0.14	0.35	-0.22	0.56	0.14	0.53	1.00	0.30	0.30
Zn_ppm	0.39	0.69	0.56	0.47	-0.17	0.63	0.61	0.47	-0.23	0.00	0.52	-0.05	-0.28	0.75	0.40	0.60	-0.11	0.58	0.14	0.53	0.30	1.00	1.00

Figure 53. Spearman rank correlation matrices. 52A. Dunderberg Shale Oxide: East Side. 52B. Dunderberg Shale Sulfide: East Side. 52C. Dunderberg Shale Oxide: West Side. 52D. Dunderberg Shale Sulfide: West Side. E. West Flank, Secret Canyon Shale Oxide. 52F. West Flank, Secret Canyon Shale Sulfide. 52G. Intrusion-related mineralization

## VII. District Surface Geochemistry

Over 3,500 soil samples and 1,200 rock chip samples have been collected at Kinsley Mountain. Values of Au, As, Hg, Mo, Sb, Te, and Tl are elevated in the area of the SHGDs (Figs. 54-56). Concentrations of Ag, Cu, Mo, Pb, Sb, Te, Zn, and W show a zonation around the southern intrusion with concentrations decreasing to the north (Figs. 55-57). Elevated lead in soil values north of the area of known SHGDs may be attributable to a specific stratigraphic interval, the Eureka quartzite. Elevated molybdenum values in the area of the SHGDs are curious as there is no correlation between gold and molybdenum in the correlation matrices derived from down-hole drill data. The molybdenum values may be contained within specific stratigraphic intervals, such as the Dunderberg Shale. Alternatively, the molybdenum values may represent an extension of the intrusion-related system. Anomalies of Ag extend into the area of the SHGDs, but are sparse and weak (<10 ppm Ag in rock-chip samples). Strongly anomalous values of silver and tungsten have been intersected in drill holes near the SHGDs, but the intercepts are limited to 0.5-1 m wide silicified and brecciated intervals. These brecciated and silicified intervals likely outcrop at surface in the area of SHG mineralization, but have not been documented and are unlikely to produce a strong anomaly in soil sampling due to their small size. Antimony is highly anomalous near the stock, but continues to be anomalous throughout the range. Carlin-type elemental signatures including As, Hg, Sb, Tl, and Te are largely limited to the area of the SHGDs and further north, with the exception of numerous samples with very high As, Sb, and Te concentrations proximal to the stock. Highly anomalous As and Tl values occur

throughout the range. Strong Hg and Te anomalies are found in the area of SHGDs, but Te anomalies are numerous near the stock, while the strongest Hg and Au anomalies are typically restricted to the area of the SHGDs. The Sb, As, and Tl soil anomalies along the western flank of the range north of the SHGDs may represent leakage of an underlying hydrothermal system along a high-angle faults. To summarize, the geochemical data allow for discrimination between two systems: 1) To the south, an intrusion-related system that contains highly anomalous values of Ag, As, Cu, Hg, Mo, Pb, Sb, Te, Tl, W, and Zn and 2) A SHG system with Carlin-type pathfinder elements of Au, As, Hg, Sb, Te, and Tl to the north.

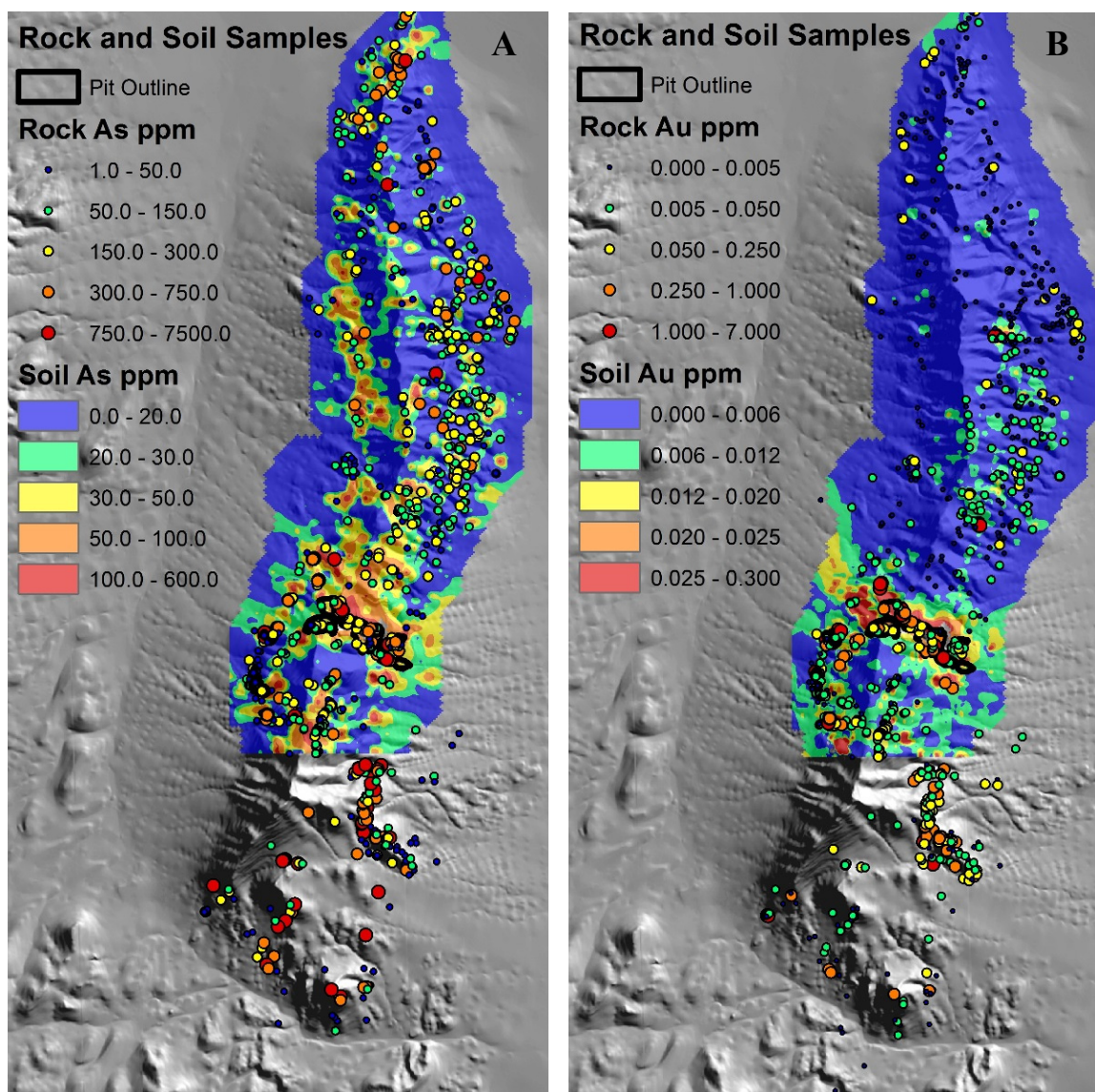


Figure 54. Surface geochemistry throughout the range. Soil samples were taken on 100 X 50 m grids. South of the soil grid in the area of the intrusion, rock-chip samples of intrusive rock, skarn, gossan, and veins were collected, mainly from old mine workings. The figures were created in ArcGIS with the Geosoft Target extension. Images of soil values were made from calculated grids using minimum curvature. Intervals of plotted rock-chip sample values were manually determined using average crustal abundances as a reference. A. Arsenic values. B. Gold values.

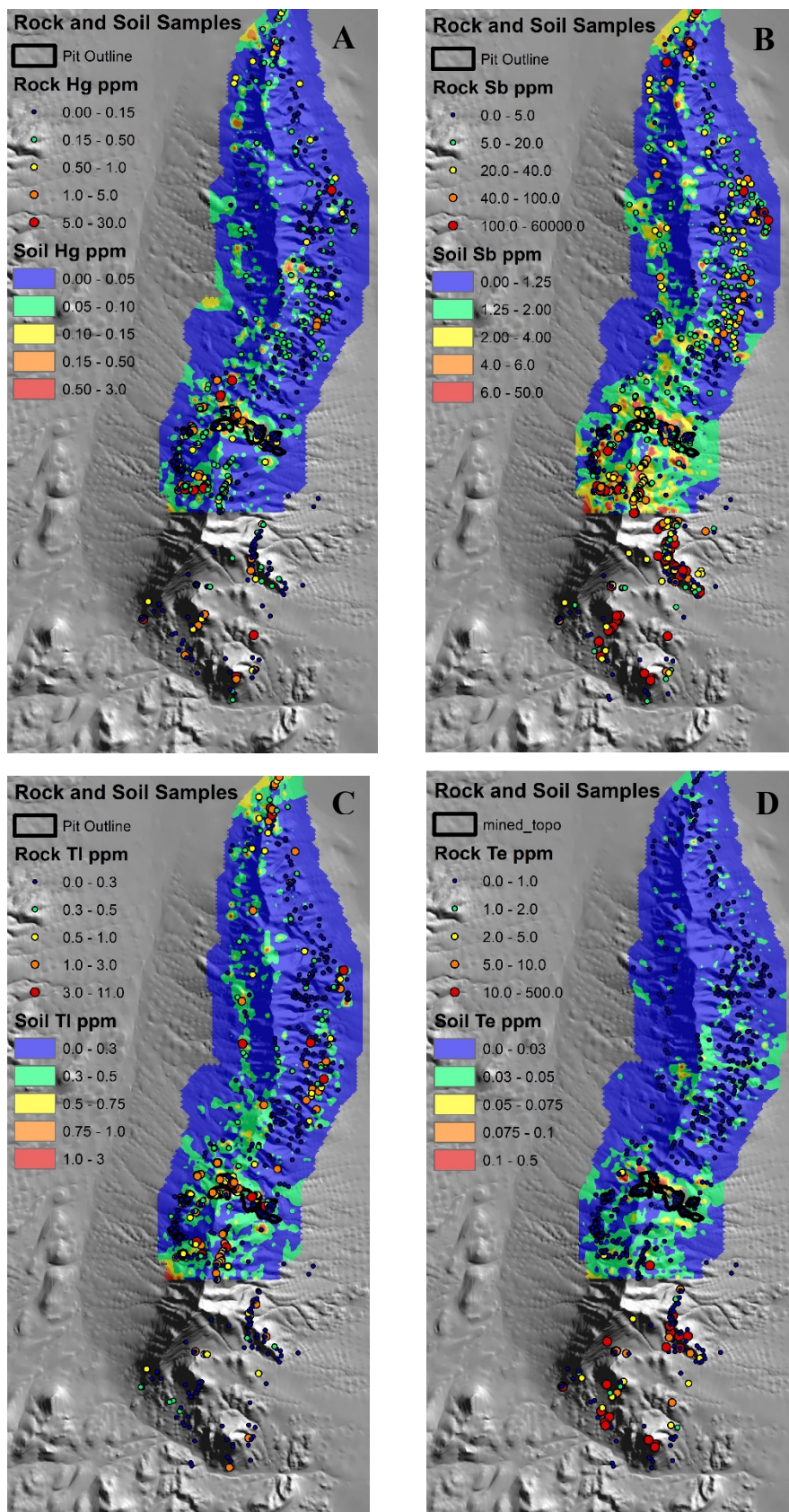


Figure 55. Surface geochemistry throughout the range. A. Mercury values. B. Antimony values. C. Thallium values. D. Tellurium values.

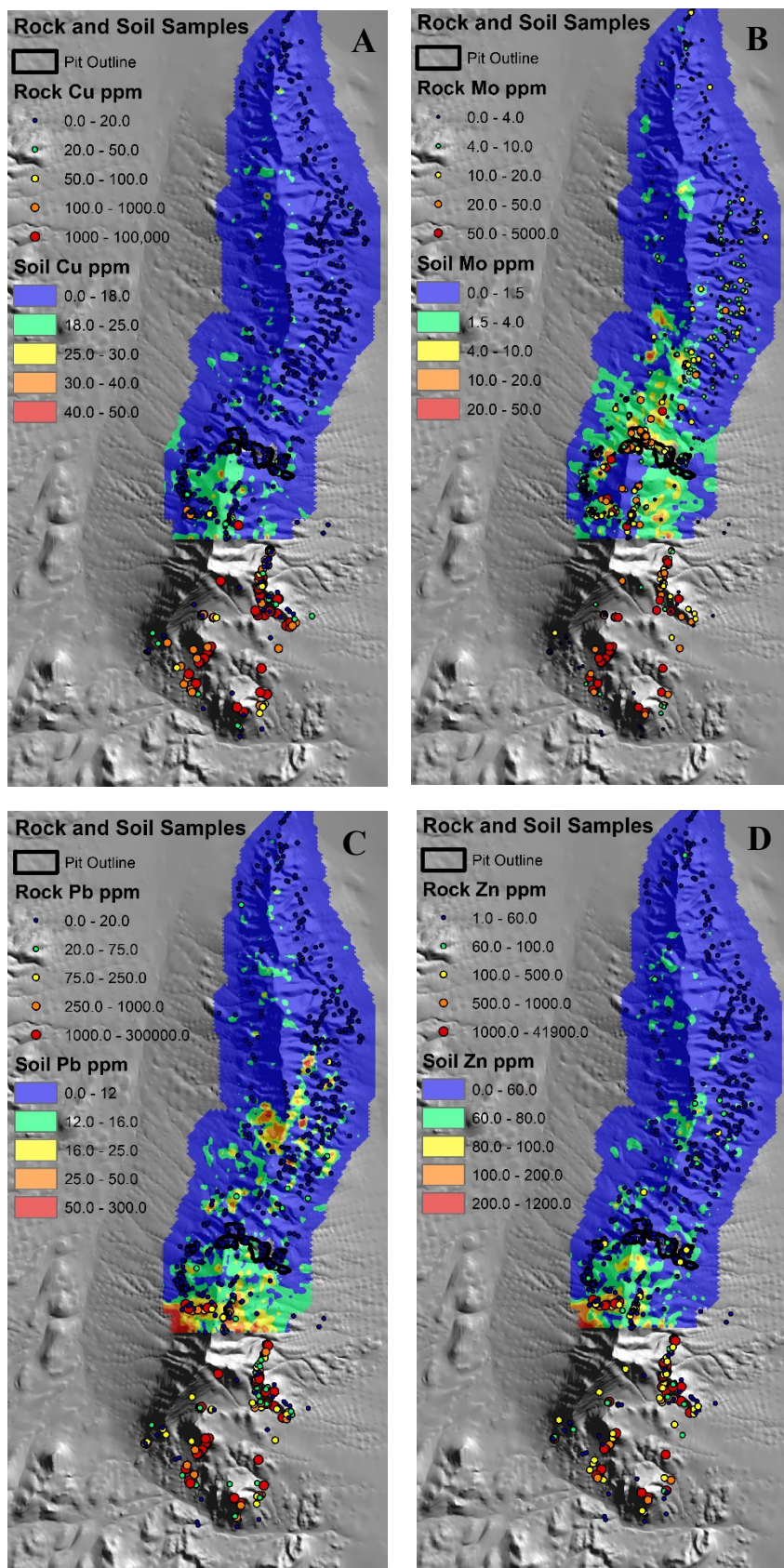


Figure 56. Surface geochemistry throughout the range. A. Copper values. B. Molybdenum values. C. Lead values. D. Zinc values.

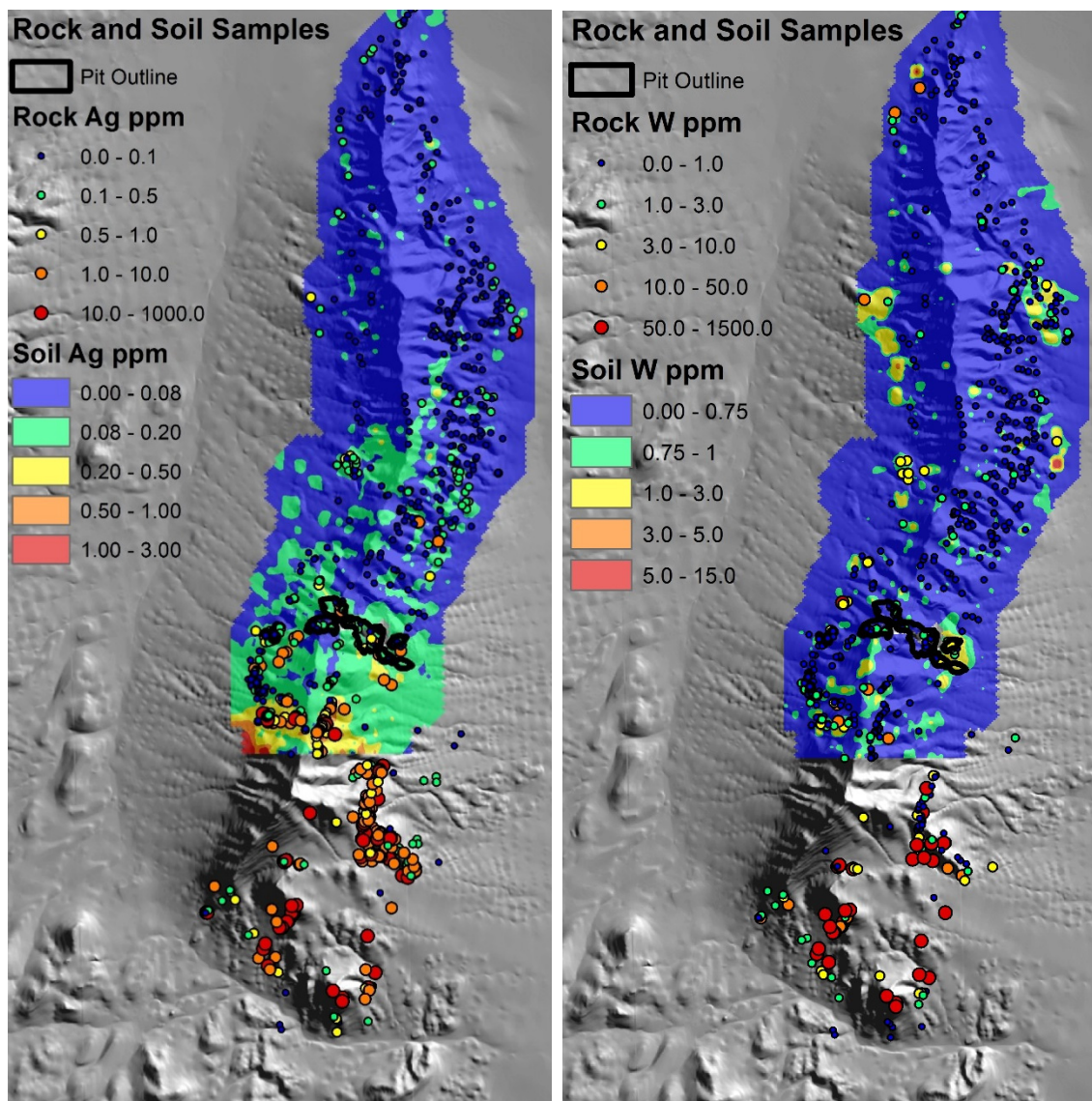


Figure 57. Surface geochemistry throughout the range. A. Silver values. B. Tungsten

## VIII. Geochronology

New U-Pb dates of zircons from the stock, dikes, and volcanic rocks were obtained using SHRIMP-RG at Stanford University. Fifteen samples were dated, and estimated ages are reported as  $^{207}\text{Pb}$  corrected  $^{206}\text{Pb}/^{238}\text{U}$  ages. Typically one spot was analyzed per zircon, with a few of the zircons having multiple spots. Four to seven zircon spots were used to calculate a date per sample. The SHRIMP beam spot size was approximately 22  $\mu\text{m}$ . A full description of the methods used for dating the samples is in Appendix E.

Prior to dating, zircon grain mounts were imaged with cathodoluminescence (CL) using a CL detector mounted to a SEM at Stanford University. Zircon fluoresces with CL because of trace elements, including Dy, Tb, Hf, Eu, and Tb (Hanchar and Miller, 1993). In this study, CL was used to evaluate the complexity of zircons (Fig. 58). Inherited zircon cores were typically much darker or brighter than younger oscillatory zoned growth rims. The inherited cores did not exhibit zoning and were typically rounded. The CL images helped placing the beam on either cores or rims, and to avoid

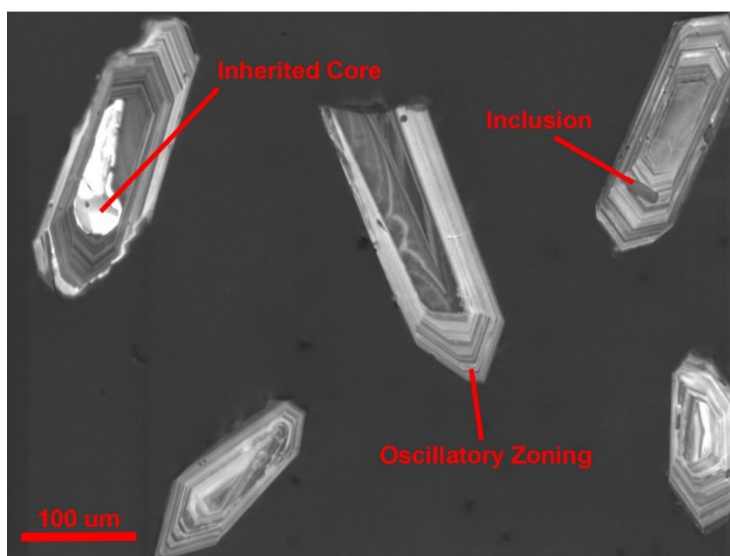


Figure 58. Cathodoluminescence (CL) image of zircons. Zircon in the upper left shows a bright inherited zircon core surrounded by multiple younger, magmatic rims.

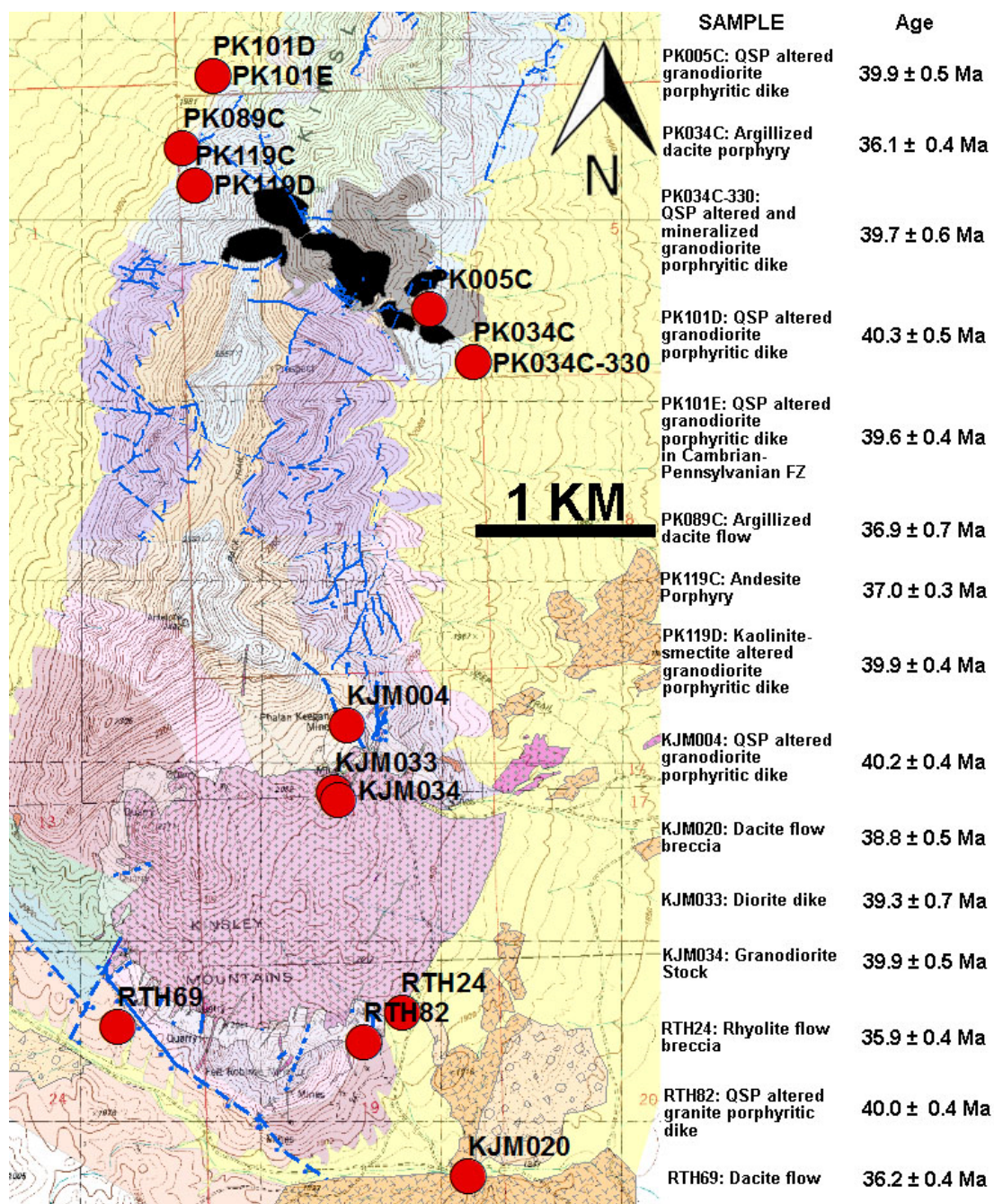


Figure 59. Map showing locations of dated samples with results summarized in adjacent table.

inclusions and fractures.

Results of the U-Pb dating are shown in Figures 59 and 60 and Table 4. Zircons that yielded discordant U-Pb isotopic results had anomalous U contents, evidence for

high common lead, or lead loss were excluded when calculating crystallization ages. A weighted mean age, standard error of the mean (reported at  $2\sigma$  or 95% confidence interval), and mean square weighted deviation (MSWD) were calculated. Standard corrected isotopic data were plotted on Tera-Wasserburg diagrams,  $^{207}\text{Pb}/^{206}\text{Pb}$  versus  $^{238}\text{U}/^{206}\text{Pb}$  with error ellipses to identify analyses that were discordant ( $^{207}\text{Pb}/^{206}\text{Pb}$  above concordia), or older than the main population and may represent an analysis of older inherited zircon or analysis of a mixture of an older core and younger rim. Conversely, an age younger than the main population may result from post-crystallization Pb-loss (Fig. 61).

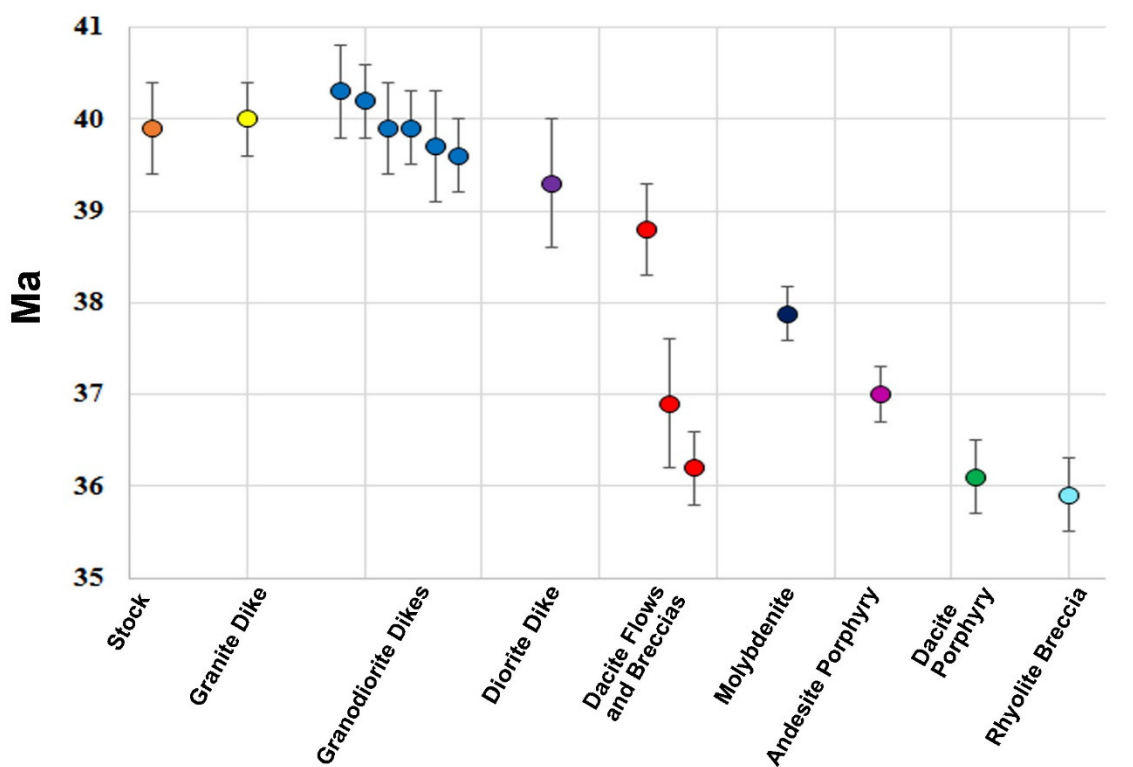


Figure 60. Summary of U-Pb SHRIMP dates plotted through time by lithology. Error bars are two sigma (95%).

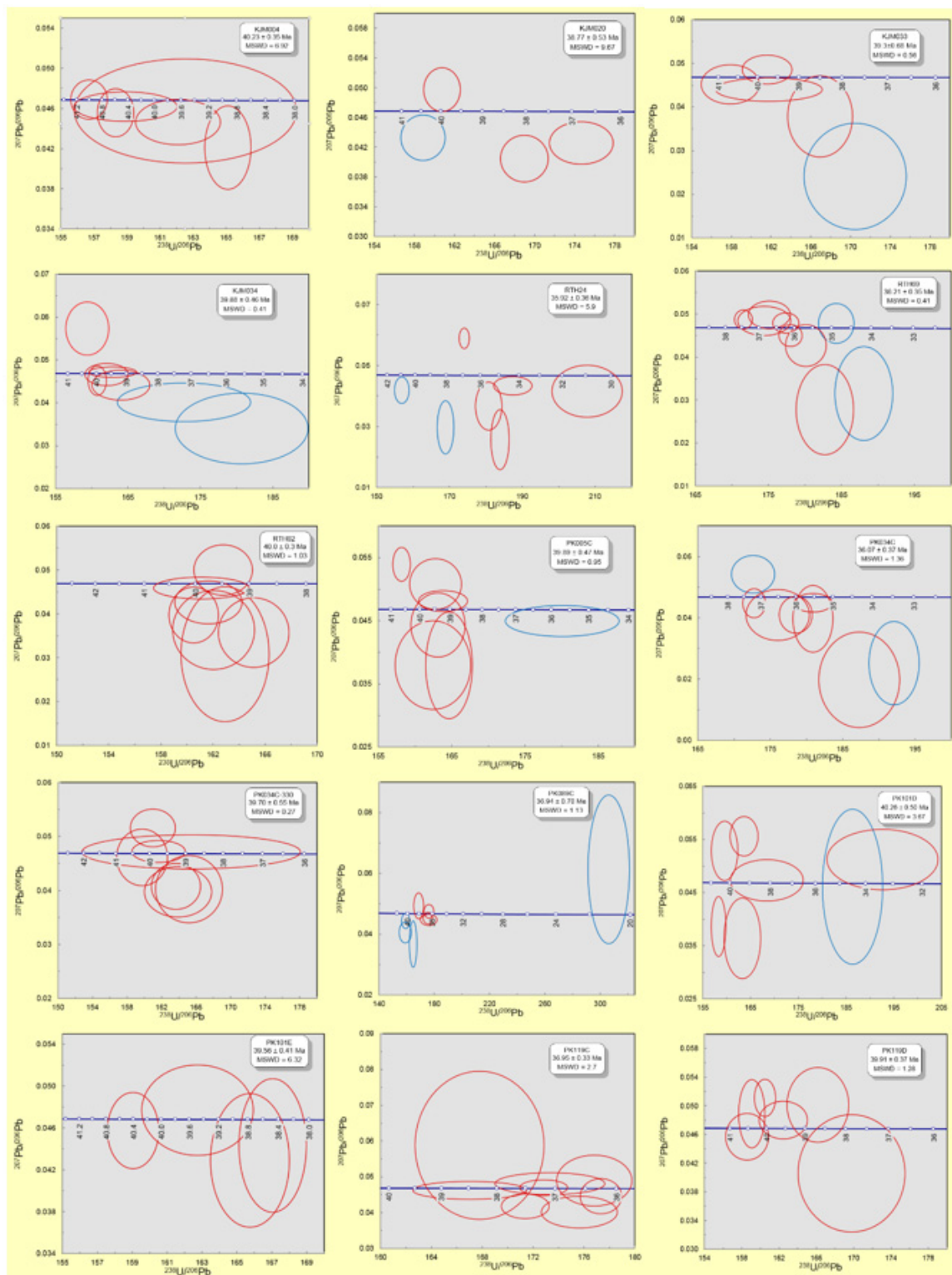


Figure 61. Tera-Wasserburg diagrams for SHRIMP U-Pb analyses. Red ovals were used in the calculation of a date while blue ovals were not used. Analyses of inherited cores that plotted far outside of the zircon rims are not shown in these diagrams.

Table 4. SHRIMP dates and sample locations.

<i>Sample ID</i>	<i>Rock Type</i>	<i>UTM E</i>	<i>UTM N</i>	<i>Th ppm<sup>1</sup></i>	<i>U ppm<sup>1</sup></i>	<b>207corr 206Pb /238U Age</b>	<b>2σ err</b>	<i>MSWD</i>
KJM004	Granodiorite porphyry	726396	4445400	111-361 (199)	378-1217 (802)	40.2	0.4	6.92
KJM020	Dacite flow breccia	727068	4442894	110-538 (298)	321-789 (593)	38.8	0.5	9.67
KJM033	Diorite dike	726328	4445027	77-973 (300)	216-1119 (489)	39.3	0.7	0.56
KJM034	Stock	726348	4444984	139-3069 (648)	379-2232 (900)	39.9	0.5	0.41
PK005C	Granodiorite porphyry	726855	4447709	50-4469 (704)	249-2284 (684)	39.9	0.5	0.95
PK034C	Dacite porphyry	727096	4447410	113-510 (296)	270-904 (496)	36.1	0.4	1.36
PK034C-330	Granodiorite porphyry	727096	4447410	167-289 (227)	424-954 (582)	39.7	0.6	0.56
PK089C	Dacite flow	725487	4448593	55-1430 (379)	89-6632 (1381)	36.9	0.7	1.13
PK101D	Granodiorite porphyry	725653	4449000	43-527 (230)	182-1907 (695)	40.3	0.6	3.67
PK101E	Granodiorite porphyry	725653	4449000	173-262 (227)	514-890 (689)	39.6	0.4	6.32
PK119C	Andesite Porphyry	725553	4448393	116-743 (382)	373-1078 (633)	37	0.3	2.7
PK119D	Granodiorite porphyry	725553	4448393	93-263 (176)	230-744 (498)	39.9	0.4	1.28
RTH24	Rhyolite breccia	726700	4443807	157-725 (348)	360-1639 (779)	35.9	0.4	5.9
RTH69	Dacite Flow	725125	4443725	89-1968 (435)	253-1472 (739)	36.2	0.4	0.41
RTH82	Granite porphyry	726491	4443638	53-348 (213)	142-734 (406)	40	0.4	1.00

<sup>1</sup> Range of values are listed followed by the average in parentheses

Results indicate that all intrusive activity at southern end of Kinsley Mountain is cotemporaneous at ~40 Ma. The granodiorite stock returned an age of  $39.9 \pm 0.5$  Ma. A diorite dike that cut the stock was dated to  $39.3 \pm 0.7$  Ma. A granite porphyritic dike and a granodiorite porphyritic dike near the stock returned ages of  $40.0 \pm 0.4$  Ma and  $40.2 \pm 0.4$  Ma, respectively. Three samples of quartz+sericite+pyrite altered, unmineralized (<5 ppb Au) granodiorite porphyry dikes from drill core in the area of SHG mineralization

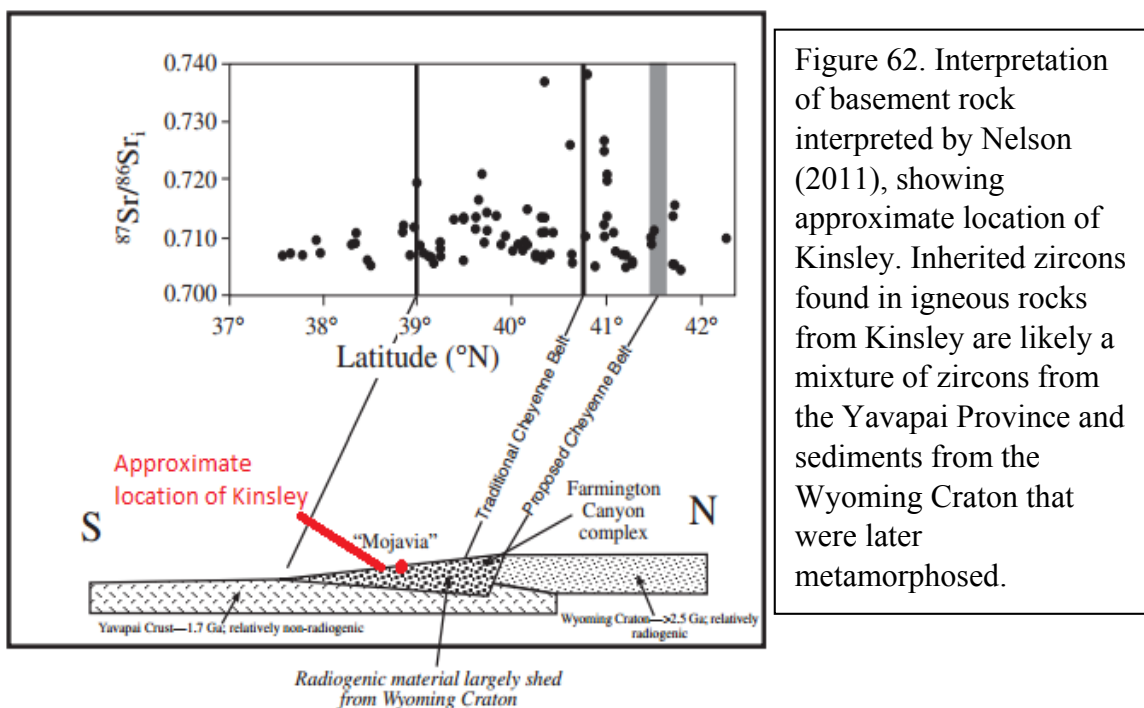
returned ages of  $40.3 \pm 0.5$  Ma,  $39.9 \pm 0.5$  Ma, and  $39.9 \pm 0.4$  Ma. In drill hole PK034C on the east side of the range near the mined-out pits, a mineralized granodiorite porphyritic dike (399 ppb Au) was dated to  $39.7 \pm 0.6$  Ma. Though field relationships show diorite and granodiorite dikes cut the stock, the dates on the dikes are statistically indistinguishable from the age of the stock based on the U-Pb dating. In the area of SHG mineralization, granodiorite dikes, including a dike that is mineralized, are indistinguishable in age (within 95% confidence) from the granodiorite dike dated near the stock and as the stock itself. The dates combined with whole-rock geochemical data suggest the stock and granodiorite porphyry dikes are cogenetic.

Andesite, dacite, and rhyolite flows, flow breccias, and porphyry dikes are significantly younger and were emplaced at  $\sim 36$  Ma. On the west side of the range, an oxidized andesite porphyry dike with minimal alteration that cuts a granodiorite porphyritic dike that has kaolinite-smectite alteration was dated at  $36.9 \pm 0.4$  Ma. Two dacite flows, one south of the stock and one from drill core on the west side of the range were dated at  $36.2 \pm 0.3$  Ma and  $36.9 \pm 0.7$  Ma, respectively. On the east side of the range, the dacite porphyry that contains fine-grained foliated and kinked biotite was dated at  $36.1 \pm 0.4$  Ma. A rhyolite breccia near the SE margin of the stock was dated at  $35.9 \pm 0.4$  Ma. Southeast of the rhyolite breccia, a dacite breccia was dated to  $38.8 \pm 0.5$  Ma, though this date was calculated from only 3 zircon spots and the zircons may have been xenocrysts derived from the older intrusive rocks or antecrysts from another magma source.

## Age of basement rock

Previous workers attempted to determine the age of the basement rock underlying northeast Nevada. Lush et al. (1988) suggested the Archean Wyoming Province may be located under this part of Nevada based on zircons dated in the Ruby Mountains.

However, Premo et al. (2008) argues the basement is either the Mojave (2.0 - 2.3 Ga) or Yavapai Province (1.70 - 1.80 Ga). Nelson et al. (2011) contends there is no true Mojave basement in northeastern Nevada, but that metamorphosed sediments shed from the Wyoming Province overlie the Yavapai Province in northeastern Nevada, suggesting a basement of mixed origin (Fig. 62). Perry (2010) used U-Pb geochronology on detrital



zircons found in the Neoproterozoic McCoy Creek Group, Prospect Mountain Quartzite, and Busby Group from the nearby Deep Creek and Pilot Ranges. Analysis of sedimentary structures showed local derivation of the sedimentary rocks that contained detrital zircons. Results showed no detrital zircons older than 2.0 Ga, leading to the interpretation that the Yavapai Province underlies Northeastern Nevada.

A total of eleven cores from eight samples were analyzed by the SHRIMP. The zircon cores were likely partially assimilated during magma ascent.  $^{204}\text{Pb}$ -corrected  $^{207}\text{Pb}/^{206}\text{Pb}$  ages and  $^{207}\text{Pb}$ -corrected  $^{206}\text{Pb}/^{238}\text{U}$  ages are reported. Most analyses are discordant, likely a result of Pb loss. Pb loss does not affect the  $^{207}\text{Pb}/^{206}\text{Pb}$  ratio, and  $^{207}\text{Pb}/^{206}\text{Pb}$  ages are more precise than standard  $^{206}\text{Pb}/^{238}\text{U}$  ages for dates older than  $\sim 1$  Ga (Compston et al., 1992). Therefore, for most samples, the  $^{204}\text{Pb}$ -corrected  $^{207}\text{Pb}/^{206}\text{Pb}$  age is the most precise. Results are located in Table 5 below. Ages younger than  $\sim 1.7$  Ga (minimum age of the Yavapai Province) are likely the result of analysis of zircon assimilated from Neoproterozoic sediments that overlie basement rock or an analysis that incorporated the younger, outer zircon rim. The results suggest the basement underlying Kinsley is no older than 2.5 Ga and is therefore Paleoproterozoic in age and likely a mixture of the Yavapai Province and sediments from the Wyoming Craton that were later metamorphosed as suggested by Nelson et al., (2011). The results indicate the Cheyenne Belt lies north of Kinsley Mountain.

Table 5. SHRIMP dates for inherited zircon cores.

Sample	$^{207}\text{Pb}/^{206}\text{Pb}$ age	$^{206}\text{Pb}/^{238}\text{U}$ age
RTH69	$1522 \pm 24$ Ma	$389 \pm 3.0$ Ma
RTH82	$333 \pm 57$ Ma	$68.3 \pm 0.9$ Ma
RTH82	$559 \pm 95$ Ma	$130 \pm 1.0$ Ma
RTH82	$1111 \pm 26$ Ma	$646 \pm 8$ Ma
KJM004	$1686 \pm 11$ Ma	$1213 \pm 18$ Ma
KJM033	$1074 \pm 54$ Ma	$181 \pm 4.0$ Ma
KJM033	$1024 \pm 26$ Ma	$343 \pm 29$ Ma
PK005C	$1072 \pm 19$ Ma	$704 \pm 20$ Ma
PK089C	$2383 \pm 78$ Ma	$1603 \pm 53$ Ma
PK101D	$672 \pm 146$ Ma	$117 \pm 7.0$ Ma
PK119D	$967 \pm 28$ Ma	$426 \pm 17$ Ma

## Zircon Geochemistry

Twelve samples were selected for REE, Hf, Y, and Ti trace element analysis of zircon, conducted simultaneously with the collection of data for age determination on the SHRIMP. A total of 60 spots from those 12 samples were analyzed. The trace element geochemistry of zircon is a useful petrogenetic indicator as it reflects the composition of the magmas from which the zircons crystallized (Barth and Wooden, 2010). The interest in trace element geochemistry of zircon for this study was to gain insight into the magma oxidation state.  $\text{Eu}/\text{Eu}^*$  is a measure of the magnitude of a negative europium anomaly by the ratio of the measured Eu content to predicted Eu content based on the adjacent REE, e.g.,  $\text{Eu}^* = (\text{Sm} \cdot \text{Gd})^{0.5}$ . The europium anomaly in zircon is typically produced by crystal fractionation when  $\text{Eu}^{2+}$  is incorporated into plagioclase while other  $\text{REE}^{3+}$  cations are not. However, Dilles et al. (2015) documented that porphyry Cu magmas and their mineralizing dikes, have relatively small negative Eu anomalies. The relatively small negative Eu anomalies could be produced by suppression of plagioclase crystallization due to high magmatic water content and by highly oxidized conditions that convert  $\text{Eu}^{2+}$  to  $\text{Eu}^{3+}$ . Dilles et al. (2015) proposed that degassing of  $\text{SO}_2$ -rich ore fluids from sulfate-rich magmas requires reduction of sulfur and simultaneous oxidation of Fe and Eu in the melt, resulting in the observed, relatively small, negative Eu anomaly.

The samples of the stock and cogenetic dikes at Kinsley show  $\text{Eu}/\text{Eu}^*$  ratios  $> 0.5$ , similar to zircons from productive porphyry Cu systems (Fig. 63) (Dilles et al., 2015). Zircons from the volcanic rocks show  $\text{Eu}/\text{Eu}^*$  ratios of  $< 0.5$ . Figure 5 shows values from Kinsley as well as values from the Emigrant Pass Volcanic Field and

associated dikes related to Carlin-type gold mineralization in northern Nevada and samples from the Western Cascades. Johnson (2015) found that Carlin and Emigrant Pass Volcanic Field magmas were relatively water-rich, but crystallized abundant plagioclase that would be expected to produce a large negative Eu anomaly. However, a small negative Eu anomaly was observed, consistent with Dilles et al. (2015) hypothesis of SO<sub>2</sub> degassing and related oxidation. Samples from Kinsley appear to be strongly oxidized based on the magnetite-titanite association previously described (Table 1). It can be postulated that oxidized magmatic sulfur content in the magmas that formed the stock and granodiorite porphyritic dikes was sufficiently elevated to produce minor Eu oxidation, but was not as elevated as most porphyry Cu magmas. Full trace element data for samples analyzed are located in Appendix F.

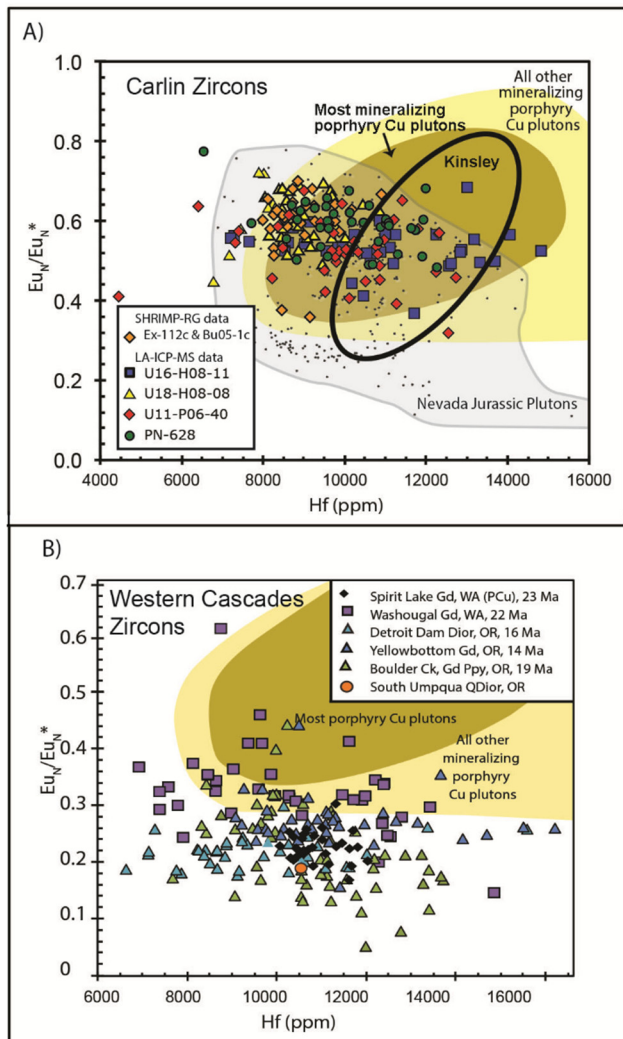
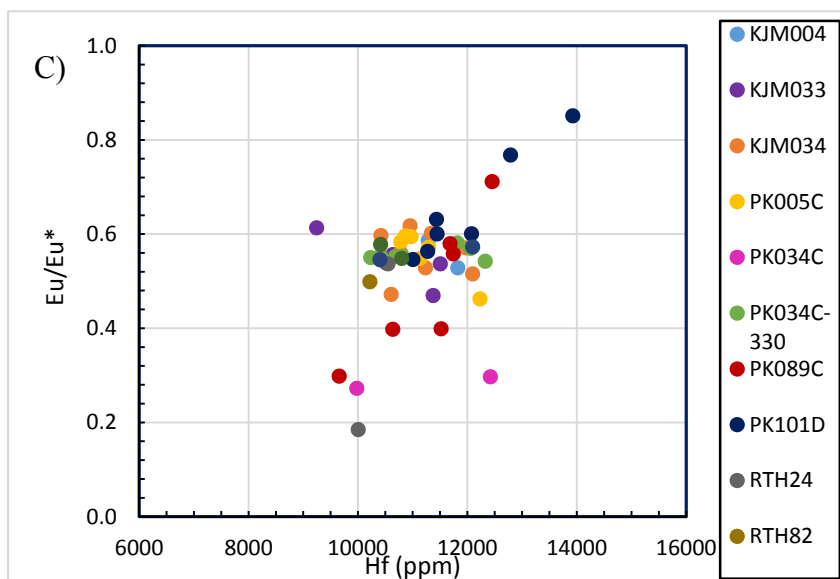


Figure 63. Zircon  $Eu/Eu^*$  vs Hf diagrams. A. Four dikes from the Carlin Trend plotted with data from Jurassic plutons in Nevada (Johnson, 2015 and Dilles et al., 2015). The black oval represents all Kinsley samples. B. Weakly mineralized and barren intrusions of the Western Cascades, Oregon (Utevsky, 2014). C. Data from intrusions and volcanic rocks at Kinsley. The Kinsley data are from granodiorite porphyry dikes (KJM004, PK005C, PK034C-330, PK101D, PK101E, PK119D), diorite porphyry dike (KJM033), granodiorite stock (KJM034), a dacite porphyry dike (PK034C), a dacite flow (PK089C); a rhyolite breccia (RTH24); and a granite porphyry dike (RTH82).



### LA-ICP-MS Geochronology

Zircons from two samples were selected for U-Pb dating by laser ablation inductively coupled mass spectrometry (LA-ICP-MS). The dating was conducted by GeoSeps Inc. using the LA-ICP-MS system at Washington State University with a spot size of 20  $\mu\text{m}$ . The two samples, RTH24 and PK034C, were also dated using the SHRIMP. LA-ICP-MS dating is typically less precise than the SHRIMP, and requires more spot analyses. CL was not used to image zircon grains. RTH24 returned an age of  $35.5 \pm 0.3$  Ma compared to a SHRIMP age of  $35.9 \pm 0.4$  Ma. PK034C returned an age of  $36.1 \pm 0.8$  Ma compared to a SHRIMP age of  $36.1 \pm 0.4$  Ma. Both samples show good agreement between LA-ICPMS and SHRIMP ages.

### Re-Os Geochronology

Though zircons provide a date of the emplacement of the Kinsley stock and dikes, the dates only constrain the age of intrusion-related mineralization to be younger than the ages of the intrusions. Molybdenite occurs at Kinsley and is a mineral that can be dated with the robust Re-Os system. The Re-Os system is able to survive high grade thermal metamorphism and incorporation of common Os and radiogenic Os loss are extremely rare (Shirey and Walker, 1998). In addition, Re and Os are not lost from individual molybdenite crystals during recrystallization (Stein et al., 2001).

A sample of molybdenite within a granodiorite porphyritic dike located within 100 m of the stock was dated. The dike contained diopside endoskarn with later retrograde tremolite and clinozoisite. Molybdenite occurs as 10 to 250  $\mu\text{m}$  disseminated

rosettes and occurs with diopside (Fig. 64). Sample separation and dating of molybdenite

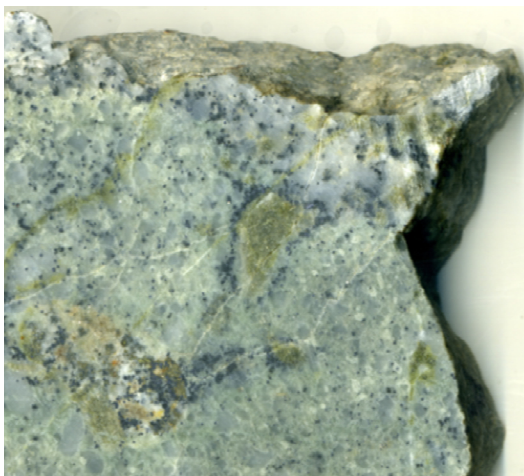


Figure 64. Hand sample of endoskarn in granodiorite porphyry dike that contains molybdenite (mo) that was dated by Re-Os.

were done by the Canadian Centre for Isotopic Microanalysis at the University of Alberta.

Molybdenite was separated by metal-free crushing followed by gravity and magnetic

concentration methods. Methods used for molybdenite analysis are described in detail by Selby & Creaser (2004) and Markey et al. (2007). The  $^{187}\text{Re}$  and  $^{187}\text{Os}$  concentrations in molybdenite were determined by isotope dilution mass spectrometry using Carius-tube, solvent extraction, anion chromatography and negative thermal ionization mass spectrometry techniques. A mixed double spike containing known amounts of isotopically enriched  $^{185}\text{Re}$ ,  $^{190}\text{Os}$ , and  $^{188}\text{Os}$  analysis is used. Isotopic analysis was made using a ThermoScientific Triton mass spectrometer by Faraday collector. Total procedural blanks for Re and Os are <3 picograms and 2 picograms, respectively, which are insignificant for the Re and Os concentrations in the molybdenite. The Chinese molybdenite powder HLP-5 (Markey et al., 1998) is analyzed as a standard. For this control sample over a period of two years, an average Re-Os date of  $221.56 \pm 0.40$  Ma (1SD uncertainty,  $n=10$ ) is obtained. This Re-Os age date is identical to that reported by Markey et al. (1998) of  $221.0 \pm 1.0$  Ma. The result of the Re-Os age determination is given below in Table 6. The age uncertainty is quoted at  $2\sigma$  level, and includes all known analytical uncertainty, including uncertainty in the decay constant of  $^{187}\text{Re}$ .

Table 6. Results of Re-Os dating of Molybdenite.

Sample	Re ppm	$\pm 2\sigma$	$^{187}\text{Re}$ ppm	$\pm 2\sigma$	$^{187}\text{Os}$ ppb	$\pm 2\sigma$	Model Age (Ma)	$\pm 2\sigma$ (Ma)
<b>KJM-029</b>	16.72	0.04	10.51	0.03	6.632	0.021	<b>37.88</b>	<b>0.20</b>

The molybdenite was dated at  $37.88 \pm 0.3$  Ma, which is approximately two million years younger than the age of the stock and dikes as determined by U-Pb dating of zircons. It is clear from field relationships and petrographic work that mineralization is younger than the stock and dikes. The mineralization does not appear to be as closely related in time to the emplacement of the stock and dikes, as in a porphyry copper system. Magmatic-hydrothermal fluids may have been released from a deep cupola zone in an underlying magma chamber after emplacement of the stock and dikes.

#### Apatite Fission-Track Geochronology

Apatite fission-track (AFT) analyses can be used to constrain the thermal history of an area. Carlin-type deposits form at temperatures between 175–250° C with the hottest fluids in primary fluid pathways grading outward to cooler temperatures away from the heat source (Hofstra and Cline, 2000). AFTs anneal at ~110–120° C, meaning a Carlin-type event should fully reset the apatite fission-track geochronometer (Gleadow et al., 1986). AFT dating was used during this study in an attempt to place constraints on the age of the SHGDs at Kinsley.

Fission-tracks in apatite form naturally as trace amounts of uranium in the apatite grains decays over time. Spontaneous fission of  $^{238}\text{U}$  occurs within apatite grains, resulting in the emission of charged particles which strip electrons from atoms found in the apatite grain, causing damage to the crystal lattice and formation of tracks (Laslett et

al., 1987; Green et al., 1989). The amount of tracks present and length of tracks in an apatite grain is function of the time since the apatite was last fully annealed, or at a temperature of  $\sim 110^{\circ}$ - $120^{\circ}$  C.

Seven samples of the Dunderberg Shale and seven samples of the Secret Canyon Shale were selected for AFT dating. Three samples from each shale unit were from mineralized drill intervals with gold concentrations  $> 1$  ppm. All other samples came from drill intervals that had gold concentration  $< 5$  ppb Au and were at least 50-75 m from any known mineralization. Apatite separates were prepared at GeoSeps Inc. of Moscow, Idaho by standard crushing and heavy liquid separation techniques described in the methods chapter. The mounting of apatite grains, counting of tracks, and reduction of data was conducted by Ray Donelick of A to Z Inc. Of the 14 samples submitted, nine returned sufficient apatite for analysis.

Results of the AFT dating are highly variable. This is largely due to the small amount of grains that were able to be analyzed and the nature of the grains themselves. It is preferable to count at least 1000 tracks from 20 to 40 grains per sample for a date with a 10% confidence interval (Donelick pers. comm.). Seven of the nine samples had 12 or fewer grains analyzed and the maximum number of fission tracks counted on any particular grain was 25. The reason for the small number of apatite analyses is due to the low number and small grain size ( $< 100$   $\mu\text{m}$ ) of the apatite. In addition, many of the apatite grains had two domains, a secondary growth rim that surrounded a primary apatite core (Fig. 65). The secondary apatite contained many inclusions and are thought to be uranium poor, resulting in a small amount of fission track formation. It is not clear when the development of secondary apatite occurred and if the secondary apatite growth was

related to hydrothermal activity at Kinsley. However, pyrite was observed as inclusions in the secondary overgrowth zones. Future work using AFT dating from sedimentary rock derived apatite should include SEM analysis of apatite grains prior to the creation of mineral separates to ensure the apatite will be conducive to AFT dating.

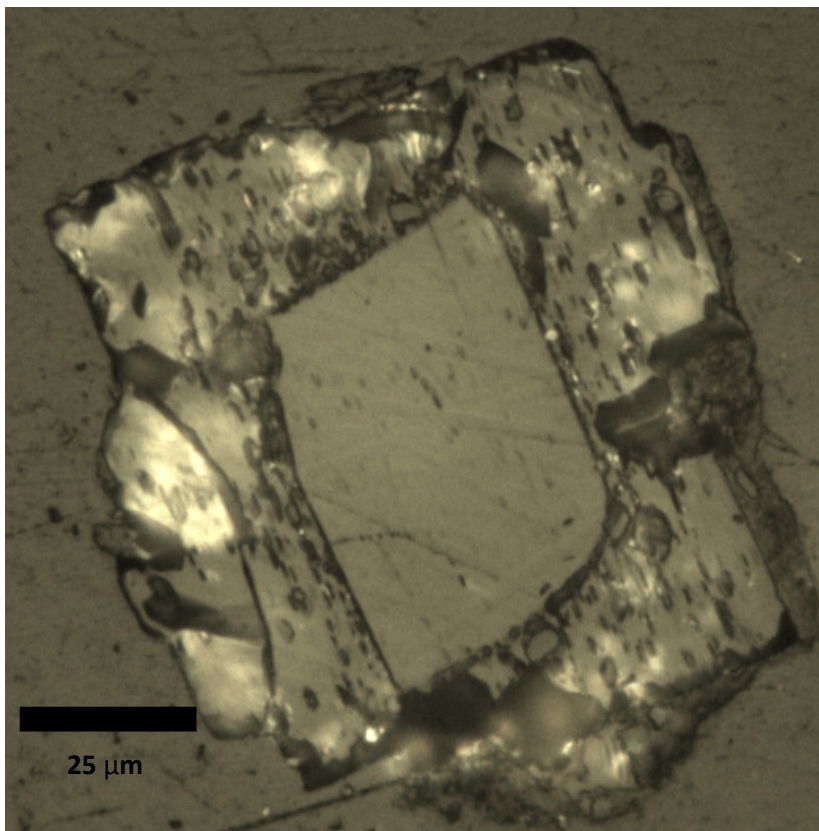
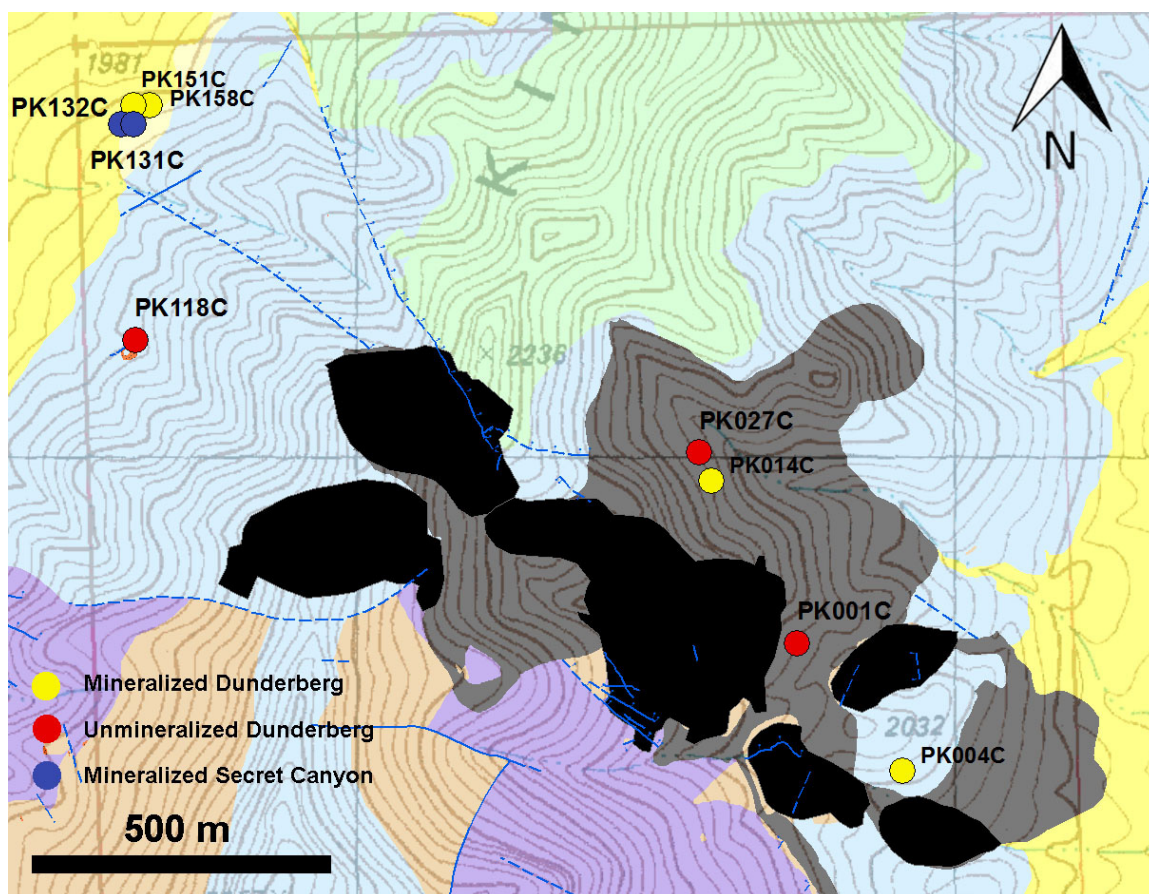


Figure 65. A transmitted light image of a primary apatite core with a secondary apatite rim (uncrossed polars, grain mount).

Results of AFT dating show no distinct difference between samples collected from mineralized intervals and samples collected from unmineralized intervals (Fig. 68 and Table 7). Samples have large errors due to the small number of tracks counted, making interpretation of the results problematic. While most samples fall within error of the suspected age of the SHG system (~40 Ma), the results are not concise enough to determine a precise age, or whether the age represents the timing of mineralization or simply uplift of the range.



PK001C: 33.0 (-10.4, +15.1) Ma    PK027C: 48.9 (-26.1, +56.0) Ma    PK132C: 144.3 (-91.6, +245.6) Ma  
 PK004C: 12.1 (-6.8, +15.5) Ma    PK118C: 31.4 (-7.4, +9.7) Ma    PK151C: 5.3 (-4.0, +16.6) Ma  
 PK014C: 76.0 (-41.5, +90.9) Ma    PK131C: 7.4 (-5.8, +26.2) Ma    PK158C: 18.4 (-5.7, +8.3) Ma

Figure 66. Locations and ages for AFT samples. Errors on dates are asymmetric and are 2 sigma or 95% confidence interval. Black areas are previously mined pits.

Table 7. Apatite fission track analyses.

Sample ID	Lithology	Mineralized?	Depth	UTM E	UTM N	Age (Ma)	95% + CI	95% - CI	# Spots	# Tracks
PK118C	Dunderberg	No	300-307'	725553	4448395	31.4	9.7	7.4	16	64
PK001C	Dunderberg	No	117-127'	726658	4447889	33.0	15.1	10.4	12	29
PK027C	Dunderberg	No	331-341'	726495	4448207	48.9	56.0	26.1	8	7
PK101C	Dunderberg	No	172-177'	725653	4449000	8.0	7.6	3.9	19	13
PK158C	Dunderberg	Yes	460-477'	725577	4448786	18.4	8.3	5.7	10	30
PK004C	Dunderberg	Yes	150-170'	726834	4447675	12.1	15.5	6.8	5	6
PK014C	Dunderberg	Yes	320-338'	726515	4448159	76.0	90.9	41.5	8	6
PK151C	Dunderberg	Yes	444-455'	725550	4448787	5.3	16.6	4.0	7	2
PK132C	Secret Canyon	Yes	844-852'	725529	4448755	144.3	245.6	91.6	7	4
PK131C	Secret Canyon	Yes	937-947'	725551	4448755	7.4	26.2	5.8	5	2

## $^{40}\text{Ar}/^{39}\text{Ar}$ Dating

Previously discussed U-Pb dates on zircon give an emplacement age of the stock and dikes. However, multiple hydrothermal systems or long lived systems can be dated more accurately by the  $^{40}\text{Ar}/^{39}\text{Ar}$  method. The blocking temperature of the  $^{40}\text{Ar}/^{39}\text{Ar}$  system is between 300-350° C (Purdy and Jager, 1976). Therefore,  $^{40}\text{Ar}/^{39}\text{Ar}$  ages record the time when a specific mineral cooled below 300-350° C. Potassium-bearing minerals were separated from three samples and prepared for  $^{40}\text{Ar}/^{39}\text{Ar}$  dating. The samples include coarse grained, retrograde phlogopite from a dike margin near the stock, a sample of biotite from a dacite flow located on the west side of Kinsley mountain taken from a depth of 1950 feet, and a sample of hydrothermal intergrown muscovite and paragonite collected from an interval of mineralized drill core from the SHG mineralization. The phlogopite sample will give an age for retrograde skarn formation that can then be compared to the U-Pb date of the stock to determine a cooling rate. The sample of biotite will give a more precise age of the emplacement for the dacite flow in comparison to the U-Pb date on zircon. Preliminary results of the muscovite/paragonite sample indicate it is detrital in origin. The samples were separated by hand picking grains until 2-3 mg of the targeted mineral were separated from each of the three samples. The three mineral separates were sent to the University of Auburn's ANIMAL lab for irradiation and  $^{40}\text{Ar}/^{39}\text{Ar}$  total fusion and step heat dating. Final results were still pending at the time this thesis was completed.

## IX. Sulfur Isotopes

Sulfur isotope analyses were conducted on 22 samples of pyrite at the University of Nevada, Reno. Sulfur isotopes can constrain the source of sulfur in ore deposits. Sulfur sourced from magmas with a significant mantle component typically has a  $\delta^{34}\text{S}$  value near zero. Pyrite formed through reduction of seawater sulfate is typically referred to as diagenetic pyrite. Pyrite found in sedimentary rocks that did not form by hydrothermal processes is classified in this study as diagenetic pyrite, regardless of genesis. Pyrite in sedimentary rocks typically forms in two ways, from the reduction of seawater sulfate by bacteria, and through thermochemical reduction (Seal, 2006). Pyrite formed through seawater sulfate reduction produces  $\delta^{34}\text{S}$  values that can vary greatly and are typically determined by the  $\delta^{34}\text{S}$  value of seawater sulfate at the time of pyrite formation. Experiments have shown that diagenetic pyrite formed through bacterial seawater sulfate reduction can have  $\delta^{34}\text{S}$  values of 2‰–46‰ lighter than the seawater sulfate (Detmers et al., 2001, and references therein). Abiotic thermochemical reduction occurs when sulfate is reduced by organic matter through chemical processes at greater depths (>2 km) and temperatures (>100 °C) than bacterial sulfate reduction (Machel et al., 1995). Thermochemical reduction can cause a fractionation of 0‰–10‰ between sulfate and subsequent sulfide (Orr 1974; Kiyosu 1980; Machel 2001).

Of the 22 samples selected for sulfur isotope analysis, eight are from intrusion-related mineralization where samples were located within 100 m of the stock. The samples include pyrite from gossanous veins, skarn, and mineralized dikes. The pyrite from intrusion-related mineralization is typically cubic and >0.25 mm in size. Seven

samples consist of pyrite that was collected from drill core intervals from the area of the SHGDs that were unmineralized (<5 ppb Au). The pyrite in these samples is interpreted to be diagenetic in origin. Of the unmineralized diagenetic pyrite samples, six were collected from Cambrian Dunderberg and Secret Canyon Shales, while one sample was taken from Pennsylvanian black shale. The diagenetic pyrite typically occurs as disseminated cubes or framboidal clusters, which are <100  $\mu\text{m}$ . Another seven samples were collected from drill core intervals from areas of SHG mineralization that assayed >1 ppm Au. Pyrite in mineralized zones, as described above, is pyritohedral and <100  $\mu\text{m}$  in size. Pyrite from drill core was separated using previously described standard heavy liquid techniques. Pyrite from intrusion-related mineralization was hand-picked from crushed samples.

Results of the sulfur isotope analyses show a wide range of values, but fall within distinct ranges for each set of samples (Fig. 69 and Table 8). Pyrite from intrusion-related mineralization has values between 3.7‰ and 7.6‰. These  $\delta^{34}\text{S}$  values are consistent with a magmatic source for sulfur. The slight elevation above 0‰ for the intrusion-related pyrites can be attributed to magmatic fluid mixing with a meteoric fluid containing heavy  $\delta^{34}\text{S}$  values, or a magma formed by anatexis of crustal material mixing with a magma sourced from the mantle (Arehart et al., 2013). Diagenetic pyrite from Pennsylvanian shale yielded a value of -8.1‰. The three Diagenetic pyrite from the Dunderberg Shale returned values of 41.4‰, 18.1‰, and 4.6‰, whereas the diagenetic pyrite from the Secret Canyon Shale yield values of 23.6‰, 4.5‰, and 2.2‰. The results demonstrate that  $\delta^{34}\text{S}$  values of diagenetic pyrite from the shales can vary widely in the same stratigraphic interval.

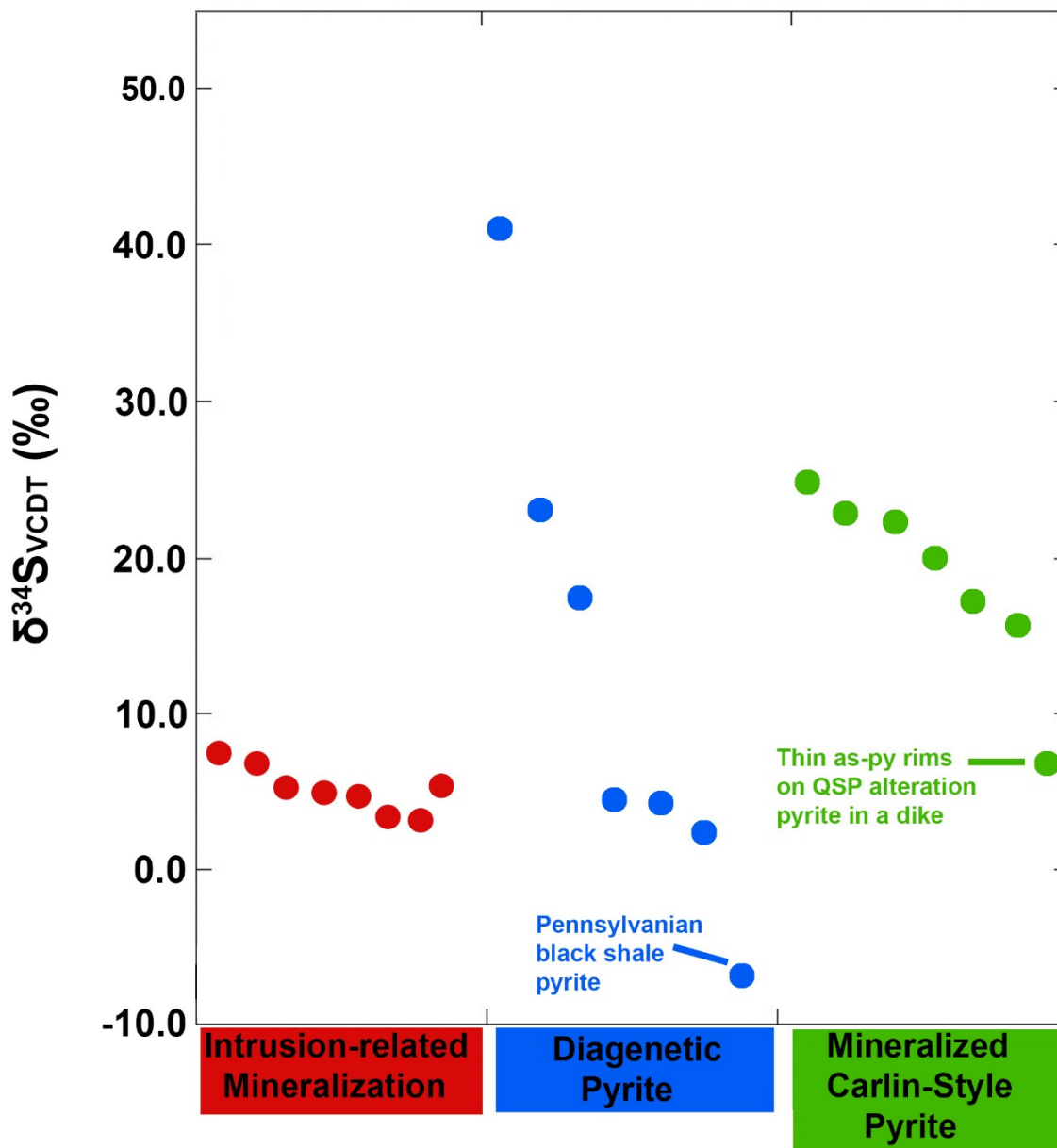


Fig 67. Results of the  $\delta^{34}\text{S}$  analyses.

Table 8. Sulfur Isotope Analyses

Sample	$\delta^{34}\text{S}$ VCDT ‰	Description
Mineralized porphyry	7.6	Granodionite Porphyry
Mineralized porphyry	7.2	Granodionite Porphyry
Retrograde skarn	5.5	Tremolite, phlogopite, talc
Mineralized porphyry	5.3	Granodionite Porphyry
Pyrite in skarn	5.2	Garnet-pyroxene
Mineralized porphyry	3.8	Granodionite Porphyry
Carbonate replacement vein	3.7	Gossan
Pyrite from QSP alteration	5.7	Granodionite Porphyry
Pyrite from QSP alteration	7.3	Granodionite Porphyry
Diagenetic pyrite	41.4	Dunderberg Shale
Diagenetic pyrite	23.6	Secret Canyon Shale
Diagenetic pyrite	18.1	Dunderberg Shale
Diagenetic pyrite	4.6	Dunderberg Shale
Diagenetic pyrite	4.5	Secret Canyon Shale
Diagenetic pyrite	2.2	Secret Canyon Shale
Diagenetic pyrite	-8.1	Pennsylvanian Shale
Mineralized SHG Pyrite	25.0	Dunderberg Shale
Mineralized SHG Pyrite	22.0	Dunderberg Shale
Mineralized SHG Pyrite	21.6	Secret Canyon Shale
Mineralized SHG Pyrite	20.0	Dunderberg Shale
Mineralized SHG Pyrite	17.7	Secret Canyon Shale
Mineralized SHG Pyrite	16.1	Dunderberg Shale

During the Middle to Late Cambrian, seawater sulfate had  $\delta^{34}\text{S}$  values between 27‰ and 33‰ (Fig. 68). Bacterial reduction of Cambrian seawater sulfate to form diagenetic pyrite should result in  $\delta^{34}\text{S}$  values of pyrite between 31‰ and -13‰ based on a fractionation factor between 2‰ and 46‰ (Detmers et al., 2001). Therefore, all  $\delta^{34}\text{S}$  values of diagenetic pyrite from Cambrian and Pennsylvanian shales can be attributed to bacterial reduction with the exception of the 41.4‰ value. Thermochemical reduction could also account two of the six values with a fractionation factor of 0‰–10‰ (Orr 1974; Kiyosu 1980; Machel 2001). Other possibilities for  $\delta^{34}\text{S}$  values lower than

Cambrian seawater include repeated cycles of oxidation and reduction, other S sources and/or fractionation processes, and exchange with magmatic S, allowing for a further decrease in  $\delta^{34}\text{S}$  values (Seal, 2006). Heavy  $\delta^{34}\text{S}$  values of diagenetic pyrite are not uncommon in the Great Basin. In a study of pyrite in sedimentary rock found in the Great Basin, Vikre et al., (2011) documented diagenetic pyrite with values up to 41‰. The formation of extremely heavy pyrite has been explained as a result of closed system conditions, in which the pyrite was formed from a  $^{34}\text{S}$ -enriched sulfate pool (Calvert et al., 1996).

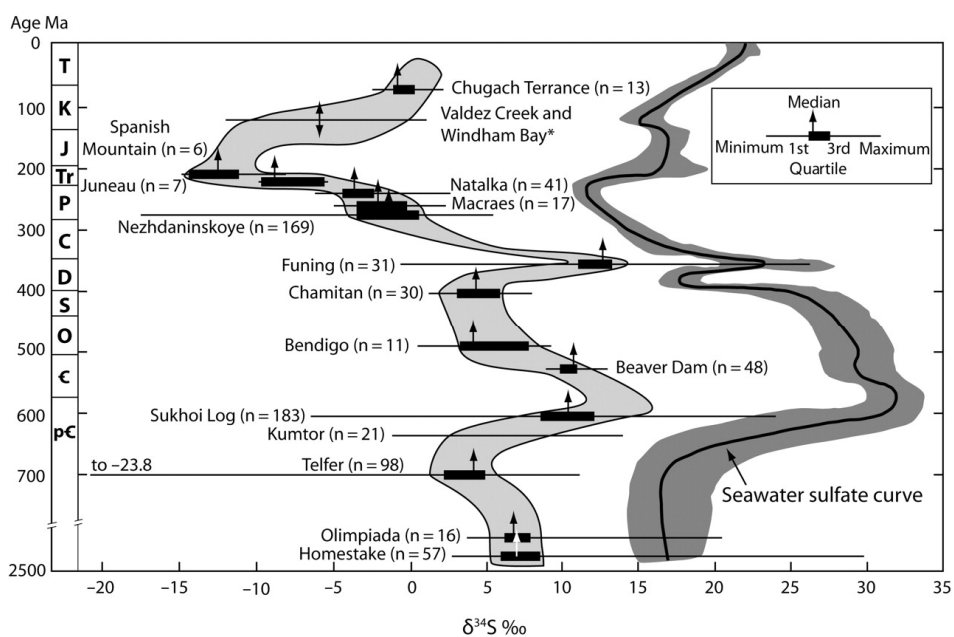


Fig 68. Seawater  $\delta^{34}\text{S}$  sulfate curve with plots of sulfides from a variety of sediment-hosted gold deposits, mainly orogenic gold deposits (Chang et al., 2008). Note the  $\delta^{34}\text{S}$  of seawater sulfate during the Cambrian to Neoproterozoic ranged from 27‰ to 34‰.

Past studies utilizing conventional sulfur isotope analyses on pyrite separates from Carlin-type gold deposits in Nevada have not resulted in tight groupings of  $\delta^{34}\text{S}$  values in mineralized samples.  $\delta^{34}\text{S}$  values typically range from 0‰ to 17‰ (Hofstra et al., 1997; Hofstra and Cline, 2000; and Emsbo et al., 2003). Arehart et al., (1993), using an ion

microprobe, found that ore-stage pyrite from the Betze-Post Carlin-type deposit had  $\delta^{34}\text{S}$  values of  $\sim 20\text{‰}$ . A study by Kesler and Ye, (2005) using an ion microprobe, found that ore-stage arsenian-pyrite from the Screamer Carlin-type deposit had  $\delta^{34}\text{S}$  values between  $-0.9\text{‰}$  and  $3.6\text{‰}$ . Previous S isotope studies analyzing bulk samples of pyrite from Carlin-type deposits are hindered by the presence of a core of diagenetic or pre-ore stage hydrothermal pyrite and a thin rim of ore-stage arsenian-pyrite. The result of analyzing bulk pyrites is a  $\delta^{34}\text{S}$  value that represents a mixture between the diagenetic, pre-ore stage pyrite, and ore-stage arsenian-pyrite.

Mineralized pyrite samples from the SHG mineralization in this study show a grouping of  $\delta^{34}\text{S}$  between  $16.1\text{‰}$  and  $25.0\text{‰}$ . The Dunderberg Shale returned four samples with  $\delta^{34}\text{S}$  values of  $25.0\text{‰}$ ,  $22.0\text{‰}$ ,  $20.0\text{‰}$ , and  $16.1\text{‰}$ . Two samples from Secret Canyon Shale returned  $\delta^{34}\text{S}$  values of  $21.6\text{‰}$  and  $17.7\text{‰}$ . A sample of mineralized pyrite taken from a granodiorite porphyritic dike returned a  $\delta^{34}\text{S}$  value of  $7.3\text{‰}$ . As mentioned above, pyrite from mineralized intervals show large arsenian-pyrite rims with either small diagenetic cores, or more commonly, no cores at all. The gold-bearing arsenian-pyrite rims typically comprise  $>80\%$  of the volume of the pyrite. It would reason that a bulk analysis of these pyrite should yield a tight grouping of  $\delta^{34}\text{S}$  values if the arsenian-pyrite rims are being precipitated during one hydrothermal event from an ore fluid with homogenous  $\delta^{34}\text{S}$  values. The  $\delta^{34}\text{S}$  value of  $7.3\text{‰}$  from the mineralized dike can be attributed to thin arsenian-pyrite rim overgrowth on coarse grained pyrite formed through hydrothermal alteration where the sulfur forming the coarse pyrite cores was magmatically sourced. Though the sample size is small, Cambrian diagenetic pyrite in this study yield an average  $\delta^{34}\text{S}$  value of  $15.7\text{‰}$ , while mineralized pyrite samples have

an average  $\delta^{34}\text{S}$  value of 20.4‰. Estimation of the isotopic composition of parent fluids is more difficult for arsenic sulfides, including arsenian pyrite, because experimental fractionation data are not available. Fractionation factors for cinnabar are commonly used to interpret isotopic data for arsenic sulfides, even though its crystal structure is significantly different (Hofstra et al. 1999). Using cinnabar fractionation factors, arsenian pyrite with  $\delta^{34}\text{S}$  values of about 16‰-25‰ require ore fluids containing  $\text{H}_2\text{S}$  with  $\delta^{34}\text{S}$  values of about 20‰ to 29‰ (Ohmoto and Rye, 1979). In addition, if the sulfur in mineralized arsenian-pyrite is magmatically sourced and ranges from 0‰-10‰, and the diagenetic cores account for only ~20% of the volume, the resulting average  $\delta^{34}\text{S}$  value of bulk analyzed pyrite should be significantly lower than 15.7‰. Conversely, to obtain a  $\delta^{34}\text{S}$  value of ~20‰ in bulk analyzed mineralized pyrite, the ore fluid must have had a  $\delta^{34}\text{S}$  value of >20‰. Therefore, it is likely that sulfur in the ore fluid that deposited gold-bearing arsenian-pyrite at Kinsley was not magmatically sourced.

## IX. Discussion

SHG mineralization at Kinsley Mountain shares many similarities with CTGDs in north-central Nevada. However, the mineralization at Kinsley has unique characteristics that require a different set of circumstances to have formed. Intrusion-related mineralization was likely forming contemporaneously with SHG mineralization. In addition, mineralization appears to have happened during rapid uplift of the range during the late Eocene.

The exposure of Cambrian strata at Kinsley contrasts with nearby mountain ranges, such as the Dolly Varden Mountains and White Horse Mountains, where the oldest units exposed are of Permian and Devonian age, respectively. The uplift of Cambrian rocks has been attributed to the development of an anticline in the hanging wall of a steep ramp in a Mesozoic thrust system that either formed in the Jurassic Elko or Cretaceous Sevier Orogeny (Robinson, 2005). Long et al., (2014, 2015), documented such a hanging wall anticline above a ramp or reverse fault in the Central Nevada Thrust Belt in the Eureka mining district 140 km southwest of Kinsley in east-central Nevada. Long et al. (2014) attributed the structural culmination to out of sequence deformation in the hinterland of the Sevier Orogeny in the Early Cretaceous (Long et al., 2014).

Low-angle faults along bedding planes likely formed during contractional deformation and were later reactivated as low-angle detachment faults, likely analogous to late Cretaceous collapse of a structural culmination at Eureka (Long et al., 2014). Also, analogous to the Eureka District, the north-northeast-striking high-angle faults at Kinsley also likely formed during initial extensional collapse of the structural culmination in the

late Cretaceous. In the area of the West Flank, the Pennsylvanian shale unit described above is overlain by Tertiary volcanic rocks. The Pennsylvanian stratigraphy is no more than 50 m thick and is in low-angle fault contact with underlying Ordovician and Cambrian units. A granodiorite dike dated at  $39.6 \pm 0.4$ , intrudes the low-angle fault, suggesting low-angle detachment faulting occurred prior to the emplacement of intrusive rocks. Most SHG mineralization is located in the Kinsley Trend, indicating the west-northwest fault and locally associated folds developed prior to formation of the SHGDs. The west-northwest Kinsley Trend possibly formed during Laramide orogeny as reactivation of a basement structure (Rhys, 2015).

The granodiorite stock and slightly later cogenetic dikes were emplaced  $\sim 40$  Ma. The dikes and intrusion-related mineralization utilized the high-angle north to northeast normal faults as conduits up to 4 km from the stock. The maximum stratigraphic thickness prior to any deformation between Permian rocks and the Hamburg Formation is estimated to be 6.5-7.5 km (Buckley, 1967; Silberling, 2002; Cook, 2015), similar to the maximum depth of emplacement of 7.5 km for the stock has estimated from aluminum-in-hornblende geobarometry.

The age of the SHGDs is constrained by Eocene intrusive activity. Three granodiorite dikes contain SHG mineralization, while several dozen granodiorite dikes show no evidence of SHG mineralization either in the dikes or in the adjacent country rocks. A granodiorite dike that contained SHG mineralization (399 ppb Au over 1.8 meters) was dated to  $39.7 \pm 0.6$  Ma. The date, coupled with the observation of many unmineralized dikes, indicates SHG mineralization in the Dunderberg Shale post-dates

exposed intrusive activity and that ore fluids locally utilized dikes as conduits, but in most cases did not. Mutual paragenetic relationships between the intrusion-related system and SHG mineralization suggest the two styles of mineralization formed at approximately the same time in the Eocene. For example, tennantite-tetrahedrite, stibnite, and galena formed prior to the development of Au-bearing arsenian-pyrite rims in mineralization in the Secret Canyon Shale. Conversely, scheelite and tennantite-tetrahedrite locally envelops arsenian-pyrite rims. It is likely that the tennantite-tetrahedrite, scheelite, galena, and stibnite are a weak distal expression of the intrusion-related mineralization. Additional evidence for a contemporaneous relationship between intrusion-related mineralization and SHG mineralization occurs in mineralization at Secret Spot in the Secret Canyon Shale. Secret Spot is 1 km closer to the stock than the West Flank mineralization and contains more characteristics of intrusion-related mineralization than other areas of SHG mineralization at Kinsley, as described above. The presence of both early and late intrusion-related base metals in SHG mineralization suggests the SHGDs formed contemporaneously with intrusion-related mineralization is as young as ~37.9 Ma, based on the Re-Os date (Fig. 69). Furthermore, unaltered volcanic lavas and associated breccia erupted from likely local sources, mainly between 37 and 36 Ma. They onlap mineralized Cambrian stratigraphy, the minimum age of SHG mineralization is 37-36 Ma.

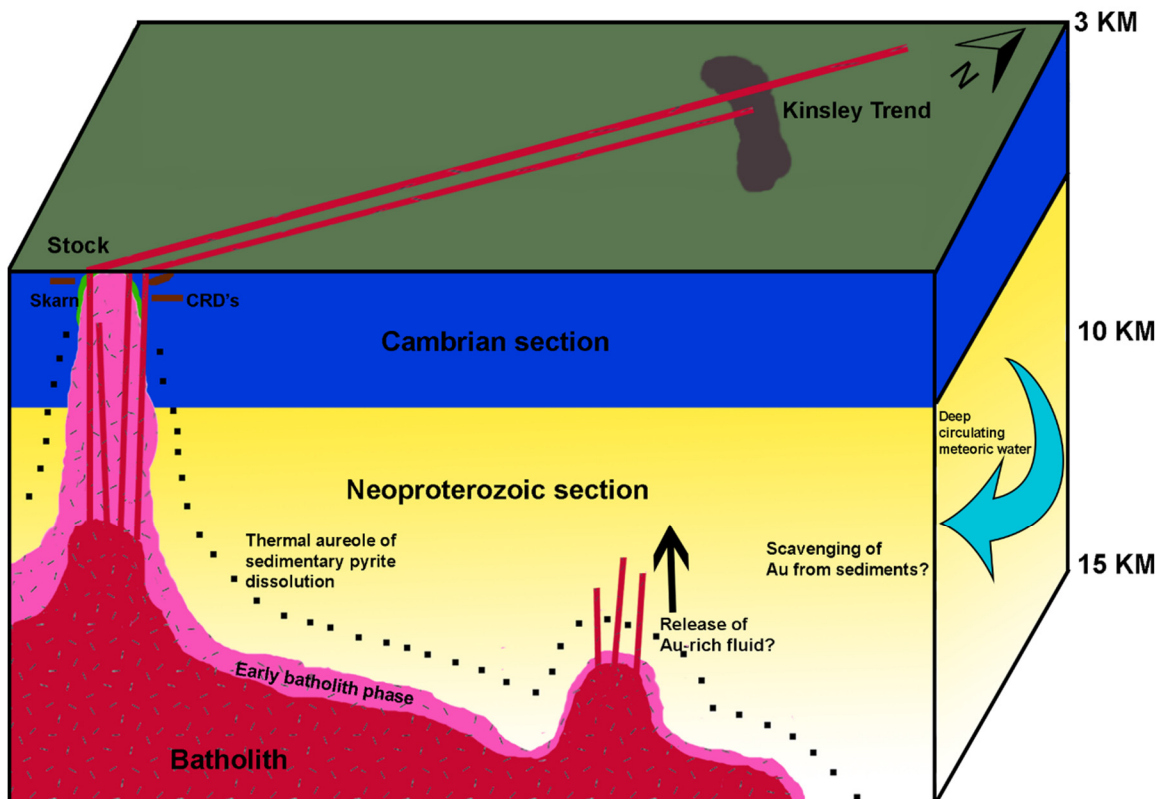


Fig 69. A schematic model for the formation of SHG mineralization at Kinsley Mountain. Gold may have been sourced from a cupola at depth, thermal dissolution of sedimentary pyrite, Neoproterozoic and Cambrian sedimentary rock, or a combination of these, as discussed in the text.

The SHG mineralization is presently located at approximately the same elevation as the stock, the same level of stratigraphic exposure is present, and no major faults lie between the stock and the Kinsley Trend. Geochronology and petrographic evidence indicate the SHG system post-dates the stock, but is cotemporaneous with intrusion-related mineralization, indicating both formed at a similar depth if no tilting occurred. As detailed above, maximum depths of ~7.5 km are estimated from aluminum in hornblende geobarometry and stratigraphic reconstructions. Depths of >3 km are supported by the presence of tungsten skarn, ductile deformation of wall-rock around the margin of the stock, lack of chilled margins along the margin of the stock, lack of retrograde skarn that

indicates minimal interaction with meteoric water, and lack of a radial fault or fracture pattern around the stock (Newberry and Swanson, 1986). Newberry and Einaudi (1981) calculated scheelite solubility at various depths and demonstrated scheelite has retrograde solubility and is best transported and deposited at relatively high temperatures and moderate pressures (see Appendix H). Additionally, Newberry and Einaudi (1981) examined numerous W skarns in the Cordillera and concluded all formed at pressures >1 kb, most >1.3 kb.

The ~37-36 Ma volcanic flows may onlap the stock near its southeastern margin and locally appear to onlap the west-northwest-striking fault south of the stock that places Permian against Cambrian south of the stock. These relationships would suggest there was significant exhumation of the range between ~40 and 36 Ma. High-angle normal faulting followed extrusive activity forming large basin and range faults that flank the range. If the range tilted northward during the ~37-40 Ma extensional event that down-faulted Permian strata against Cambrian strata south of the stock, the stock would have formed at a greater depth than the SHG mineralization.

SHG mineralization at Kinsley Mountain bears many features typical of the large CTGDs in Nevada (Table 9). However, the mineralization at Kinsley also has features not previously described in CTGDs. The geochemical signature of Kinsley is very similar to CTGDs. The elemental association of Au-As-Hg-Tl-Sb-(Te) is a fundamental fingerprint for CTGDs, and Kinsley shares this characteristic as evidenced by down-hole geochemistry and surface geochemistry. Like CTGDs, Ag:Au ratios are less than one at Kinsley. Furthermore, late realgar, orpiment, and stibnite are found peripheral to and within ore zones is typical of CTGDs. Decarbonatization and silicification are abundant

at Kinsley, as in CTGDs. However, large and numerous collapse breccias found in CTGDs are present at Kinsley, but are not common. The lack of collapse breccias may be a result of shales being the dominant host rock. Shales are not as amendable as limestones to forming collapse breccias due to the abundance of clays and other detrital material.

Table 9. Similarities between Kinsley and Carlin-Type deposits (modified from Hofstra and Cline, 2000).

Characteristic	Carlin-Type	Kinsley
Age	Mid-Tertiary	Mid-Tertiary
Igneous association	Broad spatial correlation with calc-alkaline subduction-related magmatism	Spatial overlap with calc-alkaline subduction-related magmatism
Host rocks	Calcareous sedimentary rocks of diverse facies, ±igneous rocks	Ferroan dolomite-bearing shales
Depth of formation	Intermediate, mainly 1 - 3 km	Likely >2 km
Mineralization style	Discordant and stratabound	Stratabound
Alteration types	Decarbonatization, argillization, silicification	Decarbonatization and silicification
Open-space filling minerals	Cal, orp, real, qtz, stib, py-marc, bar	Cal, orp, real, qtz, stib, bar
Ore minerals	Disseminated auriferous py, marc, aspy	Disseminated auriferous py and aspy
Residence of gold	Submicron inclusions and solid solution in py, marc, aspy	Submicron inclusions and solid solution in py and aspy
Geochemical signature	Au, As, Sb, Tl, Hg, ±Te, ±Ba	Au, As, Sb, Tl, Hg, Te
Iron mobility	Not introduced	Not introduced
Au-Ag	High, >3 to 20	2 in the Dunderberg Shale and 7 in the Secret Canyon Shale
Base metal content	Low, comparable to gold	Low, comparable to gold
Formation temperature	~250° to 150° C	Unknown, but likely >250° to 200° C
pH of ore fluid	Moderately acidic	Near neutral to moderately acidic
Au transport	Bisulfide complexes	Bisulfide complexes
Ore depositional mechanisms	Sulfidation, ±cooling, ±dilution	Sulfidation

Like CTGDs, sulfidation appears to be the main depositional process of Au in the SHGDs at Kinsley (Fig. 70). No iron appears to have been added to the SHGDs by the hydrothermal system. However, unlike CTGDs, most of the ore-stage pyrite at Kinsley are euhedral pyritohedrons with oscillatory zoned arsenian-pyrite rims. In CTGDs, the arsenian-rims are typically “fuzzy” in appearance, typically do not display zoning, and are thin in comparison to diagenetic pyrite cores. As previously discussed, galena, stibnite, and tennantite-tetrahedrite have been observed as envelopes around diagenetic pyrite with later zoned arsenian-rims at Kinsley. The arsenian-pyrite rims at Kinsley are

much thicker in comparison to diagenetic pyrite cores than typical Carlin-type rims. The presence of early base metals associated with ore-stage gold-bearing arsenian pyrite has not been documented in CTGDs. The electron microprobe data show gold is located in the arsenian-pyrite rims which is characteristic of CTGDs.

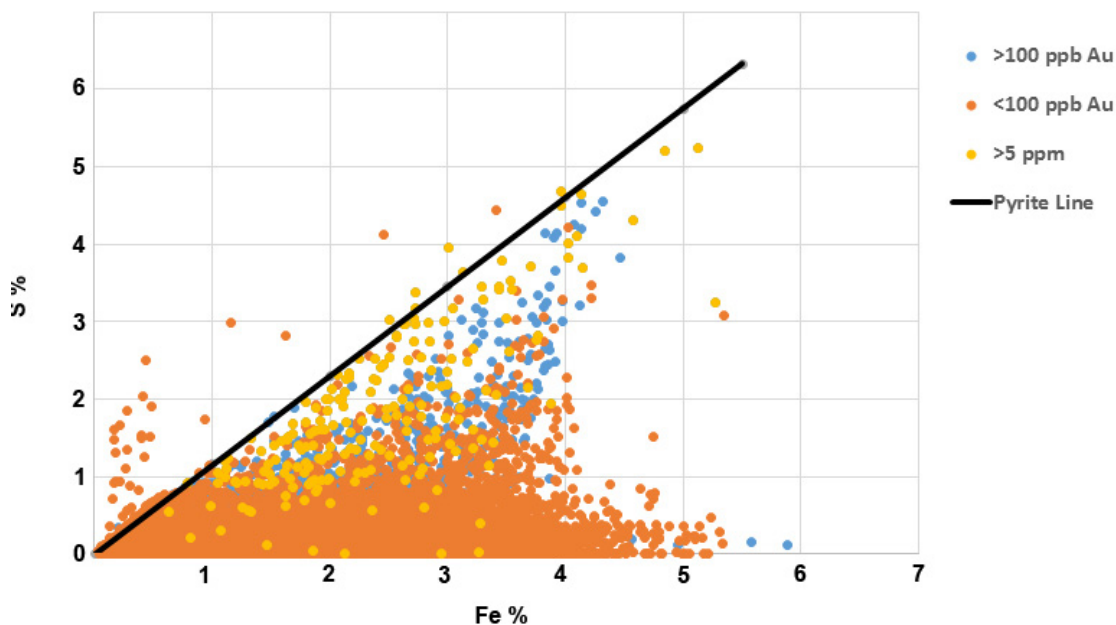


Figure 70. Sulfur versus iron data from drill hole intervals in area of SHGDs. The diagram strongly suggests sulfidation rather than pyritization occurred during ore formation. Values of iron in samples with <100 ppb Au range from 0-5.5%, while mineralized samples (>5 ppm Au) show a similar range of iron, but have higher sulfur concentrations.

The source of Au in CTGDs remains enigmatic and no significantly new insights are provided from this study. As previous hypotheses suggest, the gold at Kinsley Mountain was likely either sourced from a magma at depth or from or derived from the upper or middle crust by leaching or metamorphism (Muntean et al., 2011; Ilchik and Barton, 1997; Hofstra et al., 1999; Seedorff and Barton, 2004). Sulfur isotope data from this study suggest the sulfur was likely sourced from minerals or organic material in underlying Early Cambrian to Neoproterozoic sedimentary rocks. A favored hypothesis

then is one several authors have previously suggested, in which deep circulating meteoric waters interacting with reduced sediments would become silica- and sulfide-bearing and able to scavenge Au (Hofstra 1994, 1995; Illchik and Barton 1997; Hofstra et al., 1999). During mid-Tertiary extension hotter and more deeply buried rocks were brought to the surface, which increased the geothermal gradient allowing for the formation of a hydrothermal system. A hydrothermal fluid containing silica, sulfide, and Au would exploit fault zones as pathways, migrating to areas of low pressure where wall-rock interaction would create alteration of decarbonatization and silicification and deposit sulfur and gold.

As an alternative hypothesis, an underlying magma chamber that likely was the source for the stock, dikes, and volcanic flows may have developed a cupola zone from which a plume of gold-bearing magmatic-hydrothermal fluids was released, as hypothesized for CTGDs by Muntean et al. (2011). Such a batholith would have driven a convection cell of deeply circulating meteoric waters, which could dissolve diagenetic pyrite in the sedimentary rocks. Heat from the batholith may have also driven thermal dissolution of sedimentary pyrite or metamorphism of pyrite to pyrrhotite, which would release reduced sulfur, resulting in meteoric waters rich in reduced sulfide with heavy sulfur isotope values. The meteoric waters could mix with magmatic-hydrothermal waters, resulting in a heavy sulfur isotopic signature and increased gold solubility, allowing for transport of gold further away from the magmatic-hydrothermal plume. Multiple pulses from a magmatic-hydrothermal plume would allow for deposition of both base metals and gold-bearing arsenian-pyrite. Such pulses would lead to periods where magmatic-hydrothermal fluids were more dominant and periods where meteoric waters

were dominant. Overall, the influence of meteoric would increase outward from the area of the stock. The gold-rich, meteoric-dominant hydrothermal fluids would become increasingly acidic when cooling below 300 to 350 °C, due to disassociation of acid molecules. The acidic fluid would result in dissolution of ferroan dolomite and sulfidation of liberated iron to form gold-bearing arsenian-pyrite in the SHGDs at Kinsley.

## References

- Alvarez, A.A., and Noble, D.C., 1988, Sedimentary rock-hosted disseminated precious metal mineralization at Purísima Concepción, Yauricocha district, central Peru: *Economic Geology*, v. 83, p. 1368-1378.
- Anderson, J.L. and Smith, D.R. 1995, The effects of temperature and  $fO_2$  on the Al-in-hornblende barometer: *American Mineralogist* v. 80, p. 549-559
- Arehart, G.B., Eldridge, C.S., Chryssoulis, S.L. and Kesler, S.E., 1993, Ion microprobe determination of sulfur isotope variations in iron sulfides from the Post/Betze sediment-hosted disseminated gold deposit, Nevada, USA: *Geochimica et cosmochimica Acta* v. 57, p. 1505-1519.
- Arehart, G.B., Chakurian, A.M., Tretbar, D.R., Christensen, J.N., McInnes, B.A., and Donelick, R.A., 2003, Evaluation of radioisotope dating of Carlin-type deposits in the Great Basin, western North America, and implications for deposit genesis: *Economic Geology*, v. 98, p. 235–248.
- Arehart, G.B., DeYoung, S., Poulson, S.R., Heaton, J.S. and Weiss, S., 2013, Sulfur Isotopes in Plutonic Rocks of the Great Basin as Indicators of Crustal Architecture: *The Journal of Geology*, v. 121, p. 355-369.
- Armstrong, R.L., 1964, Geochronology and geology of the eastern Great Basin in Nevada and Utah: Ph.D. dissertation, Yale University, New Haven, CT, 241 p.
- Atkinson, W.W, Jr., Kaczmarowski, J.H., and Erickson, A.J., Jr., 1982, Geology of a skarn-breccia orebody at the Victoria Mine, Elko County, Nevada: *Economic Geology*, v. 77, p. 899–918.
- Barth, A.P. and Wooden, J.L., 2010, Coupled elemental and isotopic analyses of polygenetic zircons from granitic rocks by ion microprobe, with implications for melt evolution and the sources of granitic magmas: *Chemical Geology*, v. 277, p. 149-159.
- Barton, M.D., Seedorff, E., Ilchik, R.P., and Ghidotti, G., 1997, Contrasting siliceous replacement mineralization, east-central Nevada [extended abs.]: *Society of Economic Geologists Guidebook Series*, v.28, p. 131–134.
- Barton, M.D., Young, S., 2002, Non-pegmatitic deposits of beryllium: mineralogy, geology, phase equilibria and origin. *in* Grew, E.S. (Ed.), *Beryllium: Mineralogy, Petrology, and Geochemistry: Reviews in Mineralogy and Geochemistry*, v. 50, p. 591–691.
- Bryzgalin, O.V., 1975, On some possible forms of occurrence of tungsten in hydrothermal solutions: *Mineral. Geokhim.*, v. 'framovykh Mestrozhd., Tr. Vses. Soveshch., 3rd., p. 404-407.
- Buckley, C.P., 1967, Structure and stratigraphy of the Kinsley Mountains, Elko and White Pine Counties, Nevada: M.S. thesis, San Jose State University, San Jose, California, 50 p.
- Calvert, S.E., Thode, H.G., Yeung, D. and Karlin, R.E., 1996, A stable isotope study of pyrite formation in the Late Pleistocene and Holocene sediments of the Black Sea: *Geochimica et Cosmochimica Acta* v. 60, p. 1261-1270.
- Chang, Z., Large, R.R. and Maslennikov, V., 2008, Sulfur isotopes in sediment-hosted orogenic gold deposits: Evidence for an early timing and a seawater sulfur source: *Geology*, v. 36, p. 971-974.
- Clement, S. W. J., and Compston, W., 1994, Ion probe parameters for very high resolution without loss of sensitivity: *U.S. Geological Survey Circulation*, v. 1107, p. 62.

- Compston, W., Williams, I.S., Kirschvink, J.L., Zichao, Z. and Guogan, M.A., 1992, Zircon U-Pb ages for the Early Cambrian time-scale: *Journal of the Geological Society*, v. 149, p.171-184.
- Cook, H.E., 2015, The Evolution and Relationship of the Western North American Paleozoic Carbonate Platform and Basin Depositional Environments to Carlin-Type Gold Deposits in the Context of Carbonate Sequence Stratigraphy, *in* Pennell, W. M. and Garside, L. J., eds., *New Concepts and Discoveries: Geological Society of Nevada Symposium Proceedings*, Sparks, Nevada p. 1-80.
- De La Roche, H., Leterrier, P., Grandclaude, P. & Marchal, M., 1980, A classification of volcanic and plutonic rocks using the RI-R2 diagram and major element analyses - its relationships with current nomenclature: *Chemical Geology*, v. 29, p. 183-210.
- DeCelles, P.G., 2004, Late Jurassic to Eocene evolution of the Cordilleran thrust belt and foreland basin system, western USA: *American Journal of Science*, v. 304, p. 105-168.
- Detmers, J., Brüchert, V., Habicht, K.S. and Kuever, J., 2001, Diversity of sulfur isotope fractionations by sulfate-reducing prokaryotes: *Applied and Environmental Microbiology*, v. 67, p. 888-894.
- Dickinson W.R., 2002, The Basin and Range province as a composite extensional domain: *International Geology Review*, v. 44, p. 1–38.
- Dickinson, W.R., 2006, Geotectonic evolution of the Great Basin: *Geosphere*, v. 2, p. 353–368.
- Dilles, J.H., Kent, A.J., Wooden, J.L., Tosdal, R.M., Koleszar, A., Lee, R.G. and Farmer, L.P., 2015, Zircon compositional evidence for sulfur-degassing from ore-forming arc magmas: *Economic Geology*, v. 110, p. 241-251.
- Emsbo, P., Hofstra, A.H., Lauha, E.A., Griffin, G.L., and Hutchinson, R.W., 2003, Origin of high-grade gold ore, source of ore fluid components, and genesis of the Meikle and neighboring Carlin-type deposits, northern Carlin trend, Nevada: *Economic Geology*, v. 98, p. 1069–1105.
- Flanigan, B., Freeman, C., Newberry, R., McCoy, D., and Hart, C., 2000, Exploration models for mid and late Cretaceous intrusion-related gold deposits in Alaska and the Yukon Territory, Canada, *in* Cluer, J.K., Price, J.G., Struhsacker, E.M., Hardyman, R.F., and Morris, C.L., eds., *Geology and Ore Deposits 2000: The Great Basin and Beyond: Geological Society of Nevada Symposium Proceedings*, Sparks, Nevada, p. 591–614.
- Giesemann A., Jager H.J., Norman A.L., Krouse H.P. and Brand W.A., 1994, On-line sulfur-isotope determination using an elemental analyzer coupled to a mass spectrometer: *Analytical Chemistry*, v. 66, p. 2816-2819.
- Gleadow, A.J.W., Duddy, I.R., Green, P.F. and Lovering, J.F., 1986, Confined fission track lengths in apatite: a diagnostic tool for thermal history analysis: *Contributions to Mineralogy and Petrology*, v. 94, p. 405-415.
- Goldfarb, R.J., Ayuso, R., Miller, M.L., Ebert, S.W., Marsh, E.E., Petsel, S.A., Miller, L.D., Bradley, D., Johnson, C, McClelland, W., 2004, The Late Cretaceous Donlin Creek deposit, southwestern Alaska—controls on epizonal formation: *Economic Geology*, v. 99, p. 643–671.
- Grassineau N.V., Matthey D.P. and Lowry D., 2001, Sulfur Isotope Analysis of Sulfide and Sulfate minerals by Continuous Flow-Isotope Ratio Mass Spectrometry: *Analytical Chemistry*, v. 73, p. 220-225.

- Green, P.F., Duddy, I.R., Laslett, G.M., Hegarty, K.A., Gleadow, A.J.W. and Lovering, J.F., 1989, Thermal annealing of fission tracks in apatite 4. Quantitative modelling techniques and extension to geological timescales. *Chemical Geology: Isotope Geoscience Section*, v. 79, p.155-182.
- Gustin, M.M., Smith, M.T., and Samuelson, K., 2012, Technical report on the Kinsley Project, Elko County, Nevada, U.S.A.: NI43-101 technical report prepared for Pilot Gold USA Inc., 124 p.
- Hammarstrom, J.M., and Zen, E. A. 1986, Aluminum in hornblende: An empirical igneous geobarometer: *American Mineralogist*, v. 71, p. 1297-1313.
- Hanchar, J.M. and Miller, C.F., 1993, Zircon zonation patterns as revealed by cathodoluminescence and backscattered electron images: implications for interpretation of complex crustal histories: *Chemical Geology*, v. 110, p. 1-13.
- Hannink, R., Smith, M., Shabestari, P. Raabe, K., Spaulding, V., and Hill, T., 2015, The discovery and geology of the western Flank Zone at the Kinsley Mountain Project, Elko County, Nevada: *in* Pennell, W. M. and Garside, L. J., eds., *New Concepts and Discoveries: Geological Society of Nevada Symposium Proceedings*, Sparks, Nevada, p. 295-312.
- Henry, C.D., and Ressel, M.W., 2000, Eocene magmatism—the smoking gun for Carlin-type gold deposits: *Geology and Ore Deposits 2000: The Great Basin and Beyond: Geological Society of Nevada Symposium Proceedings*, Sparks, Nevada, p. 365–388.
- Hill, J.M., 1916, Notes on some mining districts in eastern Nevada; U.S. Geological Survey Bulletin v. 648, p. 88-95.
- Hofstra, A. H., 1997, Isotopic composition of sulfur in Carlin-type gold deposits: Implications for genetic models, *in* Vikre, P., Thompson, T.B., Bettles, K., Christensen, O., and Parratt, R., eds., *Carlin-Type Gold Deposits Field Conference: Society of Economic Geologists Guidebook Series*, v. 28, p. 119-129.
- Hofstra, A.H., Snee, L.W., Rye, R.O., Folger, H.W., Phinisey, J.D., Loranger, R.J., Dahl, A.R., Naeser, C.W., Stein, H.J., and Lewchuk, M., 1999, Age constraints on Jerritt Canyon and other Carlin-type gold deposits in the western United States—relationship to Mid-Tertiary extension and magmatism: *Economic Geology*, v. 94, p. 769–802.
- Hofstra, A.H., and Cline, J.S., 2000, Characteristics and models for Carlin-type gold deposits: *Reviews in Economic Geology*, v. 13, p. 163–220.
- Holland, T., and Blundy, J., 1994, Non-ideal interactions in calcic amphiboles and their bearing on amphibole-plagioclase thermometry: *Contributions to Mineralogy and Petrology*, v. 116, p. 433-447.
- Hollister, L.S., Grissom, G.e., Peters, E.K., Stowell, H.H., and Sisson, V.R 1987, Confirmation of the empirical correlation of Al in hornblende with pressure of solidification of calc-alkaline plutons: *American Mineralogist*, v. 72, p. 231-239.
- Ilchik, R.P., and Barton, M.D., 1997, An amagmatic origin of Carlin-type gold deposits: *Economic Geology*, v. 92, p. 269–288.
- Ireland, T. R., and Williams, I. S., 2003, Considerations in zircon geochronology by SIMS, *in* Hanchar, J., and Hoskin, P., editors, *Zircon: Reviews in Mineralogy and Geochemistry*, v. 53, p. 215–241.

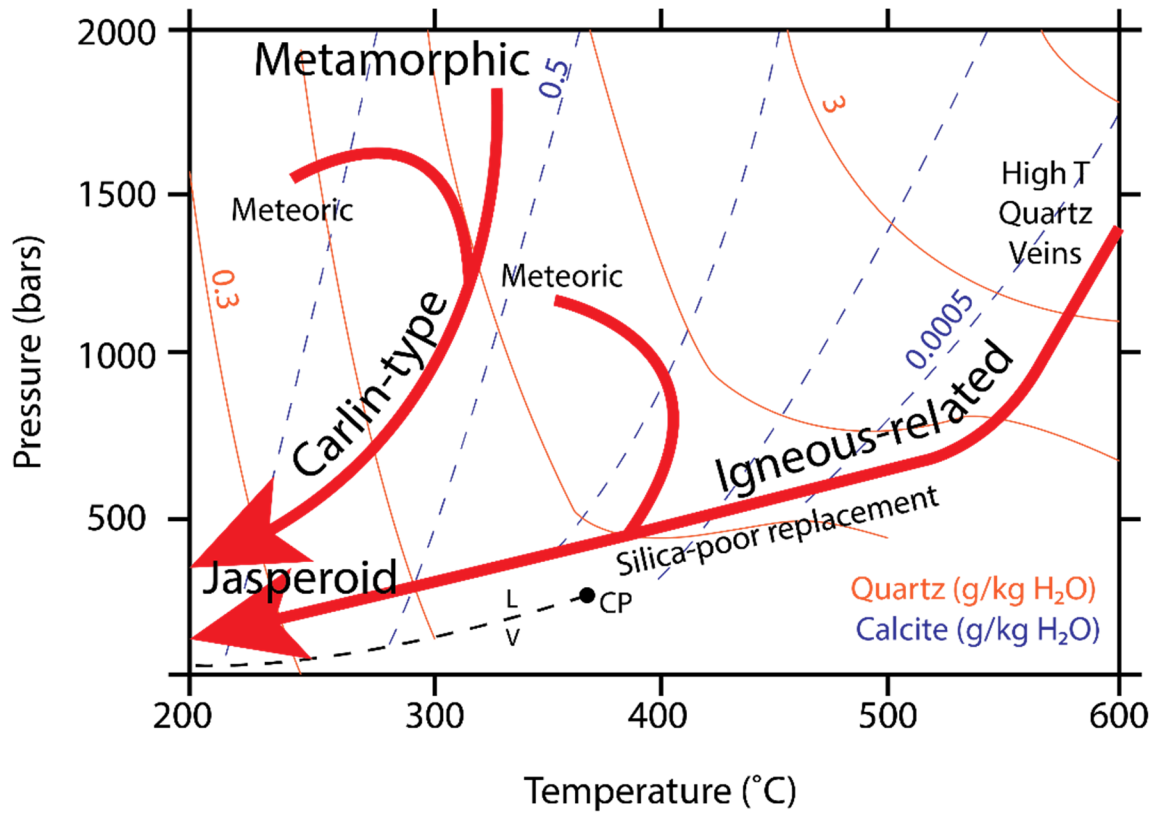
- Johnson, C.L., 2015, Petrology and geochemistry of the Emigrant Pass Volcanics, Nevada: Implications for a magmatic-hydrothermal origin of the Carlin gold deposits: M.S. Thesis, Oregon State University, Corvallis, OR, 119 p.
- Johnson, M.E., and Rutherford, M.J. 1989, Experimental calibration of the aluminum-in-hornblende geobarometer with application to Long Valley caldera (California): *Geology*, v. 17, p. 837-841.
- Johnston, M.K., and Ressel, M.W., 2004, Carlin-type and distal disseminated Au-Ag deposits: Related distal expressions of Eocene intrusive centers in north-central Nevada in *Controversies on the origin of World-class gold deposits, Part 1: Carlin-type gold deposits in Nevada*, by Muntean, J.L., Cline, J., Johnston, M.K., Ressel, M.W., Seedorff, E., and Barton, M.D.: *Society of Economic Geologists Newsletter*, v. 59, p. 12-14.
- Kesler, S.E., Riciputi, L.C. and Ye, Z., 2005, Evidence for a magmatic origin for Carlin-type gold deposits: isotopic composition of sulfur in the Betze-Post-Screamer Deposit, Nevada, USA: *Mineralium Deposita*, v. 40, p. 127-136.
- Kiyosu Y., 1980, Chemical reduction and sulfur isotope effects of sulfate by organic matter under hydrothermal conditions: *Chemical Geology* v. 30, p. 47-56.
- LaPointe, D.D., Tingley, J.V., and Jones, R.B, 1991, Mineral Resources of Elko County, Nevada: Nevada Bureau of Mines and Geology, Bulletin v. 106, 236 p.
- Large, R. R., Gemmoll, J. B., Paulick, H., 2001, The alteration box plot, a simple approach to understanding the relationship between alteration mineralogy and litho-geochemistry associated with volcanic hosted massive sulphides deposits: *Economic Geology*, v. 96, p. 957-971.
- Laslett, G.M., Green, P.F., Duddy, I.R. and Gleadow, A.J.W., 1987, Thermal annealing of fission tracks in apatite 2. A quantitative analysis. *Chemical Geology: Isotope Geoscience Section*, v. 65, p. 1-13.
- Le Maitre, R. W., Bateman, P., Dudek, A., Keller, J., Lameyre, J., Le Bas, M., Sabine, P., Schmid, R., Sorensen, H., Streckeisen, A. and Woolley, A., 1989, *A Classification of Igneous rocks and Glossary of Term: Recommendations of the International Union of Geological Sciences Subcommission on the Systematics of Igneous Rocks*. Blackwell Scientific Publications, Oxford
- Long, S.P., Henry, C.D., Muntean, J.L., Edmondo, G.P. and Cassel, E.J., 2014, Early Cretaceous construction of a structural culmination, Eureka, Nevada, USA: Implications for out-of-sequence deformation in the Sevier hinterland: *Geosphere*, v. 10, p. 564-584.
- Long, S.P., 2015, An upper-crustal fold province in the hinterland of the Sevier orogenic belt, eastern Nevada, USA: A Cordilleran Valley and Ridge in the Basin and Range: *Geosphere*, p. 404-424.
- Ludwig, K. R., 2001, *Squid, A user's manual*: Berkeley Geochronology Center Special Publication No. 2.
- Ludwig, K.R., 2003, *Isoplot 3.00, a geochronological toolkit for Excel*: Berkeley Geochronology Center Special Publication No. 4.
- Lush, A.P., McGrew, A.J., Snoke, A.W., and Wright, J.E., 1988, Allochthonous Archean basement in the northern East Humboldt Range, Nevada: *Geology*, v. 16, p. 349-353.
- Machel, H.G., Krouse, H.R. and Sassen, R., 1995, Products and distinguishing criteria of bacterial and thermochemical sulfate reduction: *Applied geochemistry*, v. 10, p. 373-389.

- Machel, H.G., 2001, Bacterial and thermochemical sulfate reduction in diagenetic settings—old and new insights: *Sedimentary Geology*, v. 140, p. 143-175.
- Maldonado, F., Spengler, R.W., Hanna, W.F., and Dixon, G.L., 1988, Index of granitic masses in the state of Nevada: U.S. Geological Survey Bulletin 1831, 81 p.
- Markey, R., Stein, H. and Morgan, J., 1998, Highly precise Re–Os dating for molybdenite using alkaline fusion and NTIMS: *Talanta*, v. 45, p. 935-946.
- Markey, R., Stein, H.J., Hannah, J.L., Zimmerman, A., Selby, D. and Creaser, R.A., 2007, Standardizing Re–Os geochronology: a new molybdenite reference material (Henderson, USA) and the stoichiometry of Os salts: *Chemical Geology*, v. 244, p. 74-87.
- McDougall, I. and Harrison, T.M., 1999, *Geochronology and Thermochronology by the  $^{40}\text{Ar}/^{39}\text{Ar}$  Method*: Oxford University Press.
- McKee, E. H., and Marvin, R. F., 1976, Summary of radiometric ages of Tertiary volcanic and selected plutonic rocks in Nevada, Part 5: Northeastern Nevada: *Isochron/West*, v. 16, p. 15-27.
- Middlemost, E.A.K., 1994, Naming materials in the magma/igneous rock system: *Earth-Science. Reviews*. V. 37, p. 215–224.
- Miller, D.M., and Hoisch, T.D., 1995, Jurassic tectonics of northeastern Nevada and northwestern Utah from the perspective of barometric studies, *in* Miller, D.M., and Busby, C., editors, *Jurassic magmatism and tectonics of the North American Cordillera*: Geological Society of America Special Paper v. 299, p. 267–294.
- Monroe, S.C., 1990, Kinsley Mountain project, Elko County, Nevada, *in* Shaddrick, D.R., Kizis, J.A., and Hunsaker, E.L., editors, *Geology and Ore Deposits of the Northeastern Great Basin, Field Guide for Field Trip No 5: Great Basin Symposium*, Geological Society of Nevada, p. 170-183.
- Muntean, J.L., Cline, J.S., Simon, A.C., and Longo, A.A., 2011, Magmatic hydrothermal origin of Nevada's Carlin-type gold deposits: *Nature Geoscience*, v. 4, p. 122–127.
- Nakamura, N., 1974, Determination of REE, Ba, Fe, Mg, Na and K in carbonaceous and ordinary chondrites: *Geochimica et Cosmochimica Acta*. v. 38, p. 757–775.
- Nelson, S.T., Hart, G.L. and Frost, C.D., 2011, A reassessment of Mojavia and a new Cheyenne Belt alignment in the eastern Great Basin: *Geosphere*, v. 7, p. 513-527.
- Newberry, R.J. and Einaudi, M.T., 1981, Tectonic and geochemical setting of tungsten skarn mineralization in the Cordillera, *in* *Relations of Tectonics to Ore Deposits in the Southern Cordillera*: Arizona Geological Society Digest, v.14, p. 99-112.
- Newberry, R.J. and Swanson, S.E., 1986, Scheelite skarn granitoids: an evaluation of the roles of magmatic source and process: *Ore Geology Reviews*, v. 1, p. 57-81.
- Newton, M.N., 2015, *Characterization of Gold and Related Mineralization at the North Bullion Carlin System, Railroad Project, a Nevada Carlin-Type Gold Prospect*: M.S. thesis, University of Nevada – Las Vegas, Las Vegas, NV 339 p.
- Nolan, T.B., Merriam, C.W., and Williams, J.S., 1956, The stratigraphic section in the vicinity of Eureka, Nevada: U.S. Geological Survey Professional Paper v. 276, 77 p.

- Ohmoto, H. and Rye, R., 1979, Isotopes of sulfur and carbon: Geochemistry of Hydrothermal Ore Deposits p. 509-567.
- Orr W. L. 1974, Changes in sulfur content and isotopic ratios of sulfur during petroleum maturation -study of Big Horn Basin Paleozoic oils: American Association Petroleum Geologists Bulletin v. 58, p. 2295-2318.
- Perry, K., 2010, Detrital zircon geochronology for Neoproterozoic to Cambrian sediment sources of the Deep Creek Range and the Pilot Range in the Southwestern United States: Senior Project, California Polytechnic State University, San Luis Obispo, CA. 40 p.
- Premo, W.R., Castiñeiras, P. and Wooden, J.L., 2008, SHRIMP-RG U-Pb isotopic systematics of zircon from the Angel Lake orthogneiss, East Humboldt Range, Nevada: Is this really Archean crust?: Geosphere, v. 4, p. 963-975.
- Purdy, J. and Jäger, E. 1976, K-Ar ages on rock-forming minerals from the Central Alps: University of Padova Institute of Geology and Mineralogy Memoir v. 30. 31 p.
- Reid, R. F., Nicholes, J., Kofoed, R., McComb, M., and Sechrist, K. J., 2010, Buffalo Valley gold mine: Porphyry copper, gold skarn or distal disseminated precious-metal deposit, *in* Steininger, R. C., and Pennell, W. M., eds., Great Basin evolution and metallogeny: Geological Society of Nevada Symposium Proceedings, Sparks, Nevada, p. 637-656.
- Rhys, D., Valli, F., Burgess, R., Heitt, D., Greisel, G. and Hart, K., 2015, Controls of fault and fold geometry on the distribution of gold mineralization on the Carlin trend, *in* Pennell, W. M. and Garside, L. J., eds., New Concepts and Discoveries: Geological Society of Nevada Symposium Proceedings, Sparks, Nevada, p. 333-389.
- Robinson, J. P., 2005, The Kinsley Mine—a structure-controlled sediment-hosted disseminated gold deposit in eastern Nevada, *in* Rhoden, H. N., Steininger, R. C., and Vikre, P. G., eds, Geological Society of Nevada Symposium Proceedings: Window to the World, Sparks, Nevada, p. 469–481.
- Sayyah, T. A., 1965, Geochronological studies of the Kinsley Stock, Nevada, and the Raft River Range, Utah: unpublished Ph.D. dissertation, University of Utah, Salt Lake City, UT, 99 p.
- Schmidt, M.W., 1992, Amphibole composition in tonalite as a function of pressure: An experimental calibration of the Al-in-hornblende barometer: Contributions to Mineralogy and Petrology, v. 110, p. 304-310.
- Seal, R.R., 2006, Sulfur isotope geochemistry of sulfide minerals, *in* Vaughan, D. J. (ed.) Sulfide Mineralogy and Geochemistry: Reviews in Mineralogy and Geochemistry, Geochemical Society and Mineralogy Society of America, Washington, DC, v. 61, p. 633-677.
- Seedorff, E., 1990, Magmatism, extension, and ore deposits of Eocene to Holocene age in the Great Basin—Mutual effects and preliminary proposed genetic relationships, *in* Raines. G.L., Lisle. RE., Schafer. R.W., and Wilkinson. W.H., eds., Geology and ore deposits of the Great Basin: Geological Society of Nevada Symposium Proceedings, Sparks, Nevada, p. 133–178.
- Selby, D. and Creaser, R.A., 2004, Macroscale NTIMS and microscale LA-MC-ICP-MS Re-Os isotopic analysis of molybdenite: Testing spatial restrictions for reliable Re-Os age determinations, and implications for the decoupling of Re and Os within molybdenite: Geochimica et Cosmochimica Acta, v. 68, p. 3897-3908.

- Shirey, S.B. and Walker, R.J., 1998, The Re-Os isotope system in cosmochemistry and high-temperature geochemistry: *Annual Review of Earth and Planetary Sciences*, v. 26, p. 423-500.
- Silberling, N.J. and Nichols, K.M., 2002, Structural evolution of the White Horse pass area: Nevada Bureau of Mines and Geology Map, v. 132
- Sillitoe, R.H., and Bonham, H. F., Jr., 1990, Sediment-hosted gold deposits: Distal products of magmatic-hydrothermal systems: *Geology*, v. 18, p. 157–161.
- Stein, H.J., Markey, R.J., Morgan, J.W., Hannah, J.L. and Scherstén, A., 2001, The remarkable Re–Os chronometer in molybdenite: how and why it works: *Terra Nova*, v. 13, p. 479-486.
- Steininger, R., 1966, Geology of the Kinsley mining district, Elko County, Nevada: Brigham Young University Geology Studies, v. 13, p. 69–88.
- Strickland, A., Miller, E.L., Wooden, J., Kozdon, R., and Valley, J.W., 2011, Syn-extensional plutonism and peak metamorphism in the Albion–Raft River–Grouse Creek metamorphic core complex: *American Journal of Science*, v. 311, p. 261–314.
- Su, W., Heinrich, C.A., Pettke, T., Zhang, X., Hu, R., and Xia, B., 2009, Sediment-hosted gold deposits in Guizhou, China: Products of wall-rock sulfidation by deep crustal fluids: *Economic Geology*, v. 104, p. 73–93.
- Thompson, J.F.H., Gale, V.G., Tosdal, R.M., and Wright, W.A., 2004, Characteristics and formation of the Jerónimo carbonate-replacement gold deposit, Potrerillos district, Chile: *Society of Economic Geologists Special Publication 11*, p. 75–95.
- Thorman, C.H., and Peterson, F., 2004, The Middle Jurassic Elko orogeny – A major tectonic event in Nevada-Utah: Search and Discovery Article #30022. Adapted from “extended abstract” for AAPG Annual Meeting, Salt Lake City, Utah, 7 p.
- Utevsky, E. S., 2014, Zircon Geochronology and Geochemistry of Plutonic Rocks of the Western Cascades, Washington and Oregon: Geological Society of America Annual Meeting, Abstracts with Programs, Vancouver, British Columbia.
- Vikre, P.G., Poulson, S.R. and Koenig, A.E., 2011, Derivation of S and Pb in Phanerozoic intrusion-related metal deposits from Neoproterozoic sedimentary pyrite, Great Basin, United States: *Economic Geology*, v. 106, p. 883-912.
- Williams, I. S., 1997, U-Th-Pb geochronology by ion microprobe: not just ages but histories: *Society of Economic Geologists Reviews in Economic Geology*, v. 7, p. 1–35.
- Wooden, J. L., Mazdab, F. K., and Barth, A. P., 2007, Hafnium and temperature (from titanium) variations in zircons: a potential new tool to evaluate petrologic processes in magmas: *Geological Society of America, Abstracts with Programs*, v. 39, p. 406.
- Zamudio, J. A., and W. W. Atkinson Jr., 1995, Mesozoic structures of the Dolly Varden Mountains and Currie Hills, Elko County, Nevada: *in* *Jurassic Magmatism and Tectonics of the North American Cordillera*, edited by D. M. Miller, and C. Busby, Boulder, Colorado, Special Paper Geological Society of America, v. 299. p. 295-311.
- Zippi, P., 2014, Palynology, Conodont, Radiolaria analysis of klippe samples from the Kinsley Mountains, southern Elko County, Nevada: Unpublished report for Pilot Gold, 6 p.

### Appendix A: Quartz and calcite solubility diagram



Quartz and calcite solubility across pressure and temperature ranges. Modified from Barton et al., (1997).

### Appendix B: Microprobe analyses of hornblende

Sample no.	KJM034_1	KJM034_2	KJM034_3	KJM034_4	KJM034_5	KJM034_6	KJM036_1	KJM036_2	KJM036_3
No. of analyses	9	4	5	6	6	5	5	6	6
SiO <sub>2</sub>	49.03	47.96	46.77	48.68	47.92	48.17	48.69	47.81	48.96
TiO <sub>2</sub>	0.68	0.79	0.84	0.70	0.86	0.82	0.58	0.72	0.69
Al <sub>2</sub> O <sub>3</sub>	5.43	6.06	6.92	5.71	6.24	6.28	5.76	5.54	5.53
FeO*	14.94	15.24	15.42	15.03	15.31	15.46	15.42	14.88	14.75
MgO	13.20	12.77	11.90	12.88	12.67	12.70	12.97	13.01	13.20
MnO	0.65	0.61	0.54	0.62	0.61	0.61	0.47	0.59	0.59
CaO	11.34	11.32	11.14	11.34	11.40	11.25	11.52	11.57	11.47
Na <sub>2</sub> O	0.99	1.13	1.03	0.96	1.07	1.07	0.93	0.94	0.88
K <sub>2</sub> O	0.49	0.60	0.71	0.55	0.60	0.63	0.53	0.53	0.52
F	0.00	0.10	0.00	0.00	0.00	0.00	0.00	0.00	0.00
Cl	0.08	0.07	0.10	0.07	0.09	0.10	0.11	0.15	0.14
g(H <sub>2</sub> O)	2.00	1.94	1.95	1.99	1.98	1.99	1.99	1.95	1.98
Subtotal	98.72	98.44	97.54	98.84	98.76	98.82	98.85	97.84	98.65
O=F or Cl	0.02	0.06	0.02	0.02	0.02	0.02	0.02	0.03	0.03
Total	98.74	98.50	97.58	98.85	98.70	98.85	98.88	97.87	98.68
Number of moles based on 13 T + O									
Si(T)	7.22	7.11	7.04	7.20	7.09	7.10	7.17	7.14	7.22
Al(T)	0.78	0.89	0.96	0.80	0.91	0.90	0.83	0.86	0.78
Sum T	8.00	8.00	8.00	8.00	8.00	8.00	8.00	8.00	8.00
Al(M)	0.16	0.17	0.27	0.20	0.18	0.20	0.18	0.12	0.18
Mg(M)	2.90	2.82	2.67	2.84	2.79	2.79	2.85	2.90	2.90
Fe(M)	1.78	1.85	1.90	1.81	1.86	1.85	1.86	1.83	1.77
Mn(M)	0.08	0.08	0.07	0.08	0.08	0.08	0.06	0.07	0.07
Ti(M)	0.08	0.09	0.10	0.08	0.10	0.09	0.06	0.08	0.08
Sum M(123)	5.00	5.00	5.00	5.00	5.00	5.00	5.00	5.00	5.00
Na(8)	0.15	0.16	0.16	0.15	0.15	0.16	0.14	0.12	0.13
Ca(8)	1.79	1.80	1.80	1.80	1.81	1.78	1.82	1.85	1.81
Na(A)	0.13	0.16	0.14	0.12	0.15	0.15	0.13	0.15	0.12
K(A)	0.09	0.11	0.14	0.10	0.11	0.12	0.10	0.10	0.10
Sum A	0.22	0.28	0.28	0.23	0.27	0.27	0.23	0.25	0.22
OH	1.98	1.94	1.98	1.98	1.98	1.98	1.97	1.96	1.97
Al (total)	0.94	1.06	1.23	1.00	1.09	1.10	1.00	0.98	0.96
Pressure (kb) <sup>1</sup>	1.6	1.9	2.1	1.7	2.3	2.2	1.8	1.8	1.7
Depth (km)	4.5	5.2	5.9	4.8	6.4	6.2	5.0	4.9	4.7
Temperature (°C) <sup>2</sup>	640	694	674	674	649	653	589	645	638
Percent Ab <sup>3</sup>	0.78	0.69	0.67	0.69	0.78	0.74	0.80	0.79	0.74

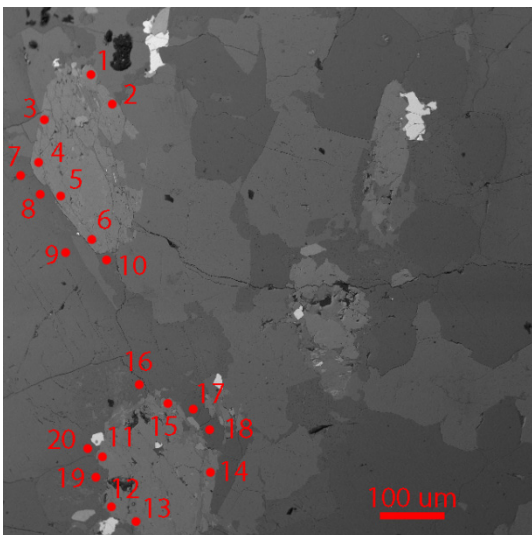
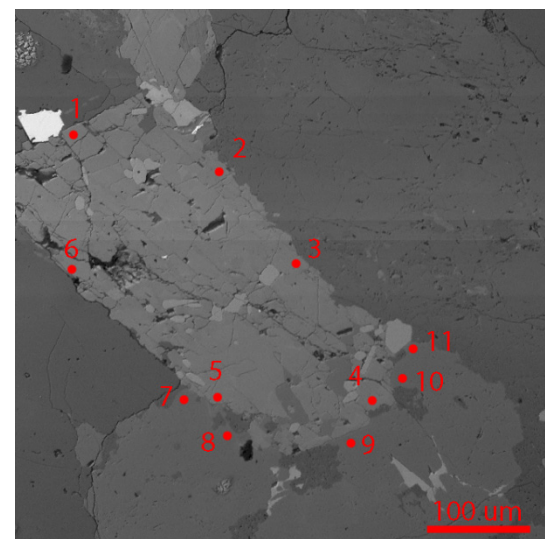
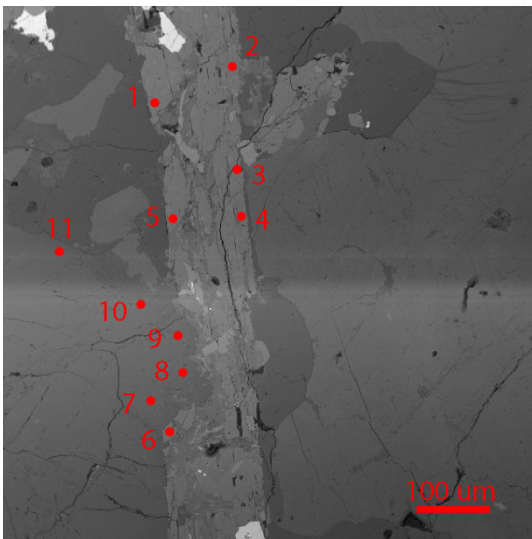
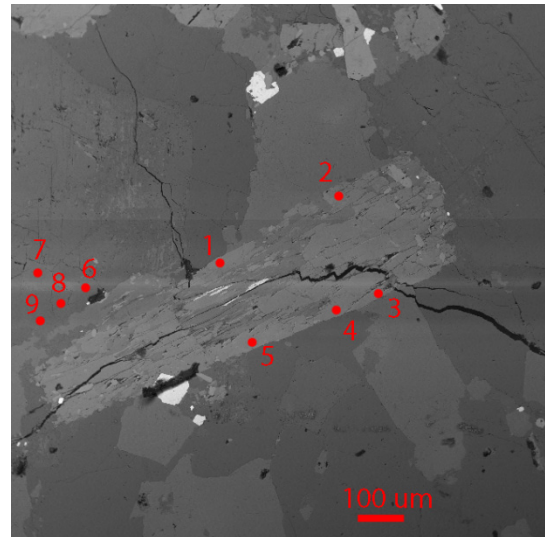
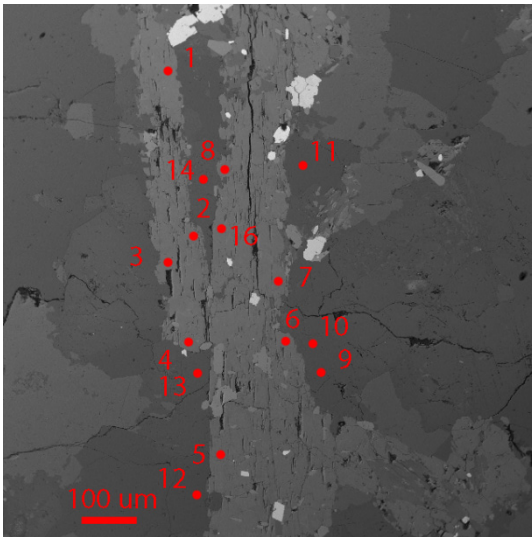
Sample no.	KJM036_4	KJM036_5	RTH085_1	RTH085_2	RTH085_3	RTH085_4	RTH085_5	RTH085_6
No. of analyses	5	6	6	6	7	4	5	7
SiO <sub>2</sub>	48.99	48.28	46.12	47.82	47.97	47.85	46.65	46.32
TiO <sub>2</sub>	0.72	0.80	1.02	0.81	0.81	0.81	0.90	1.01
Al <sub>2</sub> O <sub>3</sub>	5.45	6.04	7.30	6.29	6.08	6.49	7.24	7.56
FeO*	14.95	14.75	15.61	15.13	14.85	15.27	15.64	15.97
MgO	13.31	13.08	12.19	12.69	12.95	12.55	12.05	11.90
MnO	0.54	0.60	0.50	0.51	0.50	0.51	0.59	0.51
CaO	11.46	11.35	11.45	11.45	11.56	11.44	11.26	11.22
Na <sub>2</sub> O	0.94	0.94	1.24	1.08	0.93	1.04	1.18	1.20
K <sub>2</sub> O	0.53	0.57	0.76	0.63	0.60	0.62	0.74	0.79
F	0.00	0.00	0.00	0.00	0.00	0.00	0.00	0.00
Cl	0.09	0.13	0.13	0.17	0.17	0.17	0.10	0.13
g(H <sub>2</sub> O)	2.00	1.98	1.95	1.96	1.96	1.96	1.97	1.96
Subtotal	98.87	98.45	98.17	98.53	98.24	98.51	98.32	98.47
O=F or Cl	0.02	0.03	0.03	0.04	0.04	0.04	0.02	0.03
Total	98.89	98.48	98.20	98.57	98.28	98.54	98.34	98.50
Number of moles based on 13 T + O								
Si(T)	7.21	7.14	6.89	7.09	7.11	7.09	6.96	6.90
Al(T)	0.79	0.86	1.11	0.91	0.89	0.91	1.04	1.10
Sum T	8.00	8.00	8.00	8.00	8.00	8.00	8.00	8.00
Al(M)	0.15	0.19	0.18	0.19	0.18	0.22	0.23	0.23
Mg(M)	2.92	2.88	2.72	2.81	2.86	2.77	2.68	2.64
Fe(M)	1.79	1.76	1.93	1.85	1.81	1.86	1.92	1.95
Mn(M)	0.07	0.08	0.06	0.06	0.06	0.06	0.08	0.06
Ti(M)	0.08	0.09	0.11	0.09	0.09	0.09	0.10	0.11
Sum M(123)	5.00	5.00	5.00	5.00	5.00	5.00	5.00	5.00
Na(S)	0.14	0.14	0.14	0.15	0.13	0.15	0.17	0.17
Ca(S)	1.81	1.80	1.83	1.82	1.84	1.82	1.80	1.79
Na(A)	0.13	0.13	0.22	0.16	0.14	0.15	0.17	0.18
K(A)	0.10	0.11	0.15	0.12	0.11	0.12	0.14	0.15
Sum A	0.23	0.24	0.36	0.28	0.26	0.27	0.31	0.33
OH	1.98	1.97	1.97	1.96	1.96	1.96	1.98	1.97
Al (total)	0.94	1.05	1.29	1.10	1.07	1.14	1.27	1.33
Pressure (kb) <sup>1</sup>	1.6	2.1	2.9	2.4	2.2	2.4	3.1	3.3
Depth (km)	4.4	5.9	8.0	6.6	6.0	6.8	8.8	9.2
Temperature (°C) <sup>2</sup>	648	647	702	640	643	643	664	678
Percent Ab <sup>3</sup>	0.76	0.75	0.70	0.79	0.75	0.75	0.75	0.75

<sup>1</sup>Pressure calculated using method of Anderson and Smith (1995)

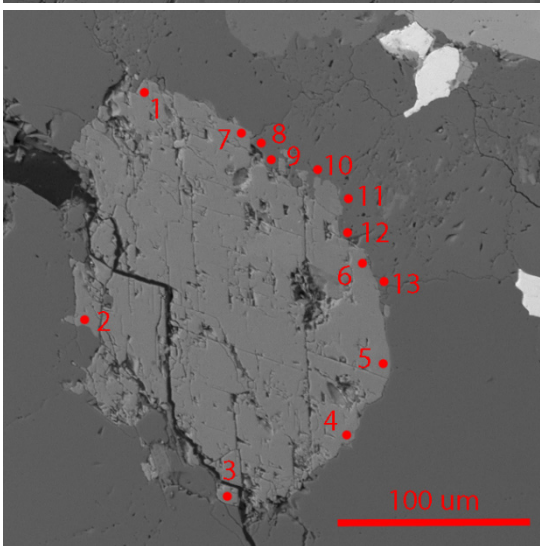
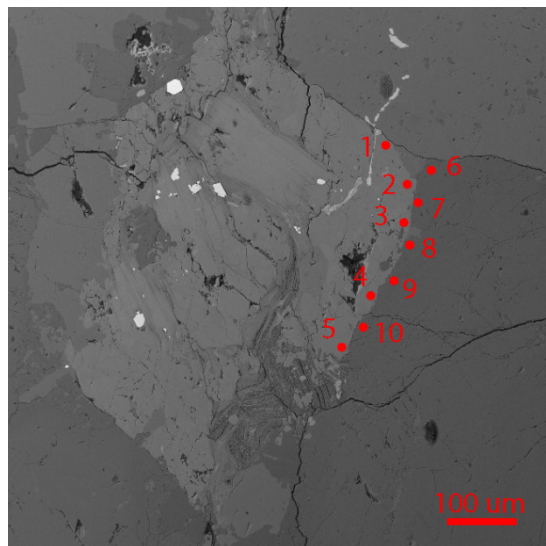
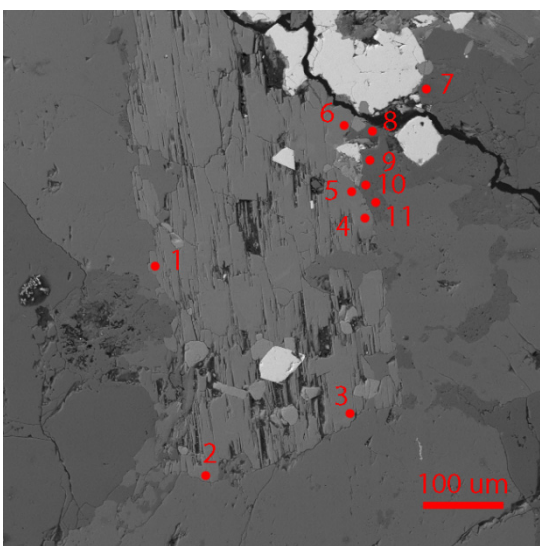
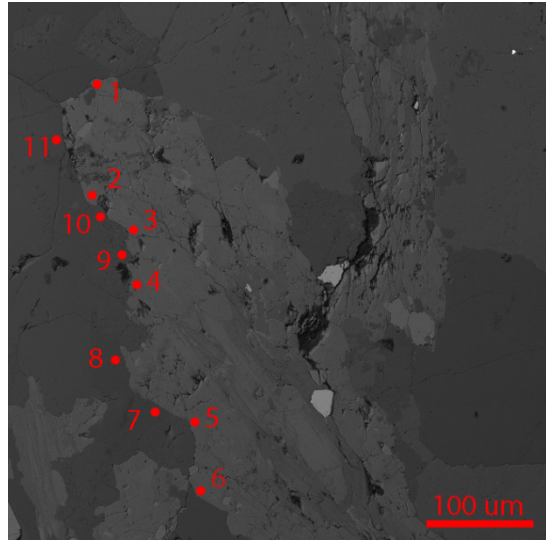
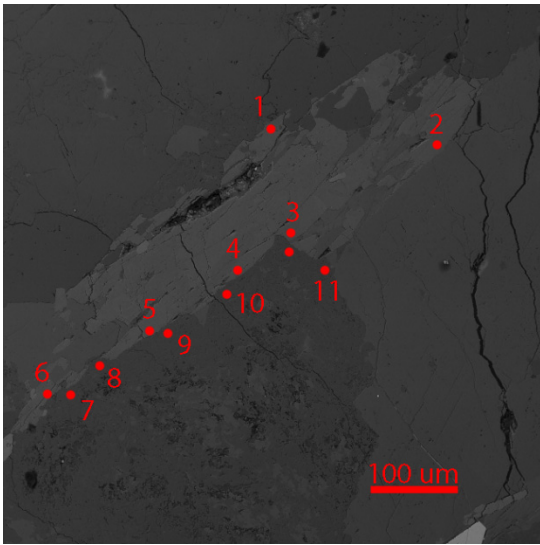
<sup>2</sup>Temperature (40C) calculated using method of Holland and Blundy (1994)

<sup>3</sup>Mole percent albite (Ab) from electron microprobe analyses for Holland and Blundy estimate

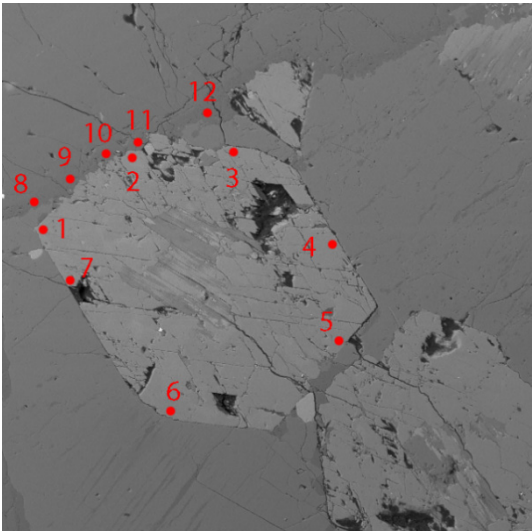
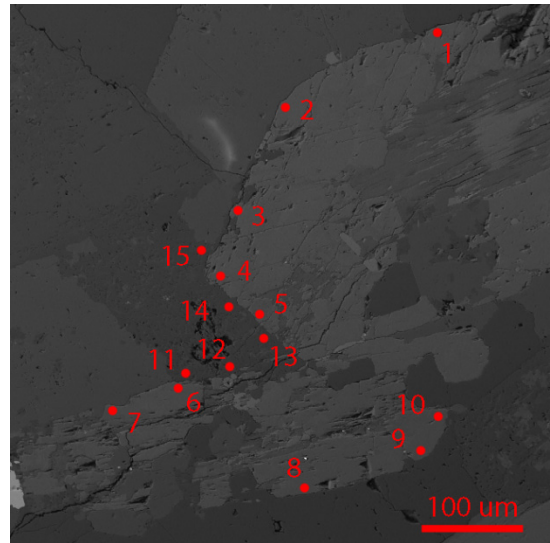
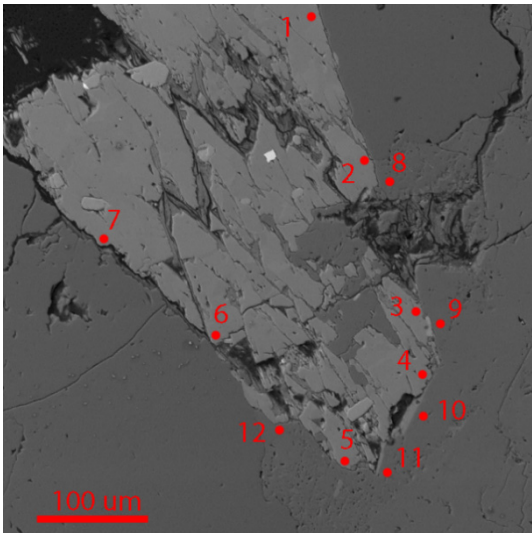
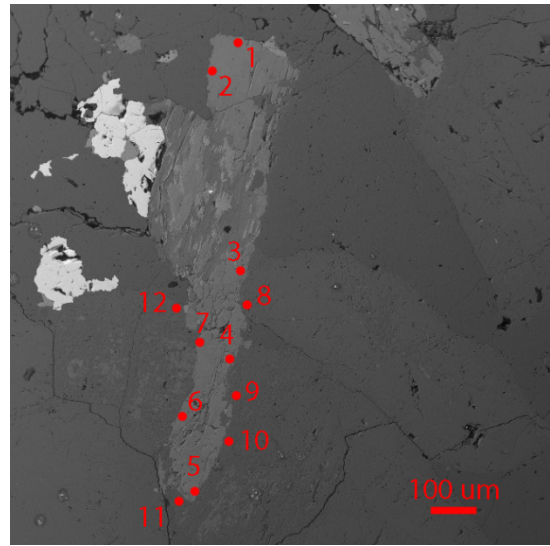
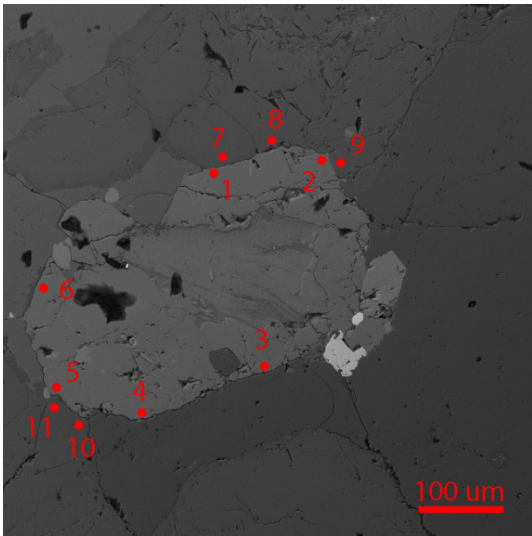
## KJM034 Spots



### KJM034 Spots



### RTH085 Spots



## Appendix C: Whole-rock Geochemistry

	Sample ID	KJM020 Dacite Breccia	KJM033 Diorite Dike	KJM034 Stock	KJM035 Granodiorite Porphyry	RTH002 Granodiorite Porphyry	RTH004 Granite Porphyry	RTH14 Granite Porphyry	RTH24 Rhyolite Breccia	RTH29 Diorite Dike	RTH56 Granodiorite Porphyry	RTH57 Granite Porphyry
Method												
ME-XRF26	Al <sub>2</sub> O <sub>3</sub>	14.9	14.95	15.3	15.65	15	13.7	14.05	12.3	14.55	15.15	14.15
ME-XRF26	BaO	0.16	0.16	0.15	0.15	0.16	0.12	0.12	0.09	0.16	0.18	0.04
ME-XRF26	CaO	2.1	4.99	3.41	4.74	1.82	0.13	0.18	1.96	2.69	3.29	0.33
ME-XRF26	Cr <sub>2</sub> O <sub>3</sub>	<0.01	0.02	0.01	0.01	0.01	<0.01	<0.01	<0.01	0.01	<0.01	0.01
ME-XRF26	Fe <sub>2</sub> O <sub>3</sub>	3.53	6.87	3.84	5.82	2.08	0.73	1.06	2.24	3.3	1.36	1.01
ME-XRF26	K <sub>2</sub> O	5.38	3.47	3.86	3.57	5.28	10.1	6.45	8.25	5.98	7.26	2.4
ME-XRF26	MgO	0.58	3.85	1.56	2.92	1.2	0.14	0.48	0.45	2.2	1.16	0.57
ME-XRF26	MnO	0.07	0.13	0.06	0.06	0.01	<0.01	<0.01	0.05	0.03	0.02	<0.01
ME-XRF26	Na <sub>2</sub> O	3.07	3.04	3.34	3.27	3.08	0.63	0.23	1.2	2.83	2.31	0.05
ME-XRF26	P <sub>2</sub> O <sub>5</sub>	0.15	0.26	0.2	0.26	0.14	0.05	0.05	0.07	0.21	0.17	0.05
ME-XRF26	SiO <sub>2</sub>	66.9	60	66.6	61.6	68.5	73.3	75	70.9	66.2	67.5	77
ME-XRF26	SrO	0.06	0.06	0.07	0.07	0.06	0.02	0.02	0.02	0.05	0.06	0.01
ME-XRF26	TiO <sub>2</sub>	0.37	0.81	0.56	0.82	0.43	0.16	0.17	0.17	0.58	0.47	0.18
OA-GR05x	LOI 1000	1.84	0.87	0.3	0.78	1.23	0.54	1.63	2.09	0.82	0.94	3.67
ME-XRF26	Total	99.2	99.58	99.34	99.82	99.15	99.67	99.5	99.86	99.68	100	99.53
ME-MS81	Ba	1405	1365	1235	1310	1480	1015	950	710	1310	1595	276
ME-MS81	Ce	80.8	69.8	120	103	99.2	57.5	86.4	79.1	100	108.5	105
ME-MS81	Cr	10	140	30	50	90	10	10	10	80	30	70
ME-MS81	Cs	4.49	2.97	1.5	3.08	2.2	2.42	5.81	3.46	2.92	1.88	5.94
ME-MS81	Dy	3.18	4.03	4.01	4.02	2.7	4.41	4.17	3.06	2.9	3.92	4.49
ME-MS81	Er	1.96	2.6	2.43	2.45	1.52	2.75	2.77	1.78	1.64	2.09	2.7
ME-MS81	Eu	1.1	1.48	1.52	1.69	1.34	0.91	1.07	0.72	1.45	1.58	0.84
ME-MS81	Ga	16.3	21.8	20.9	20.7	21.8	17.1	17.4	13.9	20.8	20.8	18.5
ME-MS81	Gd	3.99	5.53	5.31	5.62	4.14	4.59	5.08	4.01	4.55	5.18	5.22
ME-MS81	Hf	5.4	4.8	6	5.4	5	3.5	3.6	5.2	4.9	5.9	4.4
ME-MS81	Ho	0.66	0.93	0.79	0.83	0.55	0.93	0.92	0.65	0.6	0.72	0.87
ME-MS81	La	47.4	37.2	71	61	61.8	30.6	50.1	45.6	59.5	63.8	59.6
ME-MS81	Lu	0.28	0.42	0.3	0.3	0.22	0.37	0.4	0.26	0.22	0.26	0.39
ME-MS81	Nb	16	17.6	18.9	16.5	16.6	20.5	21.1	18.1	17.6	18.9	23
ME-MS81	Nd	30.2	32.2	46.1	40.2	37.1	25	33.4	29.7	37.9	41.6	40.2
ME-MS81	Pr	8.7	8.31	13.05	11.5	10.85	6.73	9.6	8.74	11.1	11.9	11.6
ME-MS81	Rb	223	135	134	155.5	213	330	251	313	246	280	179.5
ME-MS81	Sm	5.41	6.57	7.76	7.21	6.36	5.36	5.91	5.63	6.15	7.28	7.15
ME-MS81	Sn	2	3	2	2	3	3	3	1	2	3	1
ME-MS81	Sr	457	429	486	536	476	98.1	124.5	86.6	421	458	18.8
ME-MS81	Ta	1	0.6	1.1	0.9	1	1.3	1.4	1.4	1	1.1	1.5
ME-MS81	Tb	0.55	0.73	0.75	0.79	0.53	0.75	0.77	0.57	0.61	0.71	0.8
ME-MS81	Th	19.5	11.35	22.4	18.5	23.4	18.8	20.1	25	21.8	24.2	21.9
ME-MS81	Tm	0.27	0.4	0.34	0.33	0.19	0.39	0.37	0.26	0.22	0.28	0.41
ME-MS81	U	4.43	2.8	3.35	4.15	5.53	2.93	3.54	5.45	6.09	5.58	4.15
ME-MS81	V	24	112	66	123	42	8	8	10	67	49	14
ME-MS81	W	2	3	<1	1	13	18	2	2	31	1	2
ME-MS81	Y	17	22.2	20.3	20.3	13.5	23.9	23.4	15.4	14.8	18.4	24
ME-MS81	Yb	1.98	2.51	2.09	2.12	1.3	2.63	2.62	1.64	1.3	1.94	2.85
ME-MS81	Zr	207	191	224	210	187	109	110	189	197	230	136
ME-4ACD81	Ag	<0.5	<0.5	<0.5	<0.5	<0.5	<0.5	<0.5	<0.5	<0.5	<0.5	<0.5
ME-4ACD81	Cd	<0.5	<0.5	<0.5	<0.5	<0.5	<0.5	<0.5	<0.5	<0.5	<0.5	<0.5
ME-4ACD81	Co	5	17	8	12	3	2	1	2	9	2	2
ME-4ACD81	Cu	8	15	65	21	125	131	16	6	13	40	8
ME-4ACD81	Li	10	20	20	10	20	<10	20	30	10	<10	40
ME-4ACD81	Mo	<1	<1	<1	<1	3	3	<1	1	1	<1	<1
ME-4ACD81	Ni	3	38	11	17	14	3	2	2	34	8	2
ME-4ACD81	Pb	21	14	18	9	23	11	25	28	11	19	23
ME-4ACD81	Sc	4	12	6	11	4	3	4	3	7	5	4
ME-4ACD81	Zn	57	98	55	34	25	19	40	35	27	14	9
ME-MS42	As	1	0.5	0.5	0.9	2.6	24.2	107	1.8	1.5	0.7	85.1
ME-MS42	Bi	0.01	0.07	0.02	0.04	23.8	2.36	0.41	0.03	0.09	0.34	0.17
ME-MS42	Hg	0.008	0.006	0.007	<0.005	0.008	0.007	0.005	0.005	0.011	0.01	0.042
ME-MS42	Sb	0.11	0.07	0.05	0.09	0.24	0.26	1.06	0.19	0.08	0.07	0.57
ME-MS42	Se	0.4	0.5	0.2	0.3	0.4	0.3	0.4	0.4	0.4	0.4	0.4
ME-MS42	Te	0.01	0.01	0.01	<0.01	0.2	0.04	0.05	<0.01	<0.01	0.07	0.03
ME-MS42	Tl	0.08	0.31	0.28	0.1	0.04	0.04	0.11	0.1	0.03	0.03	0.12
S-IR08	S	0.02	0.01	0.01	0.01	0.03	<0.01	0.01	0.01	0.01	0.02	0.01
C-IR07	C	0.06	0.02	0.01	0.01	0.04	0.02	0.02	0.42	0.05	0.14	0.04

	Sample ID	PK003C-867.3	PK005C-21.3	PK031C-407.8	PK005C-824	PK034C-273	PK034C-335.7	PK101C-182	PK119C-560	PK119C-517	KJM004	KJM019
	Rock Type	Granodiorite Porphyry	Granodiorite Porphyry	Granodiorite Porphyry	Granodiorite Porphyry	Dacite Porphyry	Granodiorite Porphyry	Granodiorite Porphyry	Granodiorite Porphyry	Andesite Porphyry	Granodiorite Porphyry	Granodiorite Porphyry
Method												
ME-XRF26	Al <sub>2</sub> O <sub>3</sub>	14.65	15.1	12.8	14.35	15.45	14.9	14.35	15.35	15.2	15.75	15.45
ME-XRF26	BaO	0.03	0.4	0.1	0.02	0.06	0.08	0.04	0.18	0.16	0.21	0.16
ME-XRF26	CaO	4.77	8.65	0.52	4.62	0.78	5.25	3.57	1.94	5.98	3.36	2.24
ME-XRF26	Cr <sub>2</sub> O <sub>3</sub>	<0.01	<0.01	<0.01	<0.01	<0.01	0.01	0.01	<0.01	0.01	0.01	<0.01
ME-XRF26	Fe <sub>2</sub> O <sub>3</sub>	1.69	1.25	1.69	2.32	3.12	2.14	3.42	4.45	5.23	3.71	2.99
ME-XRF26	K <sub>2</sub> O	4.15	3.86	3.11	4.07	7.94	3.68	0.59	6.31	5.57	3.99	5.62
ME-XRF26	MgO	0.68	0.73	1.8	1.61	1.55	1.28	1.22	2.09	1.96	1.41	0.69
ME-XRF26	MnO	0.04	0.05	0.01	0.04	0.04	0.05	0.07	0.04	0.04	0.03	0.07
ME-XRF26	Na <sub>2</sub> O	0.06	0.06	0.04	0.05	0.12	0.04	0.07	0.39	1.26	3.39	2.5
ME-XRF26	P <sub>2</sub> O <sub>5</sub>	0.18	0.33	0.15	0.16	0.13	0.17	0.16	0.23	0.21	0.19	0.11
ME-XRF26	SiO <sub>2</sub>	66.5	58.1	75.2	64.7	65.9	64.7	68.6	63.2	55.2	66.9	66.3
ME-XRF26	SrO	0.01	0.02	0.01	0.01	0.08	0.01	0.01	0.02	0.04	0.08	0.06
ME-XRF26	TiO <sub>2</sub>	0.46	0.59	0.42	0.45	0.36	0.47	0.43	0.63	0.56	0.55	0.34
OA-GR405x	LOI 1000	6.21	9.69	3.33	6.17	4.2	6.77	7.64	4.29	7.33	0.76	2.69
ME-XRF26	Total	99.49	99.15	99.31	99.07	100.1	99.97	100.35	99.2	98.82	100.55	99.33
ME-MS81	Ba	220	2210	820	103	446	649	208	1530	1295	1745	1415
ME-MS81	Ce	96.9	166.5	89.9	88.2	163	106.5	69.8	80.8	99.9	110	96
ME-MS81	Cr	30	20	30	30	10	30	30	30	30	30	10
ME-MS81	Cs	7.33	15.45	15.45	14.1	7.71	8.41	1.55	14.1	7.23	1.77	4.1
ME-MS81	Dy	3.17	4.81	2.62	3.21	4.88	3.1	2.52	3.47	4.65	4.43	3.63
ME-MS81	Er	1.63	2.4	1.39	1.78	2.63	1.71	1.42	2.24	2.96	2.61	2.2
ME-MS81	Eu	1.22	2.44	1.15	1.44	1.66	1.38	1.04	1.28	1.55	1.71	1.17
ME-MS81	Ga	21.6	24.5	21.1	21.7	19.7	22.6	15	19	18.1	21.1	18.2
ME-MS81	Gd	3.9	6.74	3.51	4.15	5.37	4.18	3.46	4.38	5.65	5.75	4.72
ME-MS81	Hf	5.6	8	5	5.4	8.1	6.8	5.2	6.2	5.8	5.7	6.5
ME-MS81	Ho	0.55	0.9	0.4	0.64	0.88	0.59	0.44	0.71	0.94	0.97	0.78
ME-MS81	La	53.4	90.8	49.3	48.7	83	59.1	35.6	47.8	58.5	63.9	59.3
ME-MS81	Lu	0.26	0.35	0.18	0.25	0.38	0.26	0.19	0.31	0.37	0.37	0.3
ME-MS81	Nb	17.8	19.2	16.2	17.9	22.6	18.1	17.6	18.1	17.3	17.9	22.2
ME-MS81	Nd	35.3	65.5	34.7	34.1	53.8	38.8	27.1	31.8	39	42.6	36.7
ME-MS81	Pr	10.25	18.15	9.62	9.38	15.8	11.2	7.85	9.09	11.25	12.1	11.1
ME-MS81	Rb	258	224	184	256	238	207	26.9	238	229	148.5	238
ME-MS81	Sm	5.75	9.74	5.12	5.87	8.26	6.15	4.52	5.47	7.26	7.44	6.36
ME-MS81	Sn	2	2	2	2	3	2	2	2	1	2	2
ME-MS81	Sr	38.4	148.5	37.3	63	573	56.3	62.1	143.5	261	576	446
ME-MS81	Ta	1.3	1.1	1.2	1.3	1.7	1.3	1.2	1	1.1	1	1.4
ME-MS81	Tb	0.53	0.96	0.48	0.54	0.8	0.58	0.44	0.67	0.88	0.8	0.66
ME-MS81	Th	22.1	28.2	19.8	21.3	35.7	22.8	21.4	19	19.45	21.2	25.2
ME-MS81	Tm	0.23	0.35	0.2	0.26	0.37	0.25	0.22	0.32	0.38	0.38	0.3
ME-MS81	U	7.27	5.76	5.58	7.03	4.35	6.57	6.05	5.36	4.76	5.52	5.28
ME-MS81	V	51	80	49	51	28	55	43	72	65	64	22
ME-MS81	W	2	13	5	3	1	4	1	9	12	1	1
ME-MS81	Y	15.1	24	12.1	16.6	24.1	15.2	11.3	18	24	22.1	18.6
ME-MS81	Yb	1.54	2.33	1.38	1.63	2.33	1.66	1.35	2.34	2.65	2.31	2.17
ME-MS81	Zr	194	307	170	186	307	226	190	240	220	217	264
ME-4ACD81	Ag	<0.5	<0.5	1.7	<0.5	<0.5	<0.5	<0.5	<0.5	<0.5	<0.5	<0.5
ME-4ACD81	Cd	<0.5	<0.5	<0.5	<0.5	<0.5	<0.5	<0.5	<0.5	<0.5	<0.5	<0.5
ME-4ACD81	Co	4	3	3	6	4	6	5	5	6	5	3
ME-4ACD81	Cu	5	19	1	<1	2	2	5	7	10	4	6
ME-4ACD81	Li	20	40	70	40	10	40	40	50	20	10	10
ME-4ACD81	Mo	<1	<1	<1	<1	<1	<1	<1	<1	<1	2	<1
ME-4ACD81	Ni	13	10	7	16	5	11	13	12	7	7	2
ME-4ACD81	Pb	20	17	18	22	34	21	28	34	25	42	32
ME-4ACD81	Sc	4	5	4	5	4	5	4	8	9	6	4
ME-4ACD81	Zn	42	37	34	35	69	48	49	54	52	66	56
ME-MS42	As	22.4	47.5	107	12.4	3.8	27.1	0.4	5.1	10.6	4.8	1.6
ME-MS42	Bi	0.01	0.16	0.03	0.01	0.07	0.02	0.02	0.01	<0.01	0.13	0.08
ME-MS42	Hg	0.029	0.051	0.027	0.03	0.013	0.1	0.008	<0.005	0.009	0.01	0.012
ME-MS42	Sb	0.36	0.65	1.07	0.76	<0.05	1.29	0.05	3.3	5.28	1.35	0.1
ME-MS42	Se	0.5	0.6	0.6	0.6	0.6	0.3	0.4	0.5	0.5	0.2	0.4
ME-MS42	Te	<0.01	0.01	<0.01	0.01	0.01	0.01	<0.01	0.01	0.01	0.01	<0.01
ME-MS42	Tl	0.39	0.41	0.4	0.45	0.16	0.45	0.11	0.64	0.19	0.14	0.2
S-IR08	S	<0.01	0.05	0.01	0.18	0.1	0.2	0.02	<0.01	<0.01	0.04	<0.01
C-IR07	C	0.98	1.8	0.06	0.96	0.05	1.13	0.72	0.23	1.04	0.05	0.14

	Sample ID	RTH58	RTH65	RTH69	RTH70	RTH71	RTH73	RTH74	RTH79	RTH80	RTH82	RTH85
	Rock Type	Granodiorite Porphyry	Dacite Breccia	Dacite Flow	Granodiorite Porphyry	Aplite	Granodiorite Porphyry	Granodiorite Porphyry	Granodiorite Porphyry	Dionite Dike	Granite Porphyry	Stock
Method												
ME-XRF26	Al <sub>2</sub> O <sub>3</sub>	14.9	14.1	16.7	15.65	12.55	14.25	15.5	14.8	14.1	13.85	15.9
ME-XRF26	BaO	0.12	0.12	0.16	0.16	0.01	0.15	0.16	0.16	0.22	0.14	0.18
ME-XRF26	CaO	2.48	2.55	3.67	3.28	0.63	1.62	3.29	1.74	5.36	1.06	3.88
ME-XRF26	Cr <sub>2</sub> O <sub>3</sub>	<0.01	<0.01	<0.01	<0.01	<0.01	<0.01	0.01	<0.01	0.04	<0.01	0.01
ME-XRF26	Fe <sub>2</sub> O <sub>3</sub>	3.22	3.27	5.24	3.42	0.57	1.65	3.81	2.12	5.38	1.18	4.11
ME-XRF26	K <sub>2</sub> O	4.88	4.33	4.83	4.21	5.2	5.41	3.89	4.88	6	6.56	3.69
ME-XRF26	MgO	0.45	1.41	1.66	1.5	0.1	0.71	1.54	0.69	4.76	0.35	1.8
ME-XRF26	MnO	0.05	0.07	0.07	0.02	<0.01	0.02	0.05	0.01	0.13	0.05	0.06
ME-XRF26	Na <sub>2</sub> O	3.34	1.68	2.83	3.57	3.24	2.49	3.37	3.37	2.36	2.11	3.47
ME-XRF26	P <sub>2</sub> O <sub>5</sub>	0.12	0.1	0.28	0.21	0.01	0.07	0.19	0.1	0.34	0.05	0.22
ME-XRF26	SiO <sub>2</sub>	66.4	64.4	61	66.4	77	69.6	66.9	70.1	58.8	73	65.2
ME-XRF26	SrO	0.04	0.1	0.05	0.07	0.01	0.06	0.06	0.04	0.07	0.05	0.08
ME-XRF26	TiO <sub>2</sub>	0.29	0.27	0.76	0.56	0.08	0.23	0.56	0.33	0.84	0.16	0.64
OA-GRA05x	LOI 1000	3.37	6.04	1.81	0.73	0.15	1.69	0.37	0.64	0.74	0.73	0.35
ME-XRF26	Total	99.74	98.54	99.15	99.83	99.57	99.49	99.78	99.03	99.26	99.37	99.66
ME-MS81	Ba	981	1090	1410	1400	56.6	1405	1325	1415	1975	1330	1600
ME-MS81	Ce	82.9	90.7	101	99.8	27.7	107	113.5	94.3	104	84.9	94.4
ME-MS81	Cr	10	10	10	30	20	10	30	30	260	10	40
ME-MS81	Cs	4.28	2.29	8.71	1.68	3.48	7.86	1.84	2.38	1.93	14.15	1.73
ME-MS81	Dy	3.02	3.08	4.34	3.53	0.77	4.09	3.97	1.93	3.9	4.6	4.11
ME-MS81	Er	1.81	1.86	2.74	2.01	0.59	2.81	2.33	1.08	2.33	3.3	2.12
ME-MS81	Eu	1.02	1.05	1.56	1.41	0.15	1.24	1.55	1.06	1.92	1.15	1.65
ME-MS81	Ga	17	17	21	20.5	17.4	17.6	20.2	21.3	18.2	18.2	21.1
ME-MS81	Gd	3.89	4.35	5.76	5.04	0.89	4.92	5.19	3.21	5.7	5.14	5.49
ME-MS81	Hf	5.5	5.3	6.7	5.9	3.2	4.9	4.6	5.5	5.3	4	6.1
ME-MS81	Ho	0.63	0.61	0.92	0.73	0.18	0.87	0.75	0.39	0.81	1	0.81
ME-MS81	La	49	54.9	56.6	58.7	17.5	63.4	67.7	59.7	58.7	48.2	52.9
ME-MS81	Lu	0.26	0.24	0.31	0.24	0.18	0.39	0.28	0.16	0.27	0.4	0.3
ME-MS81	Nb	16.2	15.9	19.8	18.1	18.7	21.1	18.5	12.9	17.4	22.1	19.5
ME-MS81	Nd	30.6	33	41.7	38.6	8.3	39.3	42.6	31.4	43.7	32.6	38.6
ME-MS81	Pr	8.96	9.74	11.6	10.9	2.79	11.55	12.5	9.65	11.75	9.28	11.05
ME-MS81	Rb	210	160.5	227	150	241	202	135.5	166.5	144	259	120.5
ME-MS81	Sm	5.46	6.2	7.44	6.6	1.29	6.55	7.24	4.78	7.89	6.2	7.22
ME-MS81	Sn	3	2	2	2	1	2	2	1	5	2	2
ME-MS81	Sr	236	829	401	509	43.5	496	486	317	562	411	557
ME-MS81	Ta	1.2	1.1	1.2	1.1	1.3	1.5	1.1	0.9	0.9	1.5	1.1
ME-MS81	Tb	0.58	0.6	0.84	0.67	0.13	0.81	0.79	0.4	0.82	0.81	0.74
ME-MS81	Th	22.3	21.8	21.6	20.2	35.4	20.9	21.4	27.5	18.3	20.7	14.25
ME-MS81	Tm	0.24	0.25	0.35	0.28	0.11	0.4	0.34	0.15	0.29	0.42	0.31
ME-MS81	U	6.4	4.35	5.67	4.16	7.97	5.99	3.1	3.29	4.62	5.72	2.2
ME-MS81	V	18	27	89	60	<5	14	60	27	125	7	69
ME-MS81	W	2	1	1	1	6	2	1	4	2	2	1
ME-MS81	Y	15.3	16.3	21.3	18.7	5.4	22.6	19.9	9.8	20.2	25.2	19.9
ME-MS81	Yb	1.69	1.73	2.23	1.73	0.92	2.6	1.96	1.06	2.03	3.01	1.99
ME-MS81	Zr	218	203	265	241	61	173	181	194	200	124	250
ME-4ACD81	Ag	<0.5	<0.5	<0.5	<0.5	<0.5	<0.5	<0.5	<0.5	<0.5	<0.5	<0.5
ME-4ACD81	Cd	<0.5	<0.5	<0.5	<0.5	<0.5	<0.5	<0.5	<0.5	<0.5	<0.5	<0.5
ME-4ACD81	Co	4	4	12	6	<1	2	8	4	14	1	9
ME-4ACD81	Cu	5	5	10	2	29	3	98	64	51	6	16
ME-4ACD81	Li	10	10	30	10	<10	10	10	10	<10	10	10
ME-4ACD81	Mo	1	<1	<1	1	2	1	<1	2	1	2	<1
ME-4ACD81	Ni	1	2	3	9	<1	2	10	4	52	2	12
ME-4ACD81	Pb	23	27	25	14	32	16	17	23	12	27	18
ME-4ACD81	Sc	3	5	10	6	1	4	6	3	16	3	7
ME-4ACD81	Zn	47	57	86	22	5	5	48	22	68	15	53
ME-MS42	As	1.9	1.8	0.9	0.9	0.3	1.2	0.1	0.3	0.9	2.8	0.2
ME-MS42	Bi	0.13	0.08	0.03	0.07	0.12	0.1	0.02	0.07	0.03	0.1	0.03
ME-MS42	Hg	<0.005	0.006	<0.005	0.006	<0.005	0.005	<0.005	<0.005	0.007	<0.005	0.005
ME-MS42	Sb	0.22	0.09	0.08	<0.05	0.05	1.08	<0.05	<0.05	0.12	0.12	<0.05
ME-MS42	Se	0.4	0.4	0.4	0.4	0.2	0.2	<0.2	0.3	0.2	0.7	0.2
ME-MS42	Te	0.01	0.01	<0.01	0.01	0.01	0.07	<0.01	<0.01	0.03	0.01	<0.01
ME-MS42	Tl	0.1	0.35	0.17	0.06	0.03	0.07	0.31	0.11	0.03	0.11	0.3
S-IR08	S	0.02	0.01	0.01	<0.01	<0.01	0.59	0.01	0.01	0.01	0.03	<0.01
C-IR07	C	0.52	0.03	0.02	0.01	0.01	0.18	0.01	0.05	0.02	0.04	0.01

Sample ID	RTH93	RTH101	RTH102	RTH115	PKW-2	
Rock Type	Diorite Dike	Dacite	Dacite	Granodiorite Dike	Dacite	
Method						
ME-XRF26	Al <sub>2</sub> O <sub>3</sub>	16.85	14.5	16.35	14.72	14.7
ME-XRF26	BaO	0.16	0.2	0.14	0.18	0.18
ME-XRF26	CaO	5.14	2.89	2.98	2.32	3.9
ME-XRF26	Cr <sub>2</sub> O <sub>3</sub>	<0.01	0.01	<0.01	0.01	0.01
ME-XRF26	Fe <sub>2</sub> O <sub>3</sub>	2.57	3.48	4.78	3.29	4.15
ME-XRF26	K <sub>2</sub> O	3.86	4.1	4.84	4.19	4.61
ME-XRF26	MgO	1.78	1.64	0.67	1.22	2.23
ME-XRF26	MnO	0.04	0.04	0.05	0.04	0.1
ME-XRF26	Na <sub>2</sub> O	3.9	2.9	3.43	2.87	2.07
ME-XRF26	P <sub>2</sub> O <sub>5</sub>	0.33	0.19	0.21	0.17	0.23
ME-XRF26	SiO <sub>2</sub>	63.5	67	63.6	69.9	63.98
ME-XRF26	SrO	0.08	0.07	0.05	0.05	0.04
ME-XRF26	TiO <sub>2</sub>	0.79	0.53	0.49	0.47	0.6
OA-GRA05x	LOI 1000	0.48	1.91	0.94	1.19	3.69
ME-XRF26	Total	99.54	99.53	98.57	100.7	100.55
ME-MS81	Ba	1355	1790	1235	1615	1575
ME-MS81	Ce	119	92.3	83.1	93	103
ME-MS81	Cr	20	70	<10	30	20
ME-MS81	Cs	1.2	2.13	5.53	2.61	2.4
ME-MS81	Dy	3.67	3.01	3.12	2.73	4.49
ME-MS81	Er	2.33	1.79	1.82	1.47	2.49
ME-MS81	Eu	1.81	1.26	1.35	1.14	1.46
ME-MS81	Ga	21.9	20.3	19	20.7	19.5
ME-MS81	Gd	5.35	3.84	4.37	3.69	5.64
ME-MS81	Hf	6.4	4.7	5.5	5.7	6.8
ME-MS81	Ho	0.73	0.53	0.61	0.51	0.88
ME-MS81	La	69.8	55.8	48.7	51.8	56.2
ME-MS81	Lu	0.25	0.2	0.24	0.23	0.36
ME-MS81	Nb	16.2	17	16.8	18.3	18.3
ME-MS81	Nd	45.4	36.9	33.5	33.7	39.8
ME-MS81	Pr	13.05	10.55	9.38	9.6	11.05
ME-MS81	Rb	132.5	145.5	219	150.5	135
ME-MS81	Sm	7.97	5.7	5.75	5.33	7.14
ME-MS81	Sn	2	2	2	2	2
ME-MS81	Sr	593	542	350	395	271
ME-MS81	Ta	0.9	1	1.1	1.1	1
ME-MS81	Tb	0.73	0.55	0.62	0.51	0.75
ME-MS81	Th	19.4	20.3	18.55	22.2	20.2
ME-MS81	Tm	0.31	0.22	0.27	0.22	0.39
ME-MS81	U	4.96	5.71	2.8	5.52	5.82
ME-MS81	V	84	62	24	55	94
ME-MS81	W	2	1	1	1	1
ME-MS81	Y	19	13.9	15.1	13.5	23.8
ME-MS81	Yb	1.68	1.48	1.7	1.51	2.38
ME-MS81	Zr	247	180	219	186	227
ME-4ACD81	Ag	<0.5	<0.5	<0.5	<0.5	<0.5
ME-4ACD81	Cd	<0.5	<0.5	<0.5	<0.5	<0.5
ME-4ACD81	Co	6	9	4	5	8
ME-4ACD81	Cu	10	11	2	8	9
ME-4ACD81	Li	10	20	20	30	40
ME-4ACD81	Mo	<1	1	<1	1	<1
ME-4ACD81	Ni	8	29	<1	14	12
ME-4ACD81	Pb	17	34	24	31	26
ME-4ACD81	Sc	8	6	5	5	7
ME-4ACD81	Zn	27	61	80	57	67
ME-MS42	As	0.1	0.6	1.1	0.7	0.4
ME-MS42	Bi	0.11	0.05	0.01	0.05	0.05
ME-MS42	Hg	<0.005	<0.005	0.01	0.008	<0.005
ME-MS42	Sb	0.08	<0.05	0.07	0.08	0.05
ME-MS42	Se	0.3	0.4	0.2	0.3	0.5
ME-MS42	Te	0.01	0.01	<0.01	<0.01	<0.01
ME-MS42	Tl	0.05	0.18	0.32	0.17	0.15
S-IR08	S	<0.01	0.01	<0.01	0.02	<0.01
C-IR07	C	0.02	0.2	0.01	0.07	0.36

### Appendix D: Microprobe Data for Pyrite

Samples were analyzed to quantify pyrite trace element data using a JEOL-8900 Electron Probe Microanalyzer (EPMA) at the University of Nevada, Las Vegas at the Electron Microanalysis and Imaging Laboratory (EMiL). The elements Ag, Al, As, Au, Bi, Ca, Co, Cu, Fe, Hg, Mo, Na, Ni, Pb, S, Sb, Se, Si, Sn, Te, Ti, Tl, W, and Zn were measured. The EPMA point name generally consists of the line # (i.e. Line 2), the drill hole # (i.e. PK137CA), the footage (i.e. 857), the pyrite grain analyzed and spot number (ie.1-1).

#### Probe Conditions

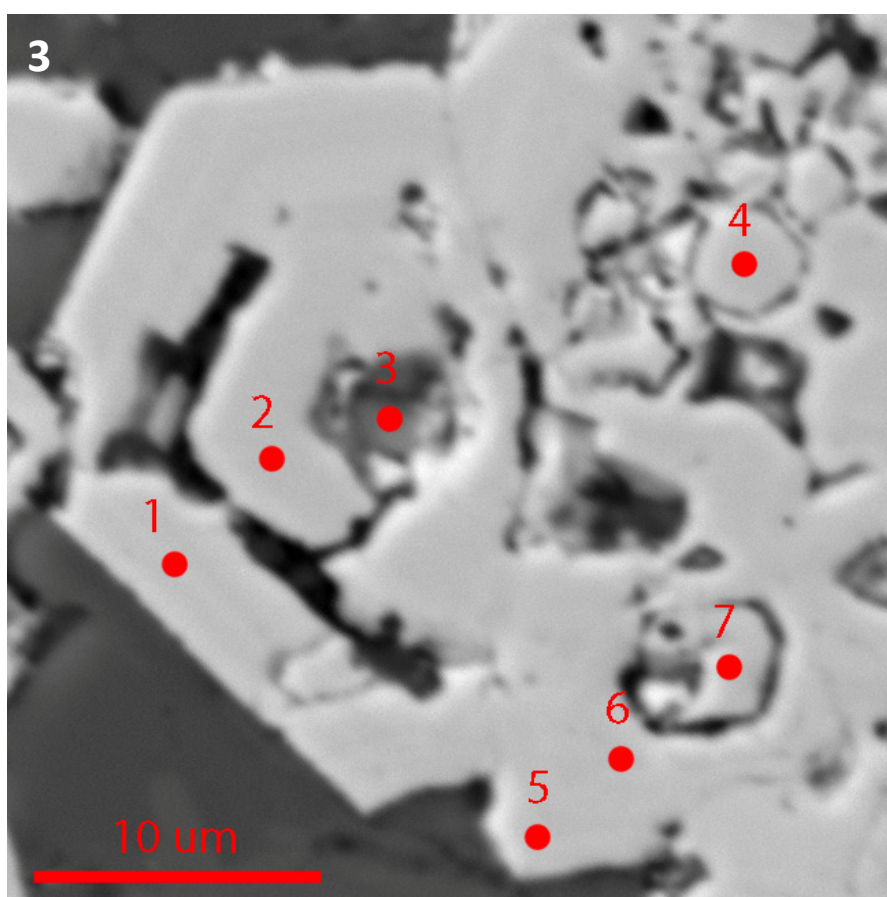
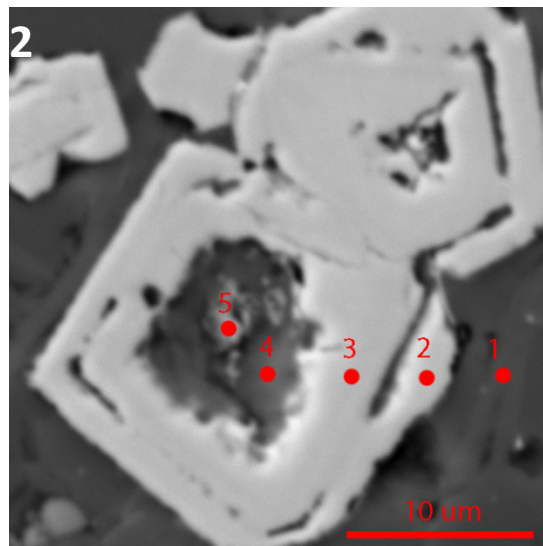
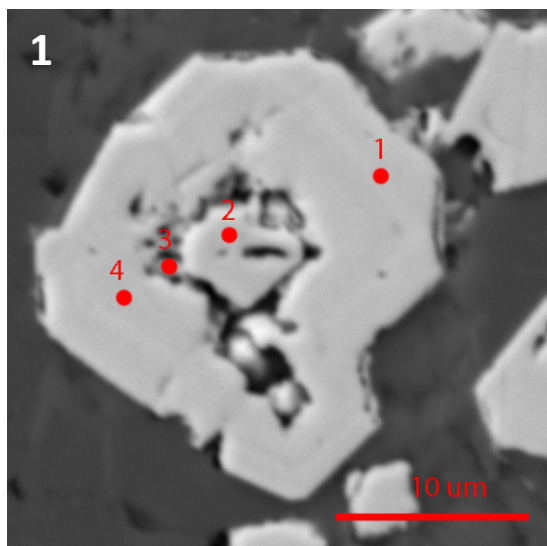
20 kV, 100nA, 1-2 $\mu$ m								
TRACE			1	2	3			
			TAP	PETH	LIF			
			Se	Ag	Tl			
			Al	Hg	Au			
			Zn	Pb	Bi			
			As	W	Cu			
			Si	Te	Ni			
				Sb	Co			
				Sn	Ti			
				Mo	Fe			
				Ca				
				c				
Element	X-ray	Spectrometer	Crystal	Peak (mm)	Peak (sec)	Back (sec)	MDL (ppm)	Standard
Ag	L $\alpha$		2 PETH	77.477	50	15	28	CM1-ag-166
Al	K $\alpha$		1 TAP	83.596	30	15	9	Gel-Al
As	L $\alpha$		1 TAP	133.17	30	15	30	MAC-as
Au	L $\alpha$		3 LIF	133.174	200	50	97	Gel-Au
Bi	M $\alpha$		3 PETH	223.53	120	50	86	Gel-Bi
Ca	K $\alpha$		2 PETH	107.92	30	15	17	SM-Plagioclase
Co	K $\alpha$		3 LIF	163.875	30	15	46	Gel-Co
Cu	K $\alpha$		3 LIF	110.413	30	15	60	MAC-cufes2
Fe	K $\alpha$		3 LIF	124.284	30	15	52	MAC-pyrite
Hg	M $\alpha$		2 PETH	97.755	150	50	39	CM2-hgs
Mo	L $\alpha$		2 PETH	115.122	30	15	43	Gel-Mo
Na	K $\alpha$		1 TAP	129.414	10	5	44	SM-Albite
Ni	K $\alpha$		3 LIF	106.899	30	15	46	Gel-Ni
Pb	M $\alpha$		2 PETH	169.253	30	15	89	MAC-pbs
S	K $\alpha$		2 PETH	134.536	30	15	14	MAC-pyrite
Sb	L $\alpha$		2 PETH	173.159	30	15	30	CM1-Sb
Se	L $\alpha$		1 TAP	180.813	30	15	31	CM1-se
Si	K $\alpha$		4 TAP	105.165	30	15	27	SM-Plagioclase
Sn	L $\alpha$		2 PETH	88.463	30	15	30	CM1-sn
Te	L $\alpha$		2 PETH	115.527	30	15	46	CM2-pbte
Ti	K $\alpha$		2 PETH	172.091	30	15	25	CM3-tio2
Tl	L $\alpha$		3 LIF	90.725	120	40	153	CM2-tlbr
W	K $\alpha$		2 PETH	105.634	30	15	106	CM1-w
Zn	L $\alpha$		4 TAP	88.413	30	15	46	Gel-Zn

Total	100.1	95.64	98.464	99.06	44.1	85.98	89.3	52.74	59.85	100.6	100.8	92.887	90.746	100.4	99.1	97	98.9	49	100	99.83	100.1	95.6	35.98	99.8	100.45	
	Na	Ag	Au	Si	As	Hg	Tl	Zn	Se	Pb	Bi	Al	W	Cu	Te	Co	Sb	Ni	Sn	Fe	Mo	Ti	S	Ca	Total	
Detection Limit (ppm)	ppm	ppm	ppm	% wt	% wt	ppm	ppm	ppm	ppm	ppm	ppm	ppm	ppm	ppm	ppm	ppm	ppm	ppm	ppm	% wt	ppm	ppm	% wt	% wt	% wt	
pk137CA857-1.1	140	BDL	1250	0.07	4.76	BDL	160	BDL	BDL	BDL	BDL	60	BDL	1080	BDL	560	170	BDL	120	45.10	7670	140	49.03	BDL	100.11	
pk137CA857-1.2	300	30	590	0.21	1.21	40	60	150	BDL	BDL	BDL	340	BDL	520	BDL	810	530	BDL	70	44.46	7930	BDL	48.64	BDL	95.64	
pk137CA857-1.3	90	140	730	0.09	1.12	BDL	BDL	160	BDL	BDL	BDL	110	BDL	420	BDL	620	670	BDL	80	44.45	8010	BDL	51.70	BDL	98.46	
pk137CA857-1.4	BDL	BDL	1290	2.33	4.69	90	210	BDL	BDL	BDL	BDL	3920	BDL	770	BDL	480	250	BDL	70	44.11	7410	1060	46.37	BDL	99.06	
pk137CA857-2.1	260	BDL	BDL	36.02	0.01	BDL	200	BDL	BDL	BDL	100	67230	BDL	BDL	BDL	BDL	430	BDL	BDL	0.69	BDL	660	0.47	BDL	44.10	
pk137CA857-2.2	240	BDL	130	2.72	1.75	BDL	520	BDL	BDL	BDL	BDL	16740	BDL	490	BDL	600	490	BDL	BDL	38.46	6420	BDL	40.49	BDL	85.98	
pk137CA857-2.3	640	160	2090	0.73	4.42	50	500	BDL	BDL	BDL	BDL	7020	BDL	760	BDL	610	680	BDL	60	41.94	6440	BDL	40.30	BDL	89.30	
pk137CA857-2.4	2580	40	390	16.77	0.20	BDL	300	70	BDL	BDL	BDL	105200	BDL	180	BDL	190	2510	BDL	BDL	11.21	1940	80	13.18	0.045	52.74	
pk137CA857-2.5	2190	140	390	12.66	0.37	BDL	180	BDL	BDL	BDL	BDL	93340	BDL	200	BDL	380	2810	110	BDL	16.89	3020	60	19.60	0.05	59.85	
pk137CA857-3.1	50	BDL	630	0.16	3.36	BDL	340	BDL	BDL	BDL	BDL	270	BDL	990	BDL	510	150	BDL	30	45.46	8110	BDL	50.49	BDL	100.57	
pk137CA857-3.2	80	BDL	BDL	0.04	0.93	BDL	220	BDL	BDL	BDL	BDL	10	170	350	BDL	640	90	350	BDL	46.31	8550	BDL	52.50	BDL	100.84	
pk137CA857-3.3	1270	BDL	BDL	8.36	0.25	BDL	330	BDL	BDL	BDL	BDL	830	BDL	150	BDL	680	350	560	50	36.67	7410	4670	45.97	BDL	92.89	
pk137CA857-3.4	560	BDL	BDL	0.32	0.44	BDL	210	490	BDL	BDL	BDL	1180	BDL	270	BDL	1750	440	520	80	45.89	7070	BDL	42.84	BDL	90.75	
pk137CA857-3.5	150	BDL	480	0.32	3.57	BDL	210	BDL	BDL	BDL	BDL	2520	BDL	870	BDL	620	170	BDL	80	45.26	8260	BDL	49.88	BDL	100.38	
pk137CA857-3.6	60	70	620	0.08	2.70	BDL	BDL	BDL	BDL	BDL	BDL	520	BDL	480	BDL	570	800	BDL	60	45.03	8010	4110	49.78	BDL	99.13	
pk137CA857-3.7	120	BDL	BDL	0.06	0.15	BDL	250	190	BDL	BDL	BDL	160	BDL	380	BDL	1180	300	100	80	46.18	7970	BDL	49.52	BDL	96.99	
pk004C-330-1.1	60	BDL	BDL	0.10	0.14	BDL	BDL	BDL	BDL	1380	BDL	410	BDL	BDL	BDL	660	3220	BDL	BDL	45.97	8040	BDL	51.18	0.122	98.93	
pk004C-330-1.2	70	BDL	BDL	18.95	0.04	50	210	BDL	BDL	BDL	BDL	80810	BDL	BDL	BDL	90	BDL	930	80	BDL	2.09	880	4470	4.90	14.21	48.97
pk004C-330-1.3	120	BDL	BDL	0.09	0.08	BDL	490	BDL	BDL	BDL	BDL	180	BDL	70	BDL	560	90	BDL	50	46.38	8480	BDL	52.44	0.031	100.03	
pk004C-330-1.4	BDL	BDL	BDL	0.01	0.02	BDL	190	120	BDL	BDL	BDL	BDL	220	BDL	BDL	540	70	BDL	50	46.38	8500	BDL	52.46	BDL	99.83	
pk004C-330-1.5	BDL	BDL	BDL	0.01	0.03	BDL	BDL	150	BDL	BDL	BDL	40	BDL	BDL	BDL	630	140	BDL	60	46.56	8560	BDL	52.53	BDL	100.09	
pk004C-330-1.6	80	BDL	BDL	0.02	0.05	BDL	390	BDL	BDL	BDL	BDL	110	BDL	BDL	BDL	580	250	BDL	130	46.06	8460	5690	51.85	BDL	99.55	
pk004C-330-2.1	230	BDL	320	22.72	0.04	BDL	280	BDL	BDL	BDL	BDL	112250	BDL	BDL	BDL	50	770	60	BDL	1.68	BDL	BDL	0.07	0.065	35.98	
pk004C-330-2.2	320	BDL	BDL	0.05	3.06	BDL	BDL	BDL	BDL	BDL	BDL	190	BDL	BDL	BDL	500	630	BDL	80	45.41	8140	BDL	50.22	BDL	99.75	
pk004C-330-2.3	240	BDL	BDL	0.04	0.07	BDL	440	BDL	BDL	BDL	BDL	130	BDL	BDL	BDL	620	90	BDL	BDL	46.61	8510	BDL	52.73	BDL	100.45	
pk004C-330-2.4	350	BDL	BDL	1.00	2.40	BDL	400	BDL	BDL	BDL	BDL	370	BDL	BDL	BDL	540	180	BDL	150	44.54	7850	BDL	48.85	BDL	97.77	
pk004C-330-2.5	140	BDL	BDL	0.05	1.92	BDL	BDL	BDL	BDL	BDL	BDL	30	BDL	80	BDL	650	230	BDL	BDL	45.69	8390	BDL	51.27	BDL	99.89	
pk004C-330-2.6	BDL	BDL	BDL	0.01	2.23	BDL	270	BDL	BDL	BDL	BDL	BDL	BDL	BDL	BDL	630	150	BDL	140	46.31	8400	BDL	50.94	BDL	100.44	
pk004C-330-2.7	80	BDL	BDL	0.64	2.09	BDL	BDL	BDL	BDL	BDL	BDL	280	BDL	BDL	BDL	650	370	BDL	90	45.18	8110	BDL	50.37	BDL	99.27	
pk004C-330-2.8	210	BDL	BDL	0.04	2.96	BDL	BDL	BDL	BDL	BDL	BDL	160	BDL	BDL	BDL	550	530	BDL	80	45.47	8320	BDL	50.26	BDL	99.73	
pk004C-330-3.1	190	BDL	BDL	17.19	0.36	BDL	BDL	60	BDL	BDL	BDL	89000	BDL	120	BDL	130	1650	BDL	BDL	9.24	1840	4350	10.53	0.031	47.09	
pk004C-330-3.2	310	BDL	BDL	5.78	1.17	BDL	BDL	290	BDL	BDL	BDL	48380	BDL	250	BDL	410	570	BDL	100	29.86	4450	BDL	26.19	0.024	68.51	
pk004C-330-3.3	60	BDL	BDL	0.05	0.03	BDL	340	BDL	BDL	BDL	BDL	320	BDL	BDL	BDL	510	420	BDL	60	46.14	8330	BDL	52.12	BDL	99.34	
pk004C-330-3.4	60	BDL	BDL	0.04	1.87	BDL	BDL	BDL	BDL	BDL	BDL	170	200	250	BDL	610	100	BDL	40	45.91	8260	BDL	51.35	BDL	100.14	
pk004C-330-3.5	350	BDL	BDL	13.79	0.90	BDL	530	380	BDL	160	BDL	91640	BDL	270	BDL	230	1880	120	BDL	19.04	3080	BDL	17.62	0.071	61.29	
pk004C-330-3.6	60	BDL	BDL	7.31	1.45	BDL	300	50	BDL	BDL	BDL	56740	BDL	BDL	BDL	400	810	BDL	BDL	31.52	5450	BDL	32.92	BDL	79.58	
pk004C-330-3.7	370	BDL	BDL	6.43	0.33	BDL	370	BDL	BDL	BDL	BDL	44070	BDL	100	BDL	500	800	BDL	BDL	36.06	6460	BDL	40.12	BDL	88.20	
pk004C-330-3.8	110	BDL	BDL	0.19	0.15	BDL	460	BDL	BDL	BDL	BDL	1660	BDL	110	BDL	580	100	BDL	BDL	46.02	8430	BDL	52.21	BDL	99.71	
pk004C-330-3.9	300	BDL	BDL	11.17	0.68	BDL	530	BDL	BDL	BDL	BDL	70440	BDL	70	BDL	260	900	BDL	BDL	29.02	4970	18420	31.98	BDL	82.44	

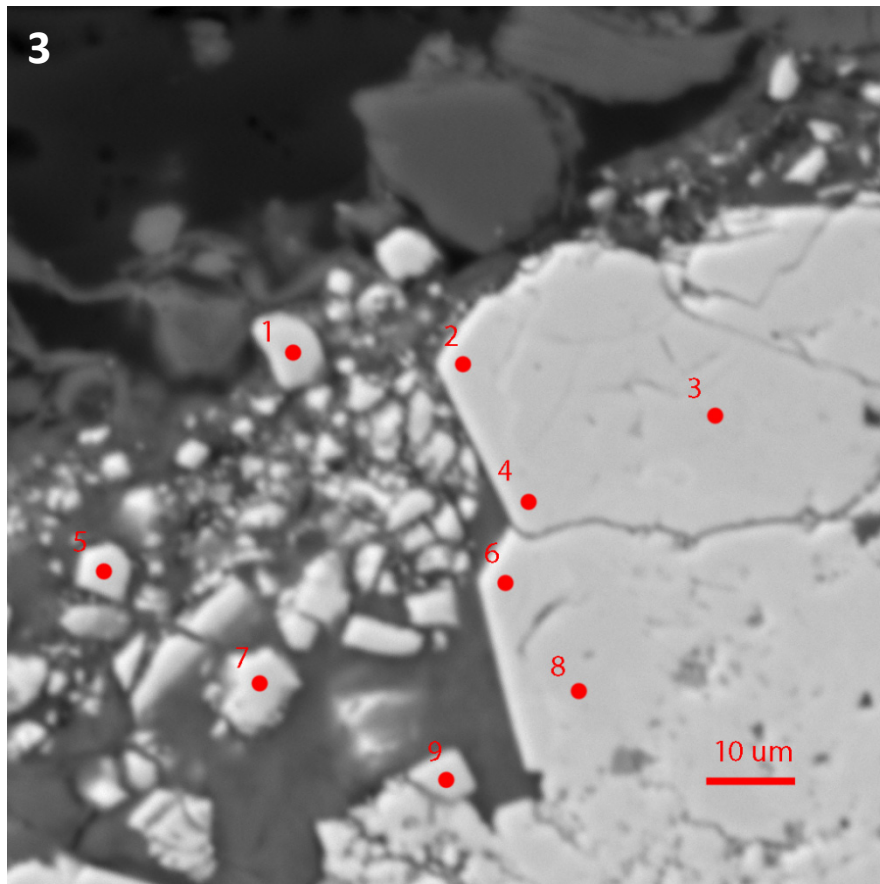
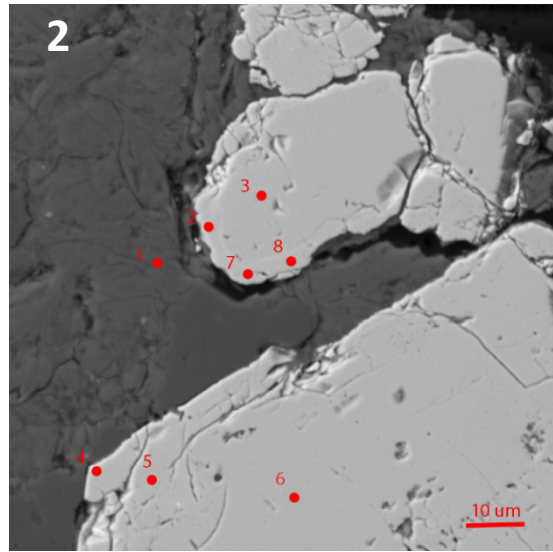
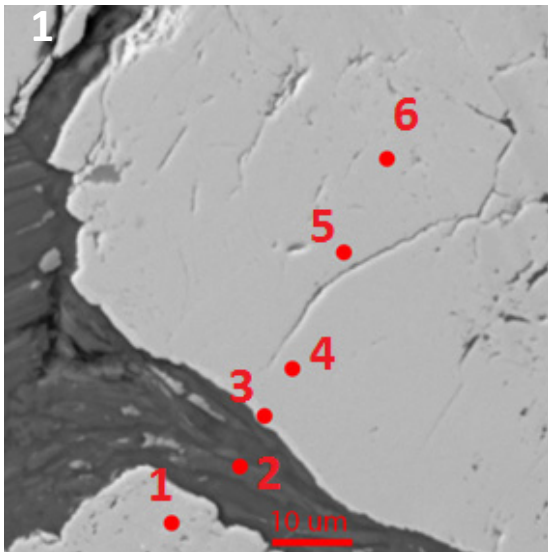
	Na	Ag	Au	Si	As	Hg	Tl	Zn	Se	Pb	Bi	Al	W	Cu	Te	Co	Sb	Ni	Sn	Fe	Mo	Ti	S	Ca	Total
	ppm	ppm	ppm	% wt	% wt	ppm	ppm	ppm	ppm	ppm	ppm	ppm	ppm	ppm	ppm	ppm	ppm	ppm	ppm	% wt	ppm	ppm	% wt	ppm	% wt
Detection Limit (ppm)	50	30	100	26.00	40.00	40	160	45	45	100	100	10	100	60	50	50	30	50	30	60	50	25	20	20	
pk004C-154-1.1	510	30	530	6.88	0.69	BDL	460	BDL	BDL	BDL	BDL	87380	BDL	610	BDL	270	620	BDL	BDL	26.24	4800	BDL	30.19	4040	73.929
pk004C-154-1.2	150	BDL	320	0.28	1.68	BDL	550	BDL	BDL	BDL	BDL	2350	BDL	290	BDL	580	970	BDL	30	44.67	8000	BDL	50.98	160	98.949
pk004C-154-1.3	170	BDL	200	4.83	0.55	BDL	330	BDL	BDL	BDL	BDL	55450	BDL	380	BDL	350	1610	BDL	BDL	29.31	5540	BDL	34.65	1110	75.85
pk004C-154-1.4	70	BDL	160	0.08	1.42	40	620	BDL	BDL	BDL	BDL	480	BDL	160	BDL	600	970	BDL	BDL	45.08	8240	BDL	51.28	1040	99.101
pk004C-154-1.5	110	BDL	180	0.37	1.06	BDL	350	210	BDL	BDL	BDL	3120	BDL	550	BDL	600	920	BDL	BDL	44.70	8270	BDL	51.28	1780	99.02
pk004C-154-2.1	480	90	150	0.08	1.82	70	700	BDL	BDL	BDL	BDL	460	BDL	740	BDL	560	1220	500	100	44.93	8010	BDL	50.60	2070	98.93
pk004C-154-2.2	80	50	BDL	0.05	2.23	BDL	750	60	BDL	BDL	BDL	120	BDL	590	BDL	2010	910	2490	40	44.44	7890	BDL	49.80	2190	98.229
pk004C-154-2.3	640	BDL	210	8.22	0.69	20	660	100	BDL	BDL	BDL	10660	BDL	690	BDL	440	790	40	70	32.71	6240	BDL	39.06	3570	83.084
pk004C-154-2.4	370	BDL	BDL	18.03	0.15	BDL	430	BDL	BDL	BDL	BDL	65100	BDL	180	BDL	120	520	BDL	BDL	11.52	2740	BDL	17.47	1690	54.287
pk004C-154-2.5	2200	BDL	200	22.48	0.07	BDL	BDL	BDL	BDL	BDL	BDL	105080	BDL	170	BDL	BDL	690	BDL	BDL	6.00	1610	BDL	9.60	14780	50.627
pk004C-154-3.1	560	BDL	BDL	1.95	0.71	BDL	370	60	BDL	BDL	BDL	16720	BDL	200	BDL	1080	560	480	BDL	40.39	7560	BDL	46.06	BDL	91.867
pk004C-154-3.2	390	BDL	BDL	0.60	0.32	BDL	270	BDL	BDL	BDL	BDL	5160	BDL	140	BDL	1170	420	490	60	44.89	8440	BDL	50.96	BDL	98.434
pk004C-154-3.3	330	BDL	BDL	0.09	0.87	BDL	460	BDL	BDL	BDL	BDL	BDL	BDL	90	BDL	530	100	BDL	70	45.99	8540	BDL	51.92	BDL	99.878
pk004C-154-3.4	540	BDL	BDL	0.12	BDL	240	BDL	BDL	BDL	BDL	BDL	BDL	BDL	BDL	BDL	700	40	180	80	45.88	8650	BDL	52.13	BDL	99.174
pk004C-154-3.5	570	BDL	BDL	0.05	2.67	BDL	210	BDL	BDL	BDL	BDL	140	BDL	1290	BDL	680	880	570	BDL	45.25	8310	BDL	50.89	BDL	100.127
pk004C-154-3.6	13010	BDL	BDL	0.03	2.74	60	BDL	BDL	BDL	BDL	BDL	30	BDL	2150	BDL	530	1220	570	BDL	45.24	8060	BDL	50.58	BDL	101.152
pk004C-154-4.1	60	BDL	620	25.24	0.26	BDL	BDL	BDL	BDL	BDL	BDL	570	BDL	160	BDL	90	380	70	60	6.98	2050	120	13.00	660	45.976
pk004C-154-4.2	140	BDL	BDL	1.49	1.10	BDL	350	BDL	BDL	BDL	BDL	10830	BDL	610	BDL	1040	630	240	BDL	42.20	7540	210	47.86	930	94.906
pk004C-154-4.3	180	30	BDL	0.70	1.32	BDL	160	BDL	BDL	BDL	BDL	3710	BDL	780	BDL	1170	680	520	80	43.61	7970	410	49.60	1000	96.894
pk004C-154-4.4	210	BDL	BDL	11.47	0.42	BDL	BDL	BDL	BDL	BDL	BDL	14690	BDL	330	BDL	380	740	BDL	BDL	29.39	4630	780	28.59	6490	72.704
pk004C-154-4.5	BDL	90	110	0.57	2.87	BDL	1020	80	BDL	BDL	BDL	4960	BDL	1210	BDL	940	1140	340	70	43.02	7730	390	47.58	560	95.898
pk004C-154-4.6	320	80	BDL	6.31	0.56	BDL	510	BDL	BDL	BDL	BDL	19070	BDL	1230	BDL	420	1110	BDL	BDL	32.93	5690	3510	34.42	2870	77.701
pk141C-453-1.1	50	BDL	BDL	0.16	6.26	BDL	260	150	BDL	BDL	BDL	420	BDL	3500	BDL	440	340	BDL	BDL	40.05	7070	BDL	43.17	22180	93.089
pk141C-453-1.2	BDL	BDL	BDL	0.05	4.69	BDL	440	50	BDL	BDL	BDL	80	120	2970	BDL	620	250	190	BDL	43.68	7880	BDL	48.37	4350	98.48
pk141C-453-1.3	110	BDL	100	0.02	0.21	BDL	BDL	BDL	BDL	BDL	BDL	40	BDL	1950	BDL	2870	80	280	70	45.33	8610	BDL	51.93	1320	99.03
pk141C-453-1.4	BDL	BDL	BDL	0.03	0.14	BDL	200	70	BDL	BDL	BDL	30	BDL	110	BDL	2140	510	540	BDL	44.40	8230	BDL	50.71	6220	97.095
pk141C-453-1.5	130	BDL	BDL	0.03	2.29	BDL	BDL	BDL	BDL	BDL	BDL	BDL	BDL	880	BDL	680	60	720	40	45.11	8140	BDL	49.95	2780	98.728
pk141C-453-2.1	BDL	BDL	BDL	0.19	0.39	BDL	190	BDL	BDL	BDL	BDL	960	BDL	3750	BDL	1280	290	760	BDL	44.30	8190	BDL	50.32	1970	96.942
pk141C-453-2.2	BDL	BDL	BDL	1.51	1.83	BDL	BDL	BDL	BDL	BDL	BDL	7000	BDL	2750	BDL	3730	440	2020	70	40.41	7660	180	45.83	2030	92.161
pk141C-453-2.3	BDL	BDL	BDL	3.50	1.15	BDL	BDL	70	BDL	BDL	BDL	2280	BDL	340	BDL	1030	460	400	60	40.77	7590	BDL	45.78	3370	92.787
pk141C-453-2.4	70	BDL	BDL	0.95	1.68	BDL	260	BDL	BDL	BDL	BDL	9140	BDL	490	BDL	1240	610	740	BDL	42.92	8060	BDL	48.42	2390	96.277
pk141C-453-3.1	380	BDL	BDL	1.09	1.67	BDL	260	BDL	BDL	BDL	BDL	4920	BDL	560	BDL	1670	680	570	BDL	39.61	7280	140	44.73	21250	90.869
pk141C-453-3.2	280	BDL	BDL	0.94	0.57	BDL	BDL	80	BDL	BDL	BDL	7690	BDL	BDL	190	BDL	520	BDL	BDL	7.93	20	580	0.34	257370	36.469
pk141C-453-3.3	570	BDL	BDL	4.15	3.19	BDL	BDL	BDL	BDL	BDL	BDL	27290	BDL	680	BDL	1910	730	620	BDL	32.20	5680	BDL	35.12	37920	82.197
pk141C-453-3.4	330	BDL	BDL	2.18	1.20	BDL	BDL	BDL	BDL	BDL	BDL	3780	BDL	180	120	460	590	240	BDL	10.86	1340	3010	7.80	183290	41.379
pk141C-453-3.5	360	BDL	BDL	2.02	3.76	BDL	170	BDL	BDL	BDL	BDL	5770	BDL	1350	BDL	3030	840	1320	70	42.11	7610	BDL	46.62	1810	96.758
pk141C-453-3.6	470	BDL	BDL	1.44	7.27	BDL	560	BDL	BDL	BDL	BDL	7150	BDL	350	BDL	1380	790	310	BDL	40.14	6890	860	43.50	8040	95.039
pk141C-453-3.7	250	BDL	BDL	0.47	0.98	BDL	230	80	BDL	BDL	BDL	2880	BDL	280	BDL	1520	400	160	100	44.36	8250	BDL	50.23	1840	97.637
pk141C-453-3.8	930	BDL	BDL	2.11	1.41	BDL	350	110	BDL	BDL	BDL	17310	BDL	450	BDL	1080	640	260	BDL	41.09	7480	BDL	46.15	1800	93.801
pk141C-453-4.1	390	BDL	BDL	7.54	7.04	BDL	BDL	170	BDL	390	BDL	21480	BDL	80	BDL	110	850	BDL	BDL	10.29	800	2870	5.40	97140	42.707
pk141C-453-4.2	BDL	BDL	BDL	16.93	6.18	BDL	420	60	BDL	700	BDL	890	BDL	1210	BDL	640	1290	140	BDL	23.70	4400	BDL	27.42	700	75.271
pk141C-453-4.3	140	BDL	BDL	2.13	1.68	60	BDL	150	BDL	330	BDL	9550	BDL	290	140	160	670	130	BDL	7.49	610	1220	3.60	185950	34.838
pk141C-453-4.4	490	BDL	BDL	8.12	1.37	BDL	290	190	BDL	BDL	BDL	8100	BDL	270	BDL	990	490	330	BDL	33.30	6580	BDL	39.72	2250	84.513
pk141C-453-4.5	400	BDL	BDL	2.07	2.20	BDL	440	BDL	BDL	BDL	BDL	17960	BDL	610	BDL	1230	720	340	BDL	39.61	7050	BDL	43.18	9540	90.883
pk141C-453-4.6	760	BDL	BDL	8.66	1.21	BDL	BDL	BDL	BDL	BDL	BDL	58070	BDL	100	BDL	BDL	530	BDL	BDL	5.36	60	4600	0.44	151730	37.274
pk141C-453-4.7	3460	BDL	BDL	0.07	0.78	BDL	250	BDL	BDL	BDL	BDL	130	BDL	BDL	BDL	1870	400	100	BDL	44.73	8100	BDL	49.88	1200	97.008
pk141C-453-5.1	119650	BDL	12970	0.89	BDL	BDL																			

	Na	Ag	Au	Si	As	Hg	Tl	Zn	Se	Pb	Bi	Al	W	Cu	Te	Co	Sb	Ni	Sn	Fe	Mo	Ti	S	Ca	Total	
	ppm	ppm	ppm	% wt	% wt	ppm	ppm	ppm	ppm	ppm	ppm	ppm	ppm	ppm	ppm	ppm	ppm	ppm	ppm	% wt	ppm	% wt	ppm	% wt	ppm	% wt
Detection Limit (ppm)	50	30	100	26	40	40	160	45	45	100	100	10	100	60	50	50	30	50	30	60	50	25	20	20		
pk004C-330A_1_1	390	30	180	0.95	0.48	BDL	260	BDL	BDL	BDL	BDL	16110	BDL	1050	BDL	2220	620	1720	BDL	44.31	6600	BDL	37.80	1900	86.65	
pk004C-330A_1_2	BDL	BDL	BDL	BDL	0.08	BDL	200	BDL	BDL	BDL	BDL	60	BDL	440	BDL	820	100	550	30	46.09	8460	BDL	52.36	BDL	99.60	
pk004C-330A_1_3	BDL	40	BDL	BDL	0.12	BDL	BDL	160	BDL	1450	BDL	160	BDL	520	BDL	1720	120	390	60	45.61	8700	BDL	51.97	BDL	99.04	
pk004C-330A_2_1	210	BDL	BDL	1.76	0.21	BDL	270	BDL	BDL	BDL	BDL	29850	BDL	520	BDL	630	90	1550	BDL	41.96	7730	BDL	48.66	BDL	96.68	
pk004C-330A_2_2	BDL	BDL	BDL	0.03	0.19	BDL	400	BDL	BDL	BDL	BDL	390	BDL	580	BDL	580	110	BDL	50	45.79	8310	BDL	52.18	BDL	99.23	
pk004C-330A_2_3	BDL	750	BDL	0.17	0.03	BDL	500	6180	BDL	880	10310	6410	BDL	300	BDL	BDL	250	90	50	16.01	2840	BDL	17.97	10900	38.13	
pk153-1575_1_1	110	BDL	BDL	0.00	0.00	BDL	240	BDL	BDL	BDL	BDL	50	210	BDL	BDL	500	40	BDL	140	47.10	8500	BDL	52.55	220	100.66	
pk153-1575_1_2	BDL	BDL	BDL	0.02	3.38	BDL	270	BDL	BDL	BDL	BDL	50	160	710	BDL	680	60	BDL	90	46.01	8080	BDL	49.98	330	100.44	
pk153-1575_1_3	420	150	BDL	0.06	3.75	BDL	590	230	BDL	BDL	BDL	19530	BDL	1050	BDL	490	500	20	90	42.84	6890	120	42.94	2040	92.80	
pk153-1575_1_4	120	30	BDL	0.05	1.89	BDL	BDL	50	BDL	BDL	BDL	3810	BDL	540	BDL	1220	430	330	50	45.58	8090	BDL	50.15	BDL	99.15	
pk153-1575_1_5	80	BDL	BDL	0.00	0.02	BDL	BDL	140	BDL	BDL	BDL	20	160	130	BDL	610	130	BDL	90	46.17	8480	BDL	52.03	BDL	99.22	
pk153-1575_2_1	BDL	40	BDL	0.03	0.20	BDL	BDL	90	BDL	BDL	BDL	6040	BDL	590	80	330	590	60	BDL	26.40	3320	BDL	20.30	209850	69.03	
pk153-1575_2_2	BDL	70	BDL	0.04	0.96	BDL	290	BDL	BDL	BDL	BDL	250	BDL	1490	BDL	500	960	80	BDL	46.12	8470	BDL	51.45	970	99.87	
pk153-1575_2_3	920	90990	BDL	0.41	5.99	3100	BDL	15120	BDL	BDL	BDL	8510	BDL	226550	BDL	210	126800	370	BDL	14.90	5290	BDL	30.90	3400	100.32	
pk153-1575_2_4	BDL	50	BDL	BDL	36.99	BDL	1280	BDL	BDL	BDL	BDL	1200	BDL	450	BDL	600	330	1380	80	37.50	3840	BDL	23.68	BDL	98.62	
pk153-1575_2_5	BDL	1320	BDL	BDL	3.72	BDL	580	BDL	BDL	BDL	BDL	920	BDL	1100	BDL	530	124650	190	BDL	39.25	7630	BDL	46.12	36740	106.46	
pk153-1575_2_6	300	10470	BDL	0.53	1.36	BDL	430	310	BDL	BDL	BDL	9240	BDL	960	BDL	700	6190	380	BDL	43.18	8060	BDL	50.07	1960	98.99	
pk153-1575_3_1	BDL	330	BDL	2.49	0.15	BDL	240	60	BDL	BDL	BDL	17960	BDL	1040	BDL	500	2630	90	BDL	41.40	7010	BDL	46.44	890	93.55	
pk153-1575_3_2	BDL	600	BDL	0.01	3.39	BDL	BDL	150	BDL	BDL	BDL	30	200	7360	BDL	510	1460	BDL	100	44.71	8230	BDL	49.95	450	99.99	
pk153-1575_3_3	BDL	320	BDL	0.02	4.60	BDL	280	BDL	BDL	BDL	BDL	30	BDL	1680	BDL	670	1010	770	70	44.96	8050	BDL	49.18	240	100.07	
pk153-1575_3_4	BDL	110	BDL	0.30	3.04	BDL	400	BDL	BDL	BDL	BDL	1450	BDL	640	BDL	540	1080	220	50	44.92	8030	BDL	49.54	310	99.09	
pk153-1575_3_5	BDL	BDL	120	0.87	2.88	BDL	430	BDL	BDL	BDL	BDL	7050	BDL	470	BDL	750	640	210	60	43.95	7640	BDL	48.67	170	98.13	
pk153-1575_4_1	BDL	BDL	BDL	BDL	0.92	BDL	230	BDL	BDL	BDL	BDL	BDL	390	1110	BDL	560	1170	BDL	50	46.18	8590	BDL	51.76	370	100.11	
pk153-1575_4_2	BDL	BDL	BDL	BDL	1.58	BDL	BDL	770	BDL	BDL	BDL	BDL	100	990	BDL	660	1190	BDL	30	45.86	8370	BDL	51.46	350	100.15	
pk153-1575_4_3	BDL	3980	BDL	BDL	2.94	BDL	340	BDL	BDL	BDL	BDL	50	130	1170	BDL	540	2580	BDL	90	45.16	8110	BDL	45.56	930	95.45	
pk153-1575_4_4	BDL	BDL	BDL	0.18	2.04	BDL	200	310	BDL	BDL	BDL	1500	BDL	980	BDL	650	540	270	130	44.92	8260	2090	46.39	150	95.04	
pk153-1575_4_5	BDL	BDL	BDL	BDL	0.81	BDL	180	BDL	BDL	BDL	BDL	190	BDL	330	BDL	730	590	420	180	46.09	8300	BDL	46.96	130	94.97	
pk153-1575_4_6	BDL	BDL	200	0.66	1.08	BDL	BDL	BDL	BDL	BDL	BDL	4950	BDL	310	BDL	860	820	1060	220	43.99	8230	1340	45.18	240	92.72	
pk153-1575_5_1	BDL	BDL	BDL	0.01	4.43	80	530	70	BDL	BDL	BDL	60	BDL	1910	BDL	590	660	50	210	44.91	8010	BDL	44.40	190	94.99	
pk153-1575_5_2	BDL	BDL	BDL	0.01	0.13	BDL	210	70	BDL	BDL	BDL	200	140	80	BDL	1690	80	880	150	46.07	8550	BDL	47.49	BDL	94.90	
pk153-1575_5_3	BDL	430	BDL	0.20	4.47	BDL	460	BDL	BDL	BDL	BDL	1520	BDL	2400	BDL	640	2150	360	140	43.35	7960	BDL	43.29	780	92.98	
pk153-1575_5_4	BDL	80	BDL	0.10	4.27	BDL	430	BDL	BDL	BDL	BDL	740	BDL	940	BDL	710	1390	1360	140	44.19	7960	BDL	44.55	430	94.53	
pk153-1575_5_5	BDL	BDL	BDL	0.48	2.25	BDL	340	70	BDL	BDL	BDL	2390	BDL	590	BDL	640	1130	310	100	43.89	7990	610	44.88	400	92.95	
pk153-1575_5_6	BDL	40	BDL	0.07	4.49	BDL	560	BDL	BDL	BDL	BDL	500	410	2380	BDL	610	840	210	170	44.46	7980	BDL	44.37	250	94.78	
pk153-1575_6_1	70	140	BDL	0.48	0.74	BDL	170	BDL	BDL	BDL	BDL	6350	BDL	200	BDL	570	680	120	190	44.20	8170	BDL	45.48	230	92.78	
pk153-1575_6_2	BDL	410	BDL	0.63	0.93	BDL	160	4360	BDL	BDL	BDL	8410	8340	BDL	190	BDL	BDL	800	BDL	90	22.80	3310	BDL	19.20	290	46.19
pk153-1575_6_3	1390	70	520	0.01	0.16	50	BDL	24570	BDL	BDL	BDL	30	BDL	1310	BDL	590	1190	BDL	110	44.58	8470	BDL	47.04	310	95.64	
pk137CA-918WF_1_1	80	BDL	BDL	2.73	0.39	BDL	350	BDL	BDL	BDL	BDL	15290	BDL	210	BDL	200	690	BDL	BDL	15.36	2100	BDL	11.78	180	32.18	
pk137CA-918WF_1_2	BDL	BDL	610	0.07	4.68	70	230	BDL	BDL	BDL	BDL	90	BDL	1880	BDL	530	240	170	210	43.89	7890	BDL	44.27	10	94.10	
pk137CA-918WF_1_3	170	BDL	270	0.01	2.41	BDL	210	50	BDL	BDL	BDL	BDL	160	510	BDL	510	480	510	180	45.20	8160	BDL	45.89	80	94.63	
pk137CA-918WF_1_4	BDL	BDL	1260	0.01	5.49	BDL	210	BDL	BDL	BDL	BDL	BDL	130	2390	BDL	510	940	BDL	130	43.13	7630	BDL	42.84	240	92.81	
pk137CA-918WF_1_5	BDL	BDL	BDL	0.06	1.50	BDL	380	BDL	BDL	BDL	BDL	170	BDL	540	BDL	530	190	50	150	41.23	7230	BDL	39.93	10	83.65	
pk137CA-918WF_2_1	110	BDL	310	0.12	4.04	BDL	640	BDL	BDL	BDL	BDL	BDL	BDL	1380	BDL	420	320	BDL	60	39.91	7060	BDL	39.07	40	84.18	
pk137CA-918WF_2_2	BDL	BDL	1540	0.06	6.54	120	370	BDL	BDL	BDL	BDL	BDL	BDL	2520	BDL	630	170	BDL	110	43.33	7830	BDL	42.90	30	94.15	
pk137CA-918WF_2_3	2540	BDL	500	13.68	0.82	BDL	220	BDL	BDL	BDL	BDL	6750	BDL	760	BDL	410	200	BDL	60	20.96	3500	BDL	20.19	40	57.14	
pk137CA-918WF_2_4	130	BDL	580	0.94	4.35	BDL	540	50	BDL	BDL	BDL	BDL	BDL	1470	BDL	640	200	BDL	190	42.60	7600	BDL	42.63	10	91.66	
pk137CA-918WF_3_1	BDL	BDL	1030	0.00	5.88	BDL	380	BDL	BDL	BDL	BDL	40	BDL	191												

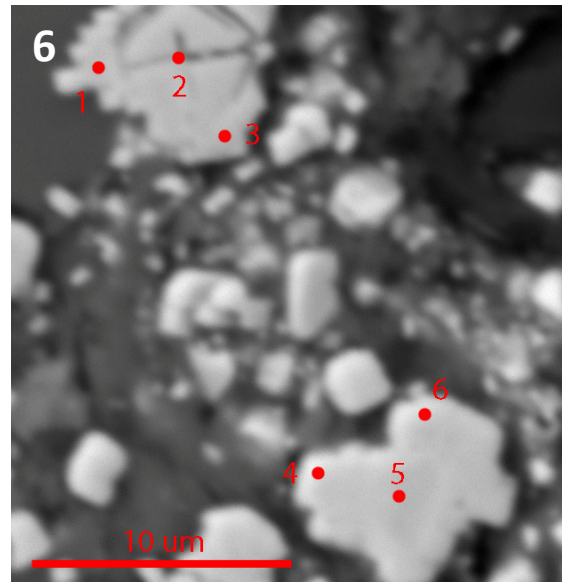
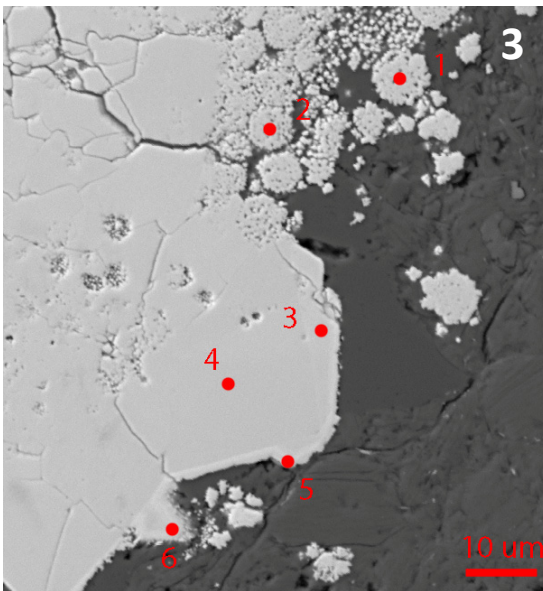
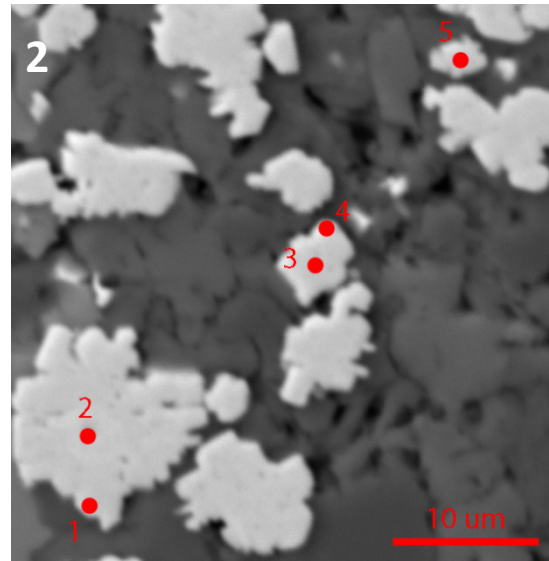
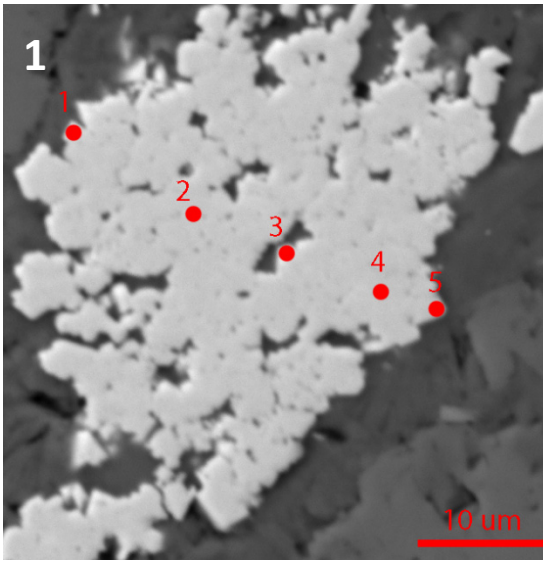
## PK137CA-857



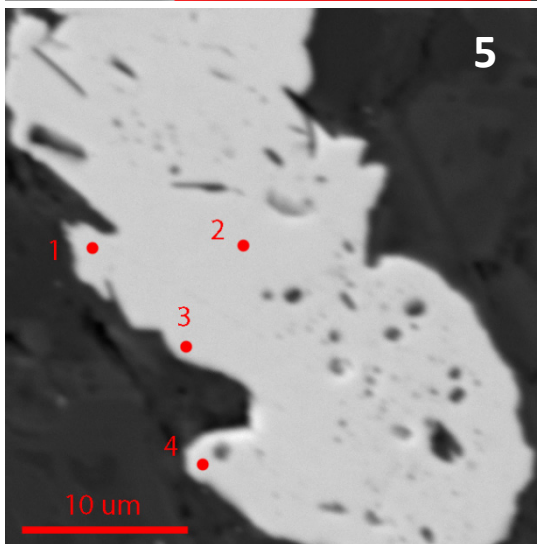
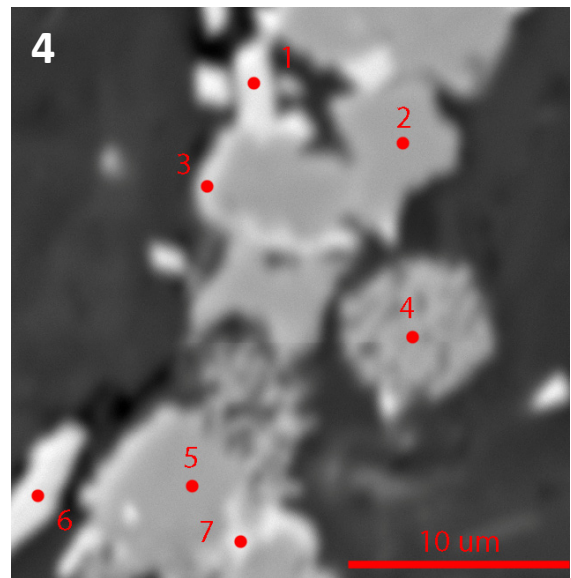
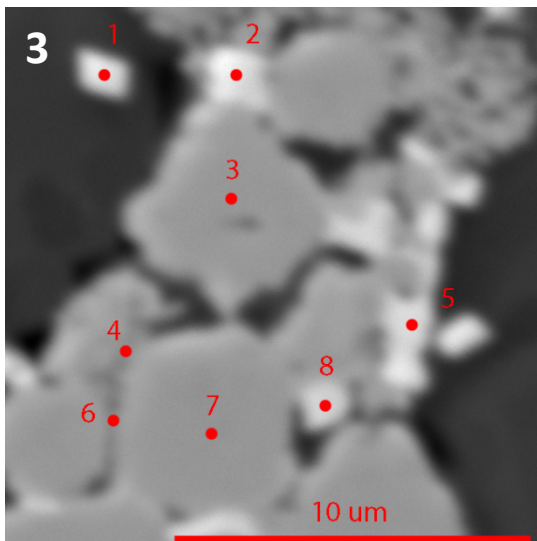
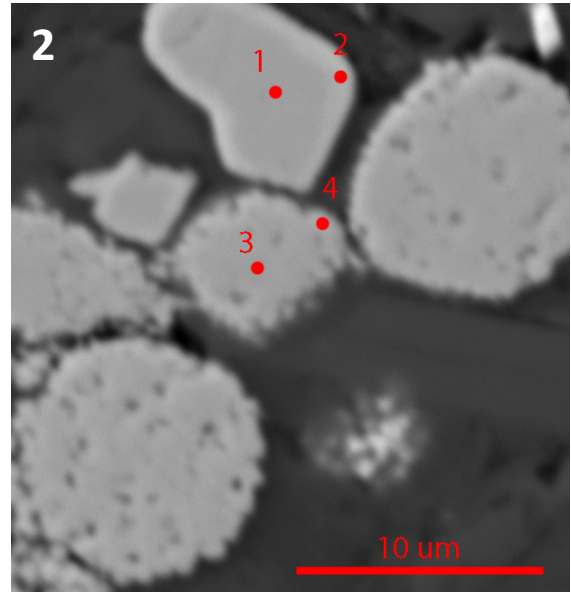
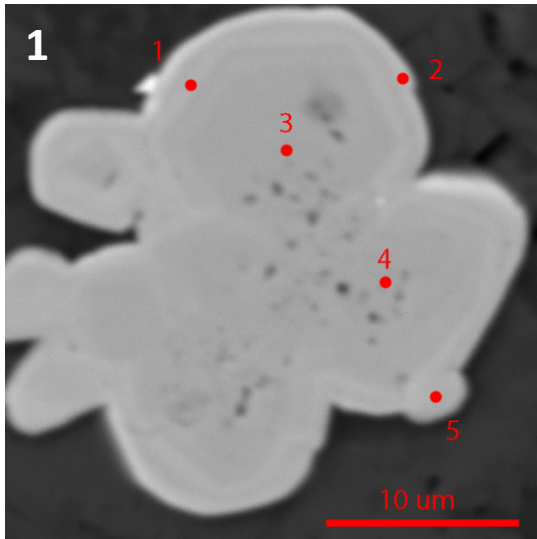
PK004C-330



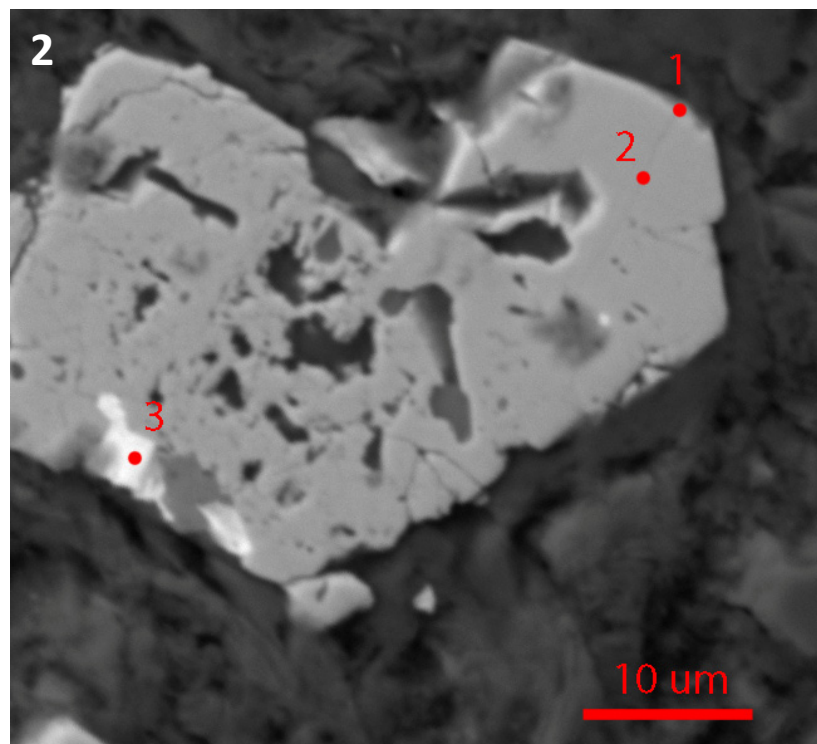
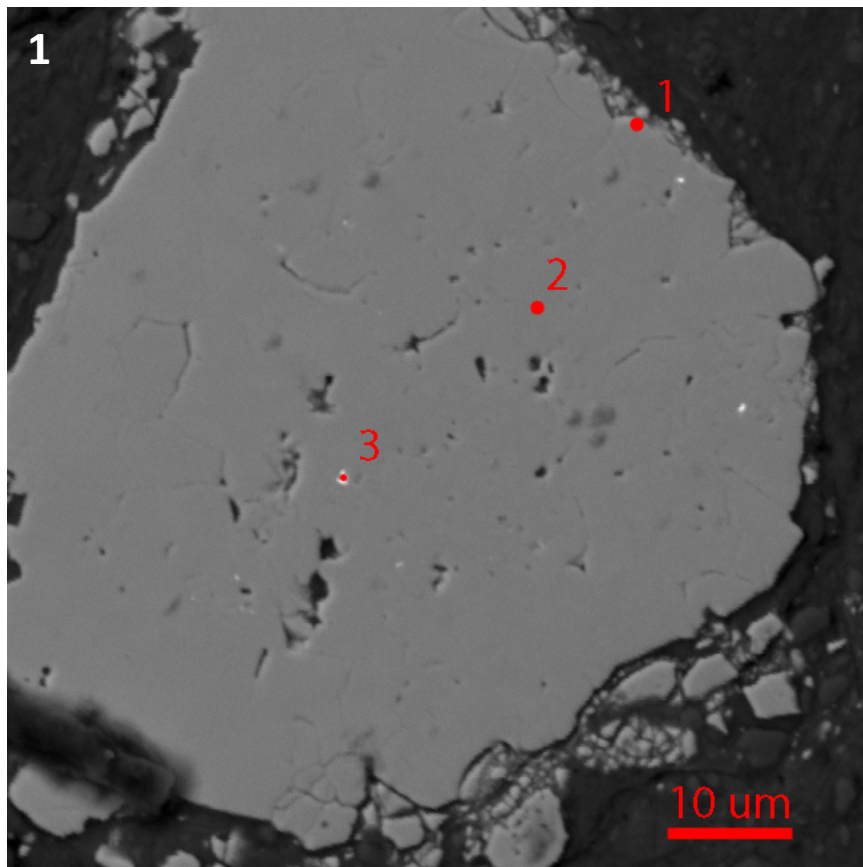
## PK004C-154



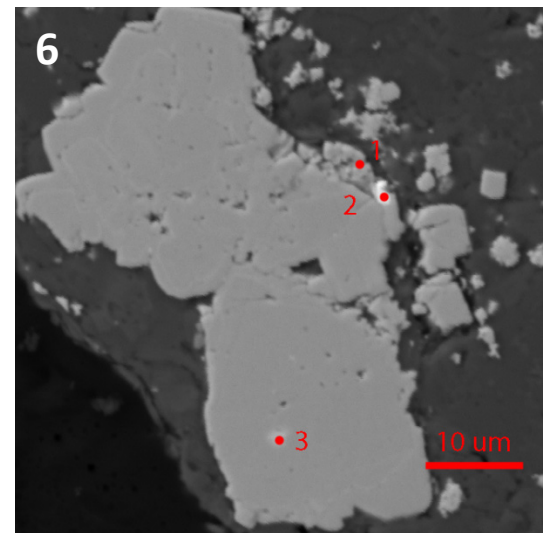
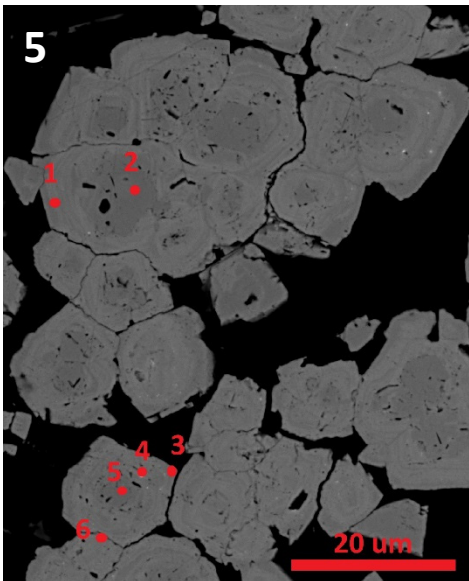
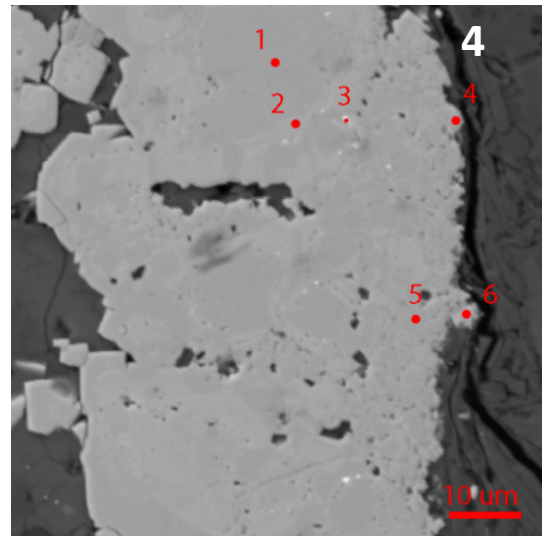
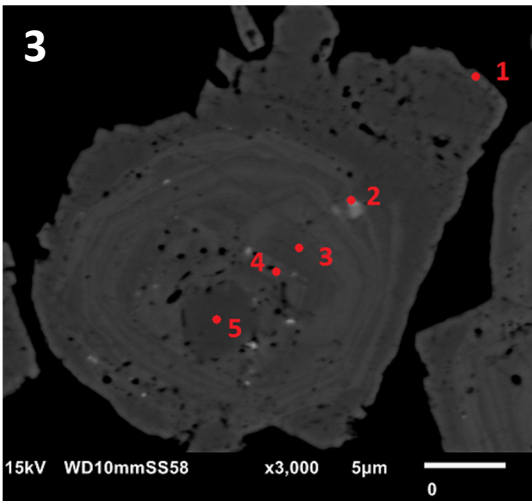
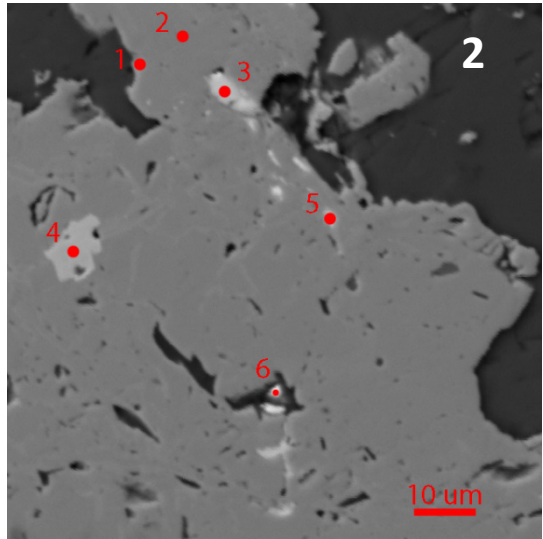
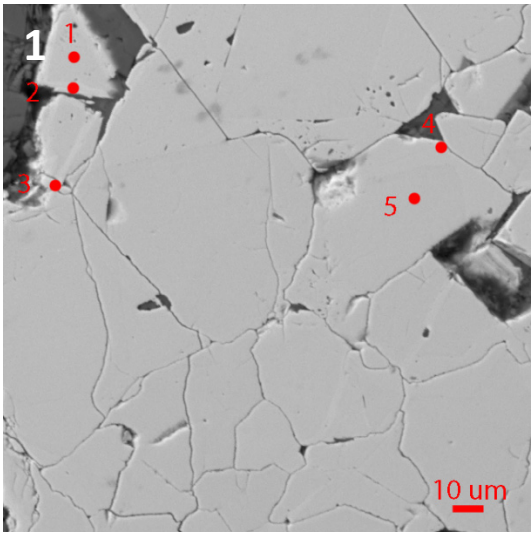
PK141C-453



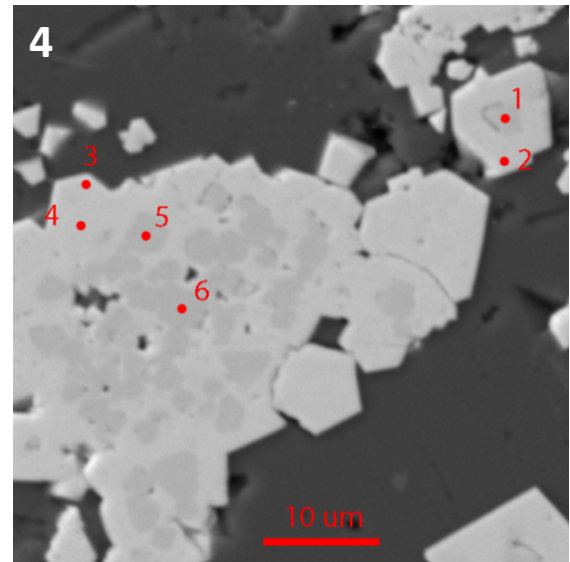
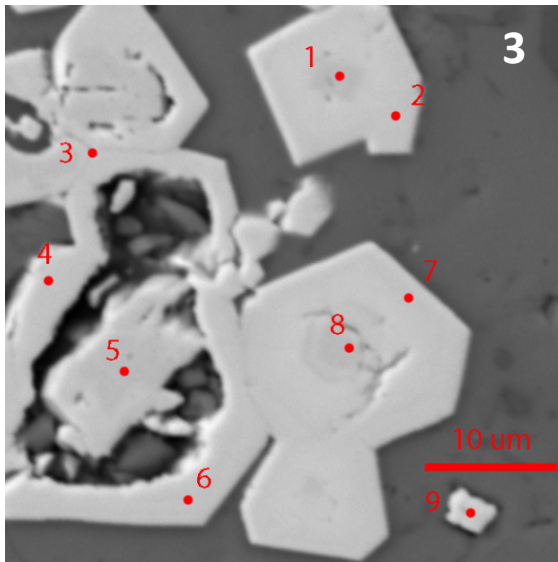
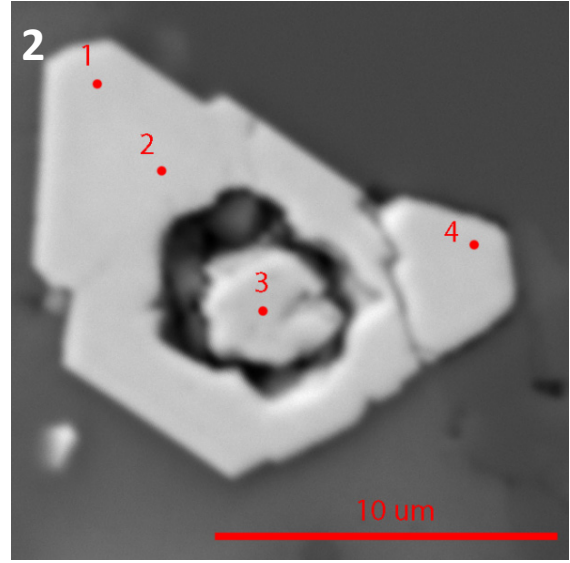
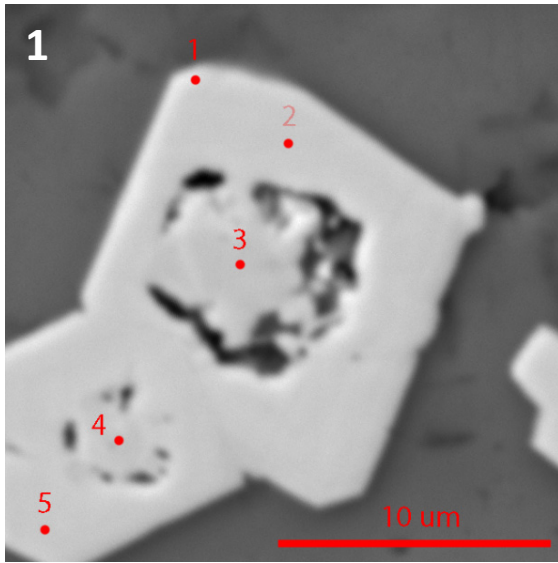
PK004C-330A



PK153-1575



PK137CA-918WF



## Appendix E: SHRIMP Methods

The following is an excerpt modified from Strickland et al., (2011). Zircon U-Th-Pb analyses were conducted on the SHRIMP-RG (reverse geometry) co-operated by U.S. Geological Survey and Stanford University in the SUMAC facility at Stanford University. Zircons, concentrated by standard heavy mineral separation processes and hand-picked for final purity, were mounted on double stick tape on glass slides in 1 X 6 mm rows, cast in epoxy, ground and polished to a 1 micron finish on a 25 mm diameter by 4 mm thick disc. All grains were imaged with transmitted light and reflected light (and incident light if needed) on a petrographic microscope, and with cathodoluminescence on a JEOL 5600 SEM to identify internal structure, inclusions and physical defects. The mounted grains were washed with a saturated EDTA solution and thoroughly rinsed in distilled water, dried in a vacuum oven, and coated with Au. Mounts typically sat in a loading chamber at high pressure ( $10^{-7}$  torr) for several hours before being moved into the source chamber of the SHRIMP-RG. Secondary ions were generated from the target spot with an  $O_2^-$  primary ion beam varying from 4 to 6 nA. The primary ion beam typically produced a spot with a diameter of 20 to 40 microns and a depth of 1 to 2 microns for an analysis time of 9 to 12 minutes. The basic acquisition routine begins with a high mass normalizing species ( $^{90}Zr_2^{16}O^+$ ) followed by  $^{204}Pb^+$ , a background measured at 0.050 mass units above  $^{204}Pb^+$ ,  $^{206}Pb^+$ ,  $^{207}Pb^+$ ,  $^{208}Pb^+$ ,  $^{238}U^+$ ,  $^{232}Th^{16}O^+$  and  $^{238}U^{16}O^+$  and  $^{232}Th^+$ . Selected sets of trace elements are also included for each analyses and are measured briefly (typically 1 sec/mass) immediately following the geochronology peaks. For zircon, these extra masses include a limited set of REE, Y, and Hf. Peak centering on both ubiquitous species and on guide peaks

adjacent to low-abundance or interference-prone species is used to eliminate any potential effects of magnet drift or peak wandering. The number of scans through the mass sequence and counting times on each peak are varied according to the sample age and the U and Th concentrations to improve counting statistics and age precision. Measurements are made at mass resolutions of  $M/\Delta M = \sim 8500$  (10% peak height), which eliminates all interfering molecular species, particularly for the REE. The SHRIMP-RG was designed to provide higher mass resolution than the standard forward geometry of the SHRIMP I and II (Clement and Compston, 1994). This design also provides very clean backgrounds and combined with the high mass resolution, the EDTA washing of the mount, and rastering the primary beam for 90 to 120 seconds over the area to be analyzed before data is collected, assures that any counts found at mass of  $^{204}\text{Pb}^+$  are actually from Pb in the zircon and not surface contamination. In practice greater than 95 percent of the spots analyzed have no common Pb. Age data for zircons were standardized against Temora (417 Ma, gabbroic diorite of Lachlan Orogen, Australia), which were analyzed repeatedly throughout the duration of the analytical session. Data reduction for geochronology follows the methods described by Williams (1997), and Ireland and Williams (2003), and use the MS Excel add-in Squid and Isoplot programs of Ludwig (2001, 2003). Data reduction for the trace element concentrations are also done in MS Excel. Average count rates of each element of interest are ratioed to the appropriate high mass normalizing species (see above) to account for any primary current drift, and the derived ratios for the unknowns are compared to an average of those for the standards to determine concentrations. Spot to spot precisions (as measured on the standards) vary according to elemental ionization efficiency and concentration. Trace

element analyses with high Fe concentrations ( $>50$  ppm), were not used in the Eu/Eu\* diagram as they are commonly associated with anomalous concentrations of Ca, Al, and F, and REEs, and may contain excess Ti from a non-zircon component (Wooden et al., 2007).

## Appendix F: SHRIMP Data

Spot	Hf (ppm)	Th (ppm)	U (ppm)	204Pb /206Pb	±%	% 206Pb <sub>2</sub>	7-corr 206Pb <sup>*</sup>	(1) 206Pb/238U Age	±%	(2) 206Pb/238U Age	±%	(1) 207Pb/206Pb Age	±%	Total 238U /206Pb	±%	Total 207Pb /206Pb	±%	(1) 207Pb <sup>*</sup> /235U	±%	(1) 206Pb <sup>*</sup> /238U	±%	err corr	
KJM004-1.1	10703	175	788	4.5E-4	58	0.70	4.2	39.5	1	39.6	1	-16	225	161	3.3	0.05233	3.5	0.03882	9.9	0.00615	3.4	0.3	
KJM004-2.1	11214	186	857	---	---	---	6.6	40.4	0.6	40.5	0.6	7.4	62	159	1.6	0.04621	2.6	0.04009	3.0	0.00629	1.6	0.5	
KJM004-3.1	10703	361	1217	1.7E-5	71	2.72	67.2	1244	17	1213	18	1686	11	5	1.5	0.10369	0.6	3.03525	1.6	0.21279	1.5	0.9	
KJM004-4.1	10814	169	378	5.8E-5	141	---	4.6	39.6	0.5	39.8	0.5	-76	101	162	1.3	0.04550	3.1	0.03797	4.3	0.00617	1.3	0.3	
KJM004-5.1	---	180	735	3.2E-4	63	0.012	3.8	38.9	0.3	39.2	0.2	-221	204	164	0.6	0.04692	3.2	0.03517	8.1	0.00606	0.7	0.09	
KJM004-7.1	---	209	1000	9.9E-5	100	0.021	5.4	40.6	0.2	40.7	0.2	-26	104	158	0.5	0.04702	2.8	0.03968	4.3	0.00632	0.6	0.13	
KJM004-8.1	---	111	642	---	---	---	3.5	41.0	0.2	41.0	0.2	41.6	82	157	0.6	0.04687	3.4	0.04124	3.5	0.00638	0.6	0.17	
KJM020-1.1	7691	110	321	---	---	---	1.6	36.8	0.5	37.0	0.6	-194	138	175	1.5	0.04256	5.5	0.03360	5.7	0.00573	1.5	0.26	
KJM020-2.1	9755	368	714	-1.3E-4	100	0.13	4.2	40.0	0.4	39.8	0.4	181	113	161	0.9	0.04783	3.1	0.04264	4.9	0.00622	0.9	0.19	
KJM020-3.1	9602	175	789	8.6E-5	141	---	3.0	40.5	0.5	40.6	0.5	-153	143	159	1.1	0.04455	3.8	0.03756	5.9	0.00629	1.1	0.20	
KJM020-4.1	10053	538	549	1.4E-4	100	---	3.7	38.0	0.4	38.3	0.4	-323	163	169	1.1	0.04254	3.5	0.03301	6.5	0.00592	1.2	0.18	
KJM033-1.1	11640	205	405	2.0E-4	63	0.01	6.0	39.7	1	39.9	1	-113	123	161	2.7	0.04688	2.5	0.03748	5.7	0.00618	2.7	0.5	
KJM033-2.1	10748	130	323	-2.1E-4	100	-0.61	2.2	40.7	0.6	40.8	0.6	-47	197	159	1.5	0.04201	4.4	0.03946	8.3	0.00633	1.5	0.2	
KJM033-2.2	10866	374	501	1.2E-3	50	-0.49	2.1	37.7	0.9	38.8	0.8	---	---	167	2.2	0.04297	5.3	0.03194	41.3	0.00587	2.5	0.1	
KJM033-3.1	9760	973	1119	1.2E-4	82	3.41	5.3	187	4	181	4	1074	54	34	2.0	0.07692	1.9	0.03498	3.4	0.02940	2.0	0.6	
KJM033-3.2	11780	183	409	7.5E-4	63	0.29	1.7	38.5	0.6	38.9	0.5	-497	534	165	1.3	0.04908	4.8	0.03126	20.1	0.00599	1.6	1.1	
KJM033-4.1	12789	77	216	7.4E-5	53	2.62	21.2	351	29	343	29	1024	26	18	8.5	0.07446	1.0	0.56690	8.6	0.05602	8.5	1.0	
KJM033-6.1	9446	155	452	9.5E-5	141	0.40	2.7	39.8	0.5	39.7	0.5	126	132	161	1.2	0.04998	3.8	0.04145	5.8	0.00619	1.3	0.2	
KJM034-1.1	10655	225	496	-5.2E-4	63	0.38	2.6	40.3	0.6	39.8	0.6	504	196	161	1.4	0.04982	3.9	0.04961	9.0	0.00627	1.5	0.2	
KJM034-2.1	11204	268	631	1.5E-4	100	0.08	3.4	40.0	0.3	40.1	0.2	-46	152	160	0.6	0.04750	3.4	0.03877	6.3	0.00622	0.6	0.1	
KJM034-3.1	11023	139	379	---	---	-0.03	2.0	39.7	0.6	39.7	0.6	29.3	109	162	1.5	0.04663	4.5	0.03967	4.8	0.00617	1.5	0.3	
KJM034-4.1	11495	478	1072	3.5E-4	50	0.32	5.6	39.2	0.8	39.3	0.8	-101	160	163	2.0	0.04932	2.5	0.03714	6.8	0.00610	2.0	0.3	
KJM034-5.1	10846	3069	2232	3.8E-5	100	0.11	11.8	39.5	0.6	39.4	0.7	56.5	50	163	1.6	0.04772	1.7	0.03993	2.7	0.00614	1.7	0.6	
KJM034-6.1	12253	277	711	4.2E-4	53	-0.04	3.6	37.2	2	37.5	2	-343	237	171	4.3	0.04647	3.1	0.03204	10.2	0.00579	4.4	0.4	
KJM034-6.2	12377	371	861	1.2E-3	37	0.59	4.2	35.8	1	36.1	1	-787	560	177	4.1	0.05144	3.4	0.02598	20.2	0.00553	4.2	0.2	
KJM034-7.1	11602	357	822	5.3E-3	119	12.75	5.1	47.6	10	46.3	10	992	4092	121	17.5	0.14791	64.3	0.07411	202.4	0.00744	21.8	0.1	
PK005C-1.1	11115	189	487	3.0E-4	82	0.25	2.6	39.4	0.7	39.5	0.7	-93	231	162	1.8	0.04885	3.9	0.03748	9.6	0.00613	1.9	0.2	
PK005C-2.1	11029	136	354	6.8E-4	63	0.17	1.9	39.0	0.6	39.5	0.5	-489	483	163	1.4	0.04814	4.6	0.03179	18.2	0.00607	1.6	0.1	
PK005C-3.1	12522	124	379	---	---	---	0.90	2.0	40.6	0.3	40.3	0.3	368	91	158	0.6	0.05394	4.0	0.04703	4.1	0.00632	0.6	0.2
PK005C-4.1	11391	196	464	-1.9E-4	100	0.16	2.4	39.5	0.7	39.3	0.7	232	149	163	1.7	0.04807	3.7	0.04304	6.7	0.00614	1.8	0.3	
PK005C-5.1	8875	4469	2284	3.9E-4	32	0.50	10.9	35.7	1	35.8	1	-58	109	179	3.5	0.05071	1.7	0.03444	5.7	0.00555	3.5	0.6	
PK005C-6.1	11225	186	460	6.2E-4	58	0.05	2.5	39.6	1	40.0	1	-486	401	161	2.5	0.04726	4.0	0.03225	15.3	0.00616	2.6	0.2	
PK005C-7.1	11557	279	795	---	---	---	0.17	4.2	39.2	0.7	39.2	0.7	105	68	164	1.7	0.04814	2.9	0.04051	3.3	0.00610	1.7	0.5
PK005C-8.1	11740	50	249	8.8E-6	141	1.51	24.7	714	20	704	20	1072	19	9	2.9	0.07527	0.9	1.21285	3.1	0.11706	2.9	1.0	
PK034C-1.1	9463	214	325	1.7E-3	47	-0.19	1.5	34.3	0.8	35.5	0.7	---	---	181	1.9	0.04524	5.6	0.01452	64.4	0.00534	2.4	0.0	
PK034C-1.2	11780	113	440	-3.8E-4	82	0.23	2.2	37.2	0.5	36.9	0.5	377	208	174	1.3	0.04856	4.4	0.04326	9.3	0.00579	1.4	0.2	
PK034C-2.1	9647	354	669	1.0E-3	39	1.18	3.3	36.5	0.7	36.8	0.7	-294	423	173	1.9	0.05615	5.2	0.03205	16.7	0.00568	2.0	0.1	
PK034C-3.1	---	510	904	1.3E-4	100	0.005	4.3	35.5	0.4	35.6	0.4	-64	133	180	1.2	0.04679	3.2	0.03419	5.6	0.00553	1.2	0.21	
PK034C-4.1	---	284	270	7.9E-4	71	0.584	1.3	35.5	0.4	35.9	0.3	-376	581	178	0.6	0.05138	5.3	0.03021	22.4	0.00553	1.2	0.06	
PK034C-5.1	---	173	296	1.4E-3	50	-0.053	1.4	33.5	0.5	34.4	0.2	---	---	187	0.6	0.04631	5.3	0.01805	44.4	0.00521	1.5	0.03	
PK034C-6.1	---	433	440	3.7E-4	82	-0.052	2.1	36.0	0.4	36.3	0.3	-293	307	177	0.9	0.04635	4.5	0.03161	12.1	0.00560	1.0	0.09	
PK034C-7.1	---	285	621	3.3E-4	71	0.359	3.1	37.2	0.3	37.3	0.2	-71	214	172	0.6	0.04963	3.6	0.03570	8.8	0.00579	0.7	0.08	
PK034C330-1.1	12345	218	577	2.5E-4	82	-0.30	3.1	39.3	0.6	39.6	0.5	-305	219	163	1.4	0.04444	3.8	0.03432	8.7	0.00611	1.4	0.2	
PK034C330-2.1	11054	234	492	5.0E-4	63	0.10	2.6	38.9	0.7	39.2	0.7	-338	327	164	1.8	0.04765	3.9	0.03358	12.8	0.00605	1.9	0.1	
PK034C330-2.2	12621	289	954	5.8E-4	41	0.19	5.0	39.2	0.8	39.6	0.8	-368	250	162	1.9	0.04837	2.9	0.03344	9.8	0.00610	1.9	0.2	
PK034C330-3.1	12096	179	549	---	---	---	0.05	2.9	39.8	0.6	39.7	0.6	59.1	85	162	1.6	0.04722	3.6	0.04027	3.9	0.00619	1.6	0.4
PK034C330-3.2	10464	265	646	-1.4E-4	100	-0.22	3.4	38.8	2	38.8	2	56.3	131	166	6.2	0.04507	4.1	0.03931	8.3	0.00604	6.3	0.8	
PK034C330-4.1	10933	167	433	3.1E-4	82	0.50	2.3	40.2	0.6	40.3	0.6	3.8	224	159	1.4	0.05079	3.9	0.03983	9.4	0.00626	1.5	0.2	
PK034C330-4.2	10650	237	424	-1.0E-4	141	0.41	2.3	39.9	0.5	39.7	0.5	265	127	161	1.3	0.05007	3.9	0.04415	5.7	0.00621	1.3	0.2	
pk089C-1.1	8942	55	89	2.9E-3	10	10.67	21.7	1698	50	1603	53	2383	78	3	3.3	0.19110	2.9	6.37229	5.7	0.30132	3.3	0.6	
PK089C-2.1	12015	428	852	2.6E-4	63	-0.30	4.6	40.4	0.9	40.7	0.9	-315	175	158	2.2	0.04445	2.9	0.03518	7.2	0.00629	2.2	0.3	
pk089C-3.1	7709	1430	762	---	---	-0.18	3.7	36.6	0.6	36.7	0.6	-39	82	175	1.5	0.04533	3.4	0.03563	3.7	0.00570	1.5	0.4	
pk089C-4.1	20592	393	6632	1.5E-2	6	28.89	18.3	21.0	0.8	20.6	0.8	652	699	222	3.4	0.27488	2.9	0.02765	32.8	0.00327	4.0	0.4	
pk089C-5.1	11788	485	1751	1.0E-4	71	-0.06	8.6	36.5	1	36.6	1	-69	83	176	2.8	0.04627	2.3	0.03508	4.4	0.00568	2.8	0.6	
pk089C-6.1	10880	150	477	-2.0E-4	100	-0.05	2.4	38.1	0.7	38.0	0.7	164	164	169	1.7	0.04642	4.0	0.04033	7.2	0.00593	1.8	0.2	
pk089C-6.2	9869	188	507	---	---	---	0.09	2.5	36.5	0.6	36.4	0.6	74	3	176	1.6	0.04752	3.8	0.03718	4.1	0.00567	1.6	0.4
pk089C-7.1	12757	116	476	7.9E-4	50	0.21	2.5	39.0	0.5	39.5	0.4	-574	460	162</									

RTH24-1.1	9488	725	1639	3.4E-4	45	0.20	7.5	34.3	0.8	34.5	0.8	-148	143	186	2.3	0.04834	2.3	0.03190	6.2	0.00534	2.3	0.4
RTH24-2.1	9655	485	1344	1.4E-3	32	1.90	5.6	30.9	1	31.1	1	-252	423	203	3.7	0.06170	2.9	0.02760	17.1	0.00481	3.8	0.2
RTH24-3.1	10006	256	555	2.6E-4	82	-0.14	3.1	40.9	0.4	41.2	0.4	-230	214	156	1.0	0.04577	3.7	0.03686	8.5	0.00637	1.0	0.1
RTH24-4.1	6975	183	387	---	---	1.535	1.9	36.9	0.2	36.4	0.3	563	101	174	0.6	0.05891	4.6	0.04667	4.7	0.00575	0.6	0.14
RTH24-5.1	8021	157	360	5.7E-4	71	-0.211	1.7	35.6	0.6	36.0	0.5	-584	475	179	1.5	0.04509	4.8	0.02795	17.6	0.00553	1.6	0.09
RTH24-6.1	8083	359	603	1.1E-3	39	0.011	3.1	38.1	0.4	38.9	0.3	---	---	165	0.7	0.04691	3.7	0.02425	24.0	0.00592	1.1	0.05
RTH24-7.1	8877	273	565	1.2E-3	41	-0.305	2.7	35.0	0.4	35.9	0.2	---	---	180	0.6	0.04435	4.2	0.01929	31.2	0.00544	1.1	0.04
RTH69-1.1	7671	162	356	1.4E-4	141	0.404	1.7	34.9	0.4	34.8	0.4	88.9	189	184	1.0	0.04994	4.6	0.03577	8.0	0.00543	1.1	0.13
RTH69-2.1	12503	123	913	-6.9E-6	100	4.975	48.8	409	3	389	3	1522	24	15	0.7	0.09462	1.3	0.85488	1.5	0.06546	0.7	0.48
RTH69-3.1	9512	271	786	4.6E-4	53	0.345	3.8	35.7	0.5	35.9	0.4	-188	234	179	1.2	0.04949	3.1	0.03266	9.5	0.00555	1.3	0.13
RTH69-4.1	8212	140	405	1.1E-3	47	0.208	1.9	34.2	0.6	34.8	0.5	-1011	842	184	1.4	0.04838	7.5	0.02311	28.4	0.00532	1.7	0.06
RTH69-5.1	8533	89	253	---	---	0.203	1.2	36.9	0.6	36.8	0.6	117	135	174	1.7	0.04838	5.7	0.03824	6.0	0.00573	1.7	0.29
RTH69-6.1	8696	275	556	8.9E-5	141	0.546	2.7	36.7	0.5	36.6	0.5	184	122	175	1.3	0.05109	3.6	0.03920	5.4	0.00571	1.3	0.25
RTH69-7.1	7760	177	386	1.1E-3	47	-0.223	1.9	35.2	0.6	36.0	0.5	---	---	179	1.4	0.04500	4.6	0.02094	30.9	0.00547	1.8	0.06
RTH69-8.1	8969	555	1071	9.5E-5	100	0.325	5.2	36.2	0.3	36.2	0.3	94.7	95	177	0.8	0.04933	2.7	0.03725	4.1	0.00564	0.8	0.20
RTH69-9.1	10200	587	1192	-1.2E-4	82	0.024	6.0	37.5	0.2	37.4	0.2	131	87	172	0.5	0.04697	2.5	0.03911	3.7	0.00583	0.6	0.15
RTH69-10.1	6765	1968	1472	2.1E-4	58	0.158	7.1	36.1	0.3	36.2	0.3	-59	113	177	0.7	0.04801	2.3	0.03482	4.7	0.00562	0.7	0.16
RTH82-2.1	11172	267	565	6.5E-4	50	0.329	3.1	40.0	0.4	40.4	0.3	-370	341	159	0.7	0.04945	3.5	0.03412	13.2	0.00623	1.0	0.07
RTH82-3.1	8973	252	344	5.7E-4	71	-0.331	1.8	38.9	0.5	39.5	0.4	-654	497	163	1.1	0.04421	4.9	0.02982	18.1	0.00606	1.3	0.07
RTH82-4.1	7856	102	142	9.7E-4	82	-0.183	0.8	39.4	0.7	40.2	0.4	-1079	1234	160	0.8	0.04539	7.3	0.02607	40.9	0.00614	1.7	0.04
RTH82-5.1	9477	192	272	-1.9E-4	141	0.049	1.4	39.5	0.4	39.3	0.4	194	219	163	1.0	0.04721	5.5	0.04236	9.5	0.00614	1.1	0.12
RTH82-6.1	8605	280	275	6.5E-4	71	-0.105	1.5	39.7	0.6	40.2	0.5	-610	553	160	1.3	0.04601	5.2	0.03088	20.4	0.00617	1.6	0.08
RTH82-7.1	9698	240	734	-3.4E-5	141	0.658	6.7	68.8	0.9	68.3	0.9	333	57	93	1.3	0.05261	2.2	0.07854	2.9	0.01073	1.4	0.47
RTH82-8.1	8571	53	216	-5.2E-5	71	1.794	19.6	657	8	646	8	1111	26	9	1.3	0.07591	1.1	1.13469	1.8	0.10736	1.3	0.70
RTH82-9.1	11442	181	628	2.6E-4	41	1.745	11.0	131	1	130	1	559	95	48	0.9	0.06252	3.3	0.16682	4.5	0.02058	0.9	0.21
RTH82-10.1	9893	348	476	2.9E-4	82	0.015	2.5	39.8	0.5	40.0	0.5	-190	235	161	1.2	0.04696	3.9	0.03637	9.5	0.00619	1.3	0.14

Errors are 1-sigma; Pb<sub>2</sub> and Pb\* indicate the common and radiogenic portions, respectively.

Error in Standard calibration was 0.30% (not included in above errors but required when comparing data from different mounts).

(1) Common Pb corrected using measured 204Pb.

(2) Common Pb corrected by assuming 206Pb/238U-207Pb/235U age-concordance

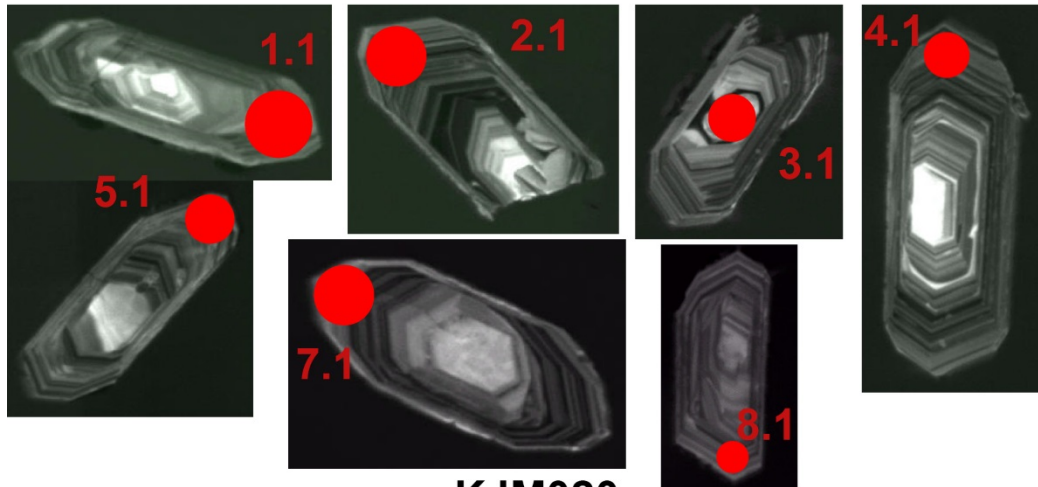
## SHRIMP Trace Element Data

	48Ti (ppm)	49Ti (ppm)	48Ti Temp (act 1.0)	Fe (ppm)	Y (ppm)	La (ppm)	Ce (ppm)	Nd (ppm)	Sm (ppm)	Eu (ppm)	Gd (ppm)	Dy (ppm)	Er (ppm)	Yb (ppm)	Hf (ppm)	Eu/Eu*
KJM004-1.1	4.12	4.08	698	1.99	1120	1.556	28.0	0.56	1.28	0.82	14.1	76	209	545	11287	0.586
KJM004-2.1	3.23	3.26	677	0.45	1240	0.010	29.6	0.32	1.54	0.93	18.6	95	221	483	11826	0.528
KJM004-3.1	4.11	4.33	697	3.84	1499	0.026	41.1	0.99	3.10	0.50	33.3	137	268	485	11286	0.151
KJM020-1.1	4.07	4.07	697	2.88	1145	1.639	27.9	0.56	1.19	0.76	13.6	77	214	565	10703	0.578
KJM020-2.1	3.19	3.25	676	0.65	1267	0.011	29.5	0.32	1.44	0.87	18.0	97	226	501	11214	0.520
KJM020-3.1	4.06	4.31	696	5.56	1532	0.027	40.9	1.00	2.89	0.47	32.1	139	274	503	10703	0.148
KJM020-4.1	3.38	3.42	681	0.75	1266	0.021	25.4	0.22	1.00	0.74	14.2	84	234	608	10814	0.600
KJM033-1.1	6.62	7.05	740	0.65	2822	0.049	114.9	1.80	5.93	2.96	61.5	260	494	925	11640	0.473
KJM033-2.1	3.89	3.98	693	0.19	847	0.013	35.4	0.44	1.44	0.81	14.5	69	157	350	10748	0.543
KJM033-2.2	3.99	4.52	695	3.43	708	1.582	40.2	0.54	1.68	0.88	13.5	54	116	253	10866	0.560
KJM033-3.1	12.66	14.58	804	0.83	1346	0.081	14.1	3.05	5.80	1.29	42.3	142	226	367	9760	0.252
KJM033-3.2	3.38	3.69	681	2.42	653	0.048	27.3	0.31	1.11	0.61	10.5	51	117	262	11780	0.541
KJM033-4.1	10.56	12.52	785	1.81	838	0.285	19.5	0.80	1.71	0.73	16.2	67	147	340	12789	0.425
KJM033-6.1	4.89	5.10	713	0.46	950	0.024	61.9	0.82	2.08	1.24	18.1	74	164	366	9446	0.617
KJM034-1.1	4.33	4.55	702	0.21	924	0.012	40.0	0.49	1.45	0.94	15.5	71	157	369	10655	0.601
KJM034-2.1	3.67	3.56	688	0.26	770	0.016	35.2	0.38	0.98	0.65	10.3	52	134	362	11204	0.622
KJM034-3.1	10.22	4.23	782	1.38	752	4.087	36.1	3.00	1.86	0.92	13.4	60	137	329	11023	0.564
KJM034-4.1	5.38	5.60	721	1.57	1080	0.054	51.2	0.65	1.61	0.90	16.5	77	185	479	11495	0.532
KJM034-5.1	5.44	6.10	722	2.07	5235	0.048	172.6	1.76	6.38	3.51	79.7	391	850	1660	10846	0.475
KJM034-6.1	2.92	2.75	669	0.55	1606	0.045	39.7	1.48	3.58	2.06	33.4	132	281	619	12253	0.575
KJM034-6.2	3.54	3.53	685	0.44	945	0.200	42.6	0.36	1.22	0.68	13.0	60	154	401	12377	0.519
KJM034-7.1	4.11	4.24	697	9.53	843	0.581	40.3	0.47	1.37	0.84	13.0	61	138	335	11602	0.606
PK005C-1.1	3.70	3.66	689	0.03	732	0.011	29.8	0.38	1.09	0.69	11.1	51	129	344	11115	0.600
PK005C-2.1	4.18	4.51	699	0.45	692	0.030	24.0	0.29	1.11	0.67	10.8	54	126	301	11029	0.588
PK005C-3.1	2.89	2.72	668	0.13	1071	0.014	17.8	0.16	1.07	0.61	15.2	90	195	416	12522	0.466
PK005C-4.1	3.57	3.71	686	0.04	585	0.013	27.5	0.39	1.03	0.60	10.7	44	103	251	11391	0.552
PK005C-5.1	8.52	9.60	764	35.39	5700	0.398	386.8	7.73	16.23	8.33	124.8	462	852	1635	8875	0.564
PK005C-6.1	4.19	4.27	699	0.07	844	0.013	34.0	0.37	1.42	0.86	13.6	61	147	353	11225	0.598
PK005C-7.1	2.89	2.76	668	0.07	1516	0.012	28.4	1.02	2.98	1.76	29.0	124	262	580	11557	0.576
PK005C-8.1	5.40	6.20	721	-0.48	805	0.260	13.4	0.54	1.70	0.38	16.1	73	147	302	11740	0.223
PK034C-1.1	5.49	6.34	723	0.14	639	0.013	21.1	0.86	2.34	0.58	18.4	64	105	190	9463	0.268
PK034C-1.2	2.34	2.14	652	0.05	640	0.011	9.1	0.17	0.91	0.30	10.5	57	115	232	11780	0.292
PK034C-2.1	5.69	6.66	726	95.20	712	0.081	22.0	0.90	2.22	0.62	19.6	70	122	229	9647	0.287
PK034C330-1.1	2.90	2.33	669	0.13	556	0.002	26.9	0.28	0.85	0.48	7.6	38	97	278	12345	0.574
PK034C330-2.1	4.26	4.34	700	0.06	869	0.076	38.7	0.61	1.63	0.93	15.9	69	152	360	11054	0.557
PK034C330-2.2	3.20	3.20	677	1.19	1896	0.084	22.7	0.58	2.24	1.40	27.4	144	329	707	12621	0.546
PK034C330-3.1	3.03	2.83	672	0.04	580	0.008	22.4	0.28	0.83	0.54	9.4	40	100	281	12096	0.585
PK034C330-3.2	3.79	3.68	690	0.06	998	0.007	35.0	0.57	1.71	0.98	17.0	80	181	422	10464	0.554
PK034C330-4.1	3.73	4.07	689	0.03	780	0.011	29.0	0.35	1.29	0.74	12.9	57	137	341	10933	0.556
PK034C330-4.2	3.34	3.62	680	0.07	1182	0.008	31.9	1.03	3.16	1.68	26.8	103	200	410	10650	0.558
PK089C-1.1	62.19	92.35	1001	2112.63	1674	0.520	10.9	2.61	5.70	2.29	49.6	171	278	434	8942	0.416
PK089C-2.1	3.39	3.24	681	0.10	670	0.013	37.3	0.47	1.10	0.66	11.7	50	113	278	12015	0.562
PK089C-3.1	7.04	8.11	746	240.15	4537	0.215	145.5	15.99	27.01	14.29	158.1	440	690	1253	7709	0.666
PK089C-4.1	51.05	56.79	973	580.14	8745	30.219	704.8	118.88	109.87	72.71	328.0	922	1166	2173	20592	1.168
PK089C-5.1	3.85	3.68	692	0.56	1369	0.035	52.2	1.49	4.11	1.56	34.3	118	215	445	11788	0.402
PK089C-6.1	3.84	4.11	692	0.16	581	0.007	32.3	0.34	1.20	0.50	12.0	53	101	215	10880	0.401
PK089C-6.2	3.60	3.51	686	0.87	934	0.013	23.6	0.70	2.14	0.63	19.0	83	159	317	9869	0.300
PK089C-7.1	2.35	2.22	652	5.89	413	0.207	31.0	0.29	0.66	0.43	5.0	25	71	226	12757	0.716
PK089C-8.1	2.83	2.70	667	0.04	999	0.009	20.6	0.24	0.93	0.62	11.1	63	176	479	11969	0.584
PK101D-1.1	3.48	3.39	684	0.08	654	0.013	26.6	0.26	0.99	0.60	9.1	45	114	306	11714	0.604
PK101D-2.1	2.50	2.28	657	0.05	393	0.012	17.0	0.15	0.53	0.34	5.6	28	70	195	12361	0.605
PK101D-2.2	11.27	14.05	792	63.15	826	0.259	22.0	2.19	3.83	1.90	26.9	88	148	295	10483	0.572
PK101D-3.1	3.35	3.66	680	3.57	1313	0.250	44.0	0.67	1.92	1.56	19.6	86	205	531	13098	0.773
PK101D-4.1	3.70	3.79	689	0.05	647	0.009	32.5	0.40	1.29	0.74	13.0	51	113	257	11258	0.550
PK101D-4.2	2.95	2.71	670	0.11	1106	0.016	24.2	0.64	1.67	1.00	17.3	79	183	438	11538	0.567
PK101D-5.1	3.51	3.70	684	0.50	801	0.518	47.4	0.87	1.73	1.09	15.6	59	130	300	11704	0.635
PK101D-6.1	2.81	2.90	666	3.95	506	0.969	14.7	0.34	0.74	0.61	6.2	32	80	250	14275	0.857
PK101E-1.1	4.54	5.13	706	0.11	920	0.010	42.8	0.69	1.79	0.99	17.7	74	166	377	9867	0.537
PK101E-2.1	2.24	2.11	648	0.20	612	0.007	19.7	0.19	0.70	0.42	7.5	40	109	315	11473	0.564
PK101E-3.1	2.77	2.79	665	0.25	828	0.218	28.3	0.54	1.02	0.68	11.8	57	138	362	11347	0.603
PK119D-1.1	9.74	15.13	777	10.29	1240	0.258	43.7	1.50	3.09	1.58	23.2	98	210	468	9877	0.569
PK119D-2.1	3.87	3.87	692	0.71	1166	0.021	38.7	0.42	1.49	0.89	17.1	84	207	515	10243	0.540
PK119D-3.1	3.27	3.18	678	0.05	882	0.010	29.0	0.33	1.25	0.73	12.8	64	151	361	10514	0.558
RTH24-1.1	2.10	1.78	643	0.51	3150	0.103	19.9	4.20	11.13	1.92	93.3	317	512	866	9488	0.182
RTH24-2.1	6.98	7.55	745	685.74	1982	3.348	239.2	9.60	11.51	3.54	66.7	202	277	455	9655	0.390
RTH24-3.1	4.75	5.68	710	0.62	1125	0.020	49.4	0.60	1.89	1.03	18.5	88	202	446	10006	0.529
RTH82-1.1	8.94	10.74	769	0.25	2276	0.019	79.5	1.72	4.38	2.18	41.8	195	423	858	9690	0.491

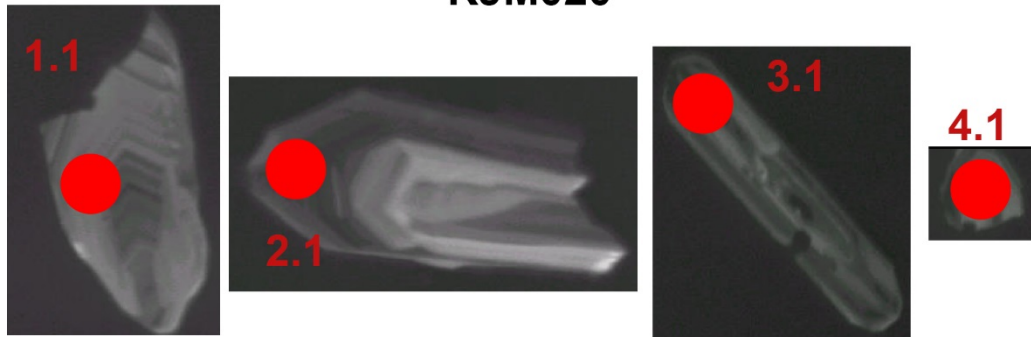
Fe ppm values in red denote possible contamination by an inclusion.

## Zircon CL images showing locations of SHRIMP analyses

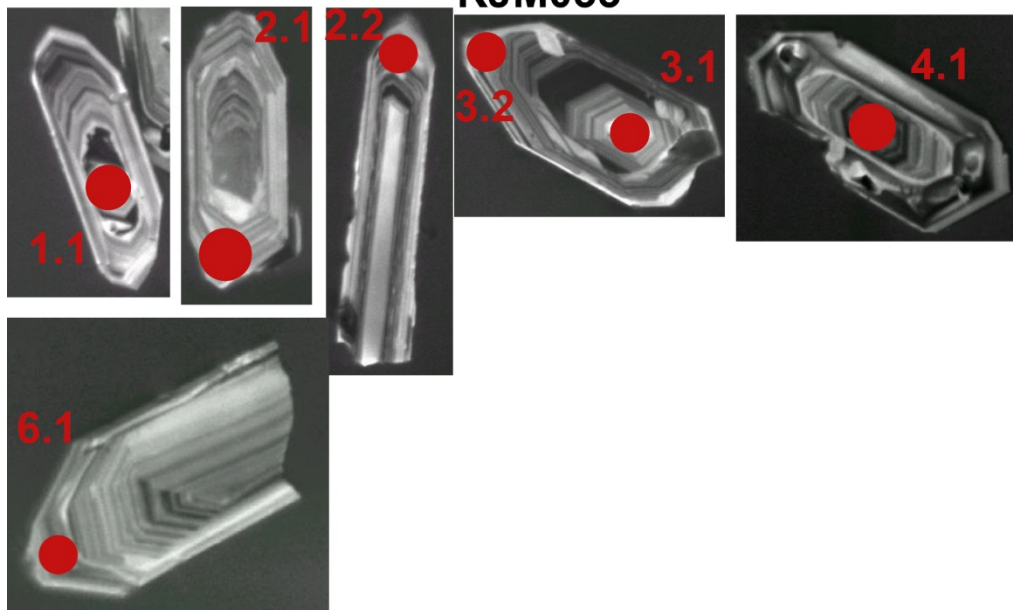
## KJM004



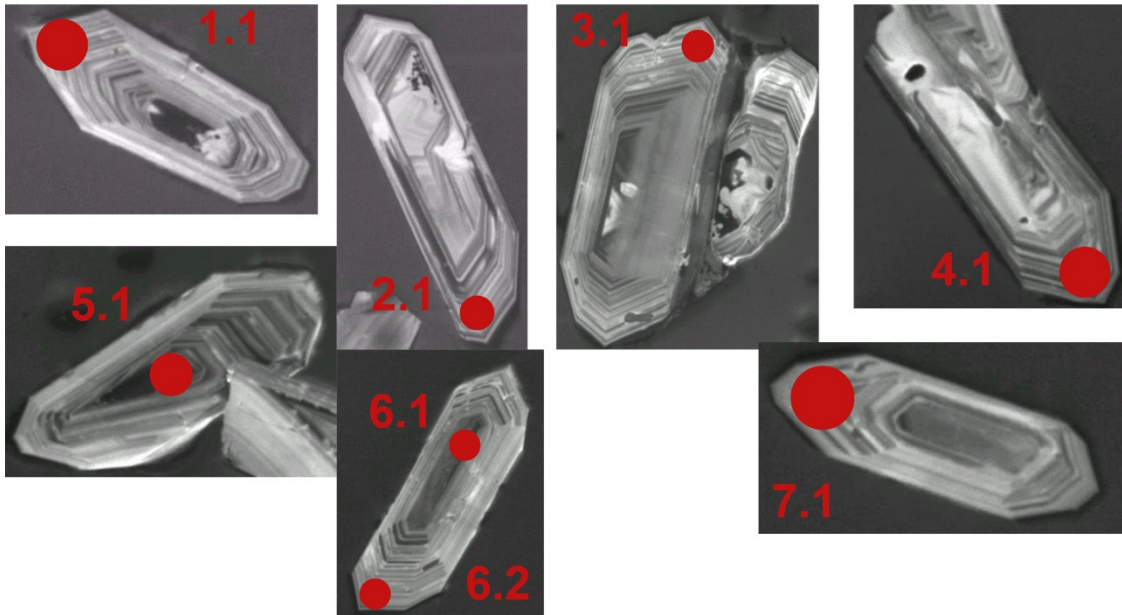
## KJM020



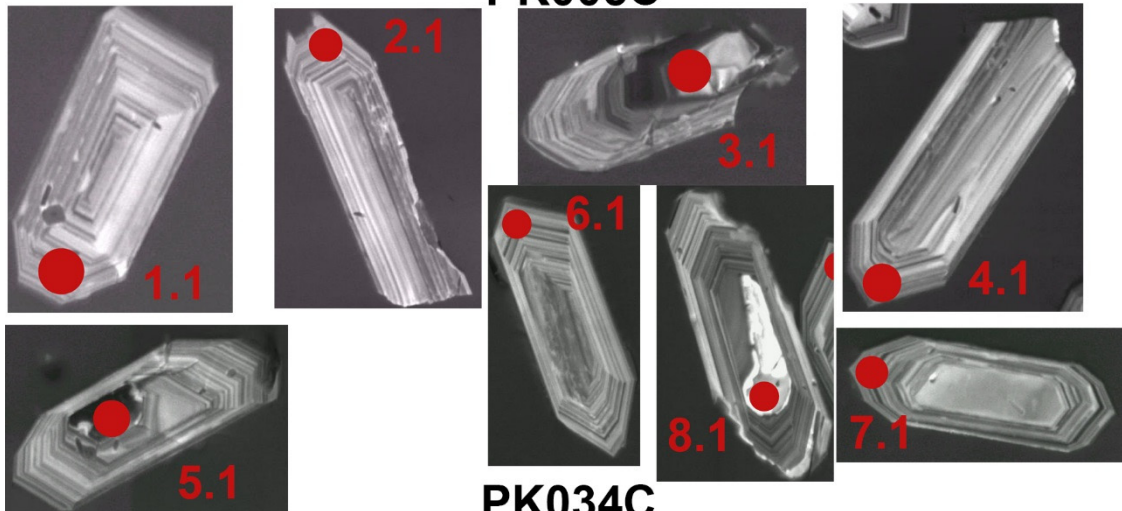
## KJM033



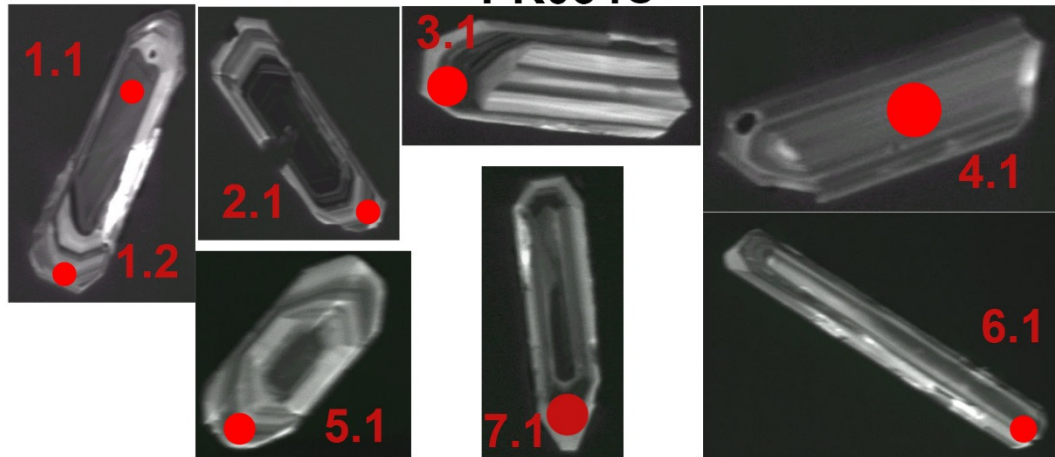
### KJM034



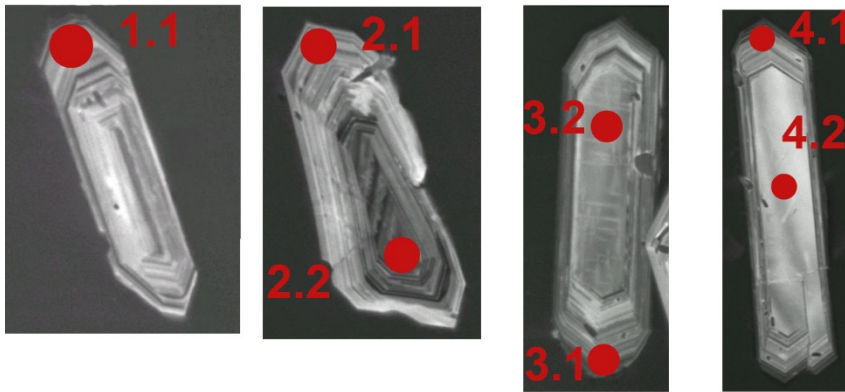
### PK005C



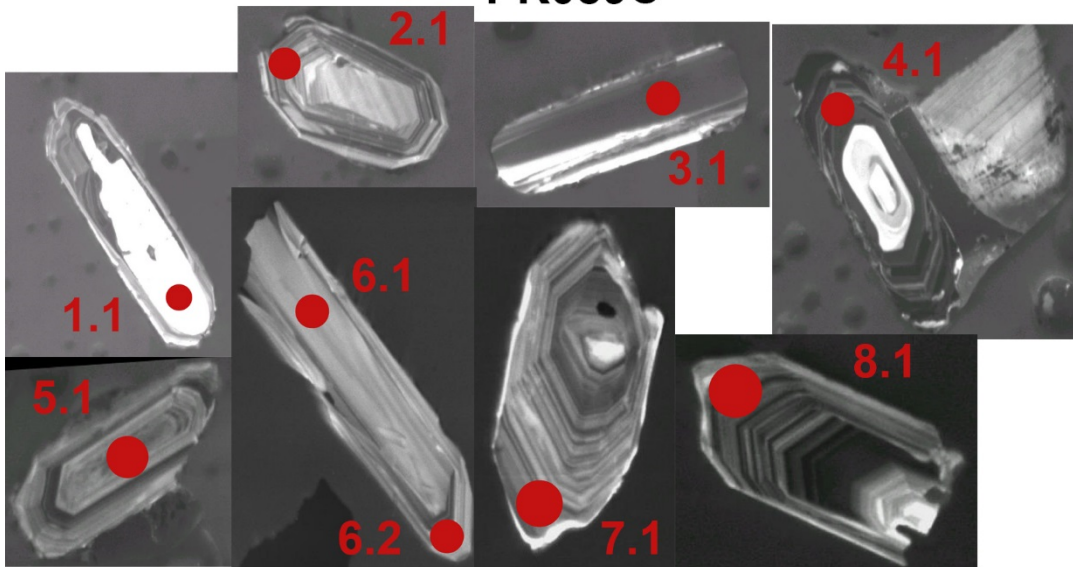
### PK034C



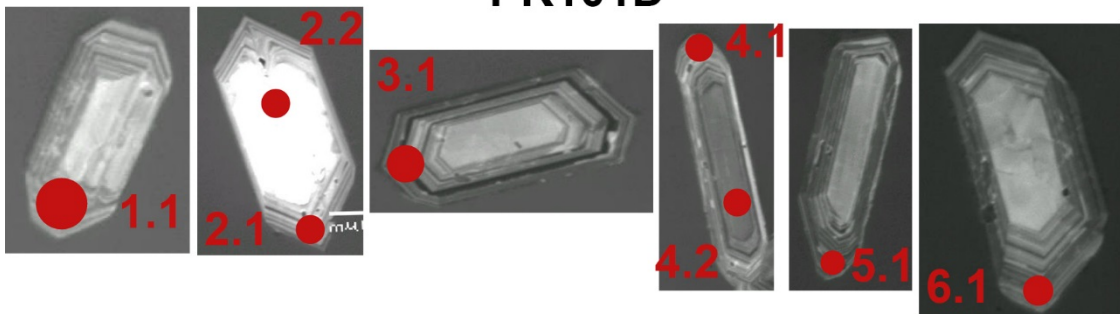
### PK034C-330

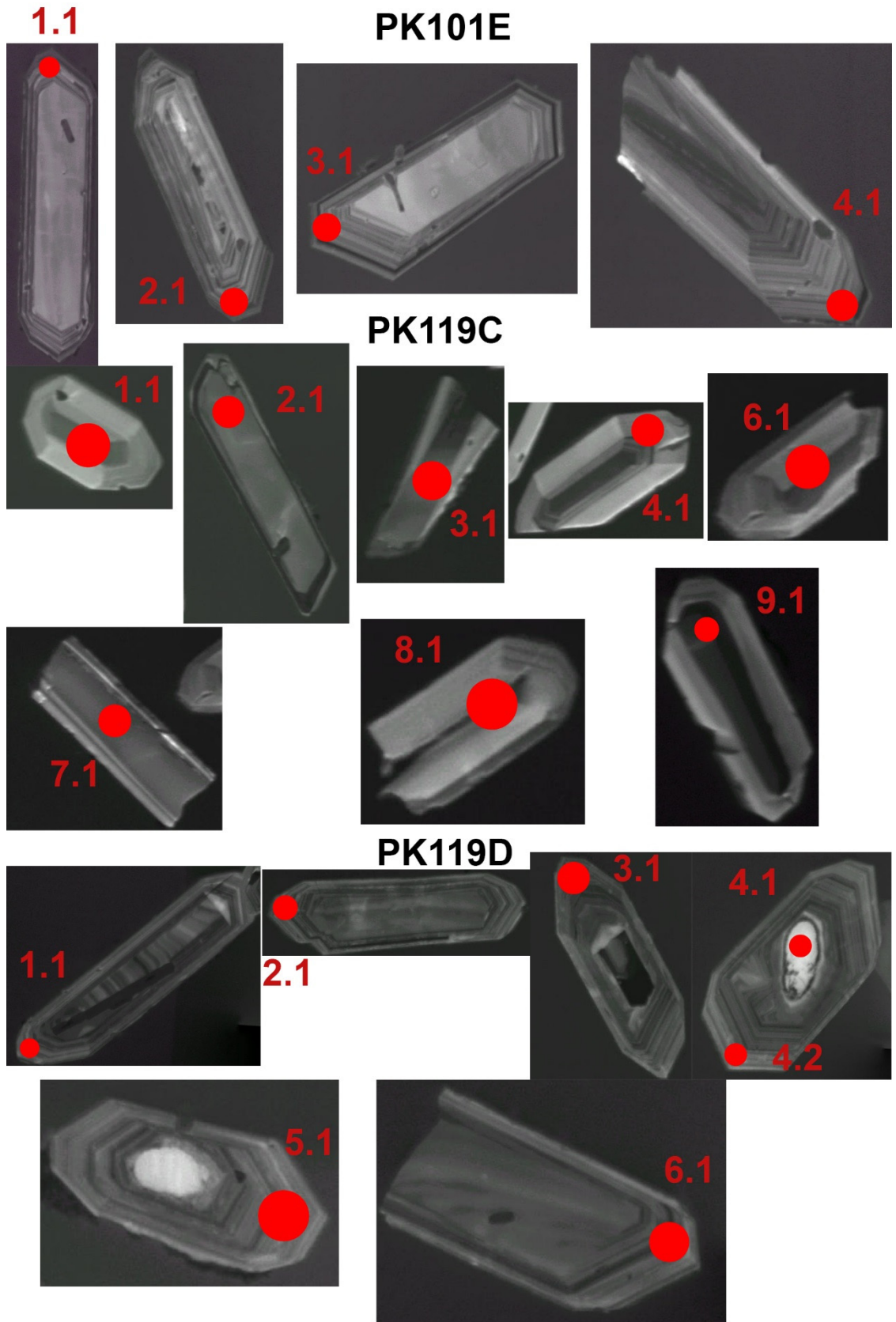


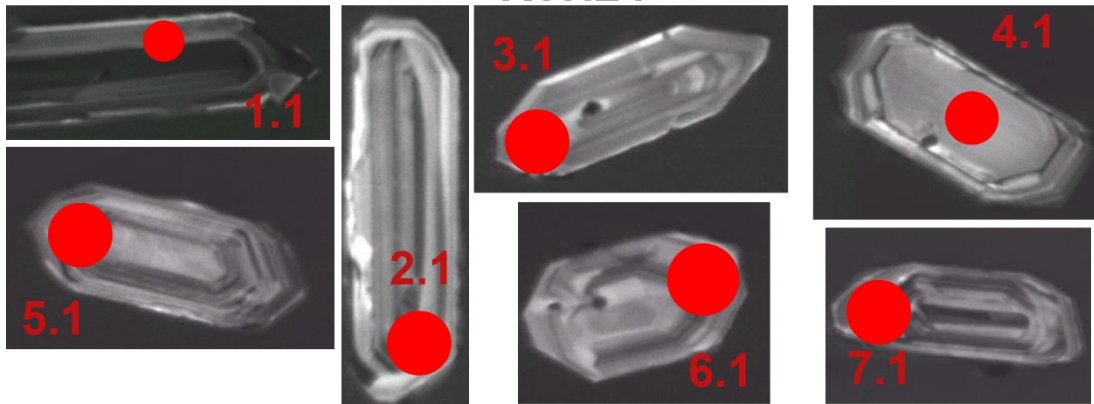
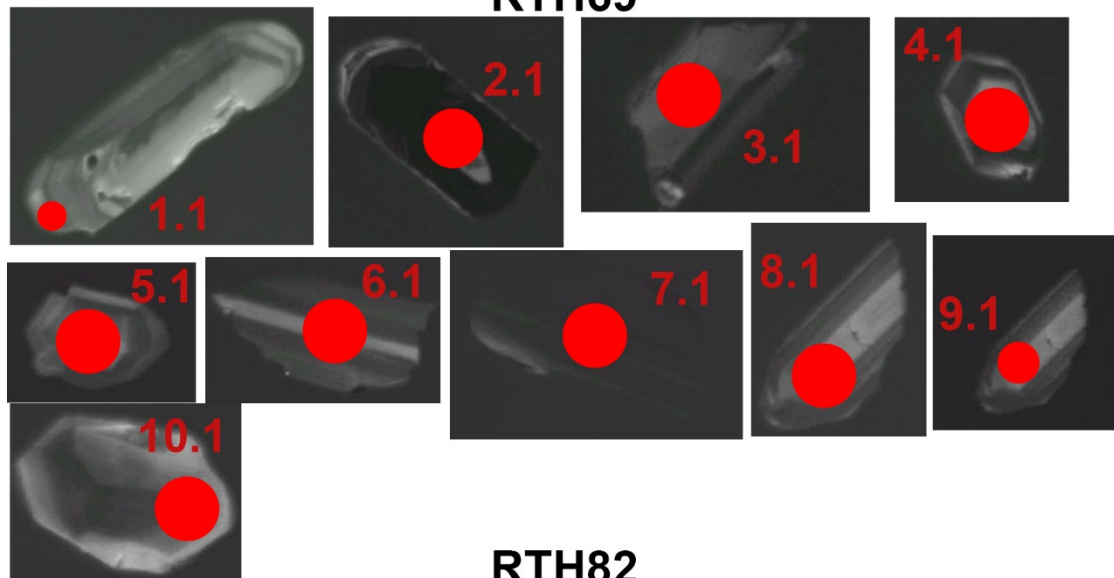
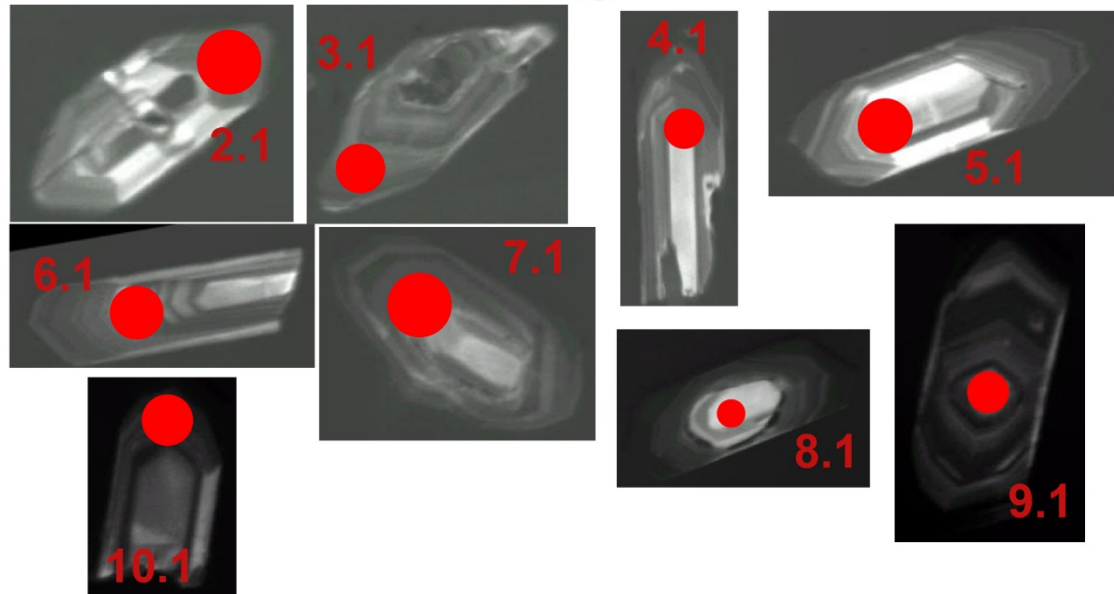
### PK089C



### PK101D



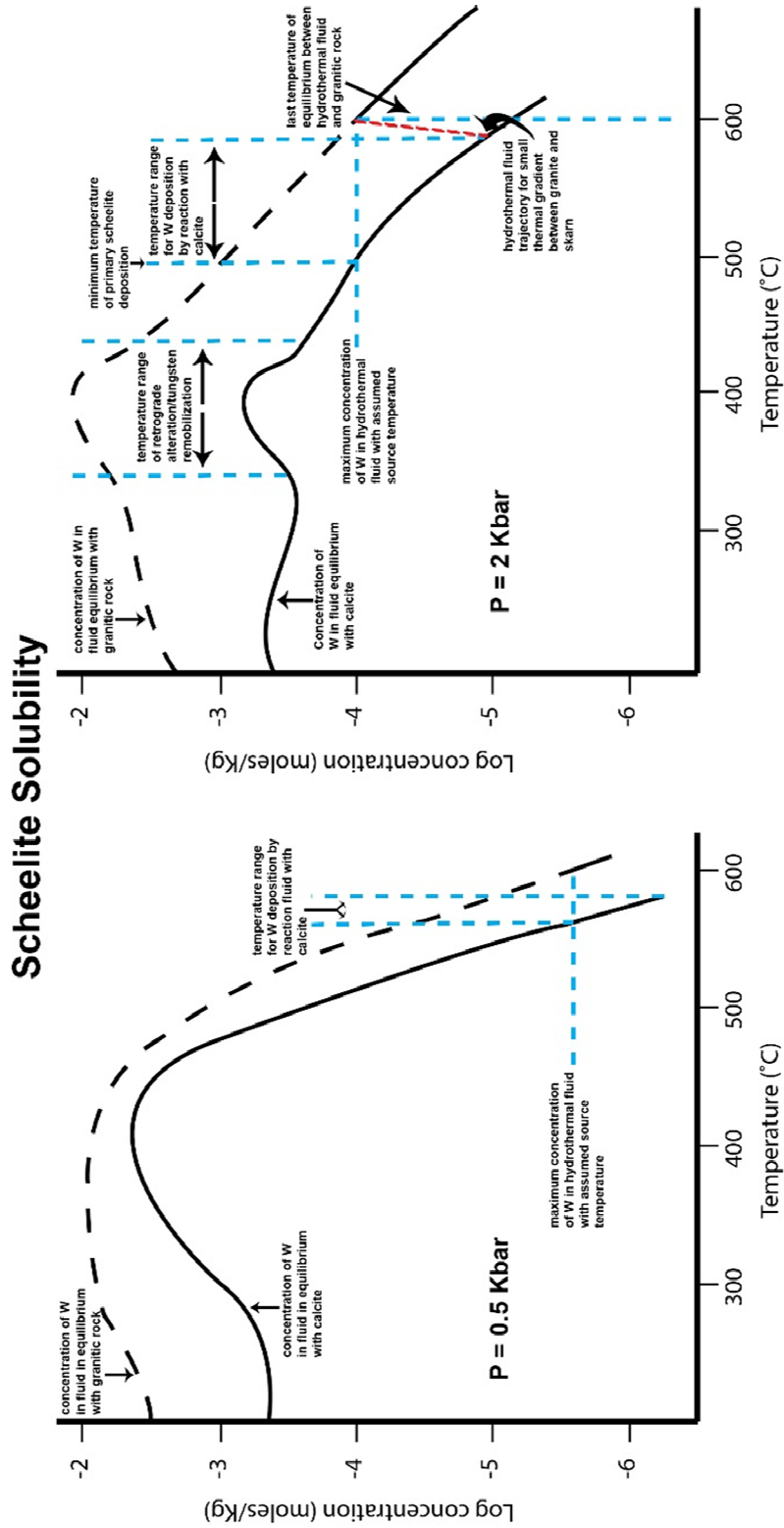


**RTH24****RTH69****RTH82**

## Appendix G: Apatite Fission Track Data

ID	Lithology	Mineralized?	Depth	UTME	UTMN	total spots attempted	spots accepted	sumNs (tracks)	sumRho ( $\times 10^5$ )	1sig sumRho ( $\times 10^5$ )	[U] (ppm)	[Th] (ppm)	[Sm] (ppm)	Zeta ( $\times 10^5$ )	1sigZeta ( $\times 10^5$ )	chi-squared	Q(chi-squared)	pooled age (Ma)	95%-CI (Ma)	95%+CI (Ma)
Durango	Standard					96	94	1015	23.625	0.169	12	283	114	7.323	0.237	219.2	0	31.4	2.7	3
Durango	Standard					51	49	606	13.745	0.123	12	283	112	7.121	0.297	85.7	0.0007	31.3	3.5	3.9
PK118C	Dunderberg	No	300-307'	725553	4448395	25	16	64	1.492	0.06	19	39	109	7.323	0.237	446.1	0	31.4	7.4	9.7
PK158C	Dunderberg	Yes	460-477'	725577	4448786	18	10	30	1.202	0.022	28	77	93	7.323	0.237	22.7	0.0069	18.4	5.7	8.3
PK001C	Dunderberg	No	117-127'	726658	4448159	16	12	29	0.651	0.017	10	52	227	7.323	0.237	0.6	1	33	10.4	15.1
PK004C	Dunderberg	Yes	150-170'	726834	4447675	5	5	6	0.351	0.01	13	34	131	7.121	0.297	1.6	0.8057	12.1	6.8	15.5
PK014C	Dunderberg	Yes	320-338'	726515	4448159	9	8	6	0.062	0.002	3	74	202	7.323	0.237	13	0.0714	75.9	41.5	90.9
PK151C	Dunderberg	Yes	444-455'	725550	4448787	9	7	2	0.276	0.011	8	45	170	7.323	0.237	1.6	0.9536	5.3	4	16.6
PK132C	Secret Canyon	Yes	844-852'	725529	4448755	15	7	4	0.02	0.001	1	35	69	7.323	0.237	1	0.9838	144.3	91.6	245.6
PK027C	Dunderberg	No	331-341'	726495	4448207	13	8	7	0.101	0.004	4	45	248	7.121	0.297	4	0.7752	48.8	26.1	56
PK131C	Secret Canyon	Yes	937-947'	725551	4448755	5	5	2	0.168	0.005	17	28	186	7.121	0.297	0.7	0.9459	7.4	5.8	26.2
PK101C	Dunderberg	No	172-177'	725653	4449000	8.0	19	13	1.173	0.214	18	133	183	7.121	0.297	64	0	8	3.9	7.5

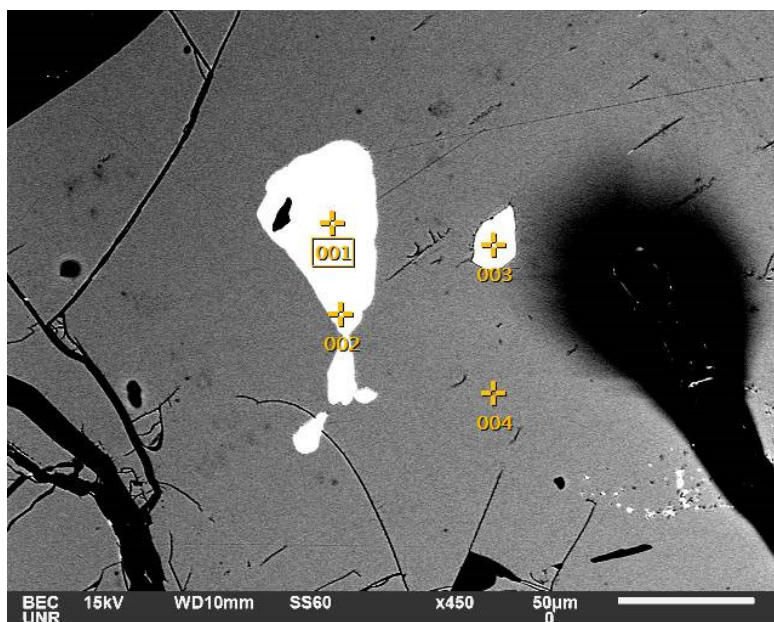
Appendix H: Scheelite Solubility Diagram



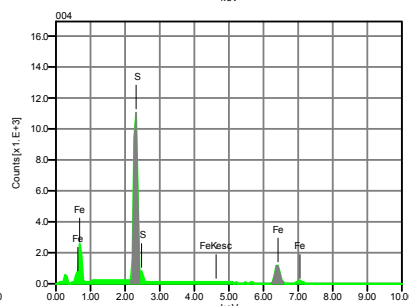
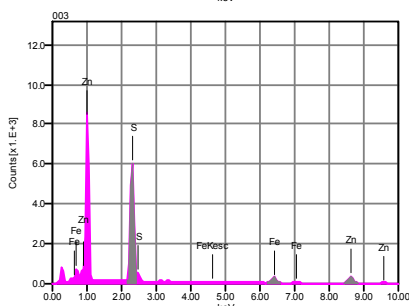
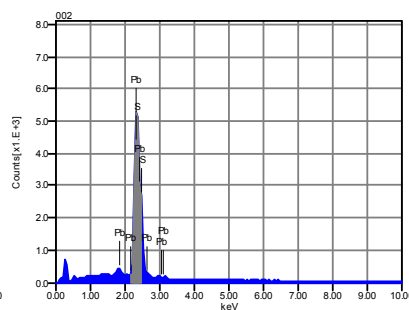
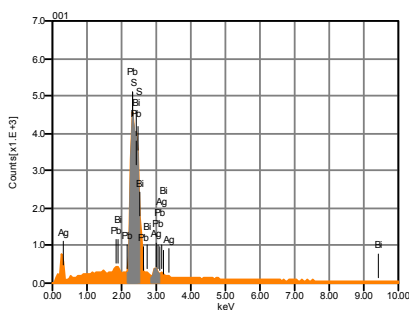
Experiment parameters:  $[\text{NaCl}] = 3 \text{ Molal}$ ;  $\text{pH} = 5$ ;  $x_{\text{CO}_2} = 5$ ;  $[\text{Ca}^{2+}]$  defined by calcite

## Appendix I: Additional SEM Images

## Mineralization in a dike near the stock



Volt : 15.00 kV  
 Mag. : x 450  
 Date : 2015/12/05  
 Pixel : 1280 x 960

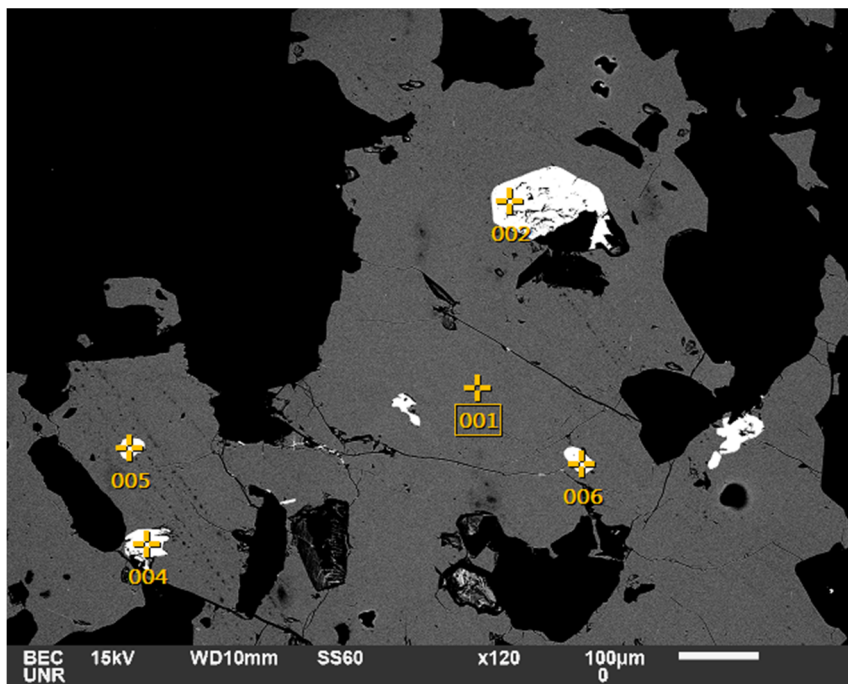


## Acquisition Condition

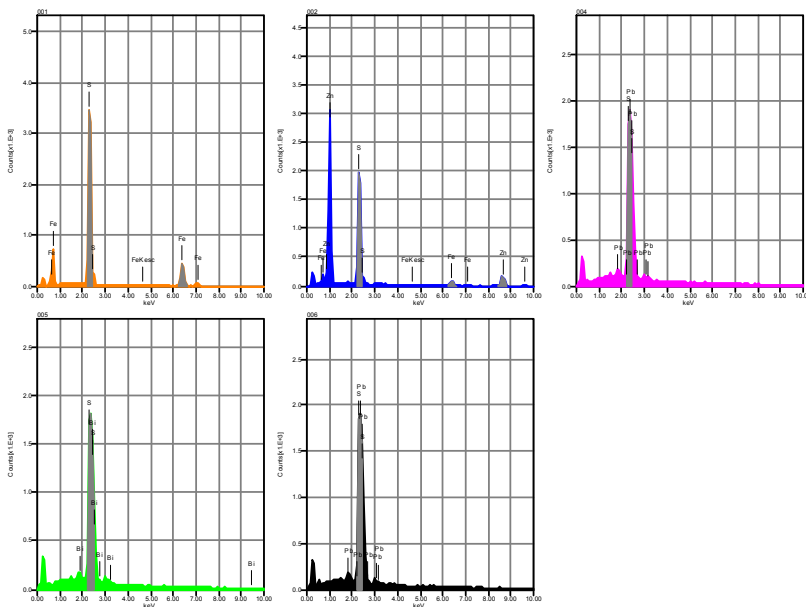
Instrument : 6510(LA)  
 Volt : 15.00 kV  
 Current : ---  
 Process Time : T4  
 Live time : 8.60 sec.  
 Real Time : 13.02 sec.  
 DeadTime : 32.00 %  
 Count Rate : 24368.00  
 CPS

	Fe	Pb	Ag	S	Zn	Bi	Probable mineral
001		32.33	5.81	15.74		46.12	Unknown
002		85.41		14.59			Galena
003	13.32			40.88	45.80		Sphalerite/marmatite
004	43.56			56.44			Pyrite

# Mineralization in a dike near the stock



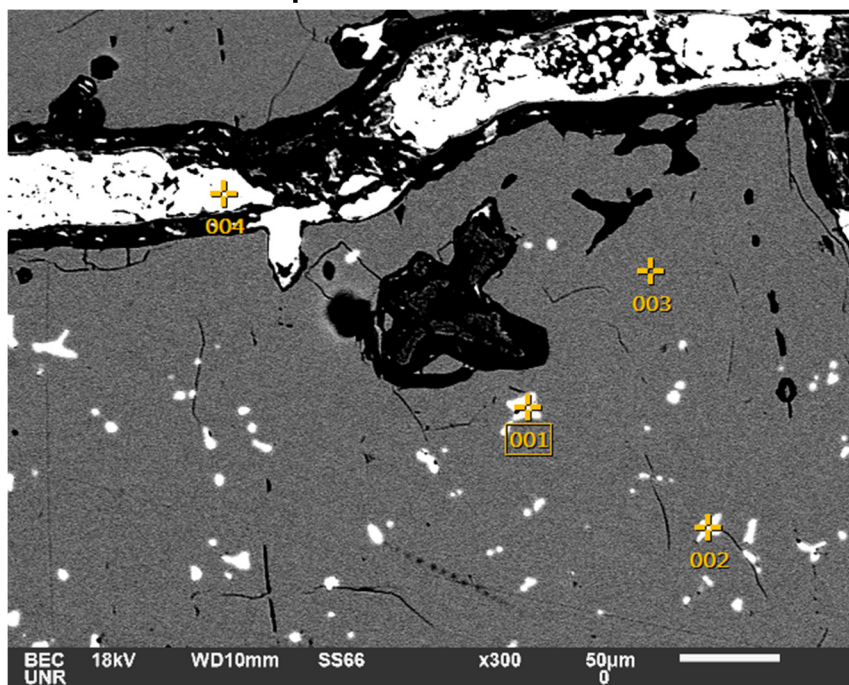
Volt : 15.00 kV  
 Mag. : x 120  
 Date : 2015/05/12  
 Pixel : 1280 x 960



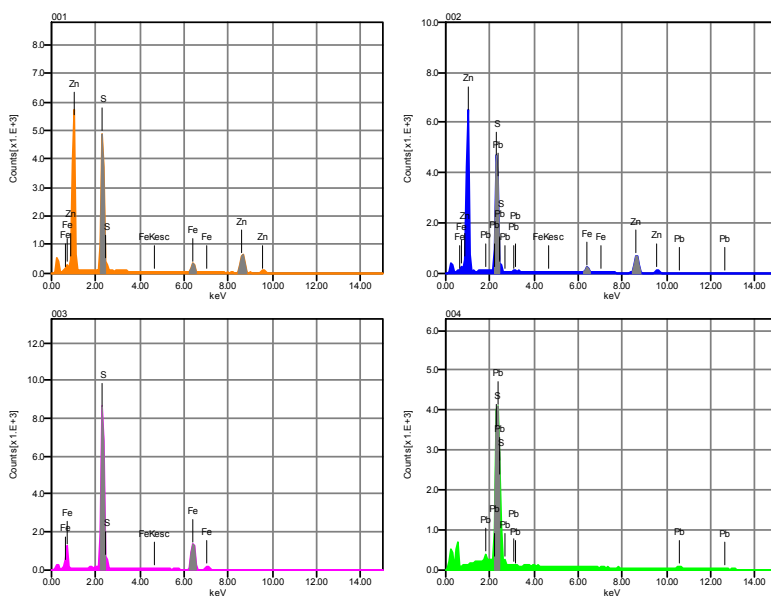
Acquisition Condition  
 Instrument : 6510(LA)  
 Volt : 15.00 kV  
 Current : ---  
 Process Time : T3  
 Live time : 14.31 sec.  
 Real Time : 15.00 sec.  
 DeadTime : 5.00 %  
 Count Rate : 5011.00 CPS

	Fe	Pb	S	Zn	Bi	Probable mineral
001	45.20		54.80			Pyrite
002	8.33		36.44	55.23		Sphalerite
004		73.63	26.37			Galena
005			28.90		71.10	Bismuthinite
006		74.93	25.07			Galena

## Carbonate replacement vein mineralization



Volt : 18.00 kV  
Mag. : x 300  
Date : 2015/06/26  
Pixel : 1280 x 960



### Acquisition Condition

Instrument : 6510(LA)

Volt : 18.00 kV

Current : ---

Process Time : T3

Live time : 13.24 sec.

Real Time : 15.00 sec.

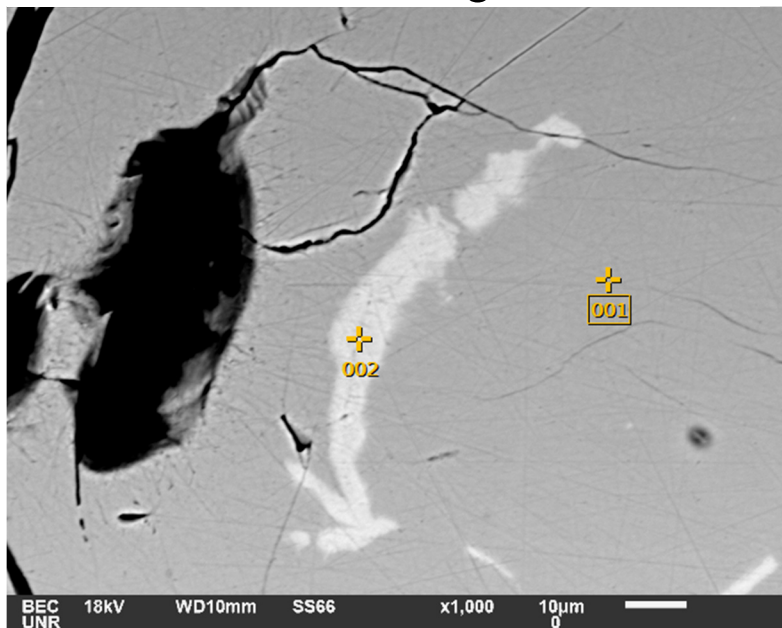
DeadTime : 12.00 %

Count Rate : 12221.00 CPS

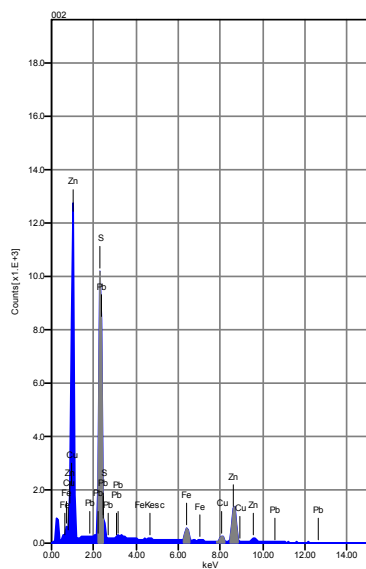
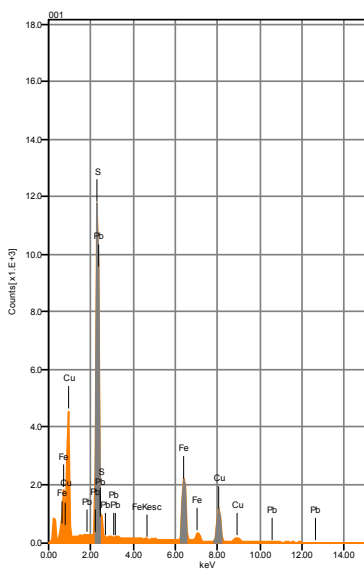
	Fe	Pb	S	Zn	Probable mineral
001	9.03		38.04	52.93	Sphalerite
002	6.36	10.13	32.51	51.00	Sphalerite
003	44.35		55.65		Pyrite
004		86.90	13.10		Galena



## Mineralization in retrograde skarn



Volt : 18.00 kV  
 Mag. : x 1,000  
 Date : 2015/06/25  
 Pixel : 1280 x 960



Acquisition Condition

Instrument : 6510(LA)

Volt : 18.00 kV

Current : ---

Process Time : T3

Live time : 10.85 sec.

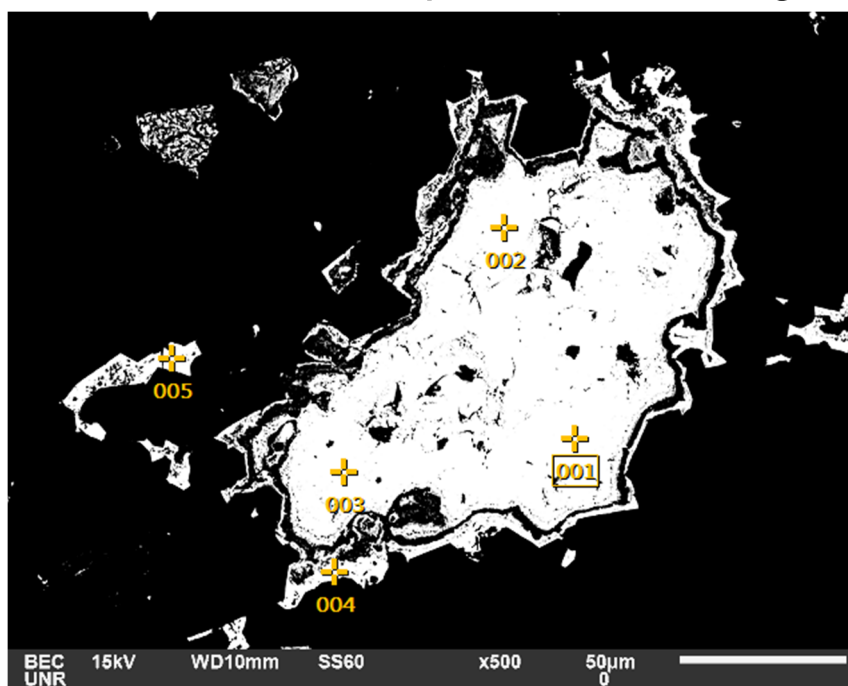
Real Time : 15.00 sec.

DeadTime : 27.00 %

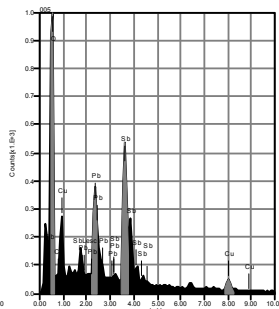
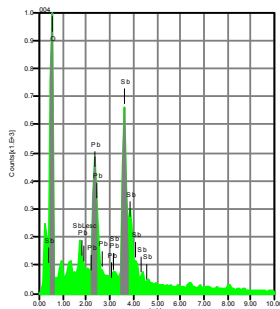
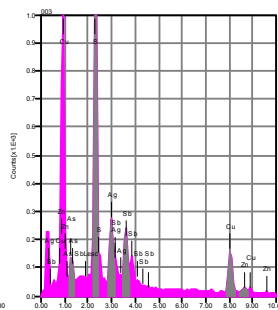
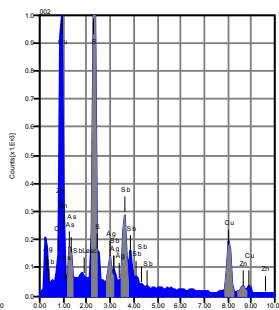
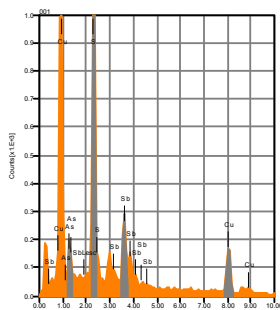
Count Rate : 32714.00 CPS

	Fe	Pb	S	Cu	Zn	Probable mineral
001	27.39	11.36	33.10	28.15		Chalcopyrite
002	6.11	12.40	31.83	5.06	44.60	Sphalerite

## Mineralization in a quartz vein cutting the stock



Volt : 15.00 kV  
 Mag. : x 500  
 Date : 2015/05/12  
 Pixel : 1280 x 960



Acquisition Condition

Instrument : 6510(LA)

Volt : 15.00 kV

Current : ---

Process Time : T3

Live time : 14.35 sec.

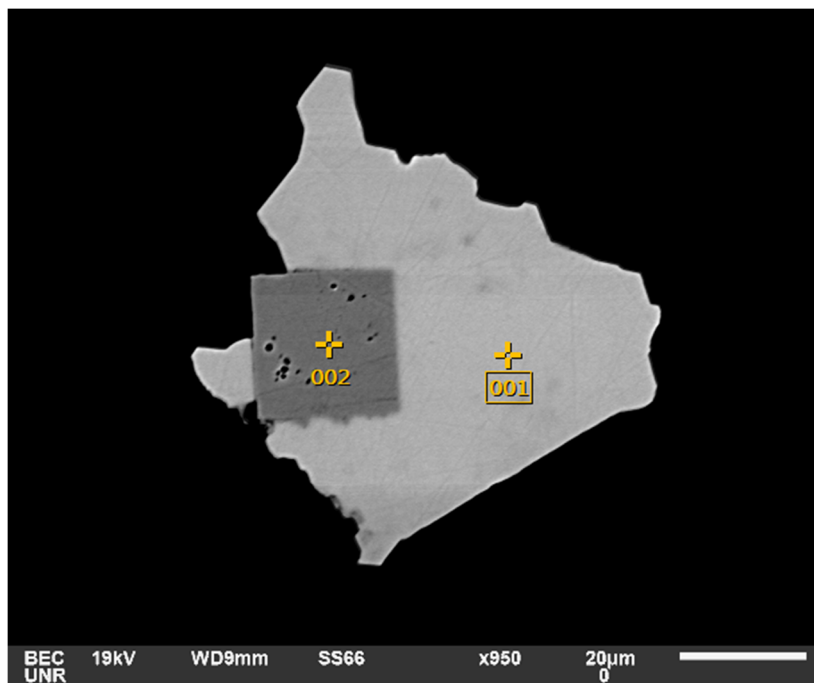
Real Time : 15.00 sec.

DeadTime : 5.00 %

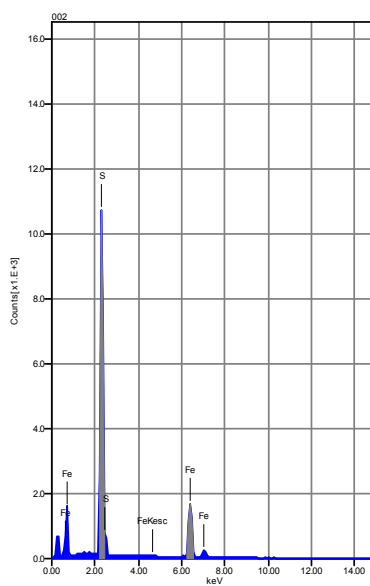
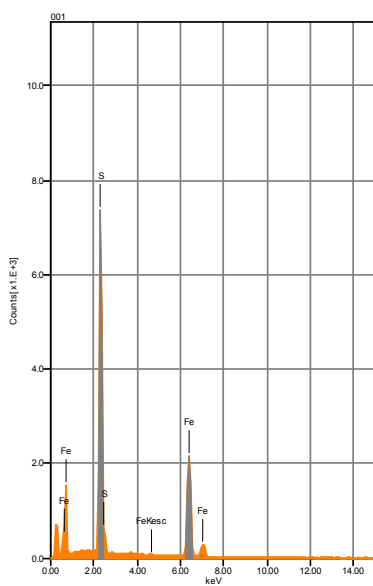
Count Rate : 4637.00  
 CPS

	O	Pb	Ag	S	Cu	Zn	As	Sb	Probable mineral
001				28.71	41.57		5.35	24.38	Tetrahedrite
002			5.12	24.82	38.69	5.40	4.68	21.29	Tetrahedrite
003			13.08	24.50	35.20	5.19	3.93	18.10	Tetrahedrite
004	18.56	31.23						50.21	Oxylumboroméite?
005	23.22	25.92			10.05			40.80	Unknown

## Two generations of pyrite in marble



Volt : 19.00 kV  
 Mag. : x 950  
 Date : 2015/12/02  
 Pixel : 1280 x 960



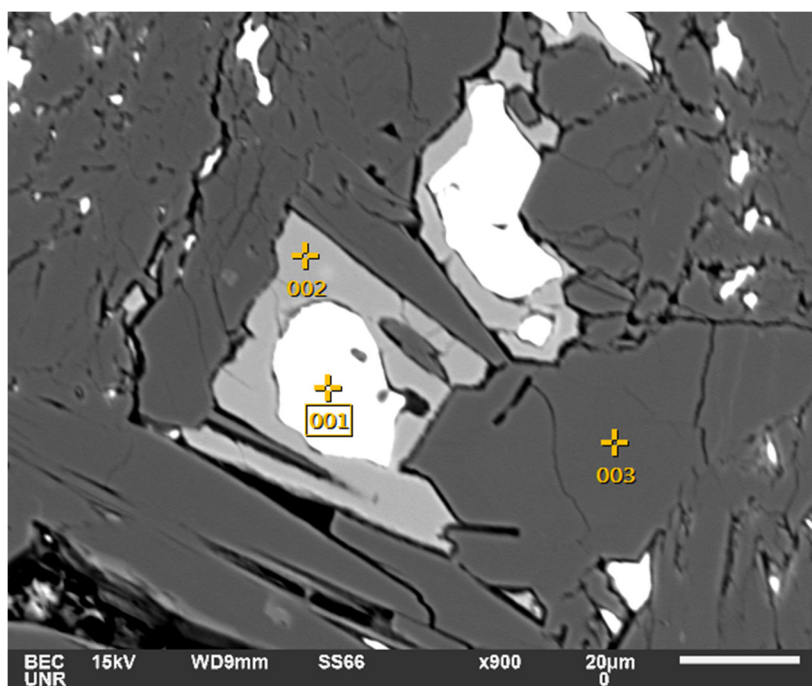
### Acquisition Condition

Instrument : 6510(LA)  
 Volt : 19.00 kV  
 Current : ---  
 Process Time : T4  
 Live time : 11.27 sec.  
 Real Time : 15.00 sec.  
 DeadTime : 25.00 %  
 Count Rate : 17771.00 CPS

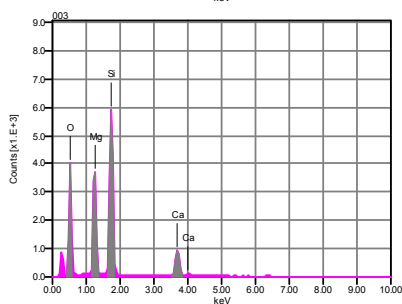
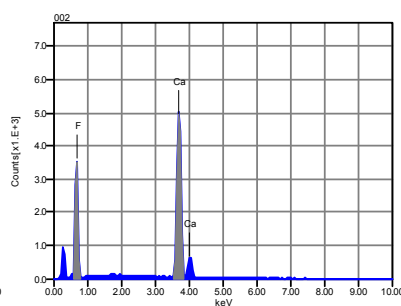
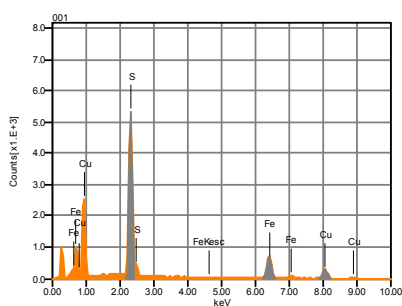
% wt	Fe	S
001	56.82	43.18
002	42.50	57.50

% mol	Fe	S
001	43.03	56.97
002	29.79	70.21

## Retrograde skarn



Volt : 15.00 kV  
 Mag. : x 900  
 Date : 2015/11/27  
 Pixel : 1280 x 960

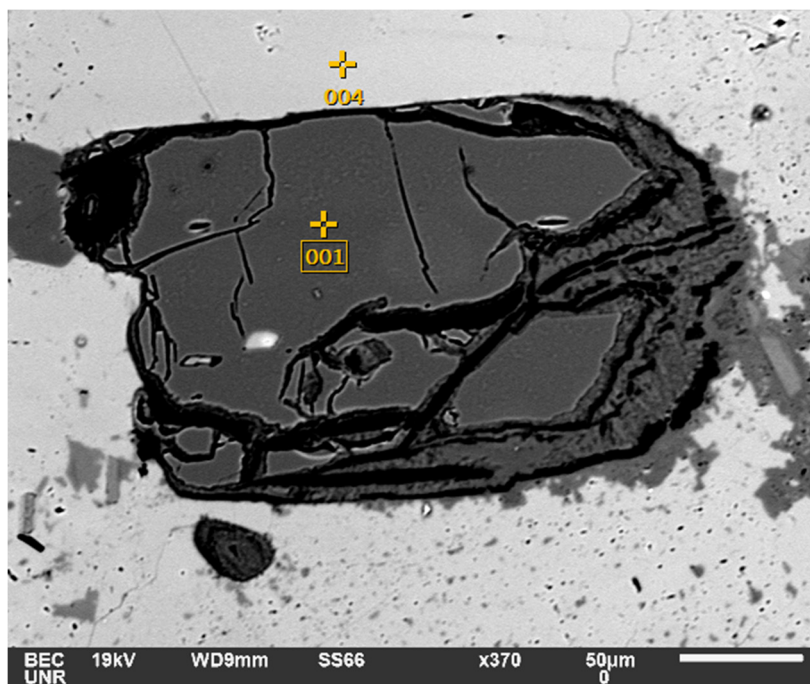


## Acquisition Condition

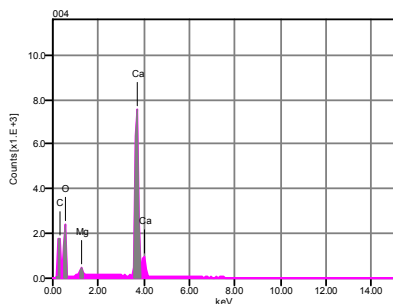
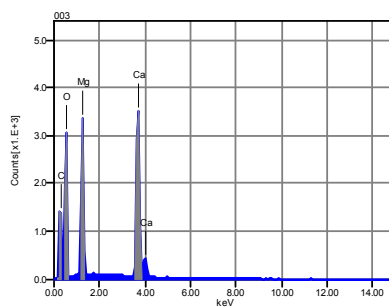
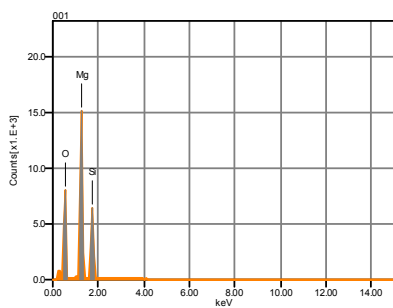
Instrument : 6510(LA)  
 Volt : 15.00 kV  
 Current : ---  
 Process Time : T4  
 Live time : 7.33 sec.  
 Real Time : 10.28 sec.  
 DeadTime : 27.00 %  
 Count Rate : 21261.00  
 CPS

	Fe	O	F	Mg	Si	S	Ca	Cu	Probable mineral
001	30.23					37.11		32.67	Chalcopyrite
002			45.59				54.41		Fluorite
003		42.75		17.23	28.90		11.11		Talc

## Forsterite in marble



Volt : 19.00 kV  
 Mag. : x 370  
 Date : 2015/12/02  
 Pixel : 1280 x 960



## Acquisition Condition

Instrument : 6510(LA)

Volt : 19.00 kV

Current : ---

Process Time : T4

Live time : 9.67 sec.

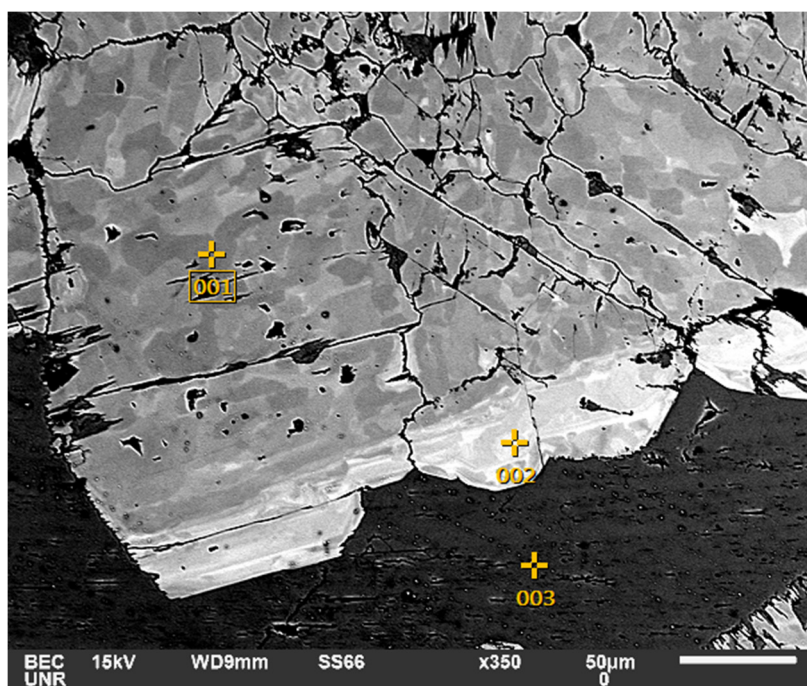
Real Time : 15.00 sec.

DeadTime : 35.00 %

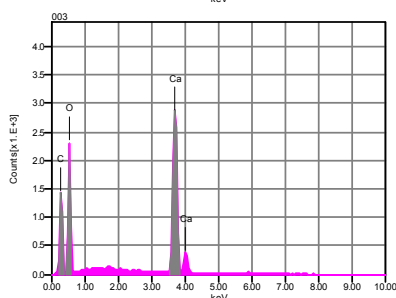
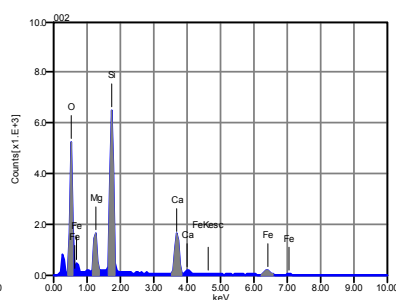
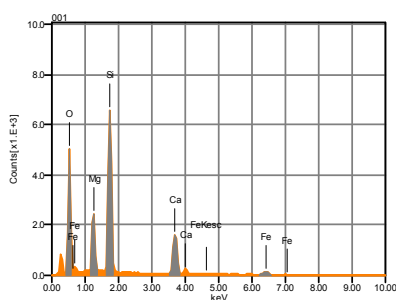
Count Rate : 28661.00  
 CPS

	O	C	Mg	Si	Ca	Probable mineral
001	42.86		36.41	20.72		Forsterite
003	46.19	24.17	12.03		17.61	Dolomite
004	45.73	20.14	1.14		32.99	Calcite

## Zoned diopside in skarn



Volt : 15.00 kV  
 Mag. : x 350  
 Date : 2015/11/21  
 Pixel : 1280 x 960



## Acquisition Condition

Instrument : 6510(LA)

Volt : 15.00 kV

Current : ---

Process Time : T4

Live time : 9.35 sec.

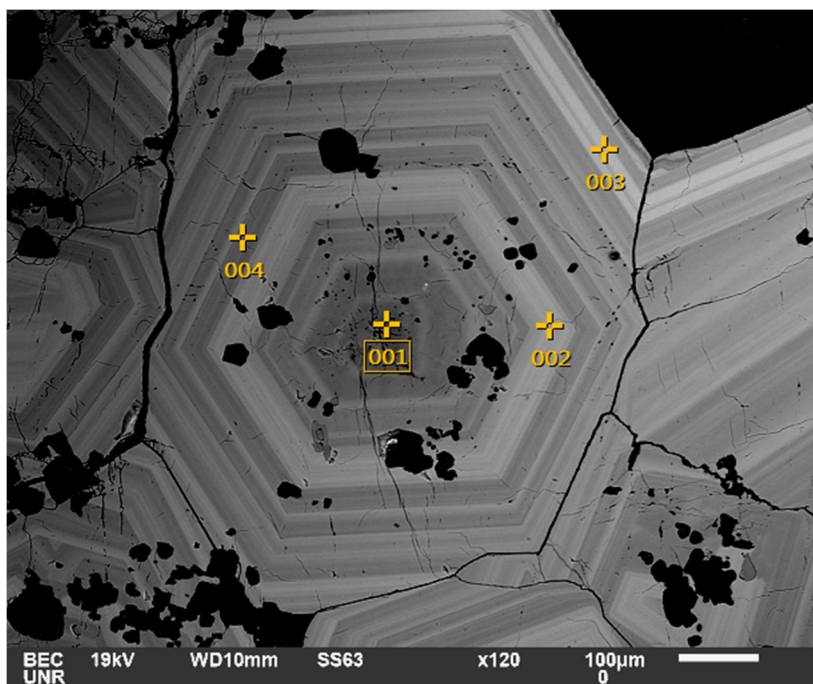
Real Time : 12.48 sec.

DeadTime : 25.00 %

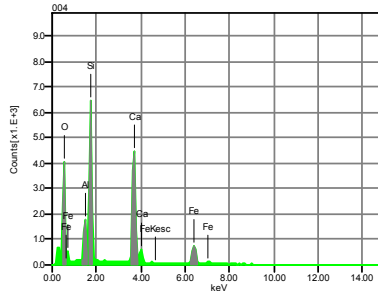
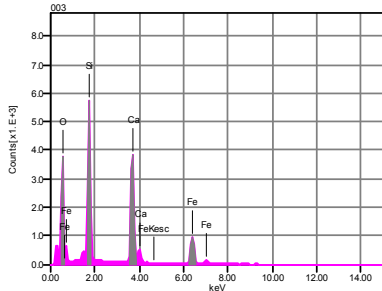
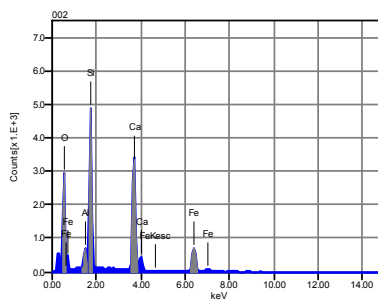
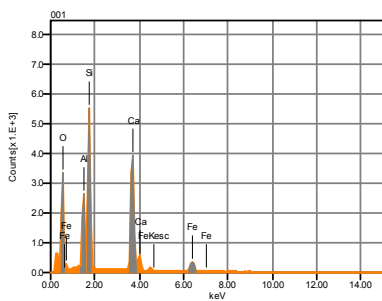
Count Rate : 18456.00  
 CPS

	Fe	O	C	Mg	Si	Ca	Probable mineral
001	4.71	45.83		9.28	24.65	15.53	Diopside
002	7.35	46.36		6.59	24.46	15.24	Diopside
003		46.86	18.83			34.31	Calcite

## Zonation in prograde garnet



Volt : 19.00 kV  
 Mag. : x 120  
 Date : 2015/12/01  
 Pixel : 1280 x 960



Acquisition Condition

Instrument : 6510(LA)

Volt : 19.00 kV

Current : ---

Process Time : T4

Live time : 11.18 sec.

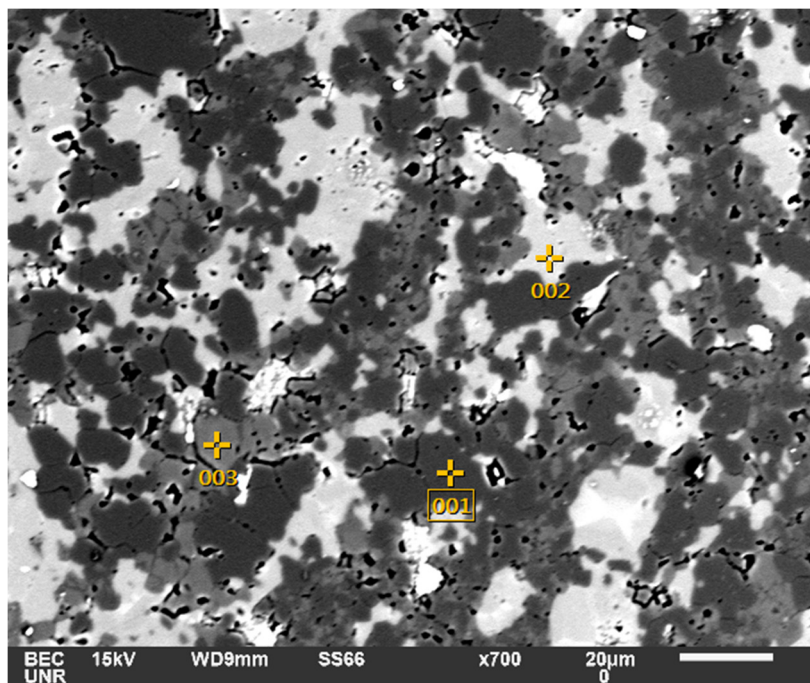
Real Time : 15.00 sec.

DeadTime : 25.00 %

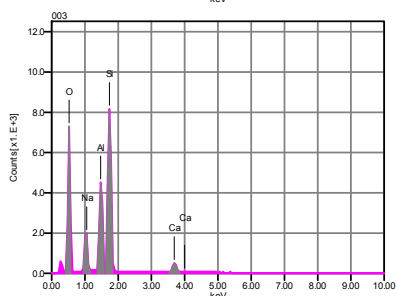
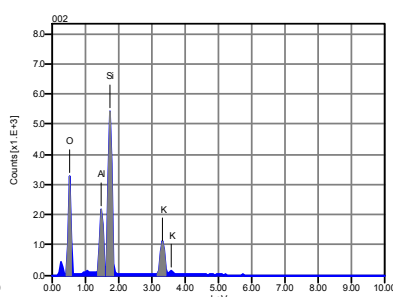
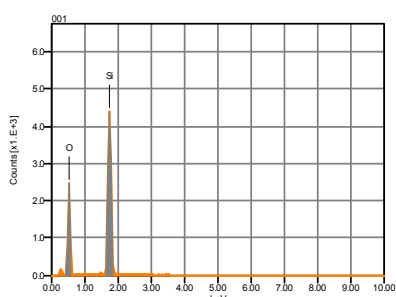
Count Rate : 18427.00  
 CPS

% wt	Fe	O	Al	Si	Ca	% mol	Fe	O	Al	Si	Ca
001	6.22	44.53	7.65	19.31	22.30		2.5	62.96	6.44	15.54	12.56
002	15.49	42.69	2.12	18.75	20.95		6.45	63.63	1.85	15.76	12.31
003	18.97	41.05	.61	18.19	21.18		8.28	62.52	.55	15.78	12.87
004	11.60	44.27	4.38	19.02	20.73		4.79	63.88	3.75	15.63	11.94

# Granodiorite porphyry groundmass



Volt : 15.00 kV  
Mag. : x 700  
Date : 2015/11/21  
Pixel : 1280 x 960



Acquisition Condition

Instrument : 6510(LA)

Volt : 15.00 kV

Current : --

Process Time : T4

Live time : 2.90 sec.

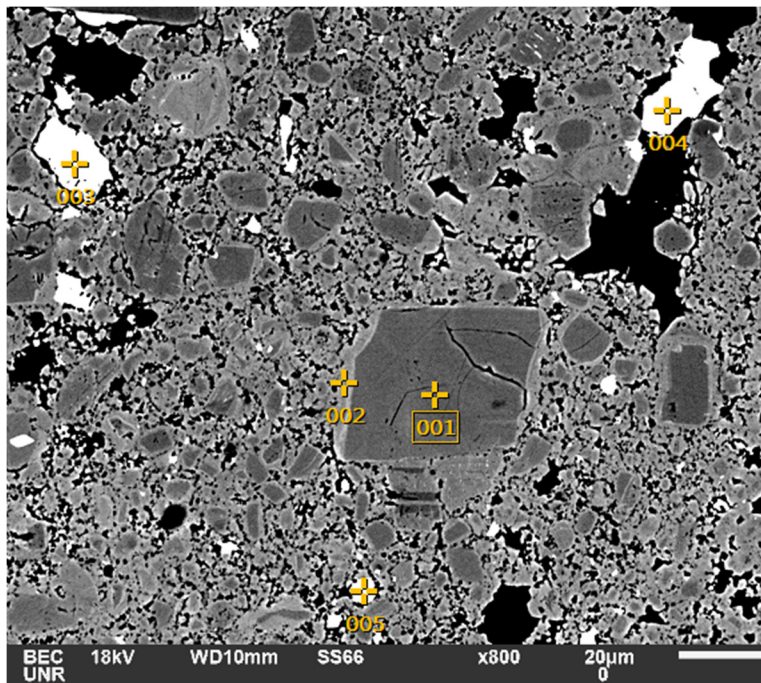
Real Time : 4.06 sec.

DeadTime : 28.00 %

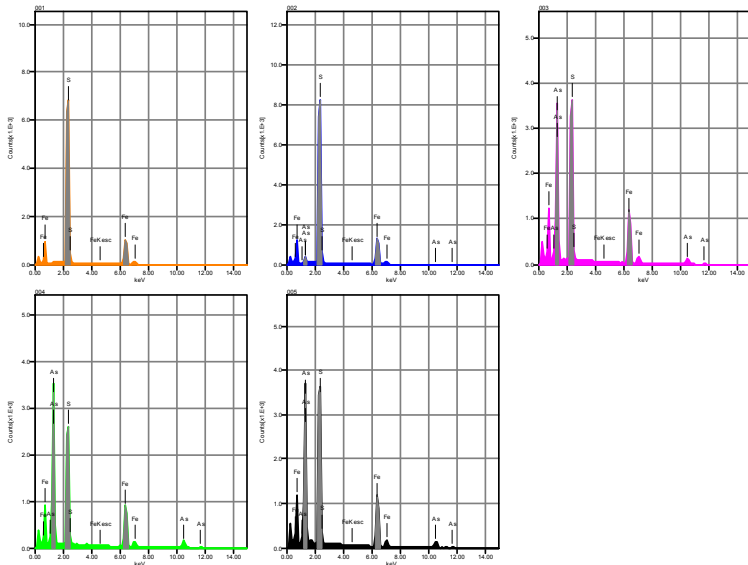
Count Rate : 22144.00  
CPS

	K	O	Na	Al	Si	Ca	Probable mineral
001		51.51			48.49		Quartz
002	14.56	44.31		10.19	30.93		Orthoclase
003		46.05	7.01	13.22	29.46	4.27	Plagioclase

# Arsenian-pyrite rims in a dike in Dunderberg Shale



Volt : 18.00 kV  
 Mag. : x 800  
 Date : 2015/06/27  
 Pixel : 1280 x 960



Acquisition Condition

Instrument : 6510(LA)

Volt : 18.00 kV

Current : ---

Process Time : T3

Live time : 10.30 sec.

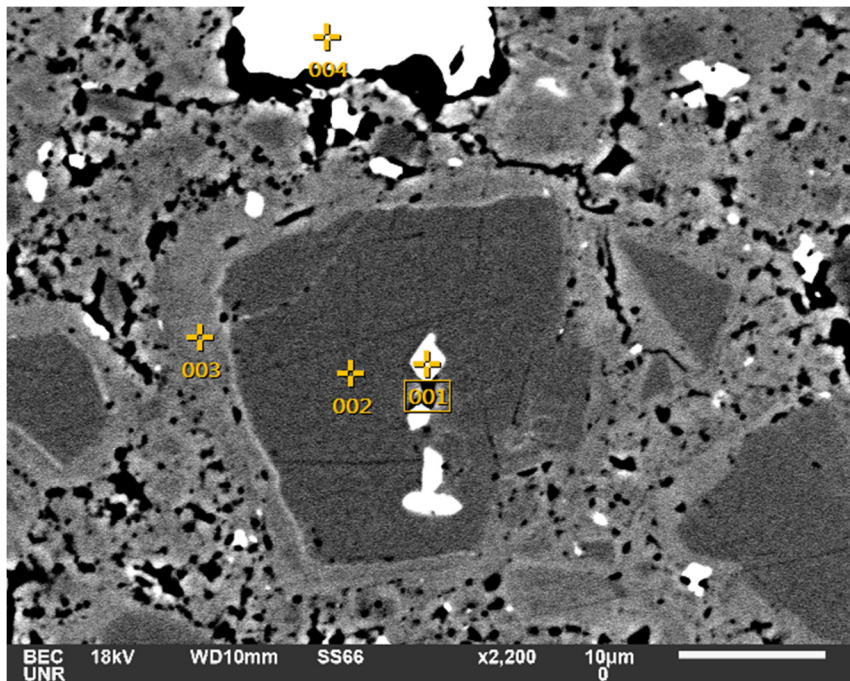
Real Time : 11.68 sec.

DeadTime : 12.00 %

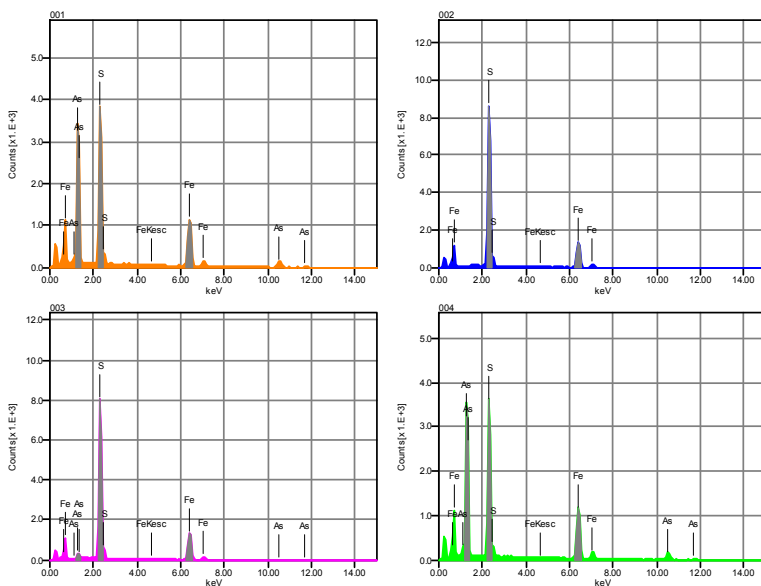
Count Rate : 13363.00 CPS

	Fe	S	As	Probable mineral
001	43.59	56.41		Pyrite
002	42.13	53.69	4.17	Arsenian-pyrite
003	30.79	24.81	44.40	Arsenopyrite
004	28.08	21.71	50.21	Arsenopyrite
005	29.78	25.35	44.88	Arsenopyrite

# Mineralization in a dike in the Dunderberg



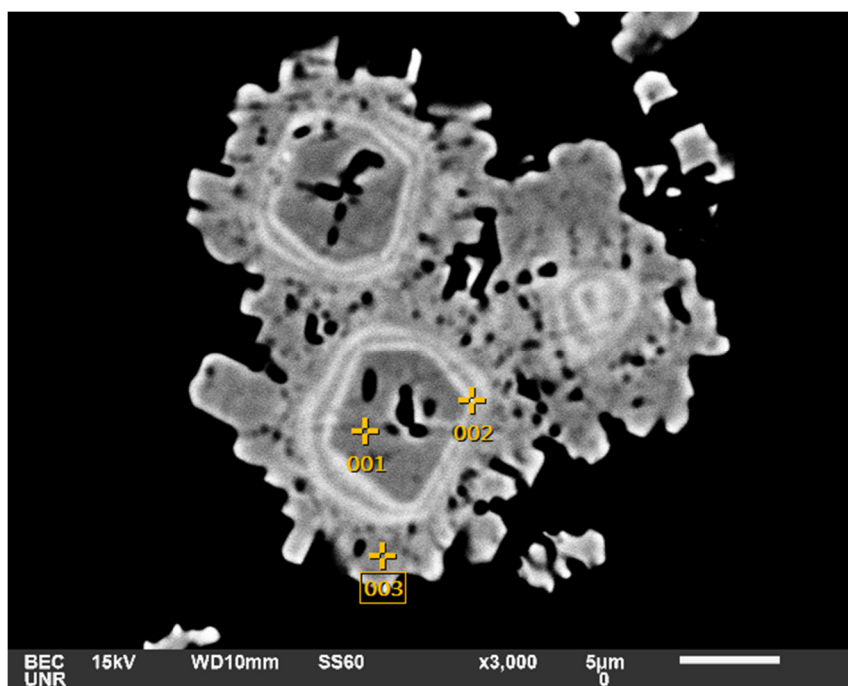
Volt : 18.00 kV  
 Mag. : x 2,200  
 Date : 2015/06/27  
 Pixel : 1280 x 960



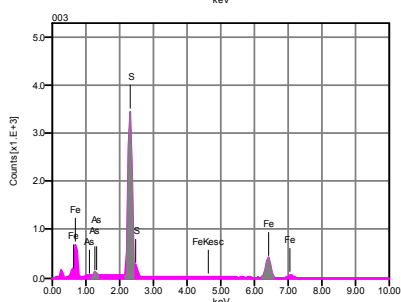
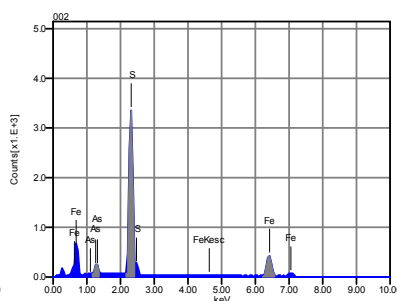
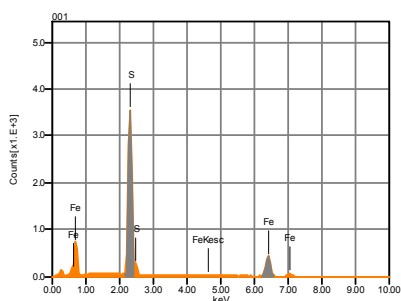
Acquisition Condition  
 Instrument : 6510(LA)  
 Volt : 18.00 kV  
 Current : ---  
 Process Time : T3  
 Live time : 13.32 sec.  
 Real Time : 15.00 sec.  
 DeadTime : 11.00 %  
 Count Rate : 12214.00  
 CPS

	Fe	S	As	Probable mineral
001	30.40	26.73	42.87	Arsenopyrite
002	43.33	56.67		Pyrite
003	42.57	52.94	4.49	Arsenian-pyrite
004	29.86	25.47	44.67	Arsenopyrite

# Dunderberg Shale mineralization



Volt : 15.00 kV  
 Mag. : x 3,000  
 Date : 2015/05/12  
 Pixel : 1280 x 960



## Acquisition Condition

Instrument : 6510(LA)

Volt : 15.00 kV

Current : ---

Process Time : T3

Live time : 14.31 sec.

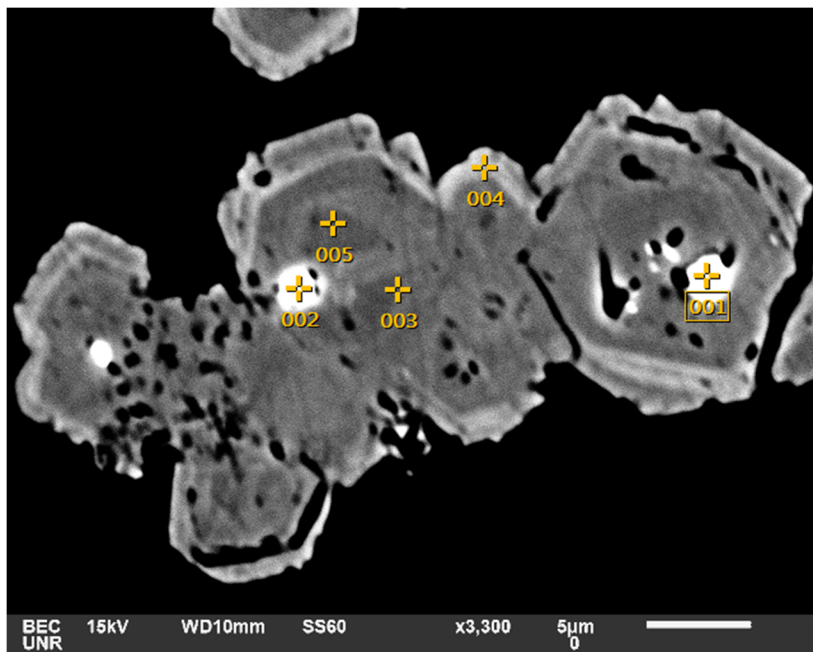
Real Time : 15.00 sec.

DeadTime : 4.00 %

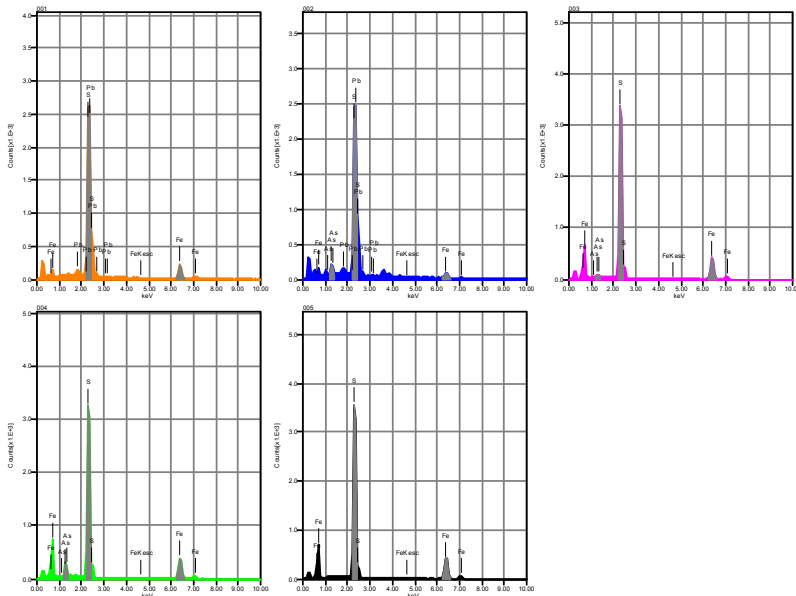
Count Rate : 4850.00  
 CPS

	Fe	S	As
001	44.69	55.31	
002	44.06	50.42	5.52
003	43.20	54.48	2.32

# Dunderberg Mineralization



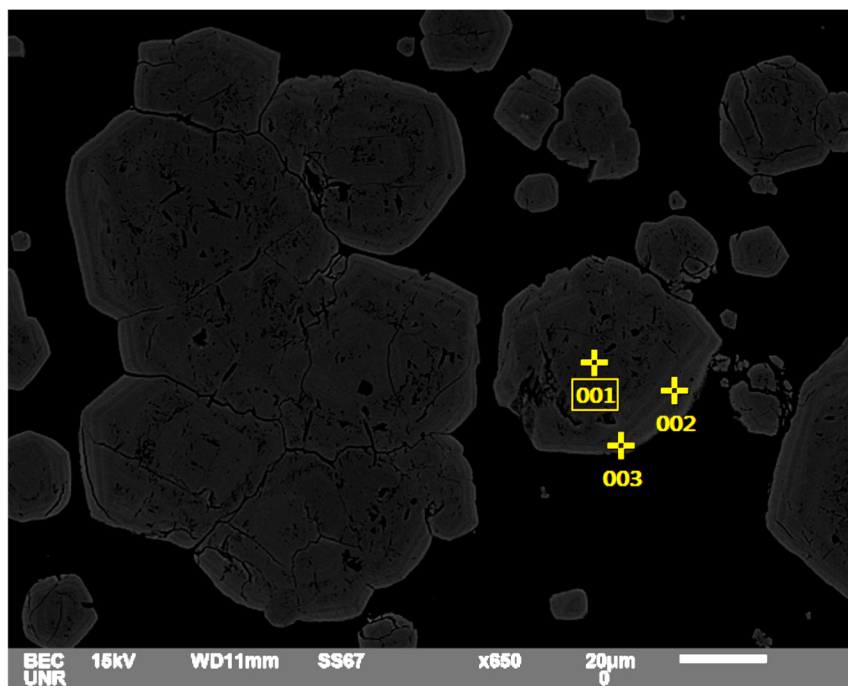
Volt : 15.00 kV  
 Mag. : x 3,300  
 Date : 2015/05/12  
 Pixel : 1280 x 960



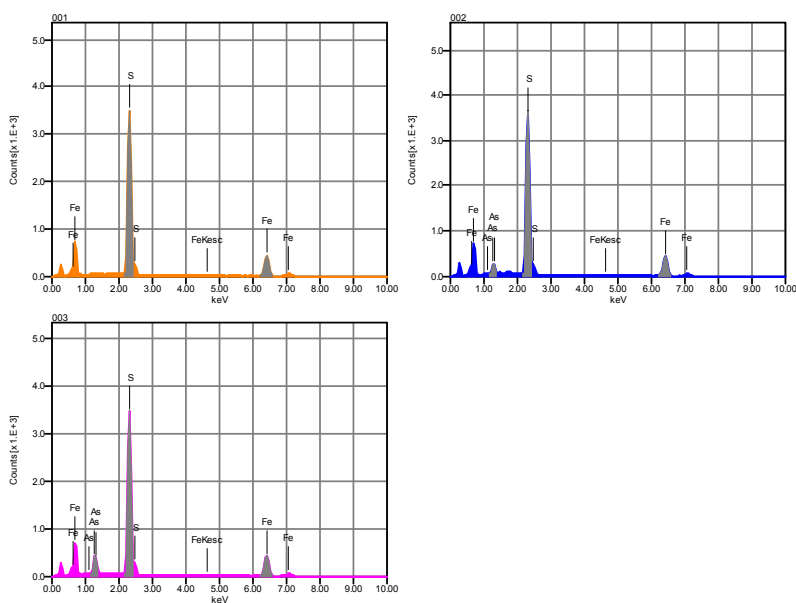
Acquisition Condition  
 Instrument : 6510(LA)  
 Volt : 15.00 kV  
 Current : ---  
 Process Time : T3  
 Live time : 14.27 sec.  
 Real Time : 15.00 sec.  
 DeadTime : 5.00 %  
 Count Rate : 5135.00  
 CPS

	Fe	Pb	S	As	Probable mineral
001	18.43	53.91	27.66		Galena
002	6.24	68.17	21.70	3.89	Galena
003	45.05		53.16	1.79	Arsenian-pyrite
004	42.09		51.36	6.55	Arsenian-pyrite
005	44.89		55.11		Pyrite

## Dunderberg Shale Mineralization



Volt : 15.00 kV  
 Mag. : x 650  
 Date : 2015/05/31  
 Pixel : 1280 x 960

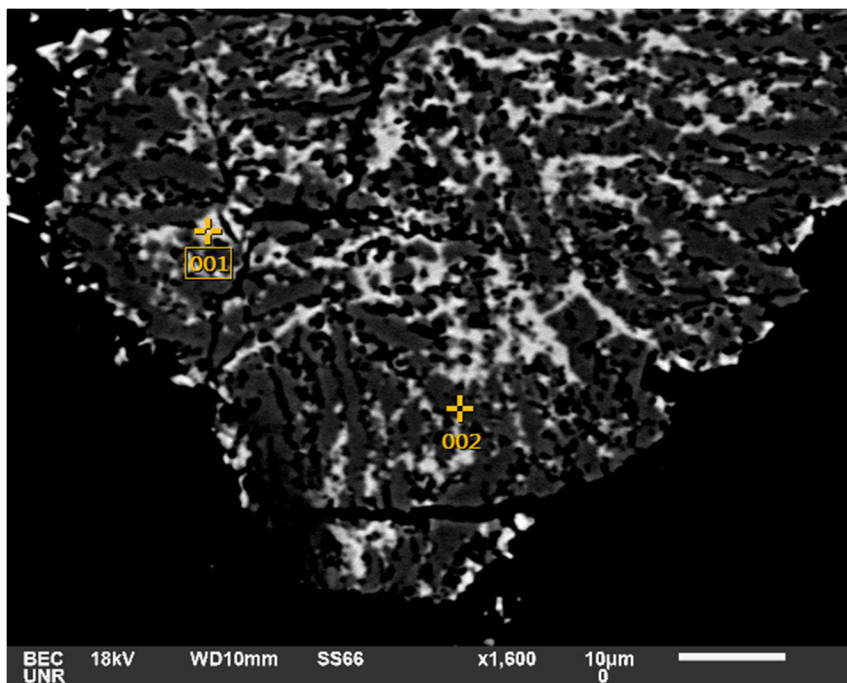


### Acquisition Condition

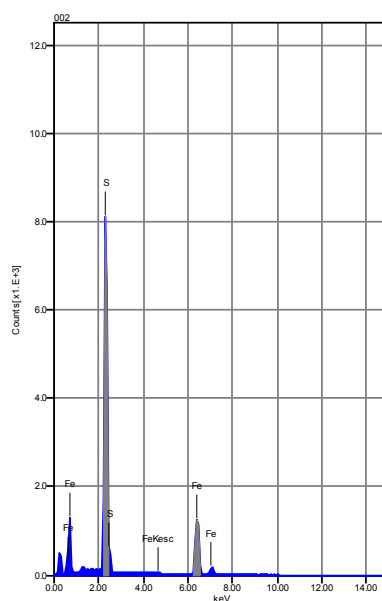
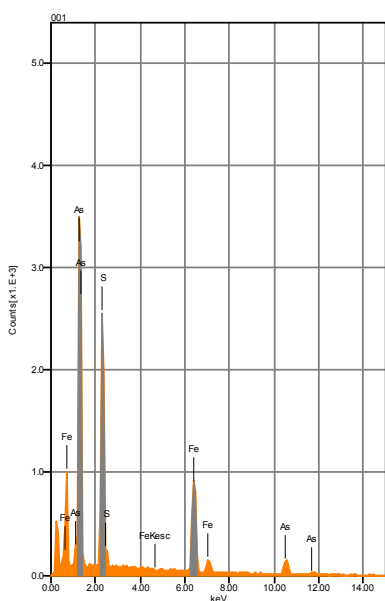
Instrument : 6510(LA)  
 Volt : 15.00 kV  
 Current : ---  
 Process Time : T3  
 Live time : 12.34 sec.  
 Real Time : 13.03 sec.  
 DeadTime : 6.00 %  
 Count Rate : 5647.00 CPS

	Fe	S	As	Probable mineral
001	45.03	54.97		Pyrite
002	42.72	51.08	6.20	Arsenian-pyrite
003	39.99	49.56	10.45	Arsenian-pyrite

## Arsenopyrite and pyrite in a dike in the Dunderberg



Volt : 18.00 kV  
 Mag. : x 1,600  
 Date : 2015/06/26  
 Pixel : 1280 x 960



### Acquisition Condition

Instrument : 6510(LA)  
 Volt : 18.00 kV  
 Current : ---  
 Process Time : T3  
 Live time : 11.69 sec.  
 Real Time : 13.09 sec.  
 DeadTime : 11.00 %  
 Count Rate : 11736.00  
 CPS

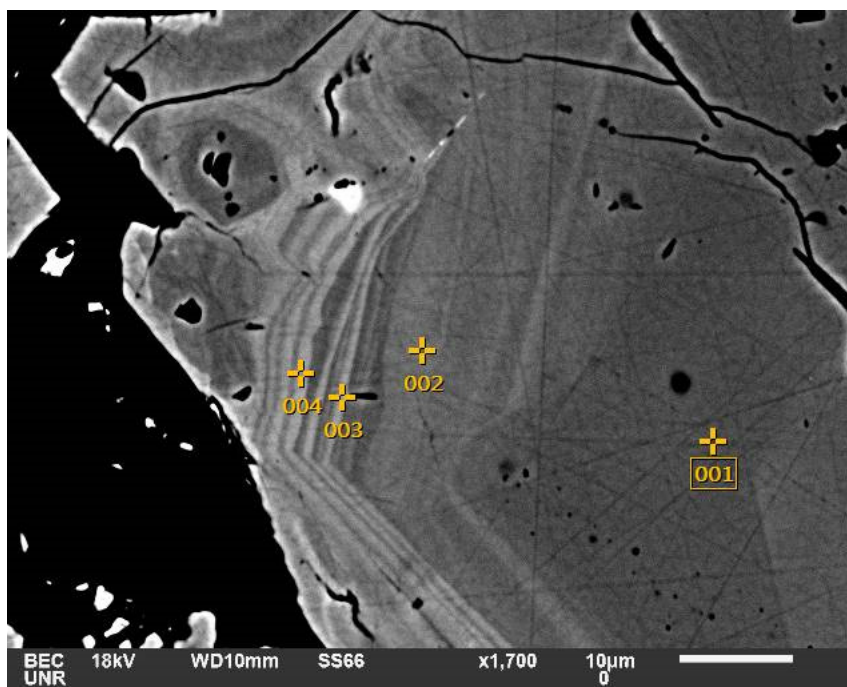
	Fe	S	As
001	28.54	20.97	50.48
002	43.72	56.28	

### Probable mineral

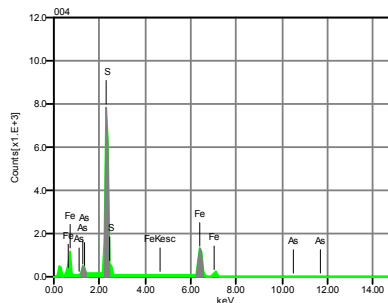
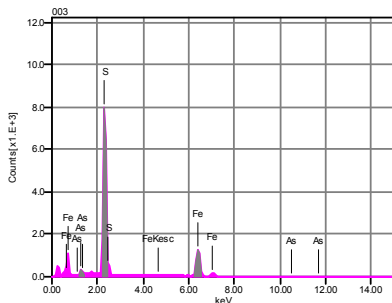
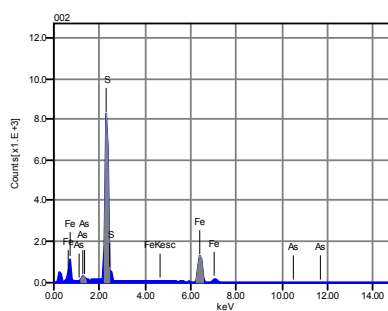
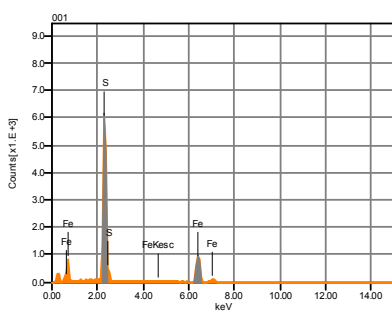
Arsenopyrite

Pyrite

## Arsenian-pyrite rims in a dike in the Dunderberg Shale



Volt : 18.00 kV  
 Mag. : x 1,700  
 Date : 2015/06/27  
 Pixel : 1280 x 960



### Acquisition Condition

Instrument : 6510(LA)

Volt : 18.00 kV

Current : ---

Process Time : T3

Live time : 9.43 sec.

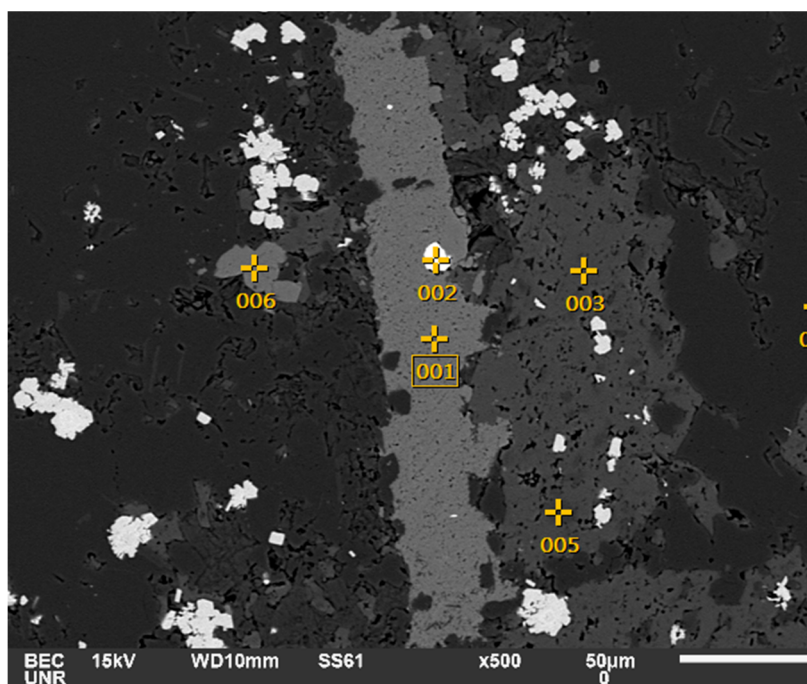
Real Time : 10.69 sec.

DeadTime : 12.00 %

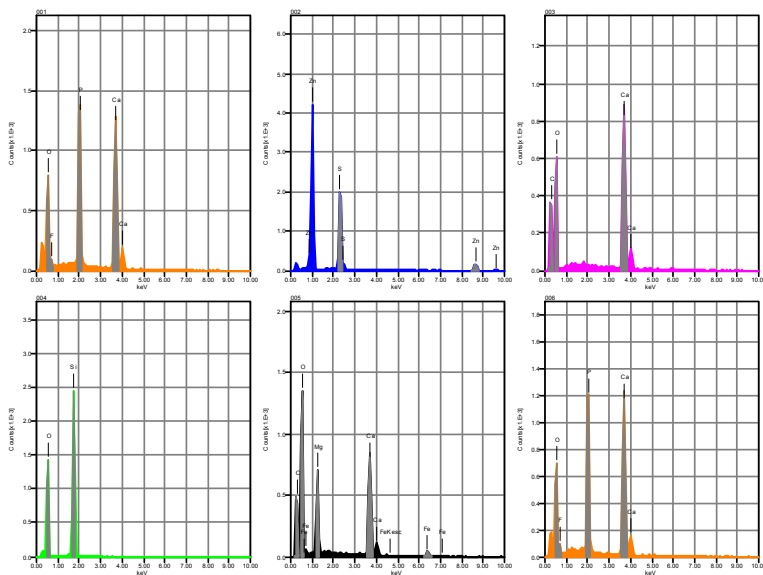
Count Rate : 12870.00  
 CPS

	Fe	S	As	Probable mineral
001	44.13	55.87		Pyrite
002	41.86	54.65	3.49	Arsenian-pyrite
003	41.57	54.43	4.00	Arsenian-pyrite
004	41.53	52.64	5.83	Arsenian-pyrite

## Secondary apatite in Dunderberg Shale



Volt : 15.00 kV  
 Mag. : x 500  
 Date : 2015/05/13  
 Pixel : 1280 x 960



Acquisition Condition

Instrument : 6510(LA)

Volt : 15.00 kV

Current : ---

Process Time : T3

Live time : 14.50 sec.

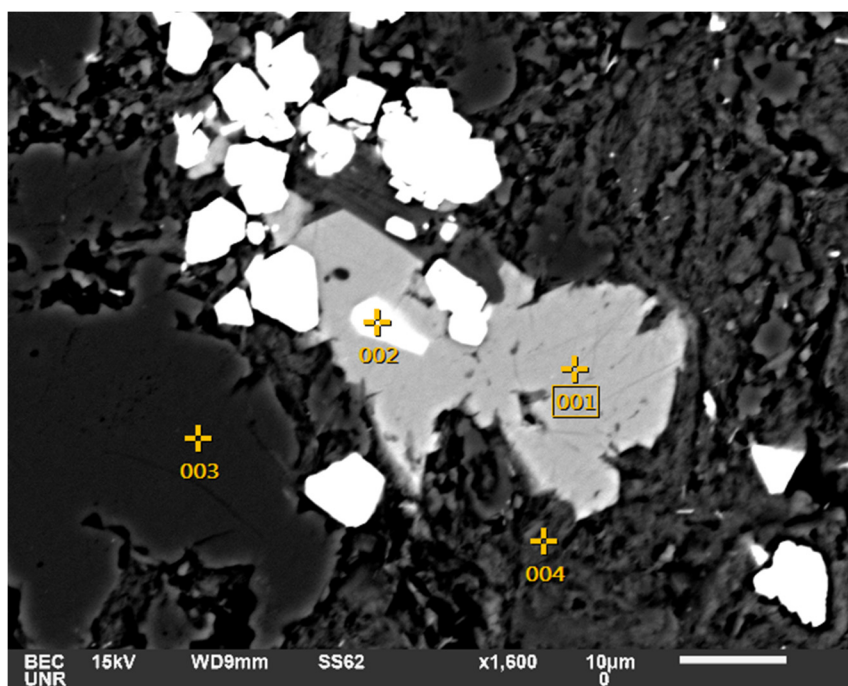
Real Time : 15.00 sec.

DeadTime : 3.00 %

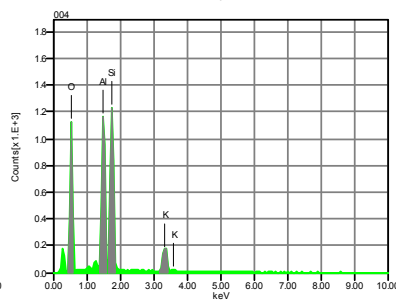
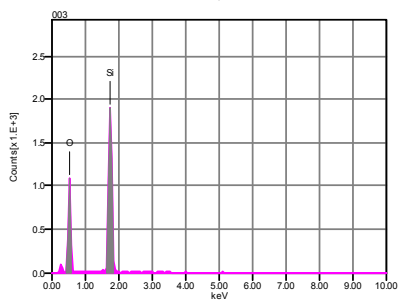
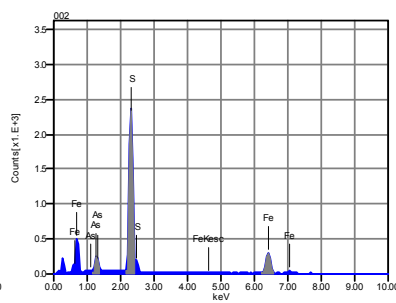
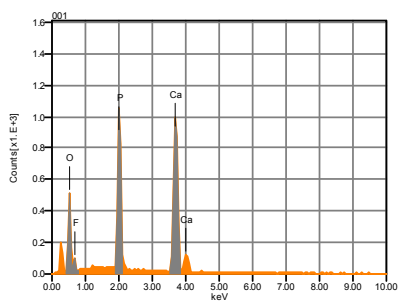
Count Rate : 3699.00  
 CPS

	P	Fe	O	F	Mg	Si	S	Ca	Zn	Probable mineral
001	19.94		38.66		4.03			37.37		Apatite
002							39.74		60.26	Sphalerite
003		4.42	47.26		8.28			21.72		Ferroan-dolomite
004			53.57			46.43				Quartz
005		4.56	48.29		8.37			20.55		Ferroan-dolomite
006	20.66		37.84		4.41			37.08		Apatite

## Dunderberg Shale mineralization



Volt : 15.00 kV  
Mag. : x 1,600  
Date : 2015/09/12  
Pixel : 1280 x 960



Acquisition Condition

Instrument : 6510(LA)

Volt : 15.00 kV

Current : ---

Process Time : T4

Live time : 14.39 sec.

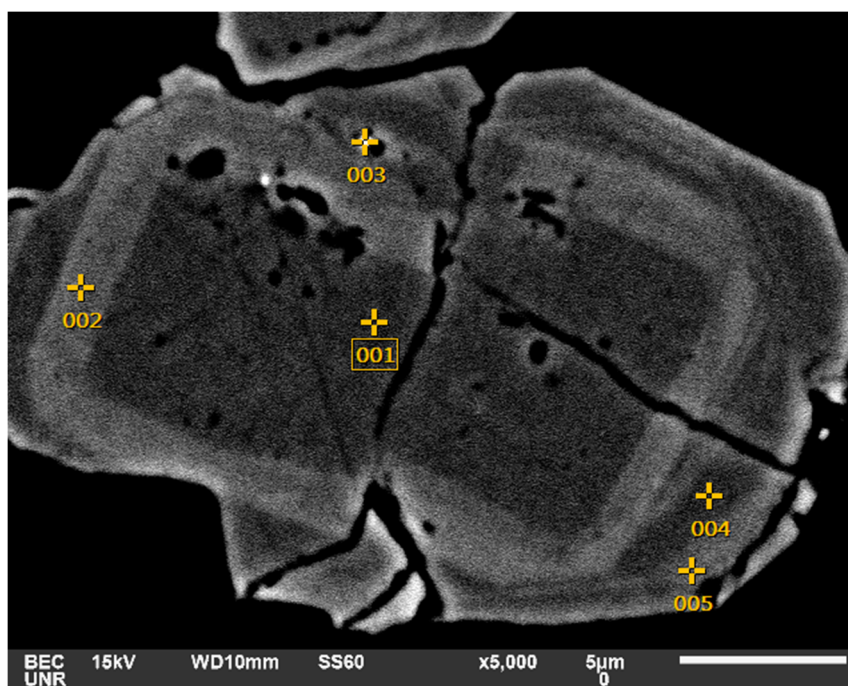
Real Time : 15.00 sec.

DeadTime : 4.00 %

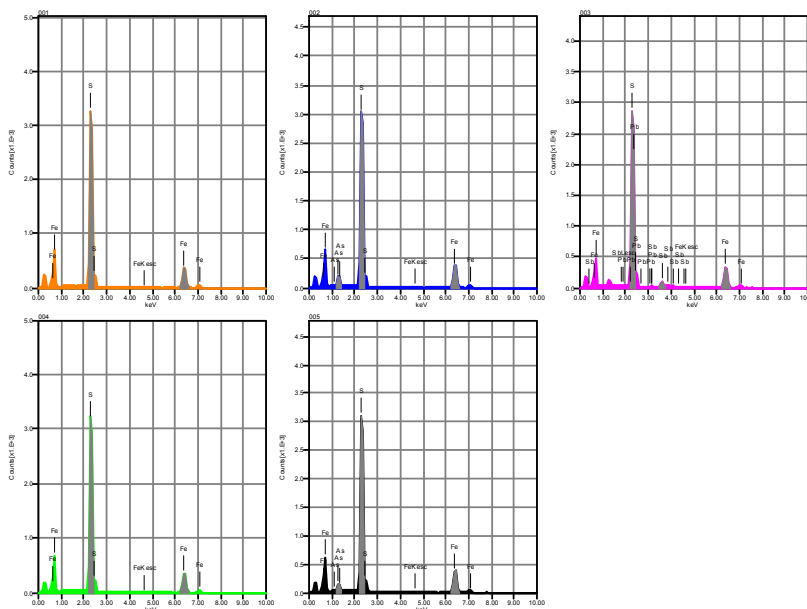
Count Rate : 2598.00 CPS

	P	Fe	K	O	F	Al	Si	S	Ca	As	Probable mineral
001	21.70				35.20	5.44			37.66		Apatite
002	40.48							51.20		8.33	Arsenian-pyrite
003				53.12			46.88				Quartz
004			7.87	46.23		19.55	26.35				Sericite

# Secret Canyon Mineralization



Volt : 15.00 kV  
 Mag. : x 5,000  
 Date : 2015/05/10  
 Pixel : 1280 x 960



## Acquisition Condition

Instrument : 6510(LA)

Volt : 15.00 kV

Current : ---

Process Time : T3

Live time : 14.37 sec.

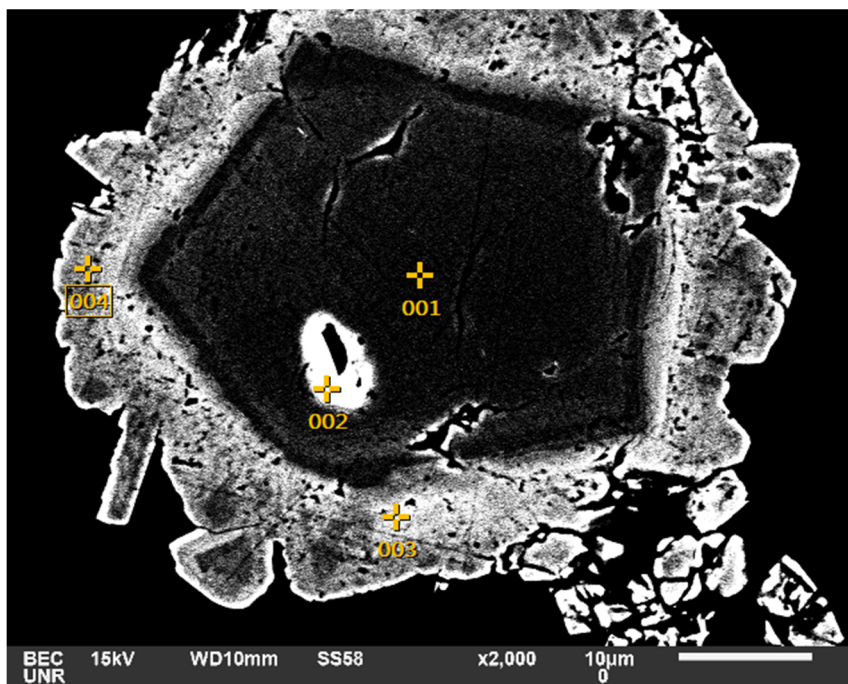
Real Time : 15.00 sec.

DeadTime : 4.00 %

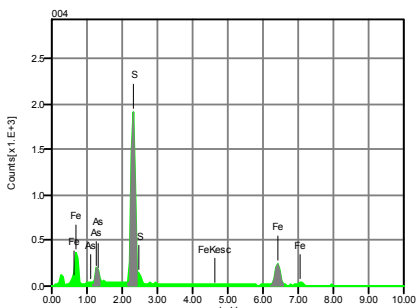
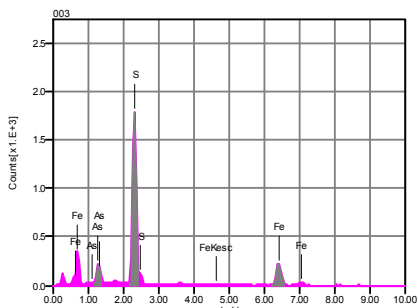
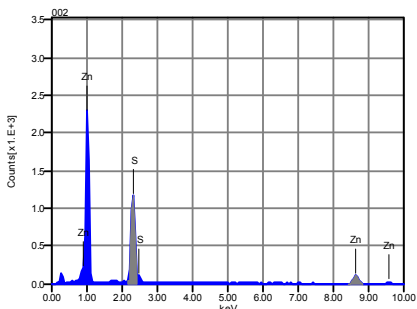
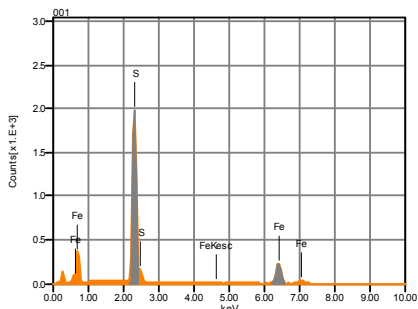
Count Rate : 4471.00  
 CPS

	Fe	Pb	S	As	Sb	Probable mineral
001	45.02		54.98			Pyrite
002	43.32		50.99	5.69		Arsenian-pyrite
003	34.03	13.09	44.63		8.24	Galena or stibnite with pyrite contamination
004	44.09		55.91			Pyrite
005	43.22		52.66	4.12		Arsenian-pyrite

# Secret Canyon Shale Mineralization



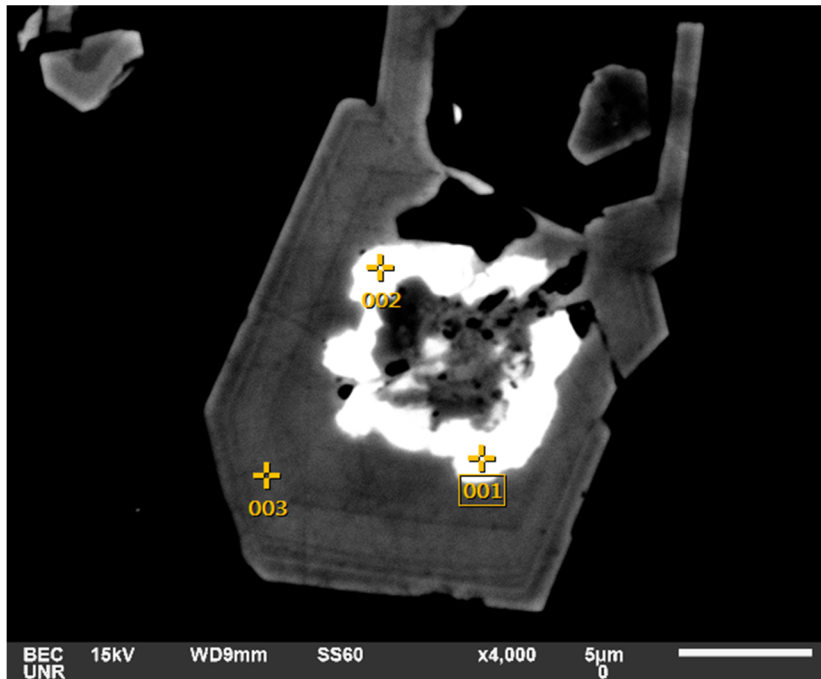
Volt : 15.00 kV  
 Mag. : x 2,000  
 Date : 2015/05/07  
 Pixel : 1280 x 960



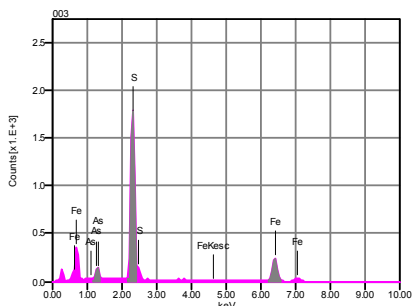
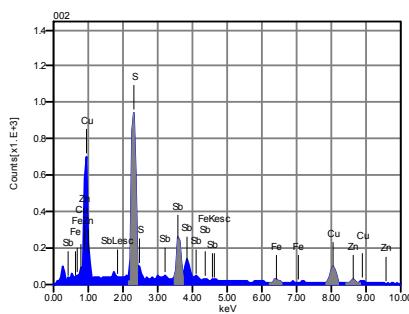
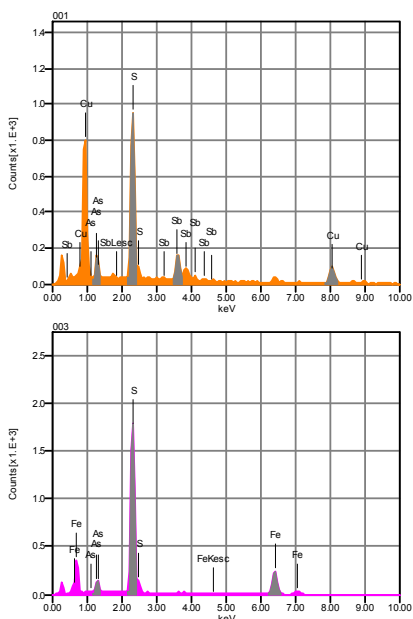
Acquisition Condition  
 Instrument : 6510(LA)  
 Volt : 15.00 kV  
 Current : ---  
 Process Time : T3  
 Live time : 14.61 sec.  
 Real Time : 15.00 sec.  
 DeadTime : 3.00 %  
 Count Rate : 2884.00  
 CPS

	Fe	S	Zn	As	Probable mineral
001	44.50	55.50			Pyrite
002		39.23	60.77		Sphalerite
003	41.92	48.36		9.72	Arsenian-pyrite
004	43.20	47.90		8.89	Arsenian-pyrite

# Secret Canyon Mineralization



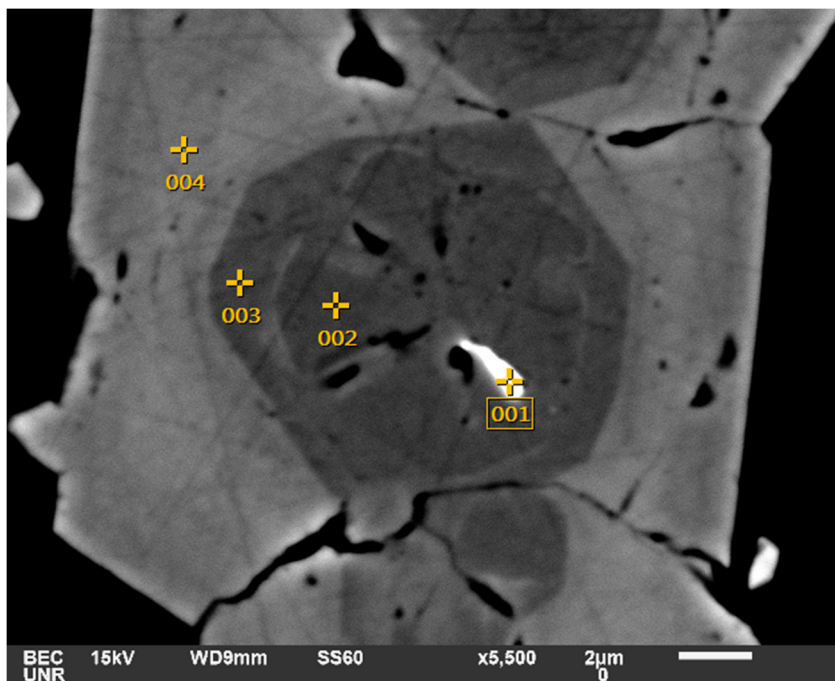
Volt : 15.00 kV  
 Mag. : x 4,000  
 Date : 2015/05/11  
 Pixel : 1280 x 960



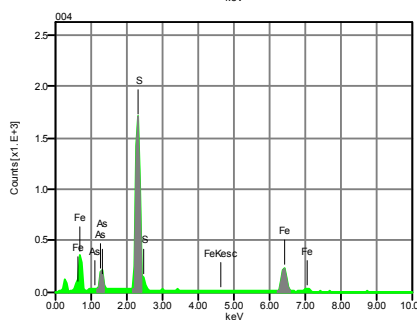
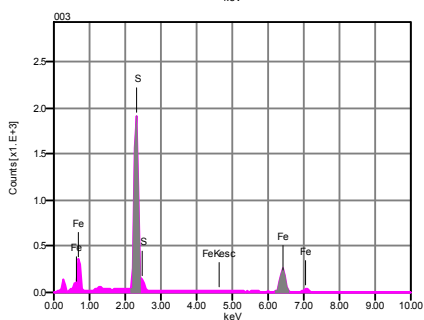
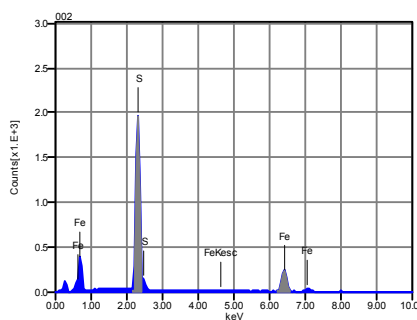
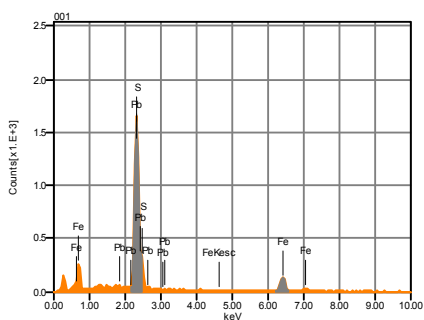
Acquisition Condition  
 Instrument : 6510(LA)  
 Volt : 15.00 kV  
 Current : ---  
 Process Time : T3  
 Live time : 14.60 sec.  
 Real Time : 15.00 sec.  
 DeadTime : 3.00 %  
 Count Rate : 2706.00 CPS

	Fe	S	Cu	Zn	As	Sb	Probable mineral
001		30.39	38.91		7.88	22.82	Tetrahedrite
002	2.74	27.54	33.46	7.29		28.97	Tetrahedrite
003	43.35	50.30			6.36		Arsenian-pyrite

# Secret Canyon Shale Mineralization



Volt : 15.00 kV  
 Mag. : x 5,500  
 Date : 2015/05/11  
 Pixel : 1280 x 960



## Acquisition Condition

Instrument : 6510(LA)

Volt : 15.00 kV

Current : ---

Process Time : T3

Live time : 14.59 sec.

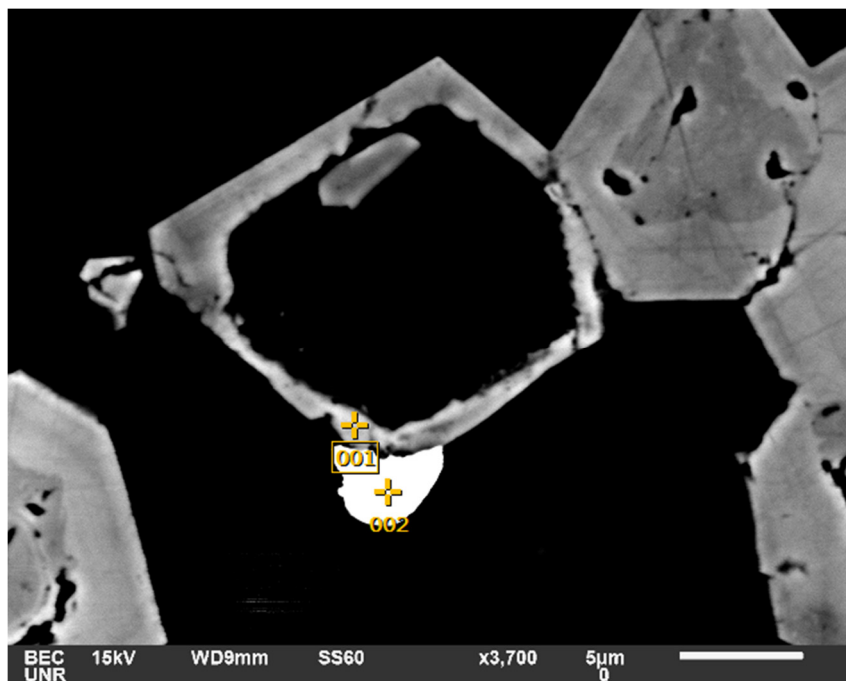
Real Time : 15.00 sec.

DeadTime : 3.00 %

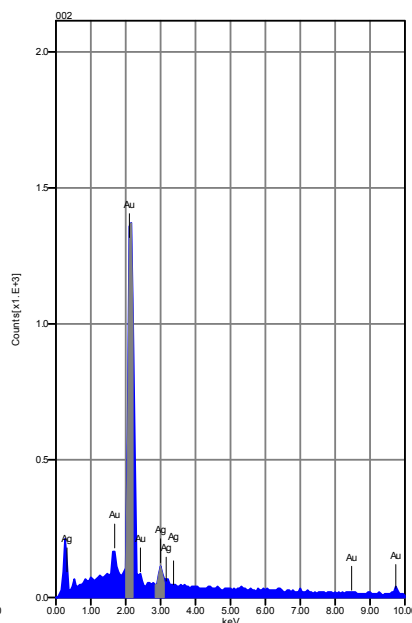
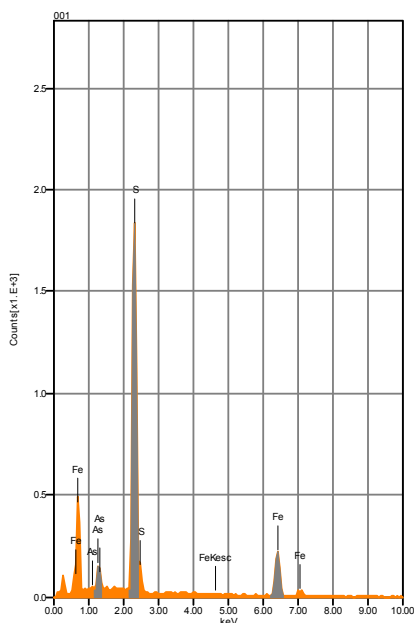
Count Rate : 2862.00  
 CPS

	Fe	Pb	S	As	Probable mineral
001	25.71	38.29	36.01		Galena
002	44.29		55.71		Pyrite
003	45.49		54.51		Pyrite
004	42.21		48.59	9.20	Arsenian-pyrite

## Native Au in Secret Canyon Shale



Volt : 15.00 kV  
 Mag. : x 3,700  
 Date : 2015/05/11  
 Pixel : 1280 x 960



Acquisition Condition

Instrument : 6510(LA)

Volt : 15.00 kV

Current : ---

Process Time : T3

Live time : 14.60 sec.

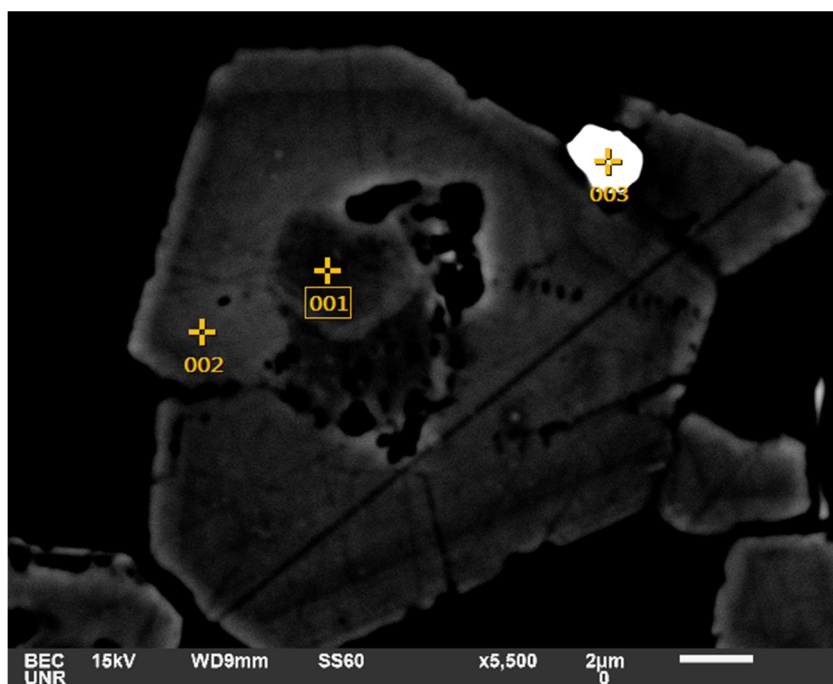
Real Time : 15.00 sec.

DeadTime : 3.00 %

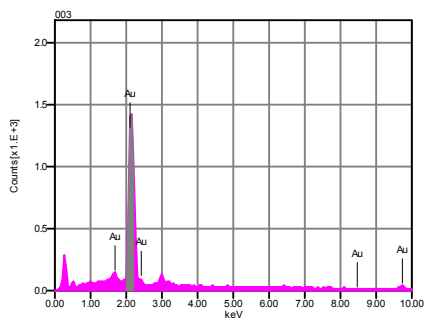
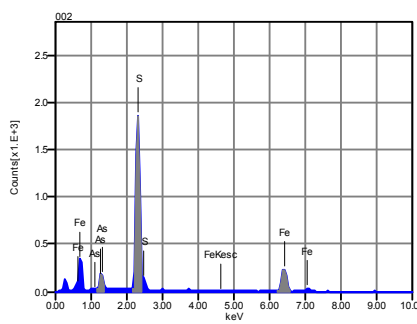
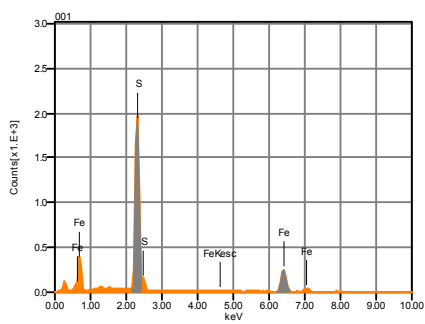
Count Rate : 2855.00  
 CPS

	Fe	Au	Ag	S	As	Probable mineral
001	40.70			52.99	6.31	Arsenina-pyrite
002		93.32	6.68			Native gold

# Native Au in Secret Canyon Shale



Volt : 15.00 kV  
 Mag. : x 5,500  
 Date : 2015/05/11  
 Pixel : 1280 x 960

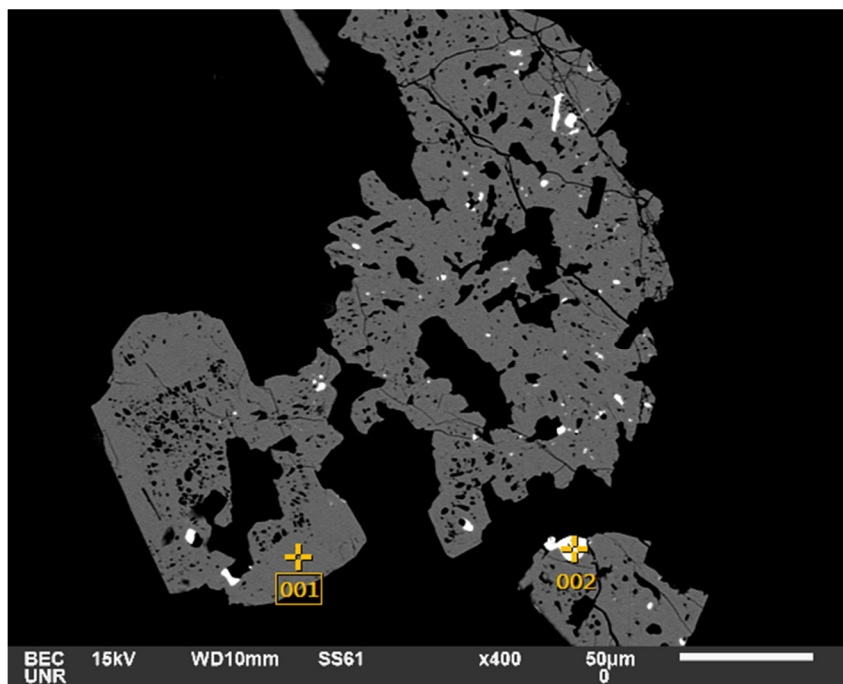


## Acquisition Condition

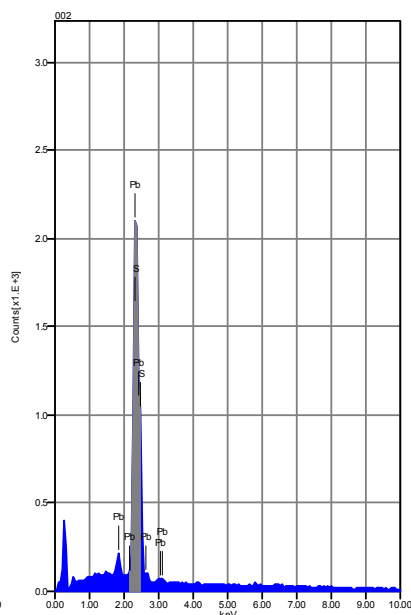
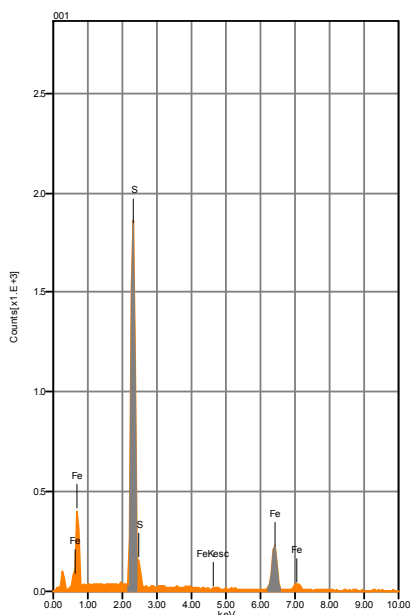
Instrument : 6510(LA)  
 Volt : 15.00 kV  
 Current : ---  
 Process Time : T3  
 Live time : 14.59 sec.  
 Real Time : 15.00 sec.  
 DeadTime : 3.00 %  
 Count Rate : 2827.00  
 CPS

	Fe	Au	S	As	Probable mineral
001	46.73		53.27		Pyrite
002	42.11		49.56	8.33	Arsenian-pyrite
003		100.00			Native gold

### Galena in QSP alteration pyrite in a dike in Secret Canyon Shale



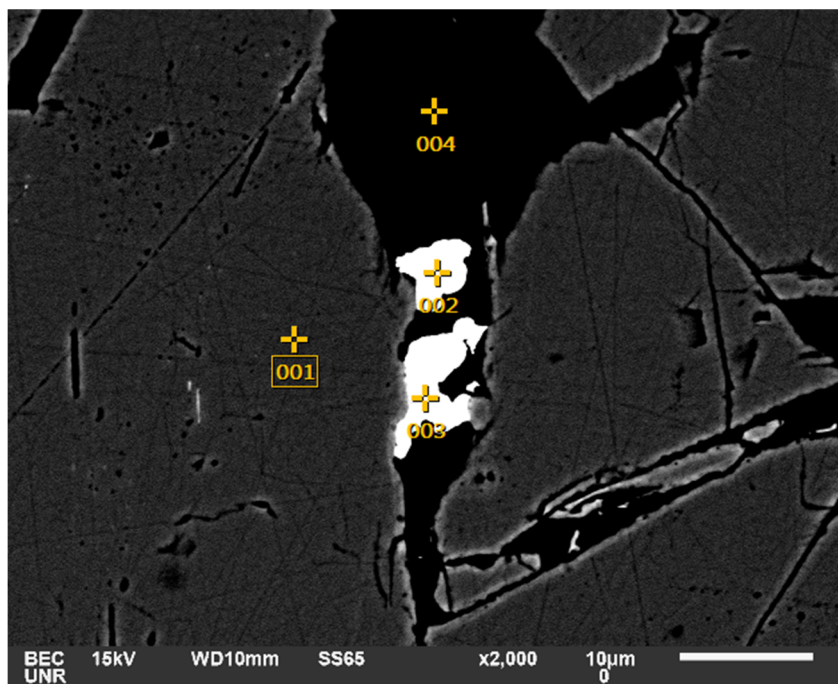
Volt : 15.00 kV  
 Mag. : x 400  
 Date : 2015/05/13  
 Pixel : 1280 x 960



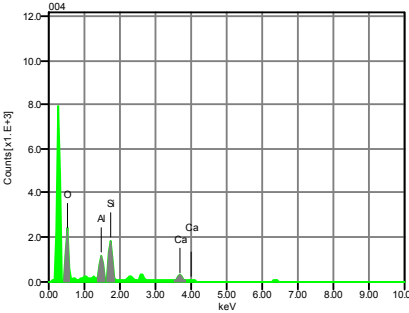
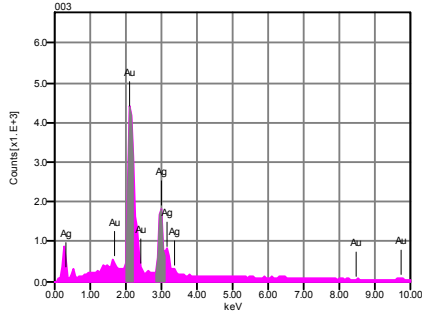
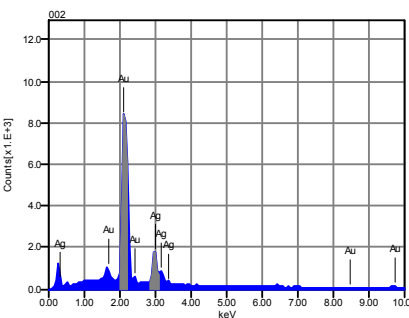
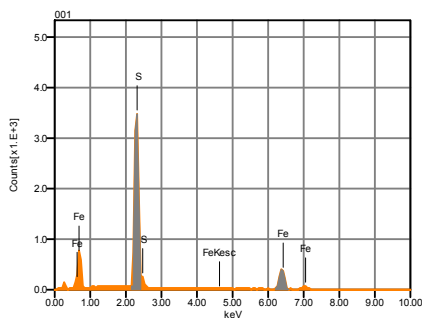
Acquisition Condition  
 Instrument : 6510(LA)  
 Volt : 15.00 kV  
 Current : ---  
 Process Time : T3  
 Live time : 6.96 sec.  
 Real Time : 7.33 sec.  
 DeadTime : 5.00 %  
 Count Rate : 5311.00  
 CPS

	Fe	Pb	S	Probable mineral
001	44.67		55.33	Pyrite
002		87.40	12.60	Galena

# Native Au in Secret Spot



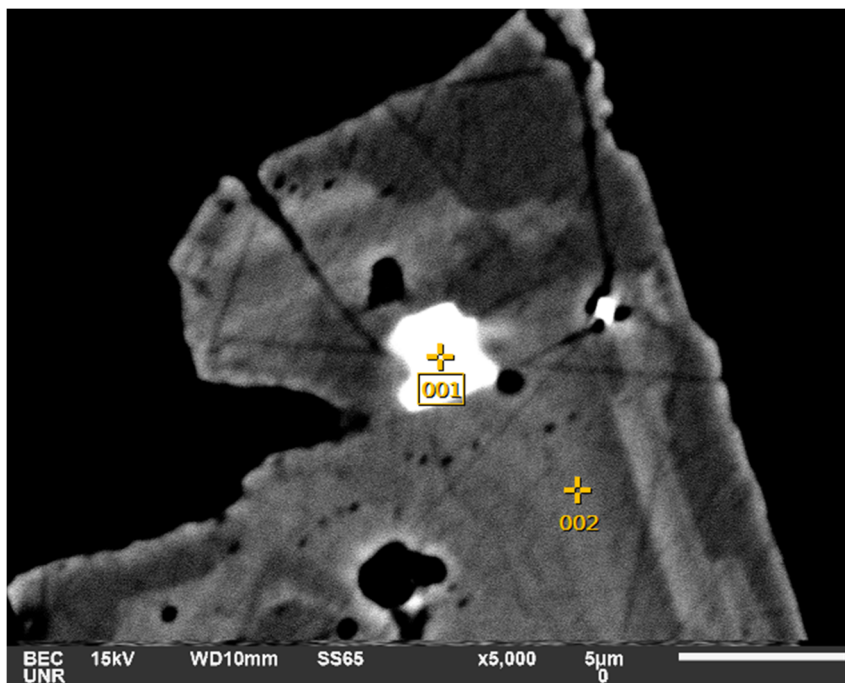
Volt : 15.00 kV  
 Mag. : x 2,000  
 Date : 2015/01/23  
 Pixel : 1280 x 960



Acquisition Condition  
 Instrument : 6510(LA)  
 Volt : 15.00 kV  
 Current : ---  
 Process Time : T3  
 Live time : 7.27 sec.  
 Real Time : 7.96 sec.  
 DeadTime : 9.00 %  
 Count Rate : 7655.00  
 CPS

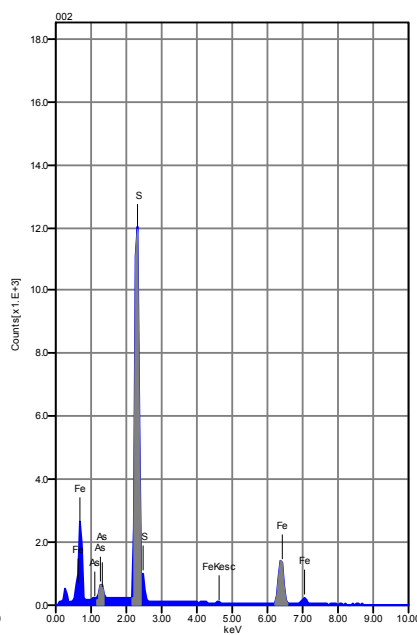
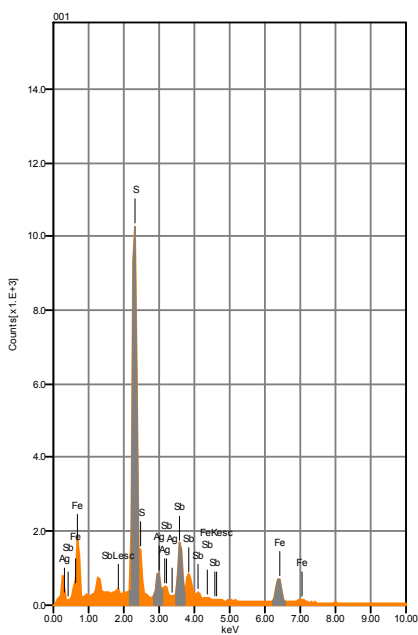
	Fe	O	Au	Ag	Al	Si	S	Ca	Probable mineral
001	44.73						55.27		Pyrite
002			79.10	20.90					Electrum
003			61.97	38.03					Electrum
004		57.97			11.28	23.05		7.70	Quartz with possible calcite/clay contamination

## Secret Spot Mineralization



Volt : 15.00 kV  
 Mag. : x 5,000  
 Date : 2015/01/23  
 Pixel : 1280 x 960

BEC UNR 15kV WD10mm SS65 x5,000 5µm 0



Acquisition Condition

Instrument : 6510(LA)

Volt : 15.00 kV

Current : ---

Process Time : T3

Live time : 30.00 sec.

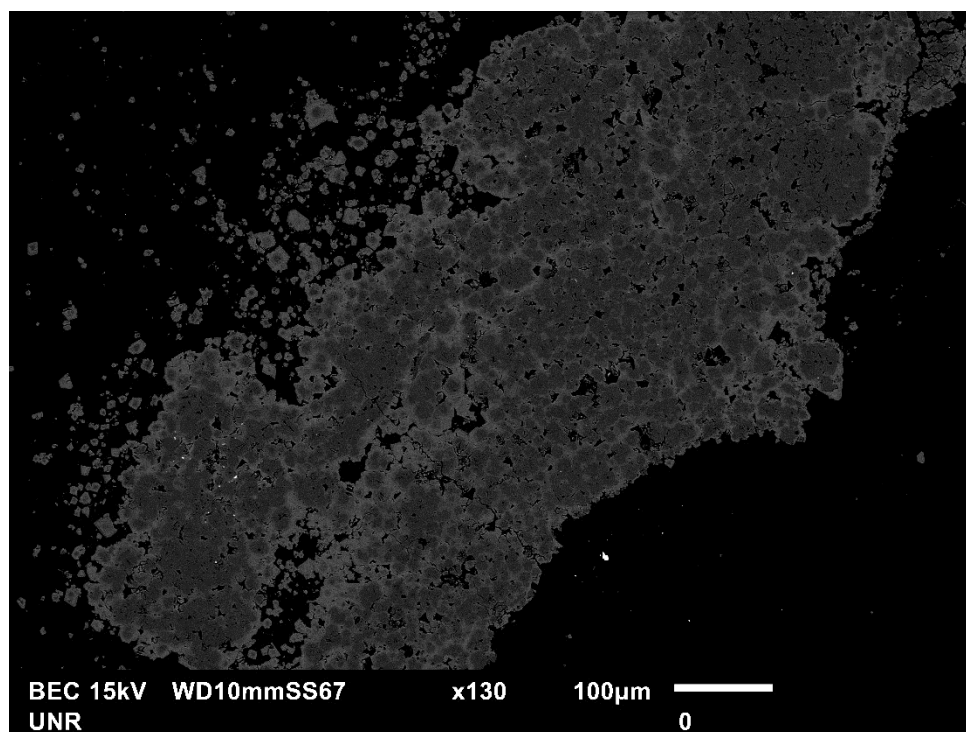
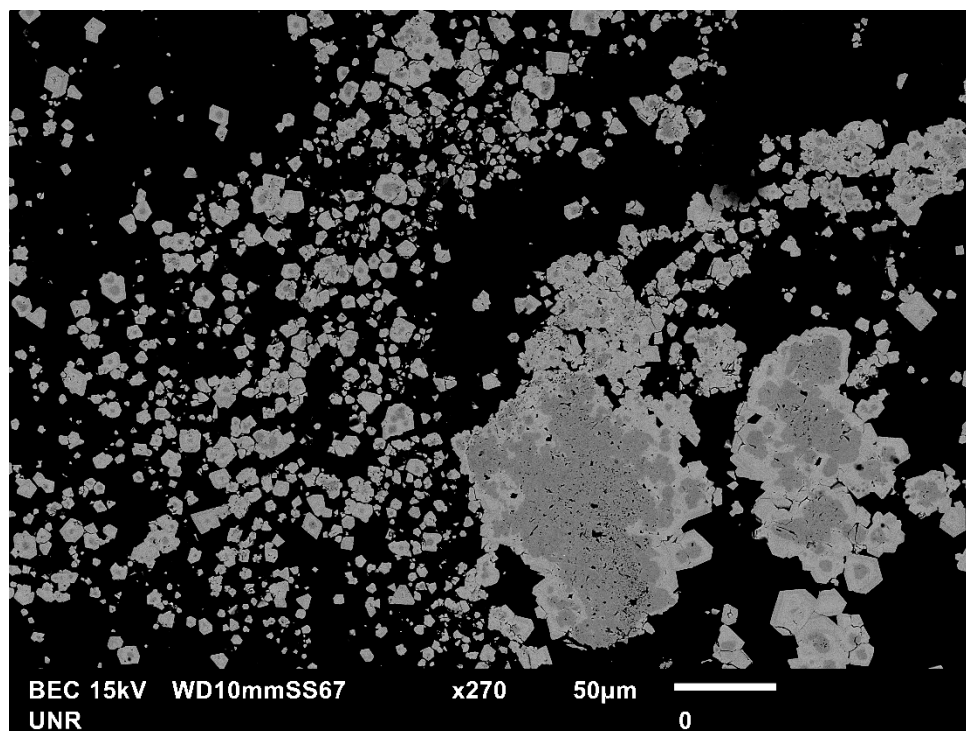
Real Time : 33.15 sec.

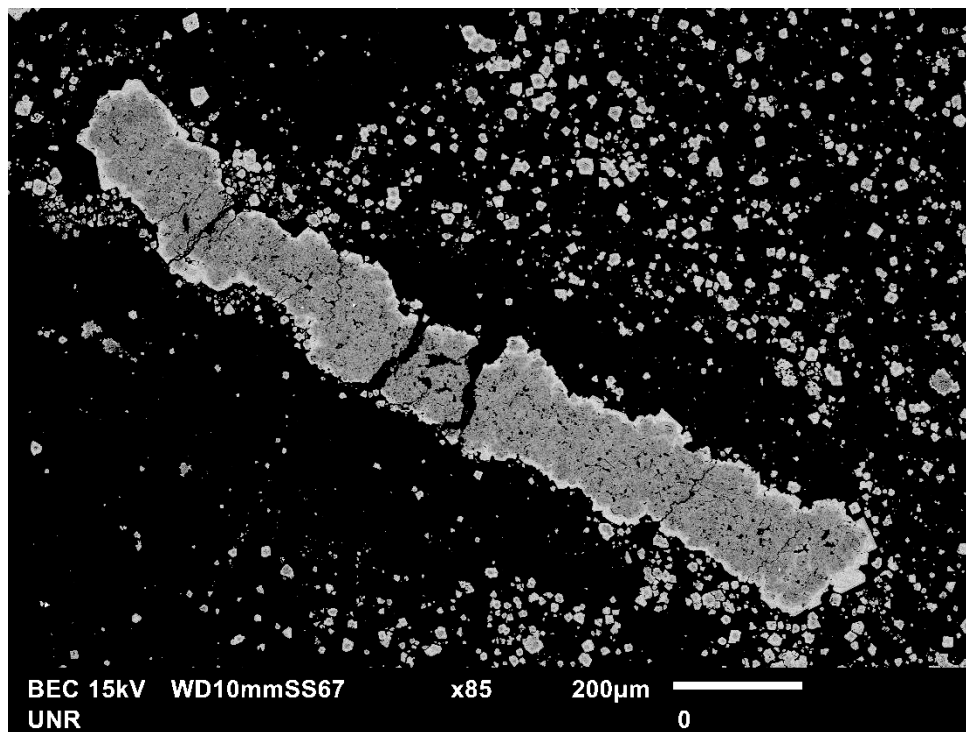
DeadTime : 10.00 %

Count Rate : 10837.00  
 CPS

	Fe	Ag	S	As	Sb	Probable mineral
001	18.58	10.28	38.55		32.60	Argentiferous-tetrahedrite
002	43.56		52.59	3.85		Arsenian-pyrite

## PK175C-967: Arsenian-pyrite SEM images





PK137CA-918': Argentiferous-tetrahedrite in arsenian-pyrite

